National Library of Canada
Acquisitions and Bibliographic Services Branch
395 Wellington Street
Ottawa, Ontario
K1A 0N4

Bibliothèque nationale du Canada
Direction des acquisitions et des services bibliographiques
395, rue Wellington
Ottawa (Ontario)
K1A 0N4

Your file Votre référence

Our file Notre référence

NOTICE

The quality of this microform is heavily dependent upon the quality of the original thesis submitted for microfilming. Every effort has been made to ensure the highest quality of reproduction possible.

If pages are missing, contact the university which granted the degree.

Some pages may have indistinct print especially if the original pages were typed with a poor typewriter ribbon or if the university sent us an inferior photocopy.

Reproduction in full or in part of this microform is governed by the Canadian Copyright Act, R.S.C. 1970, c. C-30, and subsequent amendments.

AVIS

La qualité de cette microforme dépend grandement de la qualité de la thèse soumise au microfilmage. Nous avons tout fait pour assurer une qualité supérieure de reproduction.

S'il manque des pages, veuillez communiquer avec l'université qui a conféré le grade.

La qualité d'impression de certaines pages peut laisser à désirer, surtout si les pages originales ont été dactylographiées à l'aide d'un ruban usé ou si l'université nous a fait parvenir une photocopie de qualité inférieure.

La reproduction, même partielle, de cette microforme est soumise à la Loi canadienne sur le droit d'auteur, SRC 1970, c. C-30, et ses amendements subséquents.

Canada

University of Alberta

PHOTON PROPAGATION AND DETECTION IN SPECT: THEORY, EXPERIMENTAL VALIDATION, AND APPLICATIONS

by

TERENCE ANTHONY RIAUKA

A thesis submitted to the Faculty of Graduate Studies and Research in partial fulfillment of the requirements of the degree of Doctor of Philosophy

in

Medical Physics

DEPARTMENT OF PHYSICS

Edmonton, Alberta

Spring 1995

National Library
of Canada

Acquisitions and
Bibliographic Services Branch

395 Wellington Street
Ottawa, Ontario
K1A 0N4

Bibliothèque nationale
du Canada

Direction des acquisitions et
des services bibliographiques

395, rue Wellington
Ottawa (Ontario)
K1A 0N4

Your file Votre référence

Our file Notre référence

THE AUTHOR HAS GRANTED AN IRREVOCABLE NON-EXCLUSIVE LICENCE ALLOWING THE NATIONAL LIBRARY OF CANADA TO REPRODUCE, LOAN, DISTRIBUTE OR SELL COPIES OF HIS/HER THESIS BY ANY MEANS AND IN ANY FORM OR FORMAT, MAKING THIS THESIS AVAILABLE TO INTERESTED PERSONS.

L'AUTEUR A ACCORDE UNE LICENCE IRREVOCABLE ET NON EXCLUSIVE PERMETTANT A LA BIBLIOTHEQUE NATIONALE DU CANADA DE REPRODUIRE, PRETER, DISTRIBUER OU VENDRE DES COPIES DE SA THESE DE QUELQUE MANIERE ET SOUS QUELQUE FORME QUE CE SOIT POUR METTRE DES EXEMPLAIRES DE CETTE THESE A LA DISPOSITION DES PERSONNE INTERESSEES.

THE AUTHOR RETAINS OWNERSHIP OF THE COPYRIGHT IN HIS/HER THESIS. NEITHER THE THESIS NOR SUBSTANTIAL EXTRACTS FROM IT MAY BE PRINTED OR OTHERWISE REPRODUCED WITHOUT HIS/HER PERMISSION.

L'AUTEUR CONSERVE LA PROPRIETE DU DROIT D'AUTEUR QUI PROTEGE SA THESE. NI LA THESE NI DES EXTRAITS SUBSTANTIELS DE CELLE-CI NE DOIVENT ETRE IMPRIMES OU AUTREMENT REPRODUITS SANS SON AUTORISATION.

ISBN 0-612-01754-0

Canada

University of Alberta

Library Release Form

NAME OF AUTHOR: **Terence Anthony Riauka**

TITLE OF THESIS: **Photon Propagation and Detection in SPECT: Theory, Experimental Validation, and Applications**

DEGREE: **Doctor of Philosophy**

YEAR THIS DEGREE GRANTED: **1995**

Permission is hereby granted to the University of Alberta Library to reproduce single copies of this thesis and to lend or sell such copies for private, scholarly, or scientific research purposes only.

The author reserves all other publication and other rights in association with the copyright in the thesis, and except as hereinbefore provided neither the thesis or any substantial portion thereof may be printed or otherwise reproduced in any material form whatever without the author's prior written permission.

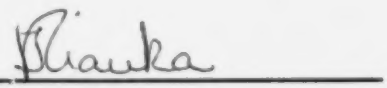

Terence A. Riauka
#2, 14916 - 56th Avenue
Edmonton, Alberta
Canada, T6H 4X9

April 18, 1995

University of Alberta

Faculty of Graduate Studies and Research

The undersigned certify that they have read, and recommend to the Faculty of Graduate Studies and Research for acceptance, a thesis entitled **Photon Propagation and Detection in SPECT: Theory, Experimental Validation, and Applications** submitted by Terence Anthony Riauka in partial fulfillment of the requirements for the degree of Doctor of Philosophy in Medical Physics.

Dr. H. R. Hooper (Supervisor)

Dr. Z. W. Gortel (Supervisor)

Dr. R. Sloboda

Dr. L. G. Greeniaus

Dr. Z. J. Koles

Dr. R. J. Jaszczak (External Reader)

Dedication

I dedicate this thesis to my loving wife.

Erica, your love and faith have made this goal possible.

Acknowledgments

I would like to take this opportunity to acknowledge all the wonderful and generous people who have helped make the completion of this thesis work possible. Firstly, I must thank my supervisors Dr. Richard Hooper and Dr. Zbigniew Gortel for their constant support, inspiration, patience, and guidance throughout the last (can you believe it) 6 years. Zbyszek provided me with a love and a deeper understanding for physics and mathematics which will last a lifetime, and that a problem must be understood before it can be solved. Rick taught me joy of applying physics and mathematics to "real" problems, and provided me with the resources and tools to investigate such problems. I would also like to thank the committee members for their insightful comments and reviews of the thesis. I would especially like to thank Dr. Ron Sloboda for his continual participation in the thesis, and for his meticulous review of the thesis which ultimately led to a better written thesis. Finally, I would like to thank Dr. David Gilland for his collaborative efforts in extending the thesis work to actual reconstructions, and for the numerous suggestions and discussions which helped significantly with the polishing of the numerical code.

The Department of Nuclear Medicine at the Cross Cancer Institute, also provided much support to the thesis work (and also lots of fun) and deserves much thanks. Ms. Carrie Morin patiently taught me the use of the gamma cameras, and then when necessary, retaught me. I must thank Ms. Lori Golberg and Mr. Ken Golberg (and also Carrie) for teaching me that a patient is not a plastic water filled cylinder, that the heart is on the left side of the body and we all (or most of us) have two kidneys, and many other finer points of clinical nuclear medicine. I would be remiss if I did not thank Cheryl Loeffler for all the extra work and pain that I have caused her over the years. Finally, I must thank Lori, Dr. Sandy McEwan, and Dr. Graeme Boniface for all the encouragement they gave to finalize the thesis, and for introducing me to the commercial applications of science.

The Department of Physics at the University of Alberta has been a constant source of support. Ms. Lynn Chandler has ensured that I never missed a deadline and was always most helpful when a problem arose - and there were a number of problems. I also want to thank all the excellent professors from whom I took courses from, and in particular Dr. Razavy for the best course I have ever taken - QM680. I must also thank the department as a whole for sponsoring and supporting numerous scholarship applications, which ultimately lead to me receiving a number of awards and scholarships.

I must thank the University of Lethbridge and in particular the Department of Physics for the excellent undergraduate education I received. I believe strongly that my success has been due to what I was taught by such exceptional lecturers and mentors as Dr. Kermat Ali, Dr. Godfrey Gumbs, Dr. David Naylor, and, last but not least, Dr. Sam Konuso.

I am most grateful to the Natural Sciences and Engineering Council of Canada (NSERC) and the Alberta Heritage Foundation for Medical Research (AHFMR) for their numerous and generous scholarships and awards. The travel allowance stipend from the AHFMR allowed me to attend numerous international conferences throughout my Ph.D. studies, which inevitably had a great influence in shaping this thesis work. I would like to thank Physics and Graduate Studies and Research for providing additional financial support whenever it was necessary.

Finally, I would like to thank my wife Erica, my family, and Erica's family for all the love, prayers, and support (financial and emotional) they have provided over the years. I would especially like to thank my sister Debbie and her husband Gerard for believing in me and giving me the opportunity and resources to pursue this dream. I am sure that none of you will ever know just how much all of you have done for me. With all my love I thank you.

Abstract

An analytical theory of photon propagation and detection for SPECT is presented. The theory accurately accounts for most of the physical processes involved with photon propagation and detection in SPECT. In particular, it accounts for photon propagation, nonuniform attenuation (including photoelectric absorption and all orders of Compton and Rayleigh scattering combinations and possibilities), the three dimensional depth-dependent collimator resolution, and the intrinsic energy-dependent detection probability function of the Anger camera (both the intrinsic energy-dependent detection efficiency and the intrinsic energy resolution of a NaI(Tl) scintillation crystal). The theory allows integral expressions for each scattering order of the photon detection kernel to be formulated separately. The photon detection kernel is central to iterative reconstruction algorithms like the Maximum Likelihood Expectation Maximization (MLEM) algorithms.

Numerical integration code is developed in order to calculate the lowest three orders of the kernel for general nonuniform imaging situations. The results calculated from the numerical code are compared with those obtained from experiment. The code is shown to provide an accurate tool for modeling nonuniform experimental imaging situations for both point and extended source distributions, provided a narrow energy window and a lower energy photon source, like ^{99m}Tc and ^{123}I, are used.

The connectivity problem of the kernel is quantitatively investigated, within the context of source voxel – projection pixel connectivity. It is demonstrated that the main factor determining the extent of the kernel connectivity is photon scattering, with 3D depth-dependent collimator hole resolution being of secondary but still significant importance. Understanding the connectivity of the kernel is necessary for both practical and efficient implementation of it in iterative reconstruction algorithms.

Finally, using the results of the kernel connectivity investigation, the kernel expressions obtained are used to compute a reconstruction kernel for a simple, but real, imaging situation. The calculated kernel is employed in an MLEM-type algorithm and the source

distribution is reconstructed from experimentally acquired projection data. The reconstructed distributions obtained from the MLEM algorithm show improved resolution within the transaxial slices as well as between the slices over the same obtained from the traditional filtered backprojection method of reconstruction.

Table of Contents

I. INTRODUCTION 1

A. Nuclear Medicine Imaging and Development 1

B. Nuclear Medicine Tomographic Imaging 9

C. Overview of Thesis 14

II. BACKGROUND - NUCLEAR MEDICINE PHYSICS 21

A. Physics of Photon Propagation 21

Compton Scattering 21

Rayleigh Scattering 23

Photon Scattering Interactions 24

Photoelectric Absorption 25

Linear Attenuation Coefficient 26

B. Radioactive Sources 26

C. Gamma Camera and Photon Detection Physics 28

The Anger Camera 28

Collimation 28

Energy & Intrinsic Spatial Resolution of the Anger Camera 30

D. Image Formation Process in Nuclear Medicine 35

E. Source Reconstruction in SPECT 37

The Integral Kernel Equation 37

Reconstructions - The Inverse Problem 39

F. The Radon Transform Approach 41

Correction and Compensation Methods for the Radon Transform 44

Image Processing - Filtering 45

Scatter Correction 48

Attenuation Correction 49

Summary 50

G. Iterative Reconstruction Methods 51

H. Reconstruction Kernels 53

I. Modeling Photon Detection Kernels 54

III. THEORY OF PHOTON PROPAGATION AND DETECTION IN SPECT **68**

A. Analytical Approach to Reconstruction Kernels 68

Current Densities of the Primary and Scattered Photons 69

B. Modeling the Detection Process 74

C. Modeling the Energy Response of the Detector 76

D. Integral Kernel Expressions 77

IV. KERNEL CALCULATION AND NUMERICAL METHODS **80**

A. Description of the Imaging Situation 80

Linear Attenuation Coefficient 81

Electron Density 82

B. Anger Camera Parameters 82

Collimation 82

Energy Dependent Detection Probability 84

C. Calculation of the Kernel Expressions 84

First-Order Calculation 85

Second-Order Calculation 87

Energy Spectra Calculation 88

V. EXPERIMENTAL VALIDATION **94**

A. Experimental Methods 95

B. Numerical Methods 99

C. Results 100

D. Discussion of Results 102

E. Calculation times 104

F. Summary 104

VI. INVESTIGATION OF RECONSTRUCTION KERNELS **141**

A. Kernel Connectivity 141

Methods 142

Results and Discussion 143

B. Application of Theoretical Kernel to Reconstructions 144

VII. CONCLUSIONS **159**

REFERENCES **164**

List of Figures

Figure I-1: The right hand image demonstrates the discretization process of the (continuous) image on the left into pixels. 16

Figure I-2: This figure illustrates the typical imaging geometry for SPECT. The projection plane rotates about the axis through the center of the discrete source distribution. 17

Figure I-3: The concept of voxels and transaxial slices for describing the discrete source distribution is shown. 18

Figure I-4: The 3D imaging problem in Fig. I-2 is reduced to a 2D problem by considering a single transaxial slice of the 3D source distribution. 18

Figure I-5: (a) Three 1D projections of a source distribution consisting of two square regions of activity. 19

Figure II-1: Schematic representations of (a) the Compton scattering interaction and (b) the Klein-Nishina scattering cross section. 58

Figure II-2: Fraction of the incident photon energy given to the scattered photon and the Klein-Nishina cross section versus scattering angle using Eqs. (II.1) and (II.5), respectively, for photons with incident energy $E = 140 keV$. 59

Figure II-3: Schematic representation of the Anger camera and its components. 59

Figure II-4: The concept of absorptive collimation is shown (a) from the collimator perspective and (b) from the source perspective. 60

Figure II-5: The probability for photons of energy E to trigger detection for 10%, 15%, 20%, 25%, and 30% symmetric energy windows centered at 140 keV as given by Eq. (II.20). 61

Figure II-6: The total detection probability for photons of energy E for an Anger camera employing a 3/8" NaI crystal and a 20% symmetric energy window centered at 140 keV as given by Eq. (II.22). 62

Figure II-7: Cross section of the cylindrical water-filled phantom and the five point sources. 63

Figure II-8: Projection profile of a uniform phantom with five point sources shown in Fig. II-7, assuming an ideal collimator and no attenuation. 64

Figure II-9: Projection profile of a uniform phantom with five point sources shown in Fig. II-7, using a LEAP collimator and assuming no attenuation. 64

Figure II-10: Projection profile of a uniform phantom with five point sources shown in Fig. II-7, using a LEAP collimator. The projection profile data is plotted using both a linear scale (solid line) and a logarithmic scale (dotted line). The effects of attenuation are shown for a camera with ideal energy resolution. Only primary photons are detected..... 65

Figure II-11: Projection profile of a uniform phantom with five point sources shown in Fig. II-7, using a LEAP collimator. The effects of attenuation are shown for a camera with 12% energy resolution, 3/8" NaI crystal, and a 20% symmetric energy window for ^{99m}Tc. Both scattered and unscattered photons are detected..... 65

Figure II-12: Projection profile of a uniform phantom with five point sources shown in Fig. II-7, obtained from experiment for a camera using LEAP collimator with 12% energy resolution, 3/8" NaI crystal, and a 20% symmetric energy window for ^{99m}Tc..... 66

Figure II-13: Schematic representations of the integration volume for Eq. (II.30)..... 67

Figure II-14: Geometry for Eq. (II.33) showing the relationship between the (x,y) and (t,s) coordinate systems..... 67

Figure III-1: Illustration of the three lowest scattering orders..... 79

Figure III-2: Schematic representation of parallel hole collimation..... 79

Figure IV-1: Detection geometry for cylindrical hole collimator explaining symbols introduced in the main text, and in particular Eqs. (IV.1) through (IV.3): (a) complete back/front window overlap, (b) partial overlap, and (c) no overlap..... 91

Figure IV-2: Schematic representation of the cone-like integration volume for $d_3\mathbf{r}_n$ for calculating $K^{(n)}(\mathbf{R}_i,\mathbf{r}_0)$..... 92

Figure IV-3: Schematic representation of the integration coordinate system used by Eqs. (IV.8) through (IV.14) at a fixed depth from the collimator hole..... 93

Figure V-1: Cross section of the point source configurations for the uniform phantom..... 110

Figure V-2: Cross section of the point source configurations for the non-uniform phantom and their corresponding configuration indices (11-21)..... 111

Figure V-3: Cross section of short thin cylindrical source configurations for (a) uniform phantom and (b) nonuniform phantom and their corresponding configuration indices..... 112

Figure V-4: Cross section of extended cylindrical source configurations for (a) uniform phantom and (b) nonuniform phantom configurations, and their corresponding configuration indices..... 113

Figure V-5: Projection profiles for the central row for the point source located at position 1 within the uniform phantom. Experimental results: open circles with vertical error bars. Calculated results: thin line - 0^{th}-order, open squares - 1^{st}-order, open triangles - 2^{nd}-order, and thick thin - total (the sum of the 0^{th} through 2^{nd}-orders) 114

Figure V-6: Same as Figure V-5 except for the point source located at position 2 within the uniform phantom 114

Figure V-7: Same as Figure V-5 except for the point source located at position 3 within the uniform phantom 115

Figure V-8: Same as Figure V-5 except for the point source located at position 4 within the uniform phantom 115

Figure V-9: Same as Figure V-5 except for the point source located at position 5 within the uniform phantom 116

Figure V-10: Same as Figure V-5 except for the point source located at position 6 within the uniform phantom 116

Figure V-11: Same as Figure V-5 except for the point source located at position 7 within the uniform phantom 117

Figure V-12: Same as Figure V-5 except for the point source located at position 8 within the uniform phantom 117

Figure V-13: Same as Figure V-5 except for the point source located at position 9 within the uniform phantom 118

Figure V-14: Same as Figure V-5 except for the point source located at position 10 within the uniform phantom 118

Figure V-15: Same as Figure V-5 except for the point source located at position 11 within the nonuniform phantom 119

Figure V-16: Same as Figure V-5 except for the point source located at position 12 within the nonuniform phantom 119

Figure V-17: Same as Figure V-5 except for the point source located at position 13 within the nonuniform phantom 120

Figure V-18: Same as Figure V-5 except for the point source located at position 14 within the nonuniform phantom 120

Figure V-19: Same as Figure V-5 except for the point source located at position 15 within the nonuniform phantom 121

Figure V-20: Same as Figure V-5 except for the point source located at position 16 within the nonuniform phantom 121

Figure V-21: Same as Figure V-5 except for the point source located at position 17 within the nonuniform phantom 122

Figure V-22: Same as Figure V-5 except for the point source located at position 18 within the nonuniform phantom. 122
Figure V-23: Same as Figure V-5 except for the point source located at position 19 within the nonuniform phantom. 123
Figure V-24: Same as Figure V-5 except for the point source located at position 20 within the nonuniform phantom. 123
Figure V-25: Same as Figure V-5 except for the point source located at position 21 within the nonuniform phantom. 124
Figure V-26: Same as Figure V-5 except for the short cylindrical source located at position 22 within the uniform phantom. 125
Figure V-27: Same as Figure V-5 except for the short cylindrical source located at position 23 within the uniform phantom. 125
Figure V-28: Same as Figure V-5 except for the short cylindrical source located at position 24 within the uniform phantom. 126
Figure V-29: Same as Figure V-5 except for the short cylindrical source located at position 25 within the uniform phantom. 126
Figure V-30: Same as Figure V-5 except for the short cylindrical source located at position 26 within the nonuniform phantom. 127
Figure V-31: Same as Figure V-5 except for the short cylindrical source located at position 27 within the nonuniform phantom. 127
Figure V-32: Same as Figure V-5 except for the short cylindrical source located at position 28 within the nonuniform phantom. 128
Figure V-33: Same as Figure V-5 except for the short cylindrical source located at position 29 within the nonuniform phantom. 128
Figure V-34: Same as Figure V-5 except for the short cylindrical source located at position 30 within the nonuniform phantom. 129
Figure V-35: Same as Figure V-5 except for the large cylindrical source located at position 31 within the uniform phantom. 130
Figure V-36: Same as Figure V-5 except for the large cylindrical source located at position 32 within the uniform phantom. 130
Figure V-37: Same as Figure V-5 except for the large cylindrical source located at position 33 within the uniform phantom. 131
Figure V-38: Same as Figure V-5 except for the large cylindrical source located at position 34 within the nonuniform phantom. 131
Figure V-39: Same as Figure V-5 except for the large cylindrical source located at position 35 within the nonuniform phantom. 132
Figure V-40: Same as Figure V-5 except for the large cylindrical source located at position 36 within the nonuniform phantom. 132

Figure V-41: Energy spectra for the point source located within the uniform phantom for (a) position 1, (b) position 2, (c) position 3, and (d) position 4. 133

Figure V-42: Same as Figure V-41 except for (a) position 5, (b) position 6, (c) position 7, and (d) position 8. 134

Figure V-43: Same as Figure V-41 except for (a) position 9 and (b) position 10. 135

Figure V-44: Energy spectra for the point source located within the nonuniform phantom for (a) position 11, (b) position 12, (c) position 13, and (d) position 14. 136

Figure V-45: Same as Figure V-44 except for (a) position 15, (b) position 16, (c) position 17, and (d) position 18. 137

Figure V-46: Same as Figure V-44 except for (a) position 19, (b) position 20, and (c) position 21. 138

Figure V-47: Scatter fractions for the 10 point source positions within the uniform phantom as a function of the depth of the source in water (see Table V.1). 139

Figure V-48: Scatter fractions for the 11 point source positions within the nonuniform phantom as a function of the depth of the source in water (see Table V.1). 140

Figure VI-1: The neighborhood cumulative fraction for an N by N neighborhood centered at the pixel geometrically connected to the point source for each position within the uniform phantom for: (a) position 1, (b) position 2, (c) position 3, and (d) position 4 as given in Table V.1. 148

Figure VI-2: Same as Fig. VI-1 except for (a) position 5, (b) position 6, (c) position 7, and (d) position 8. 149

Figure VI-3: Same as Fig. VI-1 except for (a) position 9 and (b) position 10. 150

Figure VI-4: The neighborhood cumulative fraction for an N by N neighborhood centered at the pixel geometrically connected to the point source for each position within the nonuniform phantom for: (a) position 11, (b) position 12, (c) position 13, and (d) position 14 as given in Table V-1. 151

Figure VI-5: Same as Fig. VI-4 except for (a) position 15, (b) position 16, (c) position 17, and (d) position 18. 152

Figure VI-6: Same as Fig. VI-4 except for (a) position 19, (b) position 20, and (c) position 21. 153

Figure VI-7: Plot of the kernel matrix elements for one projection angle for a point source located as given in Table V-1 for (1st row) position 4, (2nd row) position 5, (3rd row) position 6, and (4th row) position 10. 154

Figure VI-8: Same as Fig. VI-7 except inverted gray scale. 155

Figure VI-9: Reconstructed transaxial slices from (upper panel) MLEM and (lower panel) filtered backprojection. 156
Figure VI-10: Same as Fig. VI-9 except inverted gray scale. 157
Figure VI-11: Profile plot along the line shown in Figs. VI-9 and VI-10. 158

List of Tables

Table V-1: Source and phantom configuration specifics corresponding to Figs. V-5 through V-46. PD is the actual depth of the source in the phantom perpendicular to the camera and EWD is the effective water depth seen by the source. For the uniform phantom configurations PD is always equal to EWD. All values are given in cm. 106

Table V-2: Relative differences (in %) between the experimental and calculated total counts as defined in Eq. (V.5) for each source configuration investigated and listed in Table V-1. The summations in Eq. (V.5) run over all 64×64 pixels of the projection for the point source configurations (i.e. 1-21), but only over the 64 pixels of the central projection row for extended source configurations (i.e. 22-36). 108

Table V-3: CPU usage times (in seconds) for a Sun Sparc 2 workstation to calculate the three lowest order contributions to the kernel for all 64×64 pixels of the camera plane for the uniform phantom configurations (columns 2-4) and for the nonuniform phantom configurations (columns 5-7) as defined in Fig. V-1 and V-2, respectively. 109

I. Introduction

A. Nuclear Medicine Imaging and Development

Nuclear medicine is a medical specialty that utilizes the properties of radioactive elements to treat and diagnose a wide variety of human diseases and disorders. Diagnostic nuclear medicine procedures generally begin with a patient receiving an intravenous injection of a substance called a radiopharmaceutical. The radiopharmaceutical is usually a complex chemical substance, such as a drug, which has been labeled with a radioactive element, and is designed to possess specific physiologic and metabolic properties of interest. The radiopharmaceutical distributes itself within the patient according to these properties, producing a three dimensional radioactive source distribution. The most useful radioactive elements for designing diagnostic radiopharmaceuticals decay by emitting photons which subsequently escape the body of the patient with sufficient probability to allow external detection. The detection of the emitted photons is accomplished by a special radiation detector called an Anger or scintillation camera. The Anger camera records the emitted photons and produces an image which is a 2D projection of the 3D radioactive source distribution onto the imaging plane of the camera. The Anger camera is mounted on a rotating gantry to allow projections of the source distribution to be obtained at any angle about the gantry's axis of rotation. Of particular diagnostic value is an imaging procedure called single photon emission computed tomography (SPECT), in which a number of projections are acquired with the Anger camera at regular angular intervals about the patient. Through a mathematical process called reconstruction, an approximate 3D representation of the source distribution is obtained from the set of projections collected at the various angles about the radioactive source distribution (i.e. patient).

The clinical significance of the procedure is that the presence of radioactivity within a certain region of the human body directly implies the presence of the radiopharmaceutical within the same region. As such, the reconstructed source distribution can be equally well regarded as the radiopharmaceutical distribution. Physiologically, the actual distribution of

the radiopharmaceutical is due to metabolization or trapping (microspheres in lung, colloid in liver, for example) by the patient's organs and tissues. Its presence or absence in various organs and tissues provides physicians with unique information about their function. Such procedures can be exploited in two ways to provide physicians with diagnostic information:

1) If it is not known how a chemical substance will be metabolized by the patient, a non-toxic volume of the substance can be labeled with a radioactive element and the subsequent process of its metabolism can then be recorded using a radiation detection device like the Anger camera, or
2) If it is known that a certain chemical substance distributes itself within certain organs and tissues of a normal patient, the absence of the substance can signal dysfunction of organs or tissues involved. By labeling the substance with a radioactive element, a radiation detection device like the Anger camera can be used to ascertain the presence or absence of the substance within a region of the patient by determining the presence of radioactivity within the same region.

The ultimate goal of diagnostic nuclear medicine imaging procedures is to provide physicians with quantitatively accurate information about the function of organs and tissues. Therefore, nuclear medicine imaging is often referred to as functional imaging. Other diagnostic imaging modalities, such as x-ray or magnetic resonance imaging, provide physicians with information regarding the structure (or morphology) of organs and tissues.

The history of events that have led to the knowledge and methods accumulated in today's nuclear medicine departments is exciting and rich in scientific genius. A complete account of these events would span nearly 100 years of the most rapid increase in scientific knowledge and is not possible here. The development of nuclear medicine and its acceptance by the medical community was directly dependent upon many of the major scientific discoveries of the 20th century, and their detailed historical accounts are given elsewhere [1,2]. The first major breakthrough was the discovery of x-ray radiation by Wilhelm K. Roentgen in late 1895 [3]. Roentgen observed that the internal structure of an

object could be visualized by exposing the object to the radiation emitted by his evacuated discharge tube and placing a photographic plate on the other side of the object. The photographic emulsions were sensitized by the x-rays, and a "shadow image" of the internal structure of the object was produced on the plate. He also observed that the denser the medium that the x-rays must transverse, the less exposed was the photographic plate. The medical implications of his discovery were immediate and gave birth to the field of radiology.

The next milestone was the discovery of naturally occurring radioactivity by A. Henri Becquerel in 1896 [4]. He noticed that uranium salts, known to become luminescent when exposed to Roentgen's tube, in their natural, unexcited state also gave off x-rays, and therefore were naturally radioactive. Marie Sklodowska-Curie, a student of Becquerel, began to study and measure this new phenomenon. Along with her husband Pierre Curie, she was able to show radioactivity in another element (thorium) using the piezoelectric phenomenon (that Pierre had discovered) as a means of radiation measurement and detection. However, it was Rutherford who first reported the radioactive properties of thorium [5]. Unlike the x-ray radiation produced by a Roentgen discharge tube, the radiation the Curies were observing was far more energetic and penetrating [6]. By 1898 Marie and Pierre Curie had isolated two more radioactive elements which were called polonium and radium. Over the next decade many more naturally occurring radioactive elements were discovered. An explanation of the cause and nature of radioactivity was proposed by Rutherford (with Frederic Soddy) in 1902 [7].

George Hevesy is generally credited with being the first researcher to exploit the new radioactive substances as radiotracers in biological systems in 1923 [8]. Using a natural radioisotope of lead, he investigated the uptake of lead in various portions of a plant. He used a gold leaf electroscope to quantify the accumulation of the lead in the plant. Further, the gold leaf electroscope was sensitive enough that non-toxic levels of lead were sufficient for his measurements, a property of great importance for radiotracers. Near the end of the 1920's, Blumgart and coworkers [9] in Boston were injecting patients with a

solution of radium C in one arm and measuring the time it took for the radium C to be present in the other arm. In their early experiments a cloud chamber was used for radiation detection, but later they began to use a prototype of the Geiger tube for this purpose. At that time the only available radioactive elements were those that occurred naturally, and except for radioiodine, these elements were of little or no physiological value.

In 1919 Rutherford demonstrated that the structure of matter could be altered by bombardment with high energy alpha particles emitted from a radium source [10]. It took fifteen more years for the implications of this discovery to be realized by Irene Curie and her husband Frederic Joliot. In 1934 they reported that *transmutation* of some light elements could be induced by bombarding a target of the stable element with radiation [11]. Using a polonium source to irradiate an aluminum foil, they observed that the aluminum foil remained radioactive after the polonium source was removed. Further, the radioactivity of the aluminum foil decayed exponentially "just as in naturally occurring radioactive elements". Subsequent chemical analysis revealed that a small fraction of the aluminum atoms had been transmuted into radioactive phosphorus 30 by the irradiation. A similar effect was observed when boron was irradiated by the polonium source, and in this case chemical analysis revealed that the boron atoms had been transmuted into radioactive nitrogen 13. Since neither of these radioactive elements had been observed to occur naturally, they became known as artificially produced radionuclides.

Three years before the Curie – Joliot discovery, Ernest Lawrence brought the first cyclotron on line in 1931 and used it to accelerate alpha particles to a high enough velocity to overcome the Coulomb barrier of the target nuclei, and thus interact with the nucleus [12]. Lawrence subsequently discovered that his targets had also become radioactive after bombardment with alpha particles. By 1934 the cyclotron became a useful tool for producing artificial radioactive elements, using deuterons instead of alpha particles for bombardment.

The discovery of the neutron in 1932 by Chadwick [13] was of paramount importance to radionuclide development. Enrico Fermi used neutrons to bombard stable targets and artificially produce radioactive elements [14]. Unlike the charged particles being used in Lawrence's cyclotron (i.e. alpha +2 and deuteron +1) which needed to be accelerated to overcome the Coulomb barrier before interacting, the neutron was uncharged. Using the techniques of Fermi, Livingood and Seaborg produced the radioisotope ^{131}I in 1938 [15]. This isotope was much better suited to clinical applications of iodine since it had an 8 day half-life instead of the short 6.5 minute half-life of the naturally occurring radioisotope ^{128}I. Also in 1938, Seaborg and Emilo Segrè co-discovered the all-important imaging radionuclide of today's nuclear medicine, technetium 99m (^{99m}Tc) [16], but it would take twenty more years before it would become widely used. It took nearly ten years from the discovery of the neutron before the nuclear reactor was available as a rich source of neutrons. By 1942 the nuclear reactor at Oak Ridge was producing many radionuclides in large quantities at a relatively low cost [17].

Hospitals began using these new more physiologically significant radionuclides both for treatment and diagnosis. Diagnostic procedures involved mapping, point by point, the uptake of the radionuclide at points of interest using a shielded, collimated Geiger-type counter [18]. Collimation provided the Geiger counter with directionality by allowing, to a crude first approximation, to only detect that activity along the line of sight of the collimator. The most useful radionuclides for diagnostic purposes were those that emitted photons (i.e. gamma rays), which subsequently escaped the patient's body with sufficient probability to be detected externally using the Geiger counter. At this time ^{131}I was the most common radionuclide being utilized because of its physiological properties associated with thyroid ailments. However, the Geiger counter was very inefficient at detecting the emitted gamma rays, requiring millicuries of activity to be injected and excessively long data acquisition times. Improved gamma ray detectors for clinical purposes provided the next major advancement in nuclear medicine.

By the late 1940's, photon interactions with matter were quite well understood. Dense matter, like lead and iodine, was very efficient at absorbing the photon energy, whereas less dense matter, like the gas used as the sensitive medium of the Geiger tube, was extremely inefficient at absorbing the photon energy. Radiation counters, such as the Geiger counter, relied on the collection of the ion pairs that were produced when photons interacted with the sensitive material of the detector. The best absorbers of photon energy could not be incorporated as the sensitive medium of detectors that relied on collection of ion pairs. An answer to this dilemma was provided by Kallmann in 1947 [19] and his basic principles of photon detection are still used today. Instead of relying on collection of ions, his detector relied on the collection of light photons which were produced by the absorption of photon energy in certain crystals of high density. The high density of the crystals ensured that a large fraction of the incident photons would interact with the crystal and deposit energy into it. The crystals of interest, which Rutherford and Becquerel had used in their original investigations of radioactivity, were those that released a burst of light (scintillations) after absorbing a photon's energy, and were termed scintillating crystals. This fact alone, although interesting, was quite useless for radiation counting detectors since the individual scintillations needed to be counted using the human eye. Kallmann had the genius to "collect" the scintillation photons using another recent invention, the photomultiplier tube (PMT) [20], which converted the scintillation photons into a useable electrical pulse. Finally, like the collimated Geiger counter, Kallmann also provided his detector with directionality using absorptive collimation and shielding. The result was a much more efficient detector for gamma radiation than the Geiger counter tube and allowed administered activities to be reduced by approximately an order of magnitude (i.e. from millicuries to 100-200 microcuries).

The next obstacle to be removed was the time consuming, manual, point by point measurement by a technician. This was first accomplished by Benedict Cassen in 1951, who used a device similar to but more efficient than Kallmann's, and also provided automated control between the detector and a recording device [21]. In the first generation of the scanner the recording device was a simple mechanical pen and paper,

similar to a graphic plotter of today. The paper was mechanically moved in unison with the detector. When the detector would respond (i.e. detect photons) the pen contacted the paper leaving a dot of ink. An image of the radionuclide distribution could be obtained using a mechanical raster-type scanning of the detector over the object of interest. In the second generation of the rectilinear scanner the pen and paper were replaced with a spark recorder which burned holes in the paper when the detector responded. The major drawback of this device was that only one point of interest (i.e. small field of view) could be counted at a time, and therefore image formation was a lengthy procedure.

Hal O. Anger invented a detector in 1958 that revolutionized diagnostic nuclear medicine [22]. He envisioned the idea of collecting counts simultaneously over a large field of view to produce an image which was, to a good approximation, a 2D projection of the 3D radionuclide distribution. To accomplish this he employed a large crystal of NaI(Tl) with seven PMT's optically attached to the back and placed in a close packed hexagonal arrangement. Spatial resolution was obtained through absorptive collimation which allowed only photons with a certain direction of propagation to pass and interact with the scintillation crystal. Those that did interact produced scintillations which were seen by all the PMT's. A series of resistive weighting circuits processed the separate outputs of the PMT's to determine the position of the interaction in the crystal. Also, the energy transferred by the incident photon to the crystal could be obtained by summing the outputs from all PMT's. The spatial information was used to deflect the electron gun of a cathode ray tube (CRT) to a certain position, and the electron beam was activated briefly to produce a flash on the screen of the CRT if the energy of the photon was within a predetermined range. The CRT allowed one to visualize the dynamic formation of the image since there was a one-to-one mapping between the scintillation crystal area (i.e. camera field of view) and the display screen. Another advantage of the Anger camera was that it was especially well suited for the detection of lower energy gamma rays emitted by ^{99m}Tc. By 1964 the Anger camera was commercially available and ^{99m}Tc began to dominate as the imaging radionuclide of choice.

By the middle of the 1960's projections of a 3D radioisotope distribution could be easily obtained with an Anger-type camera. The projection of a 3D distribution onto a 2D imaging plane made it difficult to delineate overlying and underlying activity since, due to collimation, activities along a given line of sight of one of the detector elements were superimposed (i.e. integrated). The camera head was mounted on a rotating gantry which allowed projection data to be acquired at various angles about the patient. By acquiring projections at different angular positions one could mentally envision, at least qualitatively, the 3D nature of the distribution. David Kuhl first proposed a reconstruction technique that allowed an estimate of the 3D distribution to be obtained from a set of projections taken at regular angular intervals about the radionuclide distribution through a process called backprojection [23,24]. An analytical formulation of the reconstruction problem was given by Cormack in 1963 [25-27], which assumed the source distribution could be related to the acquired projection data through a mathematical transformation. For historical reasons, Cormack's approach has become known as the "Radon Transform approach to image reconstruction from projections" [28]. Cormack's technique also required that a number of projections be taken about the object of interest (i.e. the 3D radionuclide distribution) at regular angular intervals. The set of projections were then used to reconstruct the 3D object using a technique that has subsequently been termed filtered backprojection. It took Anger camera and computer technologies nearly two decades to fulfill Cormack's requirements for this imaging technique, and by the early 1980's clinical tomographic systems were in place in many nuclear medicine departments.

The Anger camera continues to be improved but its basic components and image formation principles have remained essentially unchanged [29-33]. The crystal size (i.e. field of view) and number of photomultiplier tubes coupled to the back of the crystal have increased significantly over the years. In many cases, modern Anger cameras employ two or more camera heads, allowing projection data at a number of angular positions to be acquired simultaneously. Anger camera development has also benefited greatly from advances in electronic and microprocessor technologies. Most modern cameras are to a

large extent digital and microprocessors are used to acquire and correct for deficiencies (such as nonuniformities and nonlinearities) of the Anger camera.

More than anything, however, the implementation of a digital computer with the Anger camera was a most significant advance. First used simply as a means of storing image data and providing various display options, computers now play a central role in practically all nuclear medicine imaging and diagnostic procedures, allowing for complex data analysis and sophisticated display options such as 3D surface rendering. Further, computers were essential to the practical implementation of tomographic imaging techniques, which have became known as single photon emission computed tomography (SPECT). SPECT imaging techniques use the acquired projection data and a computer to numerically reconstruct the radioactive source distribution using Cormack's or other reconstruction techniques. In the following section the basic qualitative principles of SPECT imaging are discussed.

B. Nuclear Medicine Tomographic Imaging

In this section the qualitative aspects of nuclear medicine planar and SPECT imaging are discussed. Much of the terminology (i.e. jargon) associated with nuclear medicine imaging will also be defined. As already stated, the ultimate goal of SPECT imaging procedures is to obtain, from the set of acquired projections, the radionuclide or source distribution within the patient. Each image obtained with the Anger camera is a 2D planar projection or view of the 3D source distribution onto the camera imaging plane at a given angle. The projection image is discretized by dividing up the large field of view of the Anger camera into a number of smaller imaging elements called *pixels*. The pixels are square and arranged in a grid-like fashion on the camera (or projection) plane as shown in Fig. I-1. The projection or image is described by the intensity values contained in each pixel and can be represented by a 2D matrix of these values. Further, through the processes of absorptive collimation and photon energy discrimination, the value at each pixel is also proportional to the ray sum (or integral) of the activity along the line of sight of the pixel and perpendicular to the imaging plane, as illustrated in Fig. I-2. It is for this

reason that the image obtained from the Anger camera is often referred to as a 2D projection of the 3D source distribution. Further, it is convenient to divide up the 3D source distribution volume into many small, discrete cubic volume elements called voxels. The source distribution is then described by a 3D matrix of values corresponding to the values of the voxels. It is typical in nuclear medicine to divide the projections into 64×64 pixels with each pixel occupying an area of approximately $(0.6\,\mathrm{cm})^2$, and the source distribution into $64 \times 64 \times 64$ voxels, each voxel occupying a volume of approximately $(0.6\,\mathrm{cm})^3$. The concept of pixels, projections, and voxels is illustrated in Fig. I-2.

To reconstruct the source distribution it is necessary to obtain projection images at many angles about the source distribution. Of particular interest are the slices of the source distribution that lie perpendicular to the axis of rotation. These are termed *transaxial slices* and provide a cross-sectional view (i.e. a slice) of the source distribution as shown in Fig. I-3. Each transaxial slice lies within a transaxial plane. The voxel size can be chosen such that the spacing of the transaxial planes corresponds to the pixel spacing of the Anger camera as illustrated in Fig. I-2. Absorptive collimation and photon energy discrimination allow only those photons which are emitted within a given transaxial slice to contribute to the pixels contained within the corresponding transaxial plane[†], as also shown in Fig. I-2, and forming a pixel projection row. At each projection angle, each projection row provides an unique set of line integrals of the radioactive source distribution as shown in Fig. I-4. The reconstruction problem is reduced to obtaining a 2D distribution from a number of 1D projections taken at various angles about the axis of rotation. The full 3D distribution is then obtained, slice by slice, by reconstructing all transaxial slices. This greatly simplifies the number of computations and the memory requirements for reconstructing the 3D source distribution from the set of 2D projections.

[†] This is only true for ideal collimation and photon energy discrimination. A more complete description of absorptive collimation is given in Chapter 2 and this statement will be shown to be the ideal case.

The principles of traditional tomographic reconstruction methods are based on a mathematical process called backprojection [23-27,32,34-37]. The reconstruction process may be described qualitatively to provide an intuitive understanding as to how and why the process works. Shown in Fig. I-5a are three 1D projections of a 2D source distribution consisting of two small square regions of activity. The projection data obtained at $\theta = 0$ represents the superposition of activities along the line of sight of the projection pixel. The projection data obtained at $\theta = \pi / 2$ resolves the two separate regions of activity but tells nothing about the depth at which the regions lie. By back-projecting the pixel values along lines perpendicular to the projection axis (i.e. incrementing those voxels which lie along this line of sight by the pixel value) the two regions of activity are somewhat resolved, as shown in Fig. I-5b, but there is a disturbing streaking artifact produced by this process. The streaking is present because each reconstruction voxel along a pixel's line of sight is incremented by the value recorded at the pixel. The two voxels which actually contained activity are resolved somewhat because they receive contributions from all projection angles and thus have larger values than the other non-zero voxels. The streaking artifact can be minimized by backprojecting projection data from numerous (i.e. >>3) angles since the intensity of voxels that actually contained activity will be proportional to the number of projection angles used, whereas the intensity of the other voxels will be of the order of a single projection pixel's value, as shown in Fig. I-5c. Figure I-5c illustrates another problem that arises in backprojection reconstructions, namely how to distribute the pixel value when its line of sight is not aligned with the reconstruction voxel grid. Some method of interpolation must be used for these projection angles and this generally results in an additional blurring artifact, as also seen in Fig. I-5c. The blurring artifact is often referred to as a partial volume effect. The process illustrated in Fig. I-5b and I-5c is known as direct backprojection as opposed to the filtered backprojection technique which removes the streaking artifact to a large extent, but is still subject to the blurring artifact caused by a discrete reconstruction grid. The filtered backprojection reconstruction technique is based upon a mathematical transform of the source distribution called the Radon transform and will be discussed in detail in Chapter 2.

There are two main deficiencies in the model upon which the backprojection reconstruction methods are based:

(i) The geometrical model of the collimation process is oversimplified. Namely, due to the finite collimation angle a particular pixel records not only the activity along its own line of sight but also activities which ideally belong to pixels adjacent to it. In general this process can only be partially corrected for within the framework of backprojection reconstruction methods.

(ii) The physical model of photon propagation within the medium is over-simplified. The photons emitted by the source may be absorbed by the medium or undergo Compton scattering interactions within the medium. In the latter case, photons emerge from the medium with direction of propagation and energy different from those in which they were emitted. Modeling this process is the main subject of this thesis.

These deficiencies will be discussed in detail in Chapter II.

The above qualitative description of the reconstruction process in SPECT provides a superficial, but intuitive, overview as to how reconstruction procedures work for an ideal imaging situation and an ideal camera system. SPECT acquisitions and reconstructions are common-place in today's nuclear medicine departments and provide physicians with useful and unique diagnostic information about the function of organs and tissues. However, due to the physical processes associated with the propagation and detection of the emitted photons, and due to the necessarily low administered activities coupled with finite acquisition times, the images obtained from the Anger camera are excessively noisy (i.e. count poor) and blurred. Transaxial slices reconstructed from the Anger camera projection data are also noisy and blurred. As indicated above, the blurring is primarily because the majority of reconstruction algorithms used are based upon geometrically and/or physically over-simplified models of the imaging problem.

A model of the imaging problem constitutes a complete description of the relationship between the radionuclide source distribution, the patient medium, and the projection data

acquired by an Anger camera system. Reconstruction algorithms are strongly dependent upon the model of the imaging problem. For example, in order for the popular Radon transform approach to be applicable to the projection data acquired by the Anger camera, an over-simplified model of the imaging problem must be assumed; specifically, the processes involved with the propagation and detection of the emitted photons are ignored, and the camera system is assumed to be a true line integrator. To improve the quantitative accuracy of the reconstructed source distribution, either the projection data or the reconstructed source distribution must be corrected or compensated, after the fact, for processes not accounted for in the assumed simplified model of the imaging problem. Since it is not always possible to quantitatively correct for the physical processes ignored in the simplified model, SPECT imaging based upon the filtered backprojection algorithm is often referred to as a *qualitative* imaging technique, rather than a *quantitative* imaging technique. In other words, traditional SPECT imaging can ascertain the presence or absence of radioactivity in a certain region quite faithfully but it generally can not quantitatively determine the amount of radioactivity that is present within the region (i.e. MBq/cm3).

From a theoretical physics perspective, the reconstruction problem in SPECT can be divided into two distinct steps. First, a model of the imaging problem must be specified, which requires solving the appropriate photon transport equations for a nonuniform attenuating medium as well as accounting for the specifics of photon detection using an Anger camera system. Second, using this model of the imaging problem, the source distribution must be obtained (i.e. reconstructed) from the projection data, which most generally requires the inversion of a very large matrix equation relating the radioactive source distribution to the Anger camera projection data. If the assumed model is simplistic, a direct analytical solution to the reconstruction problem may be possible without resorting to inverting the general matrix equation. The disadvantage of such a model is that additional post-processing of the data is almost always required to obtain the most qualitatively useful diagnostic information from SPECT imaging procedures, and in some cases this is not possible.

Traditionally SPECT reconstruction algorithms have been based upon over-simplified models of the imaging problem. The bulk of the literature has focused on additional post-processing techniques which attempt to correct either the projection data, or the reconstructed source distribution, or both, for deficiencies introduced by the simplified model. The reconstruction problem has been approached from this perspective because reconstruction algorithms which attempted to accurately model the imaging situation subsequently led to reconstruction problems that were traditionally beyond the available computing resources. Such approaches are acceptable from a practical perspective since they have allowed diagnostically useful information to be obtained from acquired projection data. From a physics perspective, however, to fully understand the imaging problem and the image reconstruction problem in SPECT, an accurate physical theory is necessary. Hopefully, such an understanding is a step towards making SPECT a quantitatively accurate tool.

C. Overview of Thesis

This thesis presents a formalism which accurately and quantitatively describes the relationship between the radioactive source distribution, the attenuating medium, and the projection data recorded by an Anger camera system. The theory is derived, experimentally validated, and applied to some problems associated with SPECT reconstructions. The new approach differs from previous approaches in a number of ways, but most significantly an attempt is made to theoretically model the imaging situation accurately by exploiting available *a priori* information about it. The problem is investigated using the methods of theoretical physics, and integral expressions for the central quantity in this approach, called the photon detection kernel, are derived and subsequently numerically implemented.

The thesis begins, in Chapter II, with a review of the physics related to photon propagation and detection, specifically focusing on the nuclear medicine imaging situation. A quantitative description of the most general imaging problem in SPECT is presented

based upon the concept of the photon detection kernel. The general reconstruction problem in SPECT is defined and the photon detection kernel is shown to play a fundamental role in all reconstruction techniques. Derivation of the popular Radon transform and its inverse solution are reviewed. Deficiencies of this approach and commonly used correction and compensation techniques are also discussed. Finally, iterative reconstruction techniques are discussed and the need for physically accurate photon detection kernels is motivated.

In Chapter III an analytical theory of photon propagation and detection is presented and integral expressions for the photon detection kernel are obtained. In Chapter IV, the numerical implementation and the calculation of the integral expressions for the photon detection kernel resulting from the theory are described. In Chapter V, theoretical results are compared with experiments to validate the theory and the numerical code of Chapter V. In Chapter VI the numerical challenges of implementing a physically accurate kernel in an iterative reconstruction algorithm are investigated. The thesis concludes, in Chapter VII, with a brief summary and a discussion of future work.

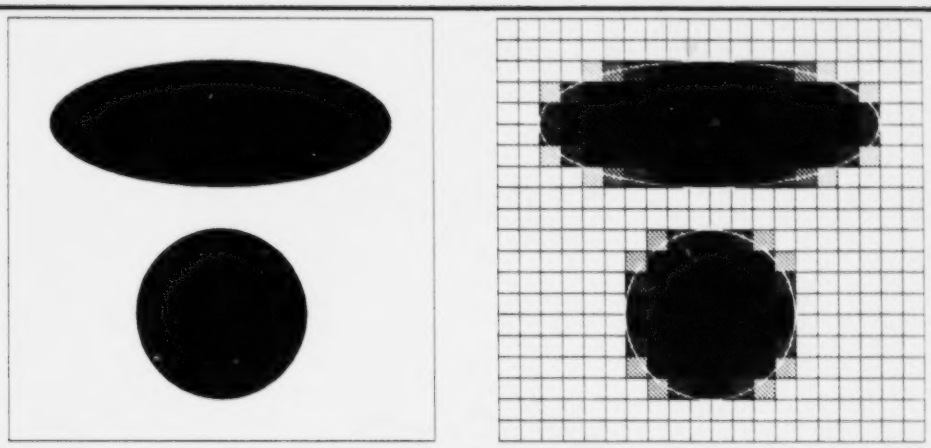

Figure I-1: The right hand image demonstrates the discretization process of the (continuous) image on the left into pixels. The white outline shown on the right hand image is the true extent of the continuous distribution on the left.

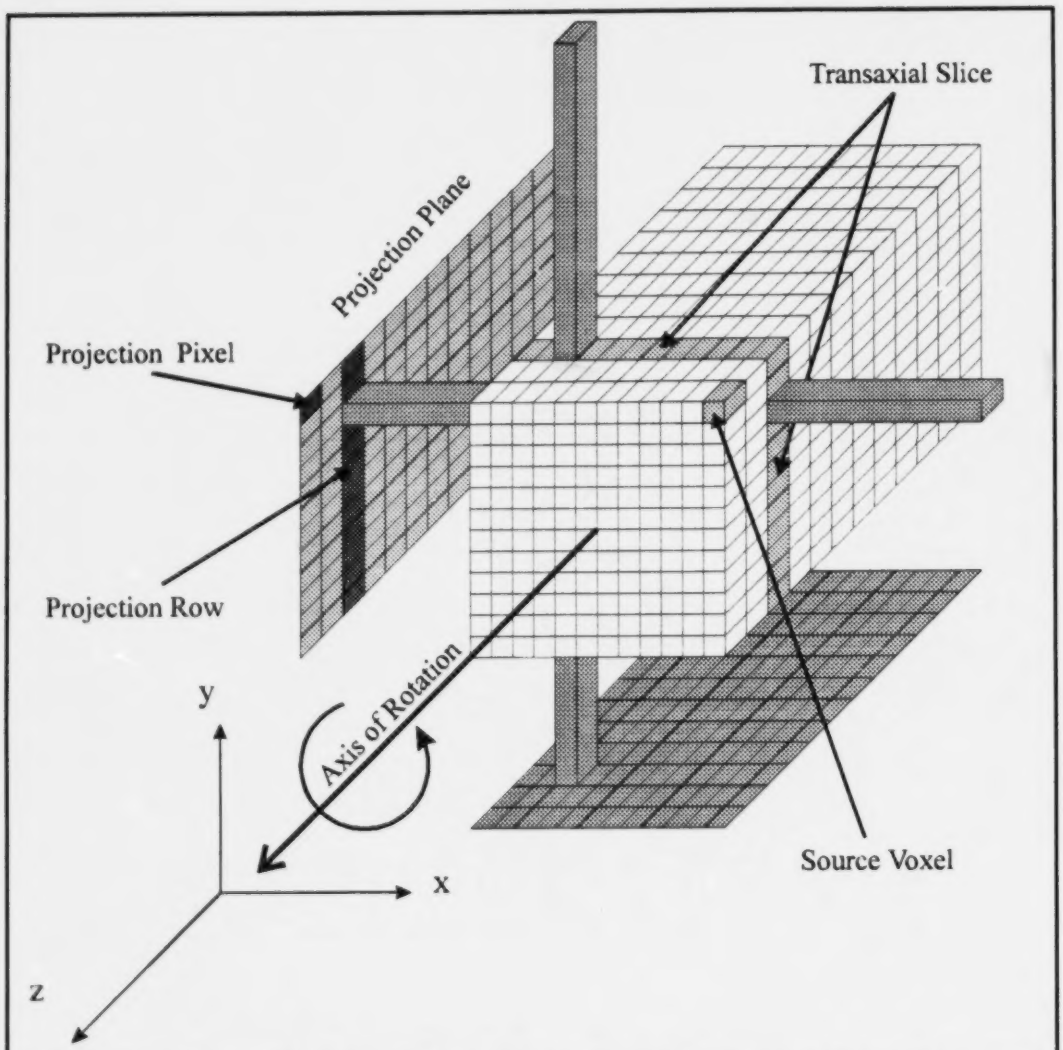

Figure I-2: This figure illustrates the typical imaging geometry for SPECT. The projection plane rotates about the axis through the center of the discretized source distribution. The line of sight for a pixel at the two projection angles is shown by extending the pixel from the projection plane through the source distribution. Note that the orientation of the coordinate system and camera axis of rotation was chosen arbitrarily for this figure and the discussions related to it.

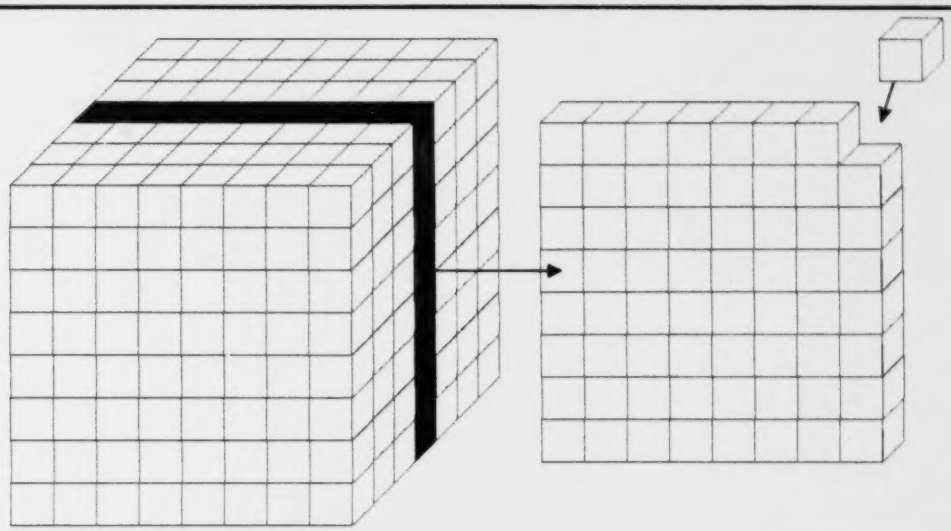

Figure I-3: The concept of voxels and transaxial slices for describing the discretized source distribution is shown. In this diagram, each transaxial plane is made up of 64 voxels (i.e. 8×8) and the 3D source distribution is made up of 7 transaxial slices and thus 448 voxels in total.

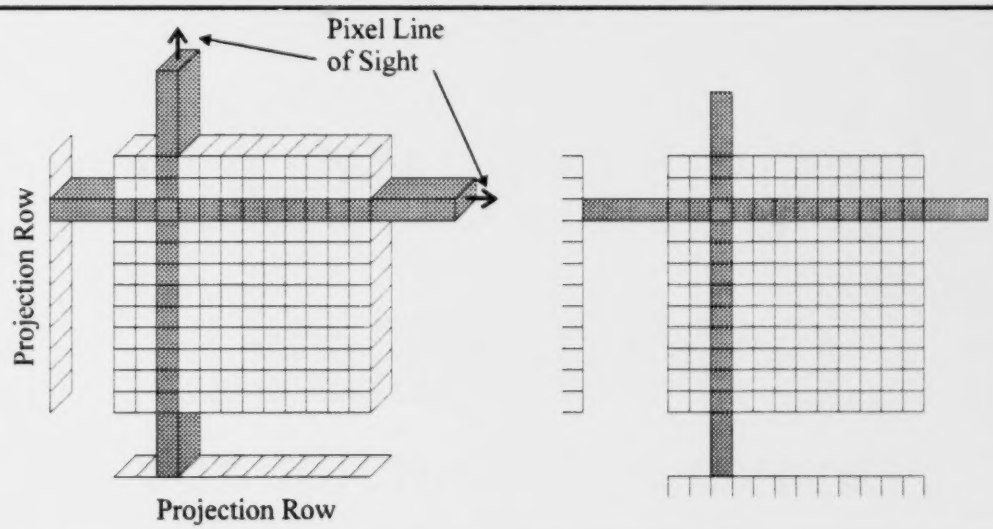

Figure I-4: The 3D imaging problem in Fig. I-2 is reduced to a 2D problem by considering a single transaxial slice of the 3D source distribution. A transaxial slice from Fig. I-2 with two projection rows parallel to the transaxial slice is shown on the left, and the imaging geometry as it is to be interpreted in 2D is shown on the right. In the idealized model the activity recorded at a given pixel is proportional to the line integral of the radioactive source distribution taken along the line of sight of the pixel as shown.

(a)

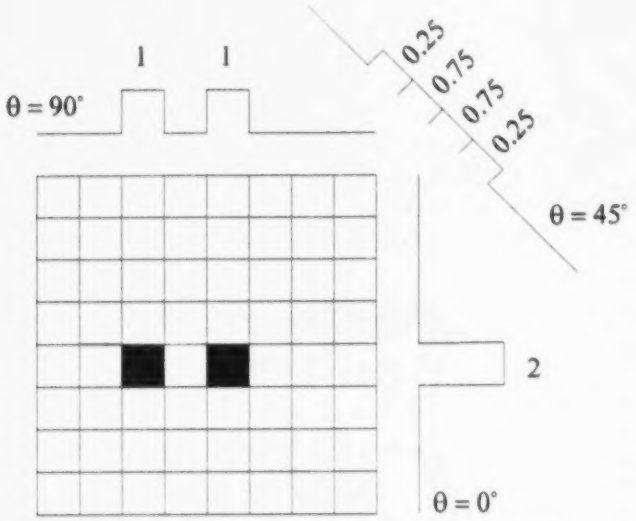

(b)

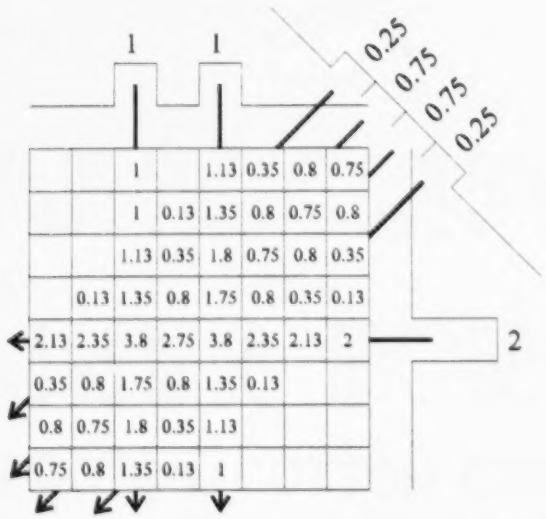

Continued on next page

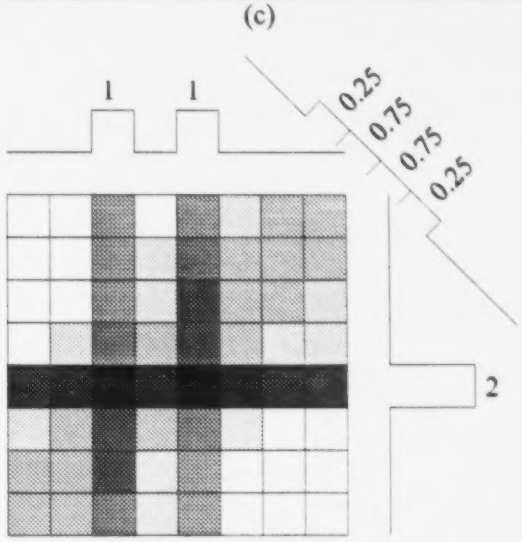

Figure I-5: (a) Three 1D projections of a source distribution consisting of two square regions of activity. (b) and (c) Schematic representation of the backprojection process in SPECT for the three 1D projections from (a).

II. Background - Nuclear Medicine Physics

In this Chapter the concept of the photon detection kernel will be introduced and the need for more physically accurate models of the imaging problem in nuclear medicine will be established. The photon-matter interactions of interest in nuclear medicine, as well as the basic components of the Anger camera, are described. A mathematical definition of the general imaging problem in nuclear medicine is presented and two popular solutions to the reconstruction problem are discussed. Finally, the chapter concludes with justification of the need for physically and quantitatively accurate models of the imaging problem for use with iterative reconstruction methods.

A. Physics of Photon Propagation

In nuclear medicine imaging the radioactive source is distributed within a complex non-uniform medium containing components of tissue, bone, and lung, as well as others. The emitted photons must traverse the medium to reach the detector and be recorded. It is desirable to have the largest fraction possible of the emitted photons escape the patient's body without interactions. However, there is a significant probability that the emitted photons will interact with the medium (i.e. the patient) before escaping. There are four possible photon-matter interaction modes: (i) photoelectric absorption, (ii) Compton scattering, (iii) Rayleigh scattering, (iv) electron-positron pair production. For the photon energy range of interest in nuclear medicine imaging (70-360 keV), pair production interactions are not possible since a photon threshold energy of greater than 1 MeV is required. Further, photoelectric absorption and Compton scattering interactions are dominant, with Rayleigh scattering interactions making only a small contribution for the energy range of interest. The combined effect of all possible interaction modes on the photon fluence is referred to as *attenuation*, and the patient's body is often called the *attenuating medium*.

Compton Scattering

In Compton scattering a photon interacts with a free or very loosely bound electron of the attenuating medium [38]. For all practical purposes, the process appears identical to

the collision (i.e. scattering) of a particle of momentum $h\nu / c$ (i.e. photon) with a particle at rest (electron) with mass m_e, as shown schematically in Fig. II-1a. In fact the kinematics of the scattering process are obtained from classical mechanics using conservation of momentum and energy. There are two significant differences between Compton scattering interactions and classical scattering processes. Firstly, in a Compton scattering interaction the incident photon is destroyed (annihilated) and a new photon is created with energy and direction of propagation satisfying the momentum and energy conservation laws. The created photon is often referred to as the *scattered photon* since classically it appears as if the incident photon was simply scattered by the electron, transferring a fraction of its energy to the electron. Quantum mechanically, however, it is forbidden for a photon to transfer a fractional amount of its energy. Secondly, the final outcome of the scattering interaction is statistical and can not be predicted from the initial conditions of the problem, as would be possible for a classical scattering process. Fig. II-1a provides a schematic representation of the Compton scattering interaction and defines the geometry and variables describing the scattering process.

The energy of the scattered photon, $E' = h\nu'$, is given by

$$E'(E,\theta) = \frac{E}{1 + \frac{E}{m_e c^2}(1 - \cos\theta)}, \tag{II.1}$$

where $E = h\nu$ is the incident photon energy and θ is the angle of the scattered photon with respect to the incident photon direction. In Fig. II-2, the ratio of the scattered to incident photon energy is plotted as a function of the scattering angle for E=140 keV. The energy transferred to the electron, T, is given by

$$T = E - E', \tag{II.2}$$

and can range from practically zero for grazing interactions (i.e. $\theta \approx 0$) to a maximum of

$$T_{max} = \frac{2E^2}{m_e c^2 + 2E}, \tag{II.3}$$

for backscattering interactions (i.e. $\theta = \pi$). The scattering angle of the electron, ϕ, with respect to the incident photon direction can be obtained from the relation

$$\cot\phi = \left(1 + \frac{E}{m_e c^2}\right)\tan\frac{\theta}{2}, \tag{II.4}$$

and lies in the range $0 < \phi < \pi/2$.

Equations (II.1), (II.2), and (II.4) provide a complete solution to the kinematics of the scattering process but, as already mentioned, do not describe its dynamics, i.e. the probability of a Compton scattering interaction to occur. The probability that a photon will interact with a *single* electron of the medium and be Compton-scattered into a small solid angle $d\Omega$ about the angle θ with respect to the incident photon direction, as shown in Fig. II-1b, is given by the differential Klein-Nishina scattering cross-section [39] as

$$\frac{d\sigma}{d\Omega}(E,\theta) = \frac{r_0^2}{2}\left(\frac{E'}{E}\right)^2\left(\frac{E}{E'} + \frac{E'}{E} - \sin^2\theta\right), \tag{II.5}$$

where $E' = E'(E,\theta)$ is defined by Eq. (II.1) and $r_0 = \left(e^2/4\pi\varepsilon_0 m_e c^2\right) \cong 2.82 \times 10^{-13}$ cm is the classical electron radius. The angular dependence of the Klein-Nishina cross section is shown for $E = 140$ keV in Fig. II-2. The probability that a photon will be scattered into any angle is given by the total Klein-Nishina cross-section [39-42], $\sigma(E)$, and can be obtained by integrating Eq. (II.5) over all possible scattering angles, i.e.

$$\sigma(E) = \int \frac{d\sigma}{d\Omega}(E,\theta)\,d\Omega = 2\pi\int_0^{\pi} \frac{d\sigma}{d\Omega}(E,\theta)\sin\theta\,d\theta. \tag{II.6}$$

Equations (II.5) and (II.6) describe the probabilities for interacting with a single electron of the medium. In a medium described by an electron density ρ_e, the Compton scattering interaction coefficient, μ_{CS}, is given by

$$\mu_{CS} = \rho_e \sigma. \tag{II.7}$$

Rayleigh Scattering

Rayleigh scattering [43] is similar to Compton scattering except that photons interact with a collection of electrons bound to atoms of the attenuating medium. The atomic electrons act as a whole (i.e. coherently) and the process is often referred to as coherent scattering. In the Rayleigh scattering process the incident photon is annihilated and a new

photon is created satisfying the energy and momentum conservation laws, similar to the Compton scattering process. However, because of the much greater rest mass of the atom, as compared to the rest mass of an electron, very little energy is transferred to the atom in this process and the created (or scattered) photon has energy differing only negligibly from that of the incident one. A closed-form analytical expression for the Rayleigh cross section is not available and tables must be employed [41]. The differential angular dependence is also not known theoretically and, in general, only incomplete experimental information is available for the photon energies of interest. For this energy range (70-360 keV) and for the media of interest, the Rayleigh scattering cross section is much smaller than the Compton scattering cross section [40-42]. Rayleigh scattering interactions begin to dominate at very low photon energies (i.e. 1-10 keV) in high-Z materials (i.e. lead). The Rayleigh scattering cross section is at most a few percent of the Compton scattering cross section for energies above 100 keV for media of interest in nuclear medicine imaging. In general, the effects of Rayleigh scattering can be ignored for all practical purposes.

Photon Scattering Interactions

Compton and Rayleigh scattering interactions do not directly reduce the number of emitted photons since for each photon destroyed a scattered photon is created. Scattering interactions degrade the energy distribution and spread out the direction of propagation of the original photon beam. Photons originally propagating towards the detector are scattered away from it, or photons not originally directed towards the detector can be scattered towards it. The overall effect of scattering interactions on the acquired projection image is to spread the photons out over a larger area of the projection plane and reduce the contrast between hot and cold regions of activity.

The effects of scattering interactions on the image formation process can be envisioned intuitively. The presence of a radioactive source in an attenuating medium activates the electrons and atoms in the medium to be a source of (scattered) photons via Compton and Rayleigh scattering interactions, respectively. It will be shown quantitatively later, that the efficiency of a given electron as sources of (scattered) photons is dependent upon many

physical factors including the type of the medium and the distance from the primary photon source. Further, each electron activates all other electrons since an emitted, primary photon may initiate a sequence of multiple scattering events before escaping the medium. In this picture, the electrons and the atoms, through the Compton and Rayleigh scattering processes, can be envisioned as a (low level) background distribution of radiation with continuously distributed photon energy always lower than the primary photon energy. It is for this reason that scattered photons reduce the contrast between hot and cold regions of the primary source distribution.

Photoelectric Absorption

In photoelectric absorption a photon interacts with an orbital electron and vanishes, giving all of its energy to the electron. The electron is given kinetic energy equal to the photon energy minus its atomic binding energy. The probability for a photoelectric interaction to occur is given by the photoelectric interaction coefficient μ_{PE} and is proportional to the fourth power of the atomic number of the medium and inversely proportional to the third power of the photon energy, i.e.

$$\mu_{PE} \propto \frac{Z^4}{E^3}, \tag{II.8}$$

for photon energies typical in nuclear medicine [40-42]. Thus photoelectric absorption interactions are most probable for lower energy photons in media with high atomic numbers. The photoelectric interaction coefficient is strongly dependent upon the electron binding energies of the medium, increasing rapidly as the photon energy approaches the electron binding energies of the medium and decreasing immediately below them. The rapid drop-off below the electron binding energies is due to the fact that the incident photon must have energy greater than the binding energy to undergo a photoelectric absorption interaction with the electron. Photoelectric absorption interactions reduce the number of photons incident on the camera face since they are destroyed in this interaction. Sources deeper in the medium are affected to a greater extent and appear to be less active than those located closer to the camera.

Linear Attenuation Coefficient

The sum of the interaction coefficients for Compton scattering, photoelectric absorption, and Rayleigh scattering is called the linear attenuation coefficient [40-42] and is simply given as

$$\mu = \mu_{CS} + \mu_{PE} + \mu_R . \tag{II.9}$$

The linear attenuation coefficient for a given medium describes the interaction probability per unit length [40] in the medium. Thus, the probability that a photon traversing an infinitesimal distance dx in the medium will interact along the way is

$$dP_{\text{int}} = \mu\, dx . \tag{II.10}$$

The type of interaction that occurs depends on the relative probabilities for each mode of interaction (i.e. μ_{CS}/μ, μ_{PE}/μ, etc.). The linear attenuation coefficient depends both upon the incident photon energy and the atomic properties of the medium. In practice, the linear attenuation coefficient is obtained experimentally and as such describes the probability of all possible photon interaction modes. A photon of energy E emitted at the position $\mathbf{r}$ of the medium has a probability $A(\mathbf{r}', \mathbf{r}, E)$, referred to as the *survival probability*, of arriving at the position $\mathbf{r}'$ of the medium *without* interacting. From Eq. (II.10) one can show that this probability is given as

$$A(\mathbf{r}', \mathbf{r}, E) = \exp\left[-\mu(E)|\mathbf{r}' - \mathbf{r}|\right], \tag{II.11}$$

for a uniform medium in which the linear attenuation coefficient $\mu(E)$ does not depend on position. In a nonuniform medium the survival probability is given by

$$A(\mathbf{r}', \mathbf{r}, E) = \exp\left[-\int_0^{|\mathbf{r}'-\mathbf{r}|} d\xi\, \mu\left(\mathbf{r} + \frac{\mathbf{r}' - \mathbf{r}}{|\mathbf{r}' - \mathbf{r}|}\xi, E\right)\right], \tag{II.12}$$

where $\mu(\mathbf{r}, E)$ is the spatially dependent linear attenuation coefficient. In any case μ depends on the energy of the photons.

B. Radioactive Sources

The activity of all radioactive sources is time dependent and is known to decrease exponentially with time. The activity of a radioactive sample at a time t is given by

$$\dot{a}(t) = \dot{a}_0 e^{-\lambda t}, \tag{II.13}$$

where $\dot{a}_0$ is the sample activity (disintegrations/second) at time $t = 0$, referred to as the *calibration activity*, and λ is the decay constant (inverse seconds). The decay constant λ describes the probability of a decay occurring per unit time per nucleus, and has a specific value for each radionuclide. The expected number of decays observed for a time independent source in the time interval T to $T + \Delta T$ is given by

$$\langle N_{TI} \rangle = \int_T^{T+\Delta T} dt' \, \dot{a}_0 = \dot{a}_0 \, \Delta T, \tag{II.14}$$

where N_{TI} is a random variable with mean $\langle N_{TI} \rangle$ and standard deviation $\sqrt{\langle N_{TI} \rangle}$. The expected number of decays observed for an exponentially decaying source for the same time period is given by

$$\langle N_{TD} \rangle = \int_T^{T+\Delta T} dt' \, \dot{a}(t') = \dot{a}_0 \int_T^{T+\Delta T} dt' \, e^{-\lambda t'} = \dot{a}_0 \frac{(1 - e^{-\lambda \Delta T})}{e^{\lambda T} \lambda}, \tag{II.15}$$

where N_{TD} is also a random variable with mean $\langle N_{TD} \rangle$ and standard deviation $\sqrt{\langle N_{TD} \rangle}$. Therefore, the expected number of decays observed for both a constant and a decaying source in a given time period are related through

$$\frac{\langle N_{TD} \rangle}{\langle N_{TI} \rangle} = \frac{(1 - e^{-\lambda \Delta T})}{e^{\lambda T} \lambda \Delta T}. \tag{II.16}$$

Further, the expectation value of any quantity dependent upon the time dependence of an exponentially decaying source can be obtained assuming first a constant source activity and then multiplying by the above factor. For example, if a radioactive source, with activity $\dot{a}_0$ at time $t = 0$, is imaged by an Anger camera at time T for a period ΔT, and the number of counts recorded at a given pixel is N, then the expected number of counts that would be recorded at the same pixel for a time-independent source, N', is given by

$$N' = N \frac{e^{\lambda T} \lambda \Delta T}{(1 - e^{-\lambda \Delta T})}. \tag{II.17}$$

In the theoretical modeling to follow, the time dependence of exponentially decaying sources is ignored since the experimental data can always be corrected for this effect, using Eq. (II.17), before any comparison with the theoretically predicted values is made.

C. Gamma Camera and Photon Detection Physics

The Anger Camera

In this section the components of the Anger camera are described. In particular the detection process from the camera point of view is discussed for each component of the Anger camera. Detailed discussion of the Anger camera components and operation can be found elsewhere [22,29-32].

A schematic representation of the basic components of the Anger camera is shown in Fig. II-3. In a typical detection event an emitted photon which escapes the attenuating medium and is incident upon the collimator within its acceptance angle interacts with the scintillation crystal. The photon deposits energy in the crystal through either a photoelectric absorption or Compton scattering interaction. A certain fraction of the energy deposited is converted into scintillation photons, i.e. into light. The array of photomultiplier tubes (PMT's) viewing the back face of the scintillation crystal collects and converts the light photons into a usable electronic pulse. The positioning and energy summation circuits collect signals from all PMT's and determine the location of interaction and the energy deposited, respectively. If the energy deposited lies within a preset energy range then the imaging element (i.e. pixel) corresponding to the interaction location is incremented and the photon is said to be detected. The components of the Anger camera are discussed in detail next.

Collimation

The collimator is a regular pattern of holes formed in a material (such as lead) which is a good absorber of photons. It provides the gamma camera with spatial resolution by allowing only those photons whose direction of propagation is within a certain acceptance angle with respect to the collimator normal to pass and interact with the sensitive material of the camera (i.e. the scintillation crystal). Photons striking the collimator outside of its acceptance angle may interact with the collimator via photoelectric absorption and scattering interactions, with photoelectric absorption being most probable. For a lead

collimator, the ratio of the probabilities for the interaction modes are $\mu_{PE} / \mu_{CS} \approx 10$ for 150 keV photons and $\mu_{PE} / \mu_{CS} \approx 3$ for 300 keV photons. Photons which scatter within the collimator medium or penetrate it (i.e. through the wall of adjacent collimator holes) further degrade the spatial resolution of the collimator. For higher energy photons (> 400 keV), the principles of absorptive collimation that provide spatial resolution are no longer as practical for two reasons: (i) Compton scattering interactions begin to dominate over photoelectric absorption interactions, and (ii) photon penetration between adjacent collimator holes becomes significant for practical hole spacing. The combined effect of these two processes is often referred to as collimator scattering and penetration.

The process of absorptive collimation is illustrated both from the collimator hole perspective and the source perspective in Figs. II-4a and II-4b. The shape and pattern of the holes determines the acceptance angle of the collimator as well as its spatial resolution and efficiency. The spatial resolution of the collimator is inversely proportional to the acceptance angle, whereas the efficiency of the collimator is directly proportional to the acceptance angle. As such, there is always a trade-off between spatial resolution and efficiency in designing collimators. The longer and thinner the holes, the smaller the acceptance angle and thus the better the spatial resolution. However, the holes must be separated by enough lead that penetration of the hole walls by the incident photons is small. This fact limits the overall density of the holes, and therefore also the collimator efficiency, independent of their size and shape.

The spatial resolution of the collimator can be characterized by the full width at half maximum (FWHM) of the response of the collimator to a point source. The FWHM of the collimator depends upon the source-to-camera distance, as shown in Fig. II-4b, and this dependence is often referred to as the depth-dependent collimator resolution. Absorptive collimation further degrades the efficiency of the camera system since photons arriving within the acceptance angle of the collimator may still not be counted if they strike the collimator material instead of one of the holes.

The concept of an *ideal collimator* will be used in later discussions. An ideal collimator is one in which there is no trade-off between spatial resolution and efficiency. Further the acceptance angle can be made so small that only those source points which lie directly along the line of sight of the collimator contribute photons that will pass the collimator without interaction. Such a collimator then acts like a line integrator of the source activity along the line of sight of the collimator holes.

The above discussion and examples pertaining to absorptive collimation have assumed that the holes have been formed parallel to one another within the septa. Such collimators are termed parallel hole collimators. Converging, fan beam, and cone beam collimators are also used in nuclear medicine imaging. In a converging collimator the collimator holes all point towards a single focal point in front of the camera. If an object is placed between the camera face and the focal point of the collimator, the image will be magnified. Fan beam and cone beam collimators are related to converging collimators and are used in SPECT. A fan bean collimator provides converging collimation along one axis and parallel collimation along the other, thus focusing on a line. A cone beam collimator converges along both axes to focus on two orthogonal lines at different depths. It is important to note that all these collimators only differ from one another in the shape and orientation of the holes. Although the theory developed in this thesis has only been applied to parallel hole collimation, it can easily be modified for fan or cone beam collimation. Detailed descriptions of parallel, converging, fan and cone beam collimation can be found in Refs. 29, 32, 44, 45.

Energy & Intrinsic Spatial Resolution of the Anger Camera

Photons which pass the collimator may interact with the sensitive material of the camera system - the NaI(Tl) scintillation crystal. For the energy range of interest in nuclear medicine (i.e. 70-360 keV) the most probable interaction between the photons and the crystal medium is photoelectric absorption (i.e. $\mu_{PE} / \mu_{CS} \approx 8$ for NaI(Tl) at 140 keV). This is because the scintillation crystal has a high atomic number (due to iodine) and is a good absorber of photons. The photons which interact with the medium may transfer all

their energy to an orbital electron through a photoelectric absorption interaction. The electron's kinetic energy (i.e. incident photon energy minus the electron binding energy) is dissipated over a very short distance through atomic interactions with other electrons, creating a cascade of secondary electrons in the medium. A significant fraction of the secondary electrons are excited from the valence band either to the conduction band or to the exciton band, creating free migrating holes and exciton pairs (electron-hole pairs), respectively. The thallium impurity centers create localized energy levels within the forbidden energy gap of pure NaI. A hole may migrate and may ionize the thallium impurity center. A free electron may then subsequently recombine radiatively with such a center and a photon is emitted with an energy equal to the electron's transition energy. As such, a fraction of the deposited energy in the crystal is converted into light photons, with the **expected** number of light photons produced being proportional to the energy deposited. NaI(Tl) is fairly efficient at converting the deposited energy into light photons, with one light photon produced for every 25 eV of energy deposited (or ≈ 5600 light photons for 140 keV energy deposited) [40]. The crystal is practically transparent to the light photons produced, which can be assumed to be emitted isotropically about the photon interaction location due to the short range of the photo-electron in the crystal medium. The back face of the scintillation crystal is viewed by an array of PMT's which collect and convert the light photons into an electronic signal.

Each PMT collects a certain fraction of the light photons depending on its distance from the interaction location, with those closest to the interaction site collecting the greatest fraction. The electronic pulse (or signal) produced by a given PMT is proportional to the number of light photons that it collects. The output signal from each PMT is split: one signal is sent to the energy summation circuits and the other is sent to the positioning circuits to determine the interaction location. The energy summation circuits sum the outputs from each PMT together to form a signal which is proportional to the total number of light photons collected by the entire PMT array, and therefore also proportional to the energy deposited in the crystal. This fact can be used to reject interaction events for photons which do not lie within a preset energy range. The energy

range for which detected photons are counted is often called the energy acceptance window.

The conversion of the incident photon energy into light photons and the subsequent process of converting the light photons into an electronic signal are both statistical processes [32,40]. Therefore, for a monoenergetic beam of photons incident upon the scintillation crystal, the magnitudes of the PMTs' output pulses are statistically distributed. If the recorded energy spectrum for a monoenergetic source is plotted, a bell-shaped distribution centered about the incident energy is obtained. This effect, referred to as the intrinsic energy resolution of the Anger camera, is typically characterized by a FWHM equal to 10-12% of the incident photon energy and is adequately modeled by a Gaussian distribution [46-48]. Thus, the probability that a photon of energy E is recorded by the detector in the energy range $E' + dE'$ is given by a Gaussian distribution

$$P(E,E') = \frac{e^{-\left(\frac{E-E'}{\sqrt{2}\sigma(E)}\right)^2}}{\sqrt{2\pi}\sigma(E)} dE', \qquad \text{(II.18)}$$

where $\sigma(E) = a\sqrt{E} + b$ with a and b determined experimentally for a given Anger camera [48]. The FWHM and the $\sigma(E)$ of a camera can be related through

$$\text{FWHM}(E) = \sigma(E)\sqrt{8\ln 2}\,. \qquad \text{(II.19)}$$

The probability that a photon of energy E is detected in a energy window $W_{\min}$ to $W_{\max}$ is obtained by integrating Eq. (II.18) as

$$F(E;W_{\min},W_{\max}) = \int_{W_{\min}}^{W_{\max}} dE'\, P(E,E') = \frac{1}{2}\left[\text{erfc}\left(-\frac{E-W_{\min}}{\sqrt{2}\sigma(E)}\right) - \text{erfc}\left(\frac{W_{\max}-E}{\sqrt{2}\sigma(E)}\right)\right], \qquad \text{(II.20)}$$

where $\text{erfc}(z)$ is the complementary error function [49]. The energy acceptance window parameters ($W_{\min}$ and $W_{\max}$) are usually expressed as a fraction of the radionuclide emission energy and are most often placed symmetrically about the radionuclide emission energy. For example, a 20% symmetric energy window for ^{99m}Tc would have parameters $W_{\min} = 126\,\text{keV}$ and $W_{\max} = 154\,\text{keV}$. Energy response functions, given in Eq. (II.20), are shown in Fig. II-5 for 10%, 15%, 20%, 25%, and 30% symmetric energy windows for

^{99m}Tc. Because of the rather poor energy resolution of the scintillation camera, a wide energy acceptance window is required to ensure that a large fraction of the emitted primary photons (i.e. those that have not undergone an interaction before reaching the camera) are accepted. Fig. II-5 demonstrates that choosing an energy window which is too narrow (i.e. less than 15%) causes the Anger camera to reject a large fraction of the lower energy photons but also a significant fraction of the primary photons, thus leading to an overall decrease in the camera's efficiency. Therefore, the suggestion that photons Compton scattered in the patient's body may be rejected to a large extent by narrowing down the energy acceptance window of the camera is impractical.

Because of the finite thickness of the scintillation crystal not all incident photons will undergo a photoelectric interaction within it (i.e. they may penetrate the crystal or Compton scatter within the crystal). This fact determines the intrinsic energy-dependent absorption efficiency, $A_E(E)$, of the crystal and is described by

$$A_E(E) = 1 - e^{-\mu_{PE}(E)d}, \tag{II.21}$$

where $\mu_{PE}(E)$ is the energy-dependent photoelectric interaction coefficient for the crystal material, d is the crystal thickness, and E is the incident photon energy. Therefore, the total detection probability distribution for the Anger camera is

$$P_D(E;W_{\min},W_{\max}) = F(E;W_{\min},W_{\max})A_E(E). \tag{II.22}$$

The detection probability distribution for photons in the energy range 100-140 keV is shown in Fig. II-6 for a 0.95 cm (3/8 inch) NaI(Tl) crystal with an intrinsic energy resolution of 12% for a 20% symmetric energy window centered at 140 keV. It follows from the preceding discussion that the statistical fluctuations in the detected photon energies are primarily due to the conversion of the deposited energy into light photons and the subsequent conversion of the light photons into an electrical pulse, which are jointly an intrinsic property of the scintillating material and the PMT's, and are not easily improved upon.

The position of the interaction point is determined by the separate PMT signals using a weighting matrix. Relative statistical fluctuations in the separate PMT signals are greater than those in the sum of all PMT signals since summing averages out the fluctuations. The weighting matrix is therefore more sensitive to the individual fluctuations and, as such, determination of the interaction point is also a statistical process. Thus if a highly collimated beam of monoenergetic photons is incident on the crystal, with all photons arriving from the same direction at the same location on the crystal face, the weighting matrix will produce a 2D distribution of interaction locations centered about the actual incident location. The width of this distribution is called the intrinsic spatial resolution of the camera system and is generally specified by a 2D FWHM which is typically 2-3mm. In modern cameras the total spatial resolution is primarily due to the spatial resolution of the collimator, and the intrinsic spatial resolution is only a minor effect which usually can be ignored.

The production of light photons in the scintillation crystal is not instantaneous but occurs over a finite time interval ($\approx 500\text{ns}$) due to the lifetimes of the excited electronic states of atoms in the crystal induced by the energetic photo-electron [40]. Additionally, there is a finite time interval required to collect and convert the light photons into an electric pulse. More time is required to determine the energy deposited and the location of the interaction. The period of time required to complete the detection of a photon is usually termed the camera processing time and is much greater than the lifetimes of the excited states of the atoms in the crystal. These factors limit the maximum detection (or count) rate of the Anger camera. If a second photon interacts with the crystal before processing of a previous photon is completed, the two separate events will be indistinguishable to the camera electronics. The effect is that the two separate interactions appear as a single interaction with the light (i.e. energy) production being proportional to the sum of the separate photon energies. The energy discrimination circuits will almost certainly reject such an event involving two primary photons since the energy will be too high. This phenomenon is known as pulse pile-up and can completely saturate the camera electronics to the point that no photons will be detected even though they are most

certainly arriving at a very high rate. Note, however, the energy discrimination circuits will not reject events involving two scattered photons whose combined energy lies within the energy acceptance window.

D. Image Formation Process in Nuclear Medicine

It has been shown that there are a significant number of physical and detection processes associated with image formation in nuclear medicine. Analysis of a very simplistic imaging situation will demonstrate the implications of the above described processes for image formation. More detailed accounts can be found elsewhere [34-37,50-52]. The imaging situation to be considered here is that of 5 small point-like sources of ^{99m}Tc, of equal activity, located within the central transaxial slice of a uniform water-filled cylinder as shown schematically in Fig. II-7. It will be most instructive to focus attention on the row of pixels within the central transaxial plane containing the point sources, shown at the top of Fig. II-7. For an ideal imaging situation, i.e. ideal collimation and energy discrimination and no attenuation, the distribution of counts recorded by this row would be similar to the distribution (or profile) shown in Fig. II-8. For this ideal situation only those pixels for which one of the point sources lies along their line of sight records a non-zero value and, further, the value recorded is independent of the source depth. This is truly an ideal imaging situation.

To demonstrate the effects of collimation, in Fig. II-9 the distribution obtained using a realistic, low energy all purpose (LEAP) collimator for the imaging situation in Fig. II-7 is shown. Still, no attenuation in the medium is present. The distribution obtained consists of five Gaussian-like responses, with each FWHM being proportional to the source depth. It is evident in Fig. II-9 that the FWHM is dependent upon the source depth and increases with increasing depth as schematically illustrated in Fig. II-4. The spatial resolution of the collimator is directly proportional to the FWHM of the distribution.

Including the effects of attenuation and buildup is done in two steps in order to separate the effects solely due to scatter interactions from those due to all interaction

modes. First, it is assumed that the Anger camera has perfect energy resolution and only detects the primary photons. Photons which have undergone a scattering interaction are not recorded since their energy is always less than the primary photon energy. Fig. II-10 shows that the counts recorded decrease significantly for the deeper source locations. This is because the probability that an emitted photon will undergo an interaction before escaping the medium increases with increasing source depth. The distribution is replotted using a logarithmic vertical scale in Fig. II-10, demonstrating the exponential dependence in Eq. (II.11).

To include all attenuation and buildup effects a more realistic model of the energy resolution of the Anger camera must be employed. In Fig. II-11, the distribution obtained for a 0.95 cm thick scintillation crystal with an intrinsic energy resolution of 12% and a camera employing a 20% symmetric energy window is shown for the imaging situation in Fig. II-7. It is now possible that scattered photons having energies below the lower window limit (i.e. below 126 keV) will, nevertheless, be recorded because of the finite energy resolution of the camera, discussed earlier (Eqs. (II.18) through (II.22)). Actually, a significant fraction of all recorded photons are the scattered ones which arrive at the collimator face from locations in the medium different than the positions of the five primary sources. Consequently, further spatial broadening of the recorded signal is expected. This is illustrated in Fig. II-11 in which the distribution is plotted on a logarithmic vertical scale with the total distribution, the distribution due to primary (or unscattered) photons, and the distribution due to scattered photons plotted separately. As the source depth is increased, the total number of detected scattered photons begins to exceed the total number of detected primary photons as the right hand portion of the plot in Fig. II-11 demonstrates.

In Fig. II-12 the experimental distribution obtained from an Anger camera for the imaging situation in Fig. II-7 is shown. The obtained distribution is very similar to the distribution shown in Fig. II-11, except the experimentally acquired distribution contains statistical noise. The statistical noise is partly due to the electronics of the Anger camera,

but to a much greater extent it is due to the Poisson nature of the radioactive decay process [53]. If the sources were imaged until a very high count was recorded, the experimental distribution shown in Fig. II-12 would appear more like the expectation distribution (i.e. infinite counts) shown in Fig. II-11.

Even for this most simplistic imaging situation the physical processes involved in image formation produce noticeable effects. Obviously these processes and their effects must be considered within the framework of a reconstruction procedure to obtain a quantitatively accurate estimate of the source distribution. In the following sections two reconstruction algorithms are considered, and the techniques used to account for the physical processes described above are discussed. However, before considering specific reconstruction algorithms, the general imaging problem must be specified. This is done next and a quantity termed the *photon detection kernel* for SPECT imaging is introduced.

E. Source Reconstruction in SPECT

The Integral Kernel Equation

The relationship between the radioactive source distribution, the attenuating medium, and the projection data recorded by an Anger camera is complicated due to the physical processes affecting photon propagation and due to the specifics of detection detailed in the previous sections. The imaging problem in SPECT (often referred to as the *forward projection problem* or the *image formation problem*) can be most generally described by an integral kernel equation [54] of the form

$$P(\mathbf{R}_i) = \int_{Source} d^3\mathbf{r}\, K(\mathbf{R}_i,\mathbf{r})\bar{\sigma}(\mathbf{r}), \qquad \text{(II.23)}$$

where $P(\mathbf{R}_i)$ is the number of photons detected by the imaging element (i.e. pixel or collimator hole) identified by the discrete position vector $\mathbf{R}_i$, $\bar{\sigma}(\mathbf{r})$ is the source distribution function (i.e. expected emissions per unit volume within the imaging time ΔT) about the point $\mathbf{r}$ (c.f. Eq. (II.25)), and $K(\mathbf{R}_i,\mathbf{r})$ is the photon detection kernel. The kernel $K(\mathbf{R}_i,\mathbf{r})$ is a dimensionless quantity which describes the probability that a photon

emitted at the position $\mathbf{r}$ will trigger detection of a photon in the imaging element $\mathbf{R}_i$. Ideally, the kernel should contain all of the physics of photon propagation and detection related to the particular imaging situation, including nonuniform attenuation (i.e. photoelectric absorption, Compton and Rayleigh scattering), collimator depth-dependent resolution, and the energy-dependent detection probability of the Anger camera. In this way, the particular model of the imaging problem can be completely contained within the formulation of the kernel, and the terms "kernel" and "model" can, therefore, be used interchangeably.

It must be noted that a radioactive source always has at least one time-dependent component, i.e. its exponential decay. Further, the source distribution may not be a static distribution in the most general imaging situation. In this work, dynamic source distributions are not considered, but the exponential decay of the source activity at each point within a static distribution must be taken into account. To account for the exponential decay of a static source Eq. (II.23) must be written in a more general form as

$$\begin{aligned} P(\mathbf{R}_i) &= \int_T^{T+\Delta T} dt \int_{Source} d^3\mathbf{r}\, K(\mathbf{R}_i,\mathbf{r})\dot{\sigma}(\mathbf{r},t) \\ &= \int_{Source} d^3\mathbf{r}\, K(\mathbf{R}_i,\mathbf{r}) \int_T^{T+\Delta T} dt\, \dot{\sigma}(\mathbf{r},t) \end{aligned}, \tag{II.24}$$

where $\dot{\sigma}(\mathbf{r},t)$ is the source efficiency distribution function (i.e. expected emission per unit volume per unit time), T is the time lapsed between the source calibration and the start of data acquisition, and ΔT is the acquisition time. For a static source distribution with only simple exponential decay time dependence, the time integration can be performed analytically giving Eq. (II.23) through the relation

$$\begin{aligned} \bar{\sigma}(\mathbf{r}) &= \int_T^{T+\Delta T} dt\, \dot{\sigma}(\mathbf{r},t) = \int_T^{T+\Delta T} dt\, \dot{\sigma}_0(\mathbf{r}) \exp[-\lambda t] \\ &= \left[\frac{1-\exp[-\lambda \Delta T]}{\lambda \exp[\lambda T]}\right] \dot{\sigma}_0(\mathbf{r}) \end{aligned}, \tag{II.25}$$

where $\dot{\sigma}_0(\mathbf{r})$ is the calibration activity of the source, always taken at time $t = 0$: $\dot{\sigma}_0(\mathbf{r}) = \dot{\sigma}(\mathbf{r}, t = 0)$. Throughout the remainder of this thesis the time dependence of the source is suppressed since it will be implicitly assumed that the source distribution is static.

The effects of time-dependent exponential decay of the source can always be accounted for after the fact using the above correction procedure. As such, Eq. (II.23) provides a sufficient description, for our purposes, of the most general imaging situation.

Reconstructions - The Inverse Problem

The ultimate goal in SPECT imaging is to obtain the source distribution from the recorded projection data provided the imaging situation (i.e. the kernel) is known. This procedure has been traditionally termed *reconstruction* and most generally requires inverting the integral kernel equation (Eq. (II.23)) for the source distribution as a function of the projection data. For typical imaging situations the kernel possesses neither point nor translational symmetries, and therefore theoretical inversion techniques are of very little use. In practice the source distribution is generally reconstructed numerically using a computer.

As already discussed in Chapter I, in actual applications continuous positions within the source distribution must be quantized. Specifically, the source distribution is divided into many small voxels V_j, each of volume V, over which both the photon detection kernel and the source distribution vary negligibly. Thus, labeling the source voxels with an index j, replacing the (discrete) argument $\mathbf{R}_i$ with an index i, and defining the discrete source distribution, s_j, and the discrete transition probability matrix (or simply, the kernel), $K_{i,j}$, as

$$s_j = \int_{V_j} d^3\mathbf{r}\,\bar{\sigma}(\mathbf{r}), \tag{II.26}$$

$$K_{i,j} = \frac{1}{V}\int_{V_j} d^3\mathbf{r}\,K(\mathbf{R}_i,\mathbf{r}), \tag{II.27}$$

the integral relation Eq. (II.23) can be expressed in matrix form as

$$P_i = \sum_j K_{i,j} s_j . \tag{II.28}$$

Equation (II.28) is more commonly used in SPECT than the integral kernel equation, Eq. (II.23), because of its discrete nature. In practice, for small enough voxels, the matrix

elements $K_{i,j}$ can be identified with $K(\mathbf{R}_i, \mathbf{r} = \mathbf{r}_j)$, and s_j can be approximated by $V\bar{\sigma}(\mathbf{r}_j)$, where $\mathbf{r}_j$ is a representative position within the j^{th} voxel. It must be noted that the indices i and j stand for the complete set of discrete variables necessary for, respectively, a unique determination of the pixel position for all configurations of the gamma camera around the attenuating medium, and for the determination of positions of all source voxels within the medium.

All reconstruction methods in SPECT attempt to solve the large set of linear equations given by Eq. (II.28) for s_j, in which the measured projection data P_i are presumably known. Mathematically, a direct matrix inversion of Eq. (II.28), i.e.

$$s_j = \sum_i K_{j,i}^{-1} P_i , \tag{II.29}$$

would neither be stable nor in general even be unique since the projection input data P_i, and possibly also the matrix $K_{i,j}$, contain statistical noise and, furthermore, the number of projection pixels is generally different from the number of source voxels. Finally, direct inversion of the kernel matrix is computationally impractical due to its enormous size (typically $64^3 \times 64^3$).

Theoretically, the reconstruction procedure in SPECT can be viewed as a two-step process. First, the photon detection kernel for the imaging situation must be specified and the kernel elements $K_{i,j}$ must be calculated. Second, given the calculated kernel elements, Eq. (II.23) or (II.28) must be inverted to obtain the source distribution from the measured projection data. The complete physics of the imaging problem enters the procedure of designing or calculating the kernel. Once the kernel is specified there exist several techniques to invert Eq. (II.23) and (II.28) for the source distribution. The choice of the particular inversion technique used depends strongly upon the form of the kernel. To demonstrate this fact, two traditional approaches to the reconstruction problem in SPECT are considered next, beginning with the popular Radon transform approach.

F. The Radon Transform Approach

Traditionally, the photon detection kernel has been based upon a simplistic model of photon propagation and detection, which will be called the *Radon model* or *Radon kernel* in this work. Essentially, within the Radon model only those source points which lie along the line of sight of a given collimator hole can contribute photons recorded by that collimator hole. Therefore, for the collimator hole of radius R_c centered around the position $\mathbf{R}$, as shown in Fig. II-13, the probability $K(\mathbf{R},\mathbf{r}_0)$ that a photon from the source point $\mathbf{r}_0$ gets recorded by this collimator hole is unity if $\mathbf{r}_0$ is within the cylindrical volume of radius R_c extending from the front face of the collimator into the source distribution (shaded region in Fig. II-13) and is zero otherwise. Obviously, this model for the kernel can only be valid if R_c is much smaller than both the length of the collimating cylinder and the distance from the collimator to the source because the fact that the photon flux decreases with the distance from the source (i.e. that the photon beam diverges) is ignored here. This is why this kernel is so successful in astronomy. It is obvious that the Radon kernel is based on very simple geometrical considerations and does not attempt to account for the physics of photon propagation through the medium nor for the specifics of detection. The mathematical expression for the above kernel is

$$K(\mathbf{R},\mathbf{r}_0)=\int_{-\infty}^{0} du\int_0^{R_c} d\rho\,\rho\int_0^{2\pi} d\phi\;\delta^{(3)}(\mathbf{r}_0-(\mathbf{R}+\mathbf{r})). \tag{II.30}$$

Substituting Eq. (II.30) into Eq. (II.23) and performing the integration over $d_3\mathbf{r}_0$ gives

$$P(\mathbf{R})=\int_{-\infty}^{0} du\int_0^{R_c} d\rho\,\rho\int_0^{2\pi} d\phi\;\bar{\sigma}(\mathbf{R}+\mathbf{r}). \tag{II.31}$$

If the collimator hole radius R_c is small then the source density distribution varies negligibly over the cross section of cylindrical integration volume allowing the source term to be taken outside the $d\rho$ and $d\phi$ integrations, giving

$$P(\mathbf{R})=\pi R_c^2\int_{-\infty}^{0} ds\,\dot{a}_0(\mathbf{R}-s\hat{\mathbf{n}}_{\mathbf{R}}), \tag{II.32}$$

where $\hat{\mathbf{n}}_{\mathbf{R}}$ is a unit vector normal to the face of the collimator hole at $\mathbf{R}$. With no loss of generality for the Radon kernel, as previously discussed, it is convenient for computational purposes to consider the source distribution to be divided into thin transaxial slices (i.e.

averaged over the range $z_0 \le z \le z_0 + dz$). In such a geometry, the line integrals in Eq. (II.32) corresponding to a given transaxial slice can be rewritten in a simpler 2D form as

$$\begin{aligned} P(t,z;\theta) &= \pi R_c^2 \iint dx dy\, \delta(x\cos\theta + y\sin\theta - t)\bar{\sigma}(x,y,z) \\ &= \pi R_c^2 \int_{-\infty}^{s_d} ds\, \bar{\sigma}(x(t,s), y(t,s), z) \end{aligned}, \tag{II.33}$$

where the variables (x, y) and (t, s) are related through

$$\begin{pmatrix} t \\ s \end{pmatrix} = \begin{pmatrix} \cos\theta & \sin\theta \\ -\sin\theta & \cos\theta \end{pmatrix} \begin{pmatrix} x \\ y \end{pmatrix}, \tag{II.34}$$

and s_d denotes the distance of the projection row from the $t-$axis, as depicted in Fig. II-14. Note that since this kernel does not depend upon the distance between the source and collimator, s_d can be taken to infinity when it is convenient for calculation purposes.

Many reconstruction algorithms used in SPECT have been based upon the Radon transform given by Eq. (II.33). As demonstrated by Eq. (II.33), the Radon transform is simply a mathematical process by which a two-dimensional function is represented by a complete set of line integrals taken at all possible angles about the 2D function and all possible locations along the projection axis at each angle. The power of the Radon transform is that the inverse Radon transform exists and can be obtained analytically using the Fourier Slice Theorem [34-36], and is given by

$$\begin{aligned} \bar{\sigma}(x,y,z) &= \int_0^{\pi} d\theta \int_{-\infty}^{\infty} d\omega |\omega| e^{i2\pi\omega t} \int_{-\infty}^{\infty} dt'\, P(t',z;\theta) e^{-i2\pi\omega t'} \\ &= \int_0^{\pi} d\theta\, \mathbf{F}^{-1}\left[|\omega| \mathbf{F}\left[P(t,z;\theta)\right]\right] \end{aligned}, \tag{II.35}$$

where $t = x\cos\theta + y\sin\theta$, ω is the Fourier transform variable corresponding to t, and $\mathbf{F}$ is the 1D Fourier transform operator with respect to t and $\mathbf{F}^{-1}$ is its inverse. From a practical perspective, a two-dimensional function can be obtained (i.e. reconstructed) from a complete set of line integrals (i.e. all possible values of t for all possible values of θ) of that function via the inverse Radon transform, i.e. Eq. (II.35).

The application of the Radon transform to SPECT reconstructions is that the magnitude of the signal recorded at each pixel is, to a crude first approximation, proportional to the ray sum (i.e. line integral for an ideal collimator) of the activity seen along its line of sight (i.e. perpendicular to the imaging plane). Pixels forming a row within the transaxial plane perpendicular to the axis of rotation of the camera see, in the Radon model, only that activity which is contained within the same transaxial plane, i.e. the activity within the volume occupied by the corresponding transaxial source slice (c.f. Figs. I-2 through I-4)). As such, each row of pixels provides a set of discrete values corresponding to the Radon transform of the 2D source activity distribution within the transaxial slice at a single angle (i.e. for several t-values but only one θ-value). If such sets of data are available for several angles θ then they can be jointly used in the discrete version of Eq. (II.35) to reconstruct the source activity distribution within the corresponding 2D transaxial slice (i.e. for fixed z) [35]. The full 3D activity distribution can be obtained by reconstructing each 2D transaxial slice independently at various positions z along the axis of rotation. Of course, in practical applications involving projection data obtained from an Anger camera, Eqs. (II.33) and (II.35) must be discretized [34-36].

It is conventional to begin the discussion of SPECT reconstruction with the Radon Transform rather than with the integral kernel equation. This is because the Radon Transform has a very intuitive physical interpretation which mimics the detection process for an *idealized* camera system and imaging situation - i.e. collimator holes act as true line integrators of the source distribution along their line of sight and attenuation and buildup are completely ignored. This is exactly what Eq. (II.30) says mathematically and what Figure II-13 depicts schematically. The Radon transform approach to reconstruction follows, however, a proposition quite contrary to that which was outlined in the preceding sections. There, it was stated that the first step should be to accurately model the imaging situation to obtain a reliable kernel K. Obviously this is not the case for the Radon transform approach. Instead, a very simple and idealized model for the kernel is assumed which then allows Eq. (II.23) to be inverted analytically. To work in practice, it is

necessary to correct for physical processes not modeled within the Radon transform approach, but which are obviously present in the recorded projection data (c.f. Figs. II-8 through II-12). In most cases, the correction methods used do not attempt to improve the model, since then the Radon transform approach would no longer provide a viable solution to the reconstruction problem. Instead, the methods used generally process the acquired projection data to better approximate the Radon transform of the activity distribution - i.e. to convert the data actually acquired to a form which approximates, as accurately as possible, the projection data that would be recorded if the collimator acted as a true line integrator and the effects of attenuation were not present. Furthermore, other correction methods are used to modify the reconstructed transaxial slices to incorporate effects which can not be included in either the model or the projection data.

It has been known for many years that the Radon transform is a poor model of the actual imaging problem since it does not account for the physical processes associated with photon propagation, nor for the specifics of detection. Despite its deficiencies, it continues to be a very popular model of the imaging problem in SPECT, and further, practically all commercially available reconstruction software is based on it. This is primarily because the Radon kernel allows for a rather simple analytic inversion of the integral kernel equation. Another, more practical factor is that reconstruction methods based on the Radon kernel are easily calculated on presently available computer hardware. Since it is known that the projection data acquired with the Anger camera differ significantly from what the assumed model predicts (i.e. the Radon model), numerous correction methods have been (and continue to be) derived and applied to the projection data or to the reconstructed slice data to force both data sets to conform to the assumed model.

Correction and Compensation Methods for the Radon Transform

Typical nuclear medicine images obtained from an Anger camera are degraded to a large extent by statistical noise, the poor spatial and energy resolution of the Anger camera, and the effects of attenuation (i.e. both photoelectric absorption and Compton

scattering and buildup); all of which are not directly considered within the Radon approach. These processes constitute the majority, but not all, of the image degradation effects encountered in SPECT imaging. Popular techniques used to correct, or to at least compensate, for these processes, which are applicable to the Radon transform approach, are discussed briefly in the following.

Image Processing - Filtering

A very popular extension to the Radon transform approach has been to compensate and/or correct for unwanted effects using image processing techniques such as deconvolution and inverse Fourier filtering [34-37, 55-57]. The majority of these image processing techniques are based on the image degradation model, and have been termed image restoration techniques. In particular, the derivation of the Radon transform ignores the fact that the projections obtained from the Anger camera are not truly line integrals of the activity distribution, as required by the Radon transform. Ignoring the effects of attenuation for the moment, the projection data obtained can be regarded as line integral measurements of activity convolved with an instrument or blurring function. The instrument function is assumed to partially account for the loss of spatial resolution due to the effects of the depth-dependent collimator resolution. The projection data actually acquired can be expressed as

$$P_C(t,z;\theta) = P_I(t,z;\theta) * h(t,z), \tag{II.36}$$

where $P_I(t,z;\theta)$ are true line integrals, $P_C(t,z;\theta)$ are the projection data actually obtained from the Anger camera, $h(t,z)$ is the known instrument function, and $*$ is the 2D convolution operator with respect to t and z, i.e.

$$P'(t,z;\theta) = P(t,z;\theta) * h(t,z) = \int dt'dz' \, P(t',z';\theta) h(t-t',z-z'). \tag{II.37}$$

In Eq. (II.37) it has been assumed that the instrument function h is a spatially invariant function of both t and z, as required by the convolution theorem. In general the instrument function must be measured experimentally [55,56,58]. Using Fourier transform techniques, the true line integrals can be obtained from those measured by the Anger camera by deconvolving the known instrument function from the measured data:

$$P_I(t,z;\theta) = \mathbf{F}^{-1}\left[\frac{\mathbf{F}\left[P_C(t,z;\theta)\right]}{\mathbf{F}\left[h(t,z)\right]}\right], \tag{II.38}$$

where $\mathbf{F}$ is the 2D Fourier transform operator with respect to the variables t and z, $\mathbf{F}^{-1}$ is its inverse, and $\mathbf{F}\left[h(t,z)\right]$ is called the modulation transfer function (MTF) of the camera system [30,56,58]. The MTF characterizes the instrument response as a function of the spatial frequency, and must tend to zero for increasing spatial frequencies, since no instrument can accurately reproduce all spatial frequencies. This fact presents additional problems with the deconvolution process given by Eq. (II.38).

Deconvolution and inverse filtering techniques can also be applied to the problem of scatter correction [55-57,59-61]. These correction techniques assume that the acquired projection data, P_C, is the sum of two components: one due to unscattered photons, P_{US}, and another one due to scattered photons, P_S, as

$$P_C(t,z;\theta) = P_{US}(t,z;\theta) + P_S(t,z;\theta). \tag{II.39}$$

It is further assumed that P_S can be modeled by the convolution of P_{US} with a scatter convolution kernel f_S as

$$P_S(t,z;\theta) = P_{US}(t,z;\theta) * f_s(t,z) = \iint dz'\,dt'\,P_{US}(t',z';\theta)\,f_s(t-t',z-z'), \tag{II.40}$$

allowing Eq. (II.39) to be rewritten as

$$P_C(t,z;\theta) = P_{US}(t,z;\theta) + P_{US}(t,z;\theta) * f_s(t,z;\theta) = P_{US}(t,z;\theta) * \left(\delta^{(2)}(t,z) + f_s(t,z)\right), \tag{II.41}$$

where $\delta^{(2)}$ is the 2D Dirac delta function. Thus, the unscattered component is obtained through inverse filtering as

$$P_{US}(t,z;\theta) = \mathbf{F}^{-1}\left\{\frac{\mathbf{F}\left\{P_C(t,z;\theta)\right\}}{\mathbf{F}\left\{\delta^{(2)}(t,z) + f_s(t,z)\right\}}\right\}. \tag{II.42}$$

Of course, to use Eq. (II.42) in practice the scatter convolution kernel must be expressible as a spatially invariant function, as emphasized in Eq. (II.40).

The scatter convolution kernel f_s can be obtained experimentally by measuring a point source both in the presence and absence of the attenuating medium [59]. The data sets acquired must be separately corrected for the depth-dependent resolution due to collimation before they can be used in Eq. (II.42) to calculate the scatter convolution kernel. The effects of both scattering and depth-dependent resolution can be combined by acquiring data for a point source within a medium of interest and assuming a delta-like response. The blurring or instrument function that would be obtained would have a component due to scattering and a component due to the depth-dependent resolution. Such an instrument function could be used to partially deconvolve the effects of scatter and depth-dependent resolution from measured data in one operation.

To be a practical correction method, the instrument function characterizing the Anger camera and the scatter convolution kernel characterizing the medium must be spatially invariant functions. However, in reality the instrument function of the Anger camera is not spatially invariant, depending primarily upon the source to collimator distance. In general, the scatter response function is also not spatially invariant, but depends strongly upon such factors as the description of the attenuating medium and the source distribution itself [55-65]. Therefore, Eq. (II.38) and (II.42) can only provide an approximate correction based upon average instrument and/or scatter convolution functions. The main advantage of such an approach is that the effects of depth-dependent collimator resolution (which is spatially invariant for a fixed depth) can be partially corrected. Another advantage of inverse filtering techniques is that the statistical noise contained in the projection data can be reduced by combining a smoothing filter with the inverse MTF filter, producing a more visually pleasing image. The effects of scattered photons, however, are not capable of being represented accurately by the image degradation model due to the strong spatial dependence upon the medium description. Additional correction methods, which are outlined below, have been proposed to compensate or correct for the effects associated with scatter and attenuation.

Scatter Correction

Scatter correction techniques, applicable to the Radon transform approach, can be categorized into two groups. The first group of techniques attempts to correct the projection data by subtracting (or removing) the scattered photons, thus making the projection data better approximate that which would be expected if only primary photons were detected. They are termed scatter subtraction techniques. The second group of techniques attempts to account for the scattered photons and return them to their original source voxel, and when used with the Radon transform approach, these techniques are based on the inverse filtering methods described in the previous section. In this section the discussion is limited to scatter subtraction techniques.

Scatter subtraction techniques have been proposed by many authors [57,66-69]. The acquired projection data, $P_C(t,z;\theta)$, is assumed to be a sum (i.e. Eq. (II.39)) of two contributions: one due to primary photons (i.e. unscattered photons), $P_{US}(t,z;\theta)$, and another one due to scattered photons, $P_S(t,z;\theta)$. The basic difference between the various techniques is the way in which the scatter contribution is determined. For some techniques, projection data for one or more non-standard energy windows are acquired to determine the scatter contribution contained within a standard energy window through a number of weighting parameters w_k, i.e.

$$P_S(t,z;\theta) = \sum_k w_k P_k(t,z;\theta), \qquad \text{(II.43)}$$

where $P_k(t,z;\theta)$ are the counts recorded within the energy window identified by the index k. The weights w_k for each energy window are determined experimentally for a given imaging situation and, therefore, may not be applicable to other more general imaging situations. Other techniques have been proposed which use the data from various energy windows P_k in a more sophisticated way to estimate P_S, but these still require a number of parameters to be determined for each imaging situation. Further, acquiring projection data in more than two energy windows simultaneously may require substantial modifications to the existing imaging equipment.

The main advantage of scatter subtraction techniques is that they generally require little additional processing. The scatter-corrected projection data

$$P_{US}(t,z;\theta) = P_C(t,z;\theta) - P_S(t,z;\theta), \tag{II.44}$$

can be further corrected using the previously discussed deconvolution techniques to partially remove the effects of depth-dependent resolution. The main disadvantage of these techniques is two-fold [56,57,64-69]. First, they are generally based upon empirical models of the scattering process, requiring a number of parameters to be determined experimentally for a particular imaging situation. These parameters are then applied to an actual imaging situation which resembles the imaging situation which was used to obtain them. The second disadvantage is that they generally involve the subtraction of a noisy scatter image, P_s, from noisy projection data, P_C, resulting in a projection image, P_{US}, that is inherently more noisy, in fact, than would be expected for the actual count level of P_{US}.

Attenuation Correction

Attenuation is a major effect that must be compensated for to provide more quantitatively accurate reconstructed images [32,34-37,50-52,56,70,71]. However, correcting for attenuation most generally requires having a complete description of the distribution of attenuation coefficients within the medium, i.e. $\mu(\mathbf{r},E)$. The Radon transform can be extended to include the effects of uniform attenuation, which leads to the uniformly attenuated Radon transform, given by

$$P(t,z;\theta) = \pi R_c^2 \int_{-\infty}^{s_d} ds\, \bar{\sigma}(x,y,z)\exp(-\mu L(x,y,\theta)), \tag{II.45}$$

which should be used instead of Eq. (II.33). Here, μ is the uniform linear attenuation coefficient for the medium, $L(x,y,\theta)$ is the distance from the source point (x,y) to the edge of the attenuating medium along the line of sight of the pixel identified by $t,z,$ and θ, and the functions $x = x(t,s)$ and $y = y(t,s)$ are given in Eq. (II.34). A detailed description of the attenuating medium is not necessary since its properties are assumed uniform, but the boundary of the medium must be known. It is generally accepted that an analytical solution to the inverse attenuated Radon transform is not possible for imaging

situations involving nonuniform or arbitrarily shaped uniform attenuating media [70]. However, Bellini [70] successfully formulated an analytical inverse solution to the attenuated Radon transform, but it is only applicable to a uniform cylindrical attenuating medium.

Since it is not possible to invert the attenuated Radon transform analytically even for a simple uniform medium, techniques have been proposed to correct or compensate for attenuation either before, during, or after reconstruction. Techniques that attempt to correct for attenuation during the reconstruction do so by solving the inverse attenuated Radon transform. Preprocessing techniques attempt to correct the projection data whereas post-processing techniques attempt to correct the reconstructed slices for the effects of attenuation. One of the preprocessing approaches corrects the projection data by averaging projection data recorded at opposite sides of the medium and then applying an average attenuation correction factor proportional to the attenuation seen by the projection pixel along its line of sight [56]. The Chang post-processing attenuation correction is very often used to partially compensate for the effects of attenuation by processing the reconstructed transaxial slices [56,71]. In this technique the activity value at each reconstruction voxel is divided by an average attenuation factor. This factor represents the attenuation suffered by photons emanating from a given reconstruction voxel averaged over all projection angles. Although Chang's technique is very simple to implement, in practice it provides only an approximate correction and is unable to provide an accurate correction even for uniformly attenuating media. In general, attenuation is poorly handled within the Radon transform approach, and most methods developed so far are only approximate even for uniformly attenuating media. More importantly, errors introduced by such *ad hoc* approximation techniques are difficult to estimate and control.

Summary

The Radon transform approach to image reconstruction from projections is intuitive and provides adequate reconstructions for qualitative diagnostic purposes in many cases. The greatest deficiency of the Radon approach is that instead of attempting to model the

imaging situation more accurately, it leads to modifying the projection data to better suit the idealized model. Many proposed correction methods provide gains for specific well-defined imaging situations in which a point or line source is immersed in a uniform medium with a high degree of symmetry, simply because these methods rely upon an average, spatially invariant correction for which such imaging geometries are well suited. However, these same methods fail when applied to a non-uniform source distribution or to a non-uniform attenuating medium. A better approach to the reconstruction problem in SPECT is to provide a more accurate model of the imaging situation. However, such models do not allow for a simple analytic solution like the Radon approach, but must generally be solved iteratively. In the next section such a method is discussed and the need for a physically accurate modeling of the imaging situation is established.

G. Iterative Reconstruction Methods

The Radon transform approach to image reconstruction in SPECT is not capable of efficient utilization of a great deal of valuable information about the imaging problem, like attenuation, collimator response, camera energy response, etc. There exist, however, reconstruction techniques capable of utilizing the vast majority of the available information about the imaging situation. These techniques provide a solution to the inverse problem through numerical iteration, instead of doing it analytically. The distinct advantage to these iterative techniques is that, at least in theory, no simplifying assumptions about the imaging situation need to be made. An accurate model of the imaging problem can be completely contained within the kernel matrix. One particular disadvantage of these reconstruction methods is that the projection recorded by a row of pixels within a certain transaxial plane depends on the source distribution in transaxial slices belonging to adjacent transaxial planes. Therefore, slice by slice reconstruction methods can no longer be used and one must truly consider the three dimensional nature of the reconstruction problem at hand. This leads to a much more numerically demanding solution to the reconstruction problem.

One of the iterative reconstruction techniques that has received considerable attention over the last decade is the Maximum Likelihood - Expectation Maximization (MLEM)

algorithm [72-75]. The MLEM algorithms maximize the "likeliness" between the actually measured projection data P_i and the estimated projections $P_i^{(k)}$ calculated from Eq. (II.28) using the k^{th} estimate of the source distribution $s_j^{(k)}$

$$P_i^{(k)} = \sum_{j'} s_{j'}^{(k)} K_{i,j'}, \tag{II.46}$$

by minimizing statistical deviations between $P_i^{(k)}$ and P_i. The source distribution estimate is updated to $s_j^{(k+1)}$ in the next iteration, as follows

$$s_j^{(k+1)} = \frac{s_j^{(k)}}{\sum_{i'} K_{i',j}} \sum_i \frac{P_i K_{i,j}}{P_i^{(k)}}, \tag{II.47}$$

resulting in calculated projections $P_i^{(k+1)}$ more closely resembling P_i than does $P_i^{(k)}$, thereby reducing the deviations between the expected (i.e. calculated) and measured projections. The initial estimate of the source distribution, $s_j^{(0)}$, is generally obtained by setting all voxels to the same value unless there is some *a priori* information available to make a better initial estimate.

The updating procedure is continued iteratively until the differences between the calculated and the actual projections are reduced to some pre-defined tolerance. Since the deviations between the calculated and the actual projections are small, an assumption is made that the differences between the final estimate of the source distribution $s_j^{(\text{final})}$ and the true source distribution s_j will also be small. This, however, is not necessarily true if the employed kernel $K_{i,j}$ does not accurately model the actual imaging situation, as is the case when $K_{i,j}$ does *not* adequately account for all essential physical processes involved in photon propagation and detection. Given measured projection data P_i, the iterative statistical procedure will almost always lead, within the assumed tolerance bounds, to some "best" final estimate of the source distribution $s_j^{(\text{final})}$, no matter how poorly the kernel $K_{i,j}$ models the actual imaging situation. Such an estimate $s_j^{(\text{final})}$ can be very different from the true source distribution s_j, however, and will only be a reliable

representation of s_j if the kernel $K_{i,j}$, used in the reconstruction, models the actual imaging situation as accurately as possible.

It must be noted that, in general, the reconstruction problem in SPECT is severely underdetermined. Further, the noisy projection data leads to a noisy reconstructed source distribution. It is well known that at high iterations the noise content of the reconstructed distribution increases significantly with increasing iteration number, and that the algorithm generally never converges to a stable solution - not even for algorithms employing exact kernel data. Due to these issues, MLEM-based reconstructions depend heavily upon the criteria used to stop the algorithm [76-79]. The stopping criteria can significantly effect the reconstructed distribution and therefore great care must be taken when determining a stopping criteria for the algorithm.

H. Reconstruction Kernels

Observed trends towards using more sophisticated reconstruction methods, such as Maximum Likelihood, are justified since these methods inherently address the problem of noisy projection data and may use kernels $K_{i,j}$ which accurately model the actual imaging situation. Presently, there are two major obstacles in effectively implementing these powerful methods: i) kernels $K_{i,j}$ accurately modeling actual imaging situations, and in particular, accurately accounting for the effects of scatter, are not easily calculated or measured for the general imaging situation, and ii) storage and computational problems caused by the large size of $K_{i,j}$ must be dealt with.

Iterative reconstruction methods based upon the MLEM algorithm have been proposed with $K_{i,j}$ accounting for the depth-dependent collimator resolution and/or for non-uniform attenuation [80-84]. However, most methods used to date do not attempt to account for the effects of scattering directly within the kernel matrix. Instead, a simplified kernel is used in conjunction with additional signal processing (similar to the scatter correction methods discussed with respect to the Radon Transform approach), possibly at

each iteration step, to compensate for the effects of scattering as well as other physical processes not accounted for within the kernel matrix used. In other methods, attempts to account for scattering directly within the kernel are made, but they are based upon simplified models of the actual scattering process [85-87]. An accurate $K_{i,j}$ appropriate for arbitrary imaging situations is necessary if the quantitative capabilities of the iterative reconstruction algorithms are to be fully realized, and more importantly for a complete understanding of the problem. In general, however, the underlying and motivating principle is that, the more accurately $K_{i,j}$ can be specified, the more stable, precise, and unique will likely be the reconstruction of the 3D source distribution. To meet this demand the effects of scattering must be accounted for directly within the kernel.

The second obstacle, the physical size of $K_{i,j}$, can be somewhat eased by limiting the extent of the kernel by judiciously not "connecting" every source voxel j to every projection pixel i, or in other words, setting large blocks of this matrix equal to zero. Currently, this "connectivity" between the source voxels and the projection pixels is most often determined solely by the 3D depth-dependent resolution of the collimator. This greatly reduces the connectivity between the source voxels and the projection pixels, and thus it also reduces the size of $K_{i,j}$, since the 3D collimator depth-dependent resolution generally does not exceed a 2D FWHM radius of a few pixels. However, kernels which account for scattered photons will require a much larger connectivity which cannot be determined by simple geometrical considerations only, but instead, must be determined from the properties of the attenuating medium.

I. Modeling Photon Detection Kernels

There exist several models proposed for the photon detection kernel applicable to general imaging situations. In general, accounting for the effects of nonuniform attenuation within the kernel is straightforward, provided a description of the attenuating medium is available, since this only requires an evaluation of the integral in Eq. (II.12) for the source and the collimator coordinates. Further, the depth-dependent collimator

resolution is a purely geometrical effect and is easily accounted for within the kernel [88]. The major difficulty has been to develop an accurate model of the scattering component of the kernel and it still remains an area of intensive research [84-87,89-98].

There are two main difficulties in studying and modeling the scattering component of the kernel. The first one is that experimentally, except for very simplistic imaging situations, the unscattered and scattered components of the projection data cannot be separated. Further, experimental investigations of scattering are time consuming and cumbersome, simply because a large number of separate measurements are required to obtain sufficient data needed to reasonably model scattering for a given attenuating medium. The second difficulty is that, unlike attenuation and depth-dependent collimator resolution, scattering requires explicitly solving the photon transport equations for the attenuating medium, and the specifics of detection by the Anger camera must be taken into account. As a result, this problem has generally been avoided due to presumed theoretical difficulties [86,87,89,90,92,95,96].

Although direct theoretical formulation of the photon detection kernel applicable to general imaging situations is not straightforward, all individual microscopic processes are known. Most of them have been described previously in this chapter. It is possible to numerically simulate an experiment using uniform random sampling of the inverse cumulative probability distributions describing the possible photon interactions [99] and accounting for the specifics of detection [50,85,100,101]. These methods are known as Monte Carlo (MC) simulation techniques and they have drawn enormous attention from the nuclear medicine research community. The MC simulation techniques allow the degrading effects of depth-dependent collimator resolution, attenuation, and the detection process to be studied in detail and in isolation from one another. In particular, the effects of scattered photons can be investigated in detail. The only drawback of the MC simulation method seems to be that a very large number of individual photon histories must be followed to obtain statistically useful results, which requires a large amount of computational effort. Even with today's powerful computing hardware Monte Carlo

simulations are computer intensive and are always subject to a finite counting error. In any event, the application of Monte Carlo simulation techniques to photon propagation and detection in nuclear medicine must be marked as a major landmark in nuclear medicine research.

In principle, Monte Carlo simulation methods could be used to calculate the kernel matrix for practically any given imaging situation [100,101]. However, because MC simulations are computer intensive, such an approach is not practical using today's computing hardware. Instead, the Monte Carlo simulation methods have been exploited to determine parameters for use in empirical models of the kernel, and in particular those of the scattering component of the kernel [47,86,87,89-91,93,94]. The models obtained are simple to implement numerically and require significantly less computational effort than a direct MC simulation of the same problem. Further, these models allow for spatially nonhomogeneous scattering and the parameters can be tailored to provide accurate models of the kernel for a given situation. These empirical models may hold the greatest promise for the immediate future, or at least until computer resources are available to directly calculate the kernel using MC simulation or other methods. However, in most cases, parameters specific to each imaging situation must be obtained to apply such an empirical model. Thus, an accurate model of the photon detection kernel is required even if it serves no other purpose than to aid in the determination of parameters for an empirical model. The MC simulation method has been used extensively for this purpose to date.

From a physicist's point of view, the Monte Carlo simulation technique is a useful, powerful, and practical technique for studying the imaging problem in nuclear medicine, but it is somewhat short of a completely satisfactory solution to that problem. A Monte Carlo simulation technique, no matter how powerful and sophisticated, is not a physical theory, but is more akin to experiment. Simultaneously, it has been generally accepted that an analytic formulation of the photon propagation and detection problem is neither feasible nor practical. The work presented in the following chapter begins by returning to the general imaging problem, Eq. (II.23), and attacking the problem using the methods of

theoretical physics. It will be shown that an analytical formulation, i.e. a theory, of the photon propagation and detection problem in nuclear medicine imaging is both feasible and practical. As an added bonus, this formulation provides well-defined integral expressions for each scattering order of the photon detection kernel, implicitly accounting for attenuation, both Compton and Rayleigh scattering, and for the specifics of the photon detection process using a collimated Anger camera. Further, this theoretical formulation embraces the majority of advantages of the Monte Carlo simulation techniques without some of their inherent statistical drawbacks.

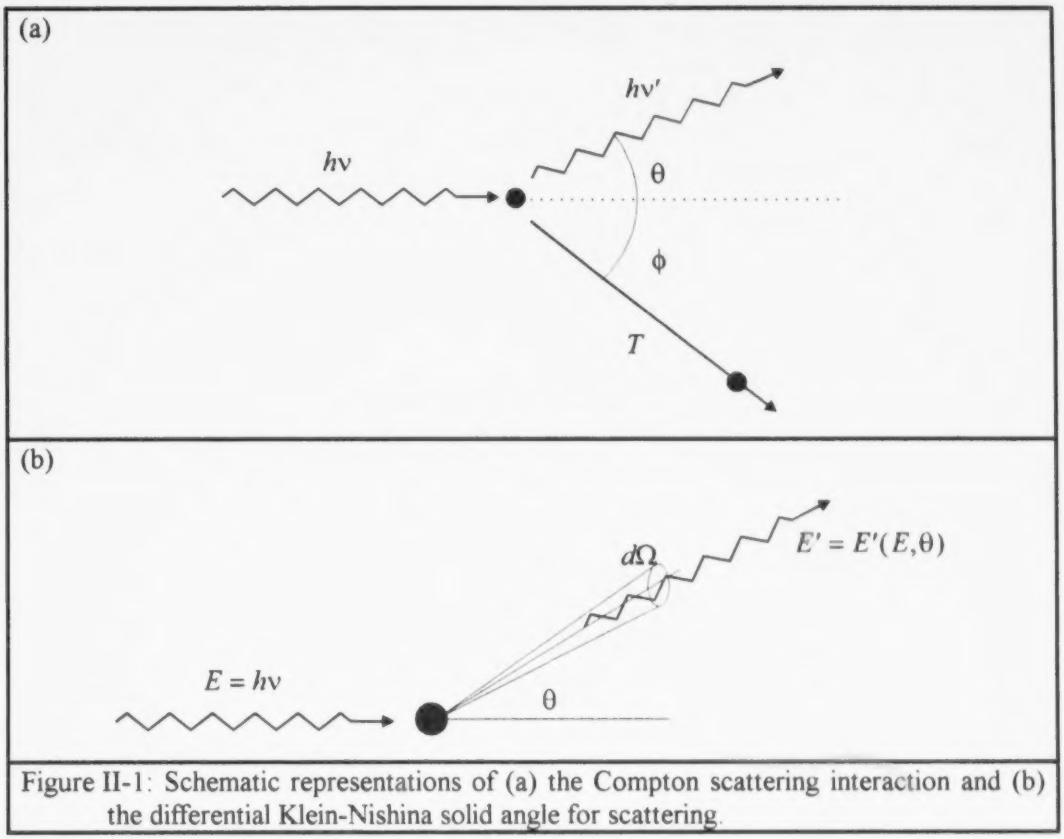

Figure II-1: Schematic representations of (a) the Compton scattering interaction and (b) the differential Klein-Nishina solid angle for scattering.

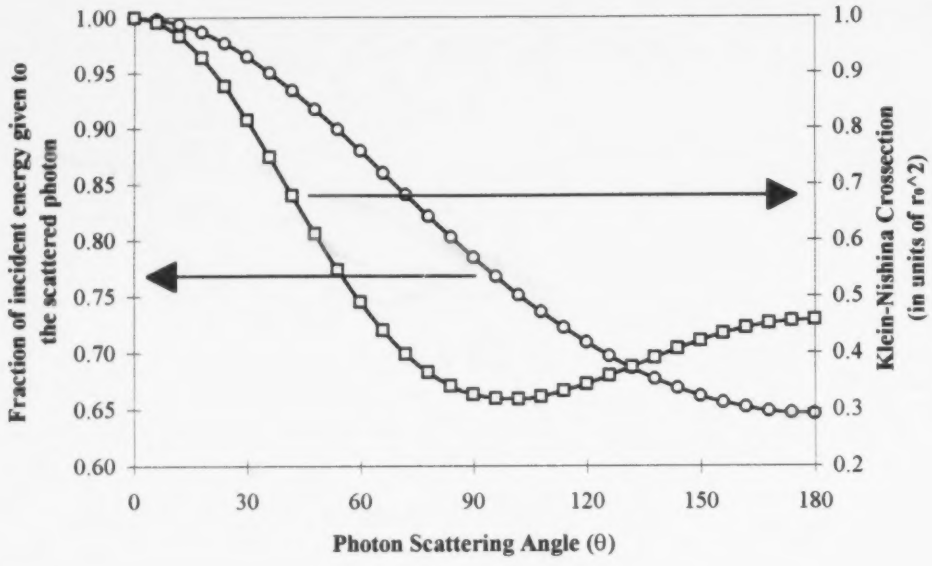

Figure II-2: Fraction of the incident photon energy given to the scattered photon (circles) and the Klein-Nishina cross section (squares) versus scattering angle using Eqs. (II.1) and (II.5), respectively, for photons with incident energy $E = 140$ keV. Here r_0 is the classical electron radius defined around Eq. (II.5)

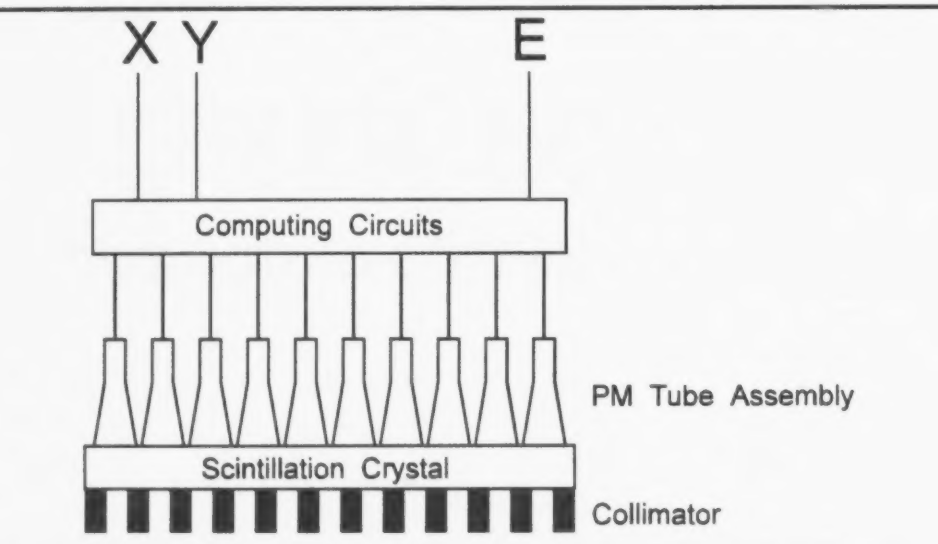

Figure II-3: Schematic representation of the Anger camera and its components.

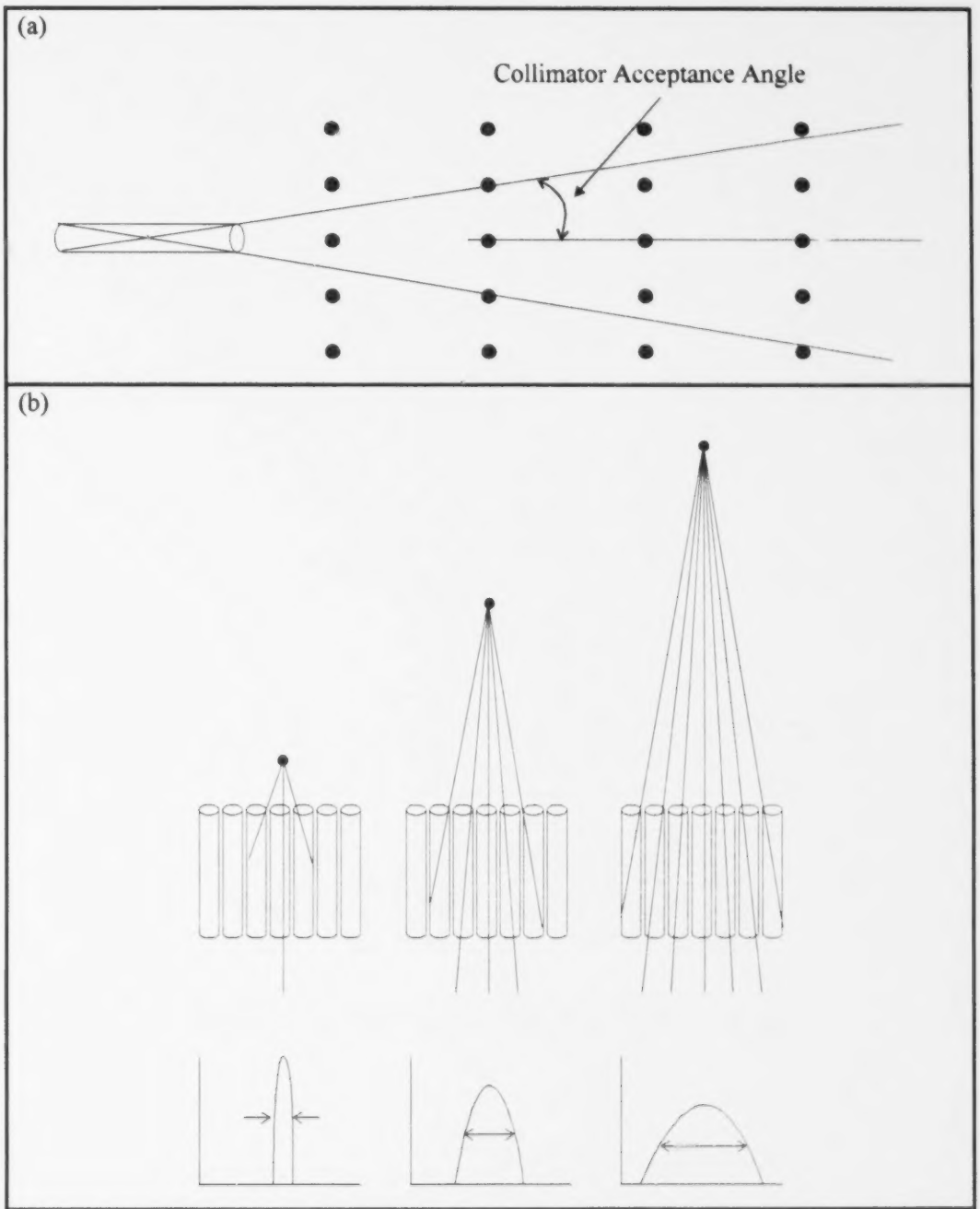

Figure II-4: The concept of absorptive collimation is shown (a) from the collimator perspective and (b) from the source perspective.

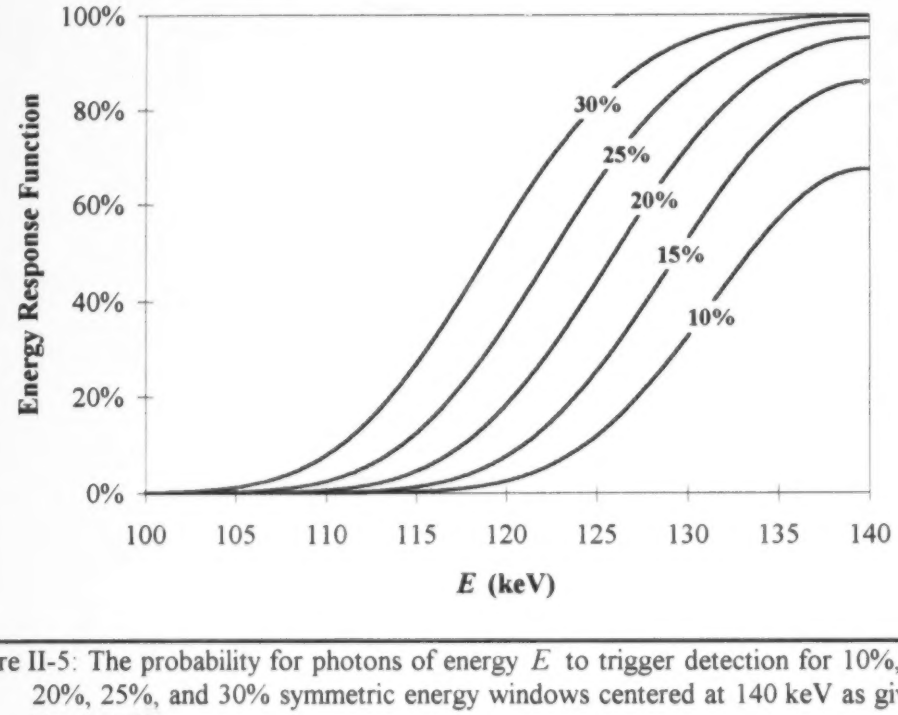

Figure II-5: The probability for photons of energy E to trigger detection for 10%, 15%, 20%, 25%, and 30% symmetric energy windows centered at 140 keV as given by Eq. (II.20).

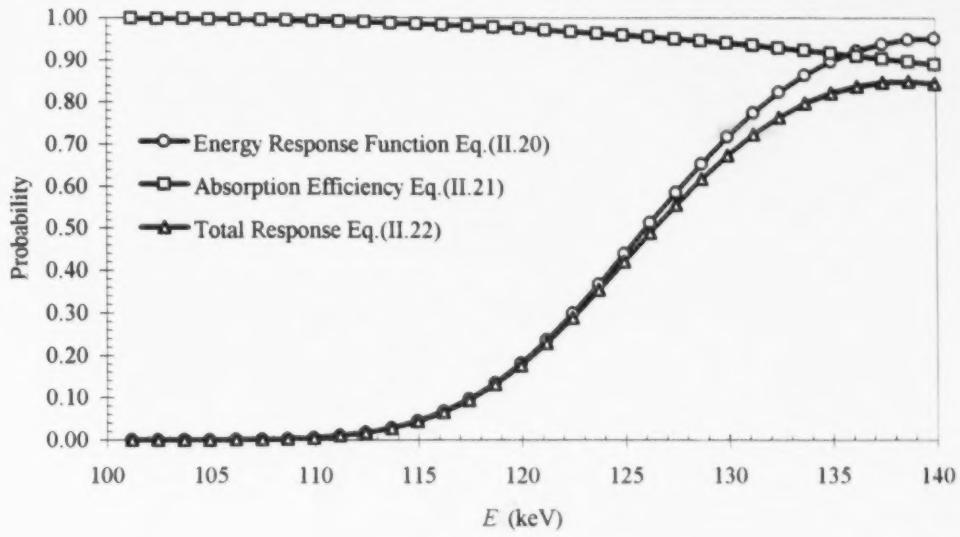

Figure II-6: The total detection probability for photons of energy E for an Anger camera employing a 3/8" NaI crystal and a 20% symmetric energy window centered at 140 keV as given by Eq. (II.22). Note that the total detection probability peaks at a photon energy E that is slightly less than 140 keV.

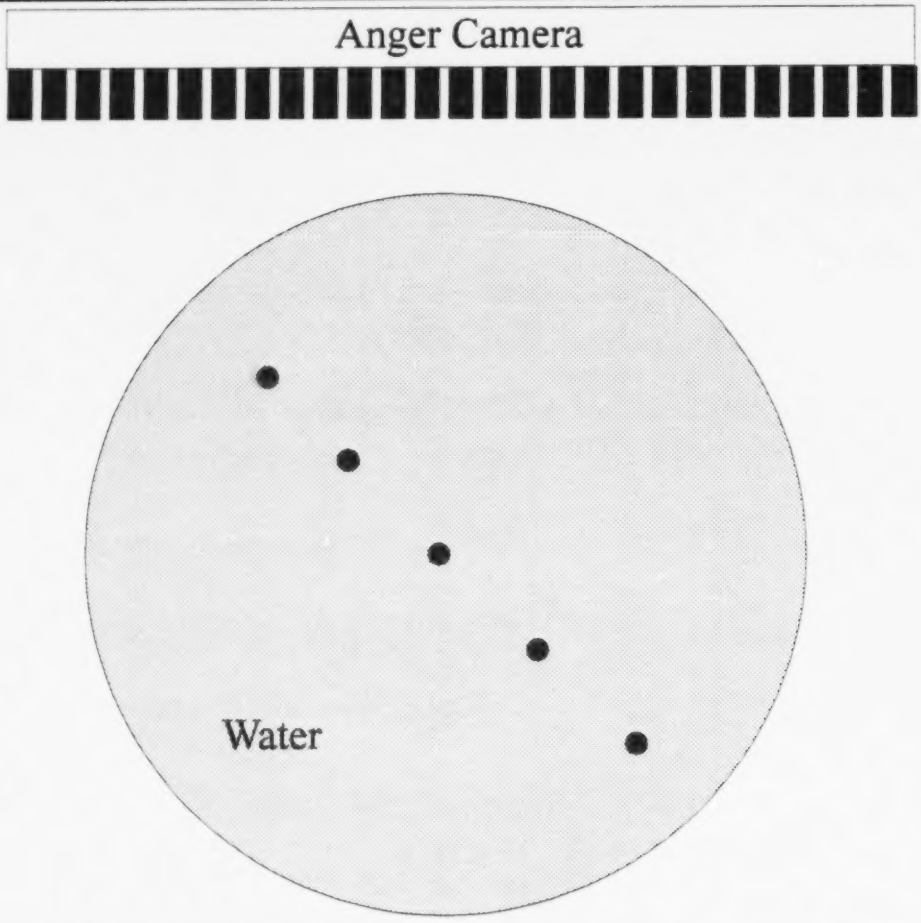

Figure II-7: Cross section of the cylindrical water-filled phantom and the five point sources.

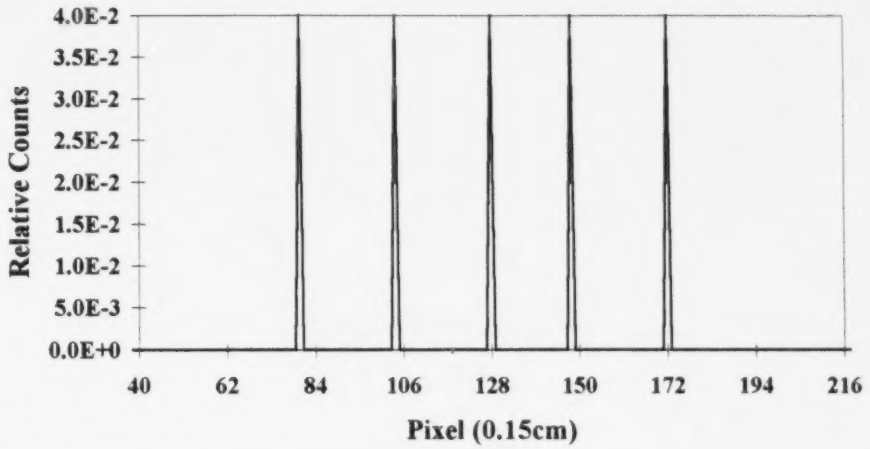

Figure II-8: Projection profile of a uniform phantom with five point sources shown in Fig. II-7, assuming an ideal collimator, ideal energy discrimination, and no attenuation.

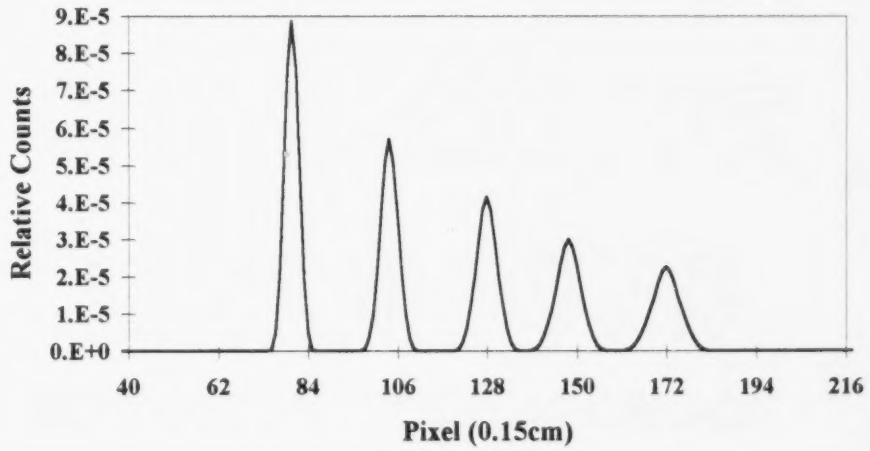

Figure II-9: Projection profile of a uniform phantom with five point sources shown in Fig. II-7, using a LEAP collimator and assuming ideal energy discrimination and no attenuation.

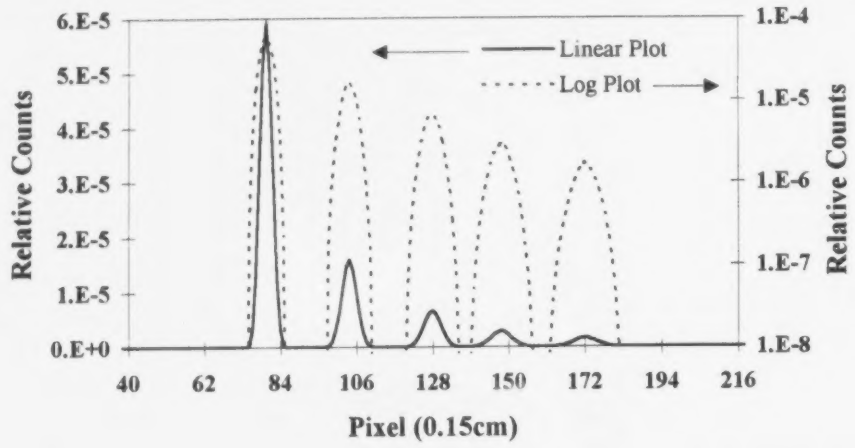

Figure II-10: Projection profile of a uniform phantom with five point sources shown in Fig. II-7, using a LEAP collimator. The projection profile data is plotted using both a linear scale (solid line) and a logarithmic scale (dotted line). The effects of attenuation are shown for a camera with ideal energy resolution. Only primary photons are detected.

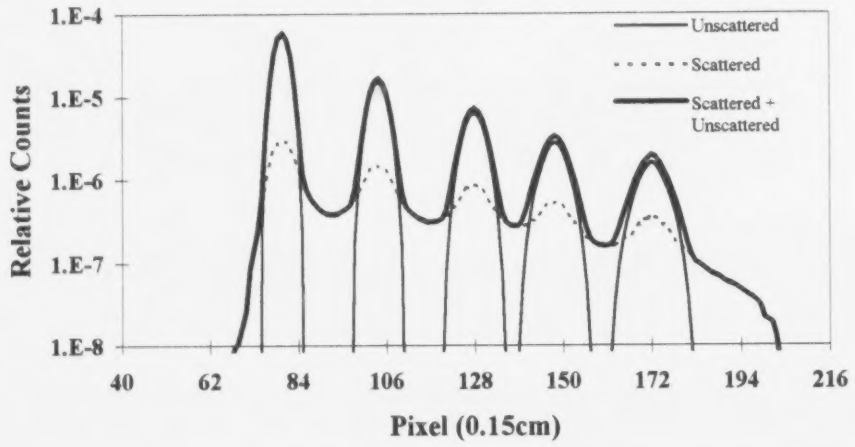

Figure II-11: Projection profile of a uniform phantom with five point sources shown in Fig. II-7, using a LEAP collimator. The effects of attenuation are shown for a camera with 12% energy resolution, 3/8" NaI crystal, and a 20% symmetric energy window for ^{99m}Tc. Both scattered and unscattered photons are detected.

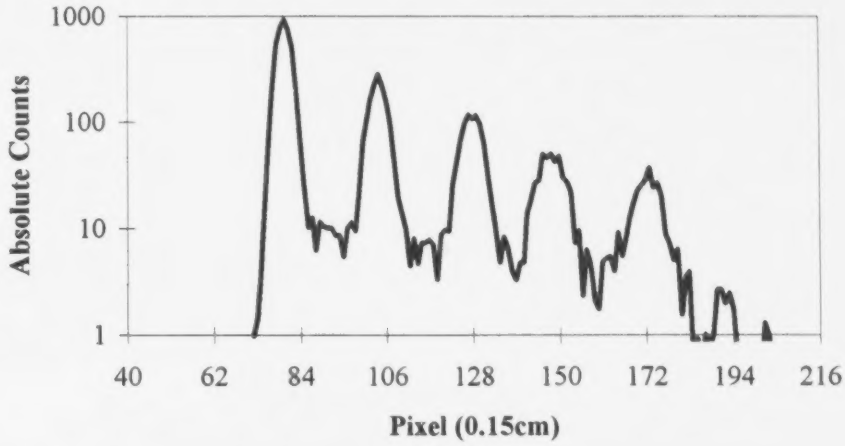

Figure II-12: Projection profile of a uniform phantom with five point sources shown in Fig. II-7, obtained from experiment for a camera, using a LEAP collimator, with 12% energy resolution, 3/8" NaI crystal, and a 20% symmetric energy window for ^{99m}Tc.

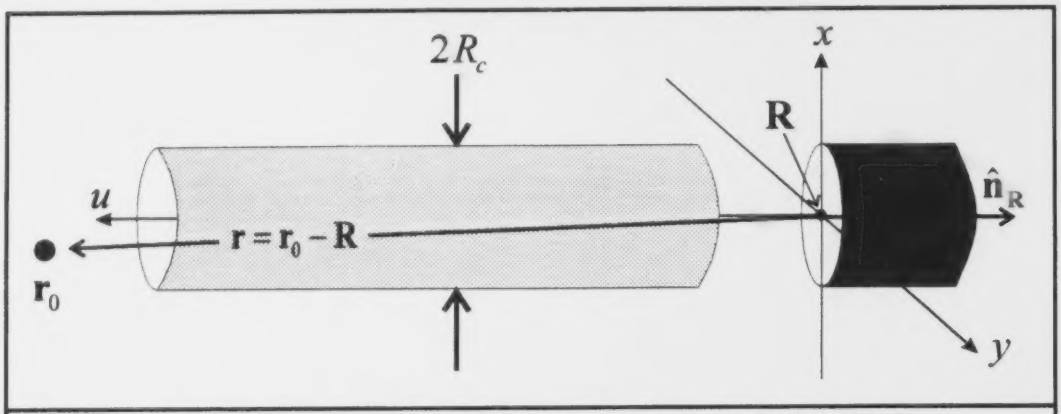

Figure II-13: Schematic representation of the integration volume for Eq. (II.30).

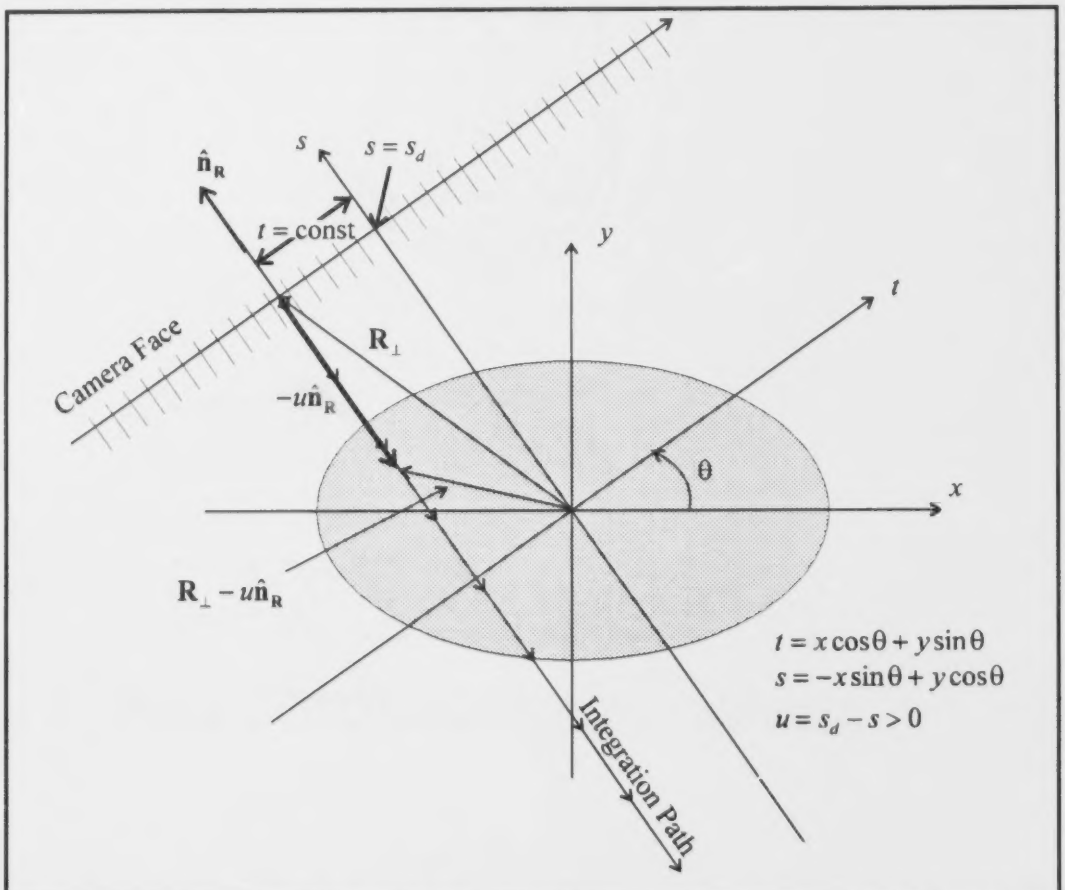

Figure II-14: Geometry for Eq. (II.33) showing the relationship between the (x,y) and (t,s) coordinate systems.

IIi. Theory of Photon Propagation and Detection in SPECT

A. Analytical Approach to Reconstruction Kernels

As discussed in Chapter 2, the photon detection kernel is a fundamental quantity required for all reconstruction methods for SPECT imaging. In this Chapter a general expression for the photon detection kernel will be derived. It is useful as an introduction to what follows to note that a photon emitted at the point $\mathbf{r}_0$ may trigger a sequence of scattering processes due to the attenuating medium, resulting in the creation of a photon which is eventually detected at $\mathbf{R}_i$. It is intuitively obvious that the total photon detection kernel, $K(\mathbf{R}_i, \mathbf{r}_0)$ can be decomposed into a sum of contributions due to each order of detected scattered photons [97,102], i.e.

$$K(\mathbf{R}_i, \mathbf{r}_0) = \sum_{n=0}^{\infty} K^{(n)}(\mathbf{R}_i, \mathbf{r}_0), \tag{III.1}$$

where $K^{(n)}(\mathbf{R}_i, \mathbf{r}_0)$ describes the probability that a photon emitted at $\mathbf{r}_0$ will trigger a sequence of n scattering processes before the photon detected at $\mathbf{R}_i$ is created. Examples of the three lowest order scattering processes (n = 0 , 1, and 2) are illustrated in Fig. III-1. The general expression for $K^{(n)}(\mathbf{R}_i, \mathbf{r}_0)$ must account, among other things, for the specifics of the detection process. First of all, only photons striking the front face of the detector which arrive within a certain acceptance angle of the collimator are detected. Secondly, photons with energies less than a threshold energy have a negligible probability of being detected within the energy response window of the detector, thus limiting the amount of the overall energy loss due to Compton scattering. The following assumptions and simplifications are used in this approach.

1. Photons are treated as classical, distinguishable particles having well defined energy ($E = h\nu$) and direction of propagation. Propagating through the attenuating medium, the photon beam is attenuated due to photoelectric absorption, Compton scattering, and Rayleigh scattering. In the latter two cases, the scattered photon has direction of propagation different from that of the incident photon. Additionally, the Compton

scattered photons can have energy significantly different from that of the incident photon (c.f. Eq. (II.1)).

2. The linear attenuation coefficient and the electron density in the medium are specified by the functions $\mu(\mathbf{r}, E)$ and $\rho_e(\mathbf{r})$ respectively, which may be analytical or tabulated, but are assumed to be known. We note here that the linear attenuation in the medium is due to *all* photon loss processes present, i.e. it accounts not only for photon absorption, but also for Rayleigh and Compton scattering in all possible orders. In principle, $\mu(\mathbf{r}, E)$ and $\rho_e(\mathbf{r})$ may be determined experimentally and, therefore, these processes are accounted for automatically once these functions are known. Measuring these functions experimentally is still a non-trivial problem in SPECT, and is a subject of vigorous research.

3. The collimator is modeled as a two-dimensional array of non-overlapping empty cylinders of radius R_c, length L_c, and face center separation D_c. The parameter R_c is chosen such that the open area of the collimator face is the same as that provided by the hexagonal or round holes of the actual collimator. The collimator septa are assumed to be made of a material opaque to photons.

4. The energy-dependent detection probability of the Anger camera is assumed to be a product of the energy response function and the absorption efficiency of the crystal as discussed in Chapter 2, Eq. (II.22).

5. Scattering in the scintillation crystal and septal penetration (i.e. partial non-opacity of the material used for the collimator) are ignored.

6. The intrinsic resolution of the camera is ignored as it can always be applied as a correction to the detection of photons at the back face of the collimator holes and is not of primary interest here.

Current Densities of the Primary and Scattered Photons

Consider the following situation. At the point $\mathbf{r}_0$ of the medium, there is a point-like isotropic source of monochromatic radiation emitting photons of energy E_0 at a constant rate $\dot{a}_0$. These photons will be referred to as primary or zeroth-order photons in what

follows. They propagate in the medium and at an arbitrary position $\mathbf{r}$ (i.e. Fig. III-1a) the current density of the primary photons is

$$\mathbf{j}^{(0)}(\mathbf{r};\mathbf{r}_0) = \left(\frac{\dot{a}_0}{4\pi}\right)\frac{\mathbf{r}-\mathbf{r}_0}{|\mathbf{r}-\mathbf{r}_0|^3} A(\mathbf{r},\mathbf{r}_0,E_0), \tag{III.2}$$

where $A(\mathbf{r},\mathbf{r}_0,E_0)$ accounts for the attenuation (both photoelectric absorption and scattering interactions) and is given in Eq. (II.11). The current density is directed radially outward from the source and would decrease in inverse proportion to the square of the distance from the source were the attenuation absent in the medium. Both arguments, the current position ($\mathbf{r}$) and the position from which the photons originate ($\mathbf{r}_0$), are explicitly written down as arguments of the current density.

The primary photon may either escape from the medium and be lost, or be accepted by one of the collimator holes and be counted. It may, alternatively, undergo a scattering interaction at some position, say $\mathbf{r}_1$, in the medium. In the latter case, a photon with energy E_1 is created at $\mathbf{r}_1$ and it propagates in a direction deviating from the direction from which the zeroth-order photon has arrived by a Compton or a Rayleigh scattering angle θ_1 (i.e. Fig. III-1b). The energy E_1 of the outgoing photon, referred to as the first-order photon from now on, depends on the primary photon energy, the scattering angle, and the scattering mode, i.e. $E_1 = E_1(E_0,\theta_1)$ is given in Eq. (II.1) for Compton scattering mode, and $E_1 \cong E_0$ for Rayleigh scattering mode. The flux of primary photons at the scattering position $\mathbf{r}_1$ is just $|\mathbf{j}^{(0)}(\mathbf{r}_1;\mathbf{r}_0)|$, and the number of first-order photons scattered by an angle θ_1 is determined by the total scattering cross section,

$$\frac{d\sigma(E_0,\theta_1)}{d\Omega} = \left(\frac{d\sigma(E_0,\theta_1)}{d\Omega}\right)_C + \left(\frac{d\sigma(E_0,\theta_1)}{d\Omega}\right)_R. \tag{III.3}$$

Therefore, the current density at $\mathbf{r}$ of the first-order photons created by scattering off an electron at the location $\mathbf{r}_1$ is

$$\mathbf{j}^{(1)}(\mathbf{r};\mathbf{r}_0,\mathbf{r}_1) = \frac{\mathbf{r}-\mathbf{r}_1}{|\mathbf{r}-\mathbf{r}_1|^3}|\mathbf{j}^{(0)}(\mathbf{r}_1;\mathbf{r}_0)|B^{(1)}(\mathbf{r},\mathbf{r}_0,\mathbf{r}_1), \tag{III.4a}$$

where

$$B^{(1)}(\mathbf{r},\mathbf{r}_0,\mathbf{r}_1)=\left\{\left(\frac{d\sigma(E_0,\theta_1)}{d\Omega}\right)_C A(\mathbf{r},\mathbf{r}_1,E_1)+\left(\frac{d\sigma(E_0,\theta_1)}{d\Omega}\right)_R A(\mathbf{r},\mathbf{r}_1,E_1=E_0)\right\}. \quad \text{(III.4b)}$$

Again, the current position ($\mathbf{r}$), the position of the source of primary photons ($\mathbf{r}_0$), and the position at which they scatter ($\mathbf{r}_1$) are all explicitly listed as arguments of the first-order photon current density. If it were not for the fact that the scattered photon energy differs for the two scattering modes, the two cross sections could have been replaced by a total scattering cross section. Instead, the two modes must be treated separately to ensure the correct scattering energy is subsequently used for the linear attenuation function $A(\mathbf{r},\mathbf{r}_1,E_1)$.

The above procedure can be continued. The first order photons can give rise to the generation of second order photons due to a scattering interaction taking place at $\mathbf{r}_2$. This is illustrated in Fig. III-1c. The current density at $\mathbf{r}$ of the second-order photons created at a *fixed* position $\mathbf{r}_2$ is

$$\mathbf{j}^{(2)}(\mathbf{r};\mathbf{r}_0,\mathbf{r}_2)=\frac{\mathbf{r}-\mathbf{r}_2}{|\mathbf{r}-\mathbf{r}_2|^3}\int d^3\mathbf{r}_1\rho_e(\mathbf{r}_1)\frac{\mathbf{r}_2-\mathbf{r}_1}{|\mathbf{r}_2-\mathbf{r}_1|^3}|\mathbf{j}^{(0)}(\mathbf{r}_1;\mathbf{r}_0)|B^{(2)}(\mathbf{r},\mathbf{r}_0,\mathbf{r}_1,\mathbf{r}_2), \quad \text{(III.5a)}$$

where

$$\begin{aligned}B^{(2)}(\mathbf{r},\mathbf{r}_0,\mathbf{r}_1,\mathbf{r}_2)=&\left(\frac{d\sigma(E_0,\theta_1)}{d\Omega}\right)_C A(\mathbf{r}_2,\mathbf{r}_1,E_1)\left(\frac{d\sigma(E_1,\theta_2)}{d\Omega}\right)_C A(\mathbf{r},\mathbf{r}_2,E_2)\\&+\left(\frac{d\sigma(E_0,\theta_1)}{d\Omega}\right)_C A(\mathbf{r}_2,\mathbf{r}_1,E_1)\left(\frac{d\sigma(E_1,\theta_2)}{d\Omega}\right)_R A(\mathbf{r},\mathbf{r}_2,E_2=E_1)\\&+\left(\frac{d\sigma(E_0,\theta_1)}{d\Omega}\right)_R A(\mathbf{r}_2,\mathbf{r}_1,E_1=E_0)\left(\frac{d\sigma(E_1=E_0,\theta_2)}{d\Omega}\right)_C A(\mathbf{r},\mathbf{r}_2,E_2)\\&+\left(\frac{d\sigma(E_0,\theta_1)}{d\Omega}\right)_R A(\mathbf{r}_2,\mathbf{r}_1,E_1=E_0)\left(\frac{d\sigma(E_1=E_0,\theta_2)}{d\Omega}\right)_R A(\mathbf{r},\mathbf{r}_2,E_2=E_0)\end{aligned} \quad \text{,(III.5b)}$$

in which the integration is performed over all possible first-order Compton and Rayleigh scattering positions ($\mathbf{r}_1$), but the position of the second-order scattering ($\mathbf{r}_2$) is kept fixed. Therefore, the current position ($\mathbf{r}$), the origin of primary photons ($\mathbf{r}_0$), and the position of the second-order Compton scattering ($\mathbf{r}_2$) are explicit arguments of the current density.

The above procedure can be continued and integral expressions for the current density for any specific scattering order can be obtained. It is possible to write down a general expression, valid for all orders, (i.e. n arbitrary), but the result would not be very transparent due to the $B^{(n)}$ terms, and particularly the dependence of E_n on the specific scattering history. $B^{(n)}$ describes all the possible scattering histories for n^{th} order photons. In general, Rayleigh scattering contributes very little to the overall current density of a given order since its total cross section is only 2% of the total Compton cross section for the energy range of interest ($\geq 100\,\text{keV}$). For a given order, the dominant contribution to $B^{(n)}$ will always come from the single term involving only Compton scattering interactions. Terms describing histories involving a single Rayleigh scattering will, in general, be only 2% of the term involving only Compton scattering. Histories involving two or more Rayleigh scattering interactions are easily ignored since they are less than 0.04% of the term involving Compton scattering only. For example, the terms of $B^{(1)}$ in Eq. (III.4b) are of the order 1 and 0.02, respectively, and the terms of $B^{(2)}$ in Eq. (III.5b) are of the order; 1, 0.02, 0.02, and 0.0004, respectively.

In cases in which it is permissible to ignore the contributions from Rayleigh scattering, $B^{(n)}$ reduces to a single term due solely to n sequential Compton scattering events, and a general expression is easily formulated which is valid for all orders of Compton scattering. The following graphical procedure allows one to obtain the current density $\mathbf{j}^{(n)}(\mathbf{r};\mathbf{r}_0,\mathbf{r}_n)$ at $\mathbf{r}$ of photons of n^{th} order created as a result of a Compton scattering at a *fixed* position $\mathbf{r}_n$ of photons of $(n-1)^{\text{th}}$ order. Start by drawing $n+2$ points and label them $\mathbf{r}_0,\mathbf{r}_1,\mathbf{r}_2,\ldots,\mathbf{r}_n$, and $\mathbf{r}$. Connect the pairs of points in the order in which they were labeled by *directed* straight lines (c.f. Fig. III-1 for $n=0$, 1, and 2). Associate the factor $(\dot{a}_0/4\pi)$ with the point $\mathbf{r}_0$. It accounts for the rate of emission of primary photons from this point. Associate with each object, consisting of a point $\mathbf{r}_{j+1}$ and a line *entering* it, a factor

$$\frac{A(\mathbf{r}_{j-1},\mathbf{r}_j,E_j)}{|\mathbf{r}_{j+1}-\mathbf{r}_j|^2}\left(\frac{d\sigma(E_j,\theta_{j+1})}{d\Omega}\right)_C, \tag{III.6}$$

to account for the propagation and the attenuation of j^{th}-order photons of energy E_j generated at $\mathbf{r}_j$ and for their subsequent Compton scattering at $\mathbf{r}_{j+1}$. Associate a factor $(\mathbf{r}-\mathbf{r}_n)|\mathbf{r}-\mathbf{r}_n|^{-3}\,A(\mathbf{r},\mathbf{r}_n,E_n)$ with the last line entering $\mathbf{r}$ to account for the propagation and the attenuation of n^{th}-order photons propagating from $\mathbf{r}_n$ towards $\mathbf{r}$. Finally, integrate over all points at which scattering takes place, *except* at $\mathbf{r}_n$, multiplying first by an appropriate electron density factor. The result is

$$\mathbf{j}^{(n)}(\mathbf{r};\mathbf{r}_0,\mathbf{r}_n)=\left(\frac{1}{4\pi}\right)\frac{\mathbf{r}-\mathbf{r}_n}{|\mathbf{r}-\mathbf{r}_n|^3}\dot{a}_n(\mathbf{r}_n;\mathbf{r},\mathbf{r}_0), \tag{III.7}$$

where

$$\dot{a}_n(\mathbf{r}_n;\mathbf{r},\mathbf{r}_0)=\dot{a}_0\int d^3\mathbf{r}_1\rho_e(\mathbf{r}_1)\cdots\int d^3\mathbf{r}_{n-1}\rho_e(\mathbf{r}_{n-1})A(\mathbf{r},\mathbf{r}_n,E_n)$$
$$\times\prod_{j=0}^{n-1}\left\{\frac{A(\mathbf{r}_{j+1},\mathbf{r}_j,E_j)}{|\mathbf{r}_{j+1}-\mathbf{r}_j|^2}\left(\frac{d\sigma(E_j,\theta_{j+1})}{d\Omega}\right)_C\right\}, \tag{III.8}$$

The factor $\dot{a}_n(\mathbf{r}_n;\mathbf{r},\mathbf{r}_0)$ may be interpreted as the emission rate of a fictitious source of n^{th}-order photons situated at $\mathbf{r}_n$, as perceived by the observer at $\mathbf{r}$. Due to the attenuation, this rate depends on the position $\mathbf{r}$ of the observation point. Eqs. (III.7) and (III.8) yield, in particular, the lowest order current densities given in Eqs. (III.2), (III.4), and (III.5) for no Rayleigh scattering. The final attenuation factor $A(\mathbf{r},\mathbf{r}_n,E_n)$ cannot be pulled outside any of the integrals in Eq. (III.8) because the energy of higher order photons depends through the Compton scattering angles on the positions of all lower order scattering events:

$$E_j=\frac{E_{j-1}}{1+E_{j-1}(1-\cos\theta_j)/m_ec^2}=\frac{E_0}{1+E_0\left(j-\sum_{k=1}^{j}\cos\theta_k\right)/m_ec^2},\quad j=1,\ldots,n, \tag{III.9}$$

where θ_k (c.f. Fig. III-1) is the angle between $(\mathbf{r}_{k+1}-\mathbf{r}_k)$ and $(\mathbf{r}_k-\mathbf{r}_{k-1})$ for $k<n$, θ_n is the angle between $(\mathbf{r}-\mathbf{r}_n)$ and $(\mathbf{r}_n-\mathbf{r}_{n-1})$, and m_ec^2 is the electron rest energy. Finally, the Klein-Nishina scattering cross section Eq. (II.5) is written here as

$$\frac{d\sigma(E_{k-1},\theta_k)}{d\Omega} = \frac{r_0^2}{2}\left(\frac{E_k}{E_{k-1}}\right)^2\left(\frac{E_{k-1}}{E_k}+\frac{E_k}{E_{k-1}}-\sin^2\theta_k\right), \qquad \text{(III.10)}$$

and r_0 is the classical electron radius.

B. Modeling the Detection Process

Accurate modeling of the detection processes is as important as correct modeling of the propagation processes. The process of collimation is the first step in the detection process and is one of the degrading processes which must be considered. Collimation provides the camera with spatial resolution by allowing only those photons which arrived at near normal incidence to the camera face to pass the collimator and interact with the scintillation crystal.

One might wonder why, defining the current densities of various orders, the calculation of the *total* current densities, i.e. integration over the position of the last Compton scattering $\mathbf{r}_n$, has been carefully avoided. The reason is that it is not enough for the n^{th}-order photon to arrive at the point $\mathbf{r}$ at the front of the detector window in order to be detected, i.e.

$$I^{(n)}(\mathbf{R}_i,\mathbf{r}_0) \neq \int da\ \hat{\mathbf{n}}_{\mathbf{R}} \cdot \int d^3\mathbf{r}_n\, \rho_e(\mathbf{r}_n)\, \mathbf{j}^{(n)}(\mathbf{R}_i;\mathbf{r}_0,\mathbf{r}_n)\,, \qquad \text{(III.11)}$$

where the integration da is over the area of the front face of the collimator hole denoted by $\mathbf{R}_i$. Rather, in order to be detected, a photon created at $\mathbf{r}_n$ must, as seen in Fig. III-2, hit a point within that area of the front window of the collimator hole through which the back face of this collimator hole is seen from $\mathbf{r}_n$. This area will be called the active area of the collimator hole for the point $\mathbf{r}_n$ and will be denoted by $S(\mathbf{R}_i,\mathbf{r}_n)$ where $\mathbf{R}_i$ is the position of the *center* of a circular collimator hole of radius R_c and identifies this particular collimator hole. Therefore, the flux of n^{th}-order photons *passing through* the collimator hole $\mathbf{R}_i$ (i.e. the number of photons detected per second at the back face of the collimator hole) is, for $n \neq 0$, equal to

$$I^{(n)}(\mathbf{R}_i,\mathbf{r}_0) = \int d^3\mathbf{r}_n\, \rho_e(\mathbf{r}_n) \int_{S(\mathbf{R}_i,\mathbf{r}_n)} da_r\ \hat{\mathbf{n}}_{\mathbf{R}} \cdot \mathbf{j}^{(n)}(\mathbf{R}_i;\mathbf{r}_0,\mathbf{r}_n), \qquad \text{(III.12)}$$

in which $\hat{\mathbf{n}}_{\mathbf{R}}$ is a normal to the collimator hole and the inner integral is a surface integral over the active area of the collimator hole. Clearly, the order of the two integrals cannot be reversed. Of course, for primary (zero order) photons only the integral of $\mathbf{j}^{(0)}$ over the active area of the collimator hole is present. Dividing $I^{(n)}(\mathbf{R}_i, \mathbf{r}_0)$ by the activity of the primary photon source, the contribution to the total photon detection kernel due to the n^{th} -order photons is obtained as

$$K^{(n)}(\mathbf{R}_i, \mathbf{r}_0) = \dot{a}_0^{-1} I^{(n)}(\mathbf{R}_i, \mathbf{r}_0). \tag{III.13}$$

The total photon detection kernel is equal to

$$K(\mathbf{R}_i, \mathbf{r}_0) = \sum_{n=0}^{\infty} K^{(n)}(\mathbf{R}_i, \mathbf{r}_0), \tag{III.14}$$

as stated earlier. In practice the first three terms typically account for more than 97% of the total signal for narrow energy windows normally used clinically [97,102].

Further approximations can be made to simplify the calculation of the integrals in Eq. (III.12). If the typical distances of the points of the medium from the collimator hole are several times larger than the radius of the hole R_c, then $\mathbf{j}^{(n)}(\mathbf{r}; \mathbf{r}_0, \mathbf{r}_n)$ varies slowly over the active area of the hole and can be taken outside the integral after its argument $\mathbf{r}$ is replaced with some typical position within the active area, $\mathbf{r}_c$. The surface integral yields just the (active) area $S(\mathbf{R}_i, \mathbf{r}_n)$ which, being perpendicular to the unit vector $\hat{\mathbf{n}}_{\mathbf{R}}$, is equal to

$$S(\mathbf{R}_i, \mathbf{r}_n) = \Delta\Omega(\mathbf{R}_i, \mathbf{r}_n) \left(\frac{|\mathbf{r}_c - \mathbf{r}_n|^2}{\cos(\theta(\mathbf{r}_c - \mathbf{r}_n))} \right), \tag{III.15}$$

where $\theta(\mathbf{r}_c - \mathbf{r}_n)$ is the angle between $\hat{\mathbf{n}}_{\mathbf{R}}$ and $\mathbf{r}_c - \mathbf{r}_n$ and $\Delta\Omega(\mathbf{R}_i, \mathbf{r}_n)$ is the solid angle originating at $\mathbf{r}_n$ subtended by the active area $S(\mathbf{R}_i, \mathbf{r}_n)$ in Fig. III-2. Therefore, Eq. (III.12) reads

$$\begin{aligned} I^{(n)}(\mathbf{R}_i, \mathbf{r}_0) &= \frac{1}{4\pi} \int d^3\mathbf{r}_n \rho_e(\mathbf{r}_n) S(\mathbf{R}_i, \mathbf{r}_n) \frac{\dot{a}_n(\mathbf{r}_n; \mathbf{R}_i, \mathbf{r}_0)}{|\mathbf{R}_i - \mathbf{r}_n|^2} \cos(\theta(\mathbf{R}_i - \mathbf{r}_n)) \\ &= \frac{1}{4\pi} \int d^3\mathbf{r}_n \rho_e(\mathbf{r}_n) \Delta\Omega(\mathbf{R}_i, \mathbf{r}_n) \dot{a}_n(\mathbf{r}_n; \mathbf{R}_i, \mathbf{r}_0) \end{aligned}, \tag{III.16}$$

for $n > 0$. Of course, no integration is present for $n = 0$. Eqs. (III.8) and (III.9) were used to arrive at Eq. (III.16) and, for small collimator holes, the argument $\mathbf{r}_c$ was replaced by $\mathbf{R}_i$. The second line of Eq. (III.16) has a transparent interpretation: the rate of detection of n^{th}-order photons by the collimator hole at $\mathbf{R}_i$ is the summary emission rate of fictitious sources of these photons weighted by the solid angle into which the photons must be emitted by the source in order to arrive at the back face of the collimator. It is, however, the first line which is more useful in numerical calculations because the magnitude of the active area of the collimator can be easily calculated [88]. The calculation of this area for parallel cylindrical collimator holes is presented in the next chapter.

C. Modeling the Energy Response of the Detector

Finally, the energy response and the energy resolution of the detector must be accounted for. Firstly, for a given energy window, photons with an energy smaller than a certain value E_{min} have practically vanishing probability of being detected. Energy is always lost in Compton scattering so the condition $E_n > E_{min}$ together with Eq. (III.9) yields

$$\sum_{j=1}^{n} \cos\theta_j > n - m_e c^2 \left(\frac{1}{E_{min}} - \frac{1}{E_0} \right). \qquad \text{(III.17)}$$

The condition (III.17) allows for an optimization of numerical integrations by substantially narrowing down the integration regions in Eq. (III.8) for successive inner integrals. Secondly, due to the finite energy resolution of the detector, a photon of energy E_n cannot be resolved from photons having energy distributed around E_n within a standard deviation $\sigma(E_n)$. Consequently, an increasing fraction of photons of energy E_n escape detection as E_n approaches either limit, W_{min} or W_{max}, of the energy acceptance window of the detector. Similarly, some photons with energies outside the energy acceptance window limits (i.e. $< W_{min}$ or $> W_{max}$) will be detected because of the finite resolution. These facts are illustrated in Figs. II-5 and II-6. Assuming a Gaussian form for the intrinsic

energy resolution function of the detector [46-48], this effect is accounted for by multiplying the integrand in Eq. (III.8) by the factor of Eq. (II.20), i.e. by

$$F(E_n;W_{\min},W_{\max})=\frac{1}{2}\left(\operatorname{erfc}\left(-\frac{E_n-W_{\min}}{\sqrt{2}\sigma(E_n)}\right)-\operatorname{erfc}\left(\frac{W_{\max}-E_n}{\sqrt{2}\sigma(E_n)}\right)\right). \tag{III.18}$$

where $\operatorname{erfc}(z)$ is the error function [49] and $\sigma(E)=a\sqrt{E}+b$, with a and b determined experimentally [48]. Finally, only those photons which undergo a photoelectric interaction within the crystal deposit enough energy to trigger detection, and the probability that a photon of energy E_n will undergo such an interaction is given by the absorption efficiency function of Eq. (II.21), i.e. by

$$A_E(E_n)=1-\exp\left[-\mu_{PE}(E_n)d\right], \tag{III.19}$$

where $\mu_{PE}(E)$ is the energy dependent photoelectric absorption interaction coefficient of the scintillation crystal and d is the crystal thickness. The effects of the crystal energy resolution and absorption efficiency and of energy windowing are included by incorporating these two factors into $\dot{a}_n$ in the integrand of Eq. (III.16):

$$\begin{aligned}\dot{a}_n(\mathbf{r}_n;\mathbf{r},\mathbf{r}_0)=\dot{a}_0\int d^3\mathbf{r}_1\rho_e(\mathbf{r}_1)\cdots\int d^3\mathbf{r}_{n-1}\rho_e(\mathbf{r}_{n-1})A(\mathbf{r},\mathbf{r}_n,E_n)\\ \times\prod_{j=0}^{n-1}\left\{\frac{A(\mathbf{r}_{j+1},\mathbf{r}_j,E_j)}{|\mathbf{r}_{j+1}-\mathbf{r}_j|^2}\left(\frac{d\sigma(E_j,\theta_{j+1})}{d\Omega}\right)\right\}F(E_n;W_{\min},W_{\max})\,A_E(E_n)\end{aligned}. \tag{III.20}$$

D. Integral Kernel Expressions

Using Eqs. (III.13), (III.16), and (III.20) the following integral expressions are obtained for the three lowest Compton scattering contributions to the photon detection kernel $K(\mathbf{R}_i,\mathbf{r}_0)$,

$$K^{(0)}(\mathbf{R}_i,\mathbf{r}_0)=\frac{1}{4\pi}\frac{S(\mathbf{R}_i,\mathbf{r}_0)}{|\mathbf{R}_i-\mathbf{r}_0|^2}A(\mathbf{R}_i,\mathbf{r}_0;E_0)F(E_0;W_{\min},W_{\max})A_E(E_0), \tag{III.21}$$

$$\begin{aligned}K^{(1)}(\mathbf{R}_i,\mathbf{r}_0)=\frac{1}{4\pi}\int d^3\mathbf{r}_1\,\rho_e(\mathbf{r}_1)\frac{S(\mathbf{R}_i,\mathbf{r}_1)}{|\mathbf{R}_i-\mathbf{r}_1|^2}\frac{1}{|\mathbf{r}_1-\mathbf{r}_0|^2}\left(\frac{d\sigma(E_0,\theta_1)}{d\Omega}\right)_C\\ \times A(\mathbf{r}_1,\mathbf{r}_0;E_0)A(\mathbf{R}_i,\mathbf{r}_1;E_1)F(E_1;W_{\min},W_{\max})A_E(E_1)\end{aligned}, \tag{III.22}$$

$$K^{(2)}(\mathbf{R}_i,\mathbf{r}_0)=\frac{1}{4\pi}\int d^3\mathbf{r}_2\,\rho_e(\mathbf{r}_2)\int d^3\mathbf{r}_1\,\rho_e(\mathbf{r}_1)\frac{S(\mathbf{R}_i,\mathbf{r}_2)}{|\mathbf{R}_i-\mathbf{r}_2|^2}\frac{1}{|\mathbf{r}_2-\mathbf{r}_1|^2}\frac{1}{|\mathbf{r}_1-\mathbf{r}_0|^2}$$
$$\times\left(\frac{d\sigma(E_0,\theta_1)}{d\Omega}\right)_C\left(\frac{d\sigma(E_1,\theta_2)}{d\Omega}\right)_C A(\mathbf{r}_1,\mathbf{r}_0;E_0)A(\mathbf{r}_2,\mathbf{r}_1;E_1)A(\mathbf{R}_i,\mathbf{r}_2;E_2)\,. \qquad \text{(III.23)}$$
$$\times F(E_2;W_{\min},W_{\max})A_E(E_2)$$

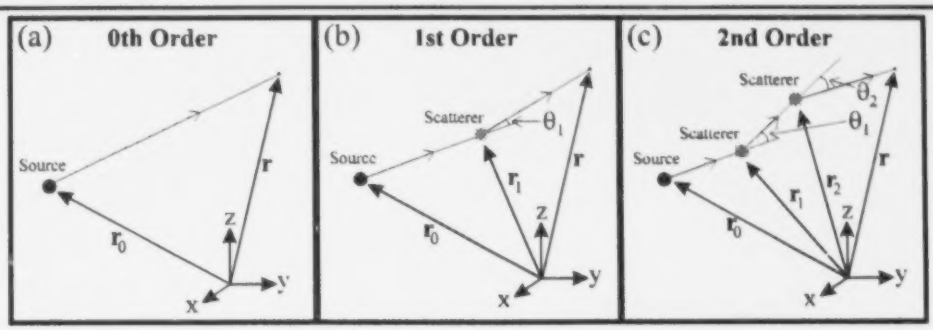

Figure III-1: Illustration of the three lowest scattering orders.

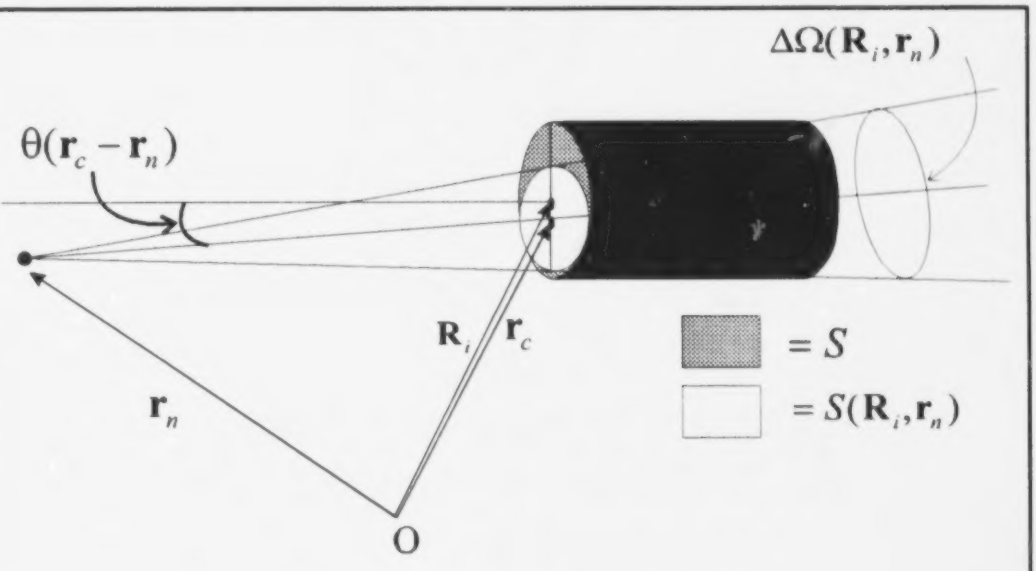

Figure III-2: Schematic representation of parallel hole collimation.

IV. Kernel Calculation and Numerical Methods

The integral expressions for the photon detection kernel derived in the previous chapter, i.e. Eqs. (III.21) - (III.23), cannot be evaluated analytically. However, the integral expressions can be calculated efficiently using standard numerical integration techniques, such as those discussed in Refs. 49 and 103. In this chapter, the author's numerical implementation and calculation of the integral expressions for the kernel are described for a general non-uniform imaging situation. Although this implementation may not be numerically the most efficient, it does allow for quite accurate calculation of the multi-dimensional integrals contained in Eqs. (III.21) - (III.23). Only the calculation of the lowest three orders of the kernel will be considered, but extension of the procedures described here to calculate higher order contributions should be straightforward. Further, Rayleigh scattering is ignored in the present implementation.

The numerical calculation of Eqs. (III.21) - (III.23) can be divided into two distinct steps. First, the specifics of the imaging situation must be described through the medium description and the specifications of the Anger camera. Second, the expression for the kernels, Eqs. (III.21) - (III.23), must be evaluated. This task requires numerical evaluation of multi-dimensional integrals. Defining the imaging situation through a number of functions and parameters is first considered from a computing perspective, and then the algorithms used to evaluate the integral expressions are discussed.

A. Description of the Imaging Situation

A number of quantities must be specified that jointly describe the specifics of the imaging situation. In particular, they pertain to the medium description, the collimator description, and the Anger camera energy-dependent detection probability. Incorporating the description of the imaging situation through these quantities is described in detail in the following.

Linear Attenuation Coefficient

The linear attenuation coefficient of the medium as a function of spatial coordinates must be quantized. In practice the analytical spatial dependence of the linear attenuation function is unknown and must be determined using experimental measurements which sample spatial and energy properties of the medium. This can be done using either x-ray computed tomography or transmission computed tomography [104,105]. X-ray computed tomography has the advantage of providing very high spatial resolution information of the linear attenuation coefficient distribution. The disadvantage of using x-ray CT data is two-fold. First, a second imaging procedure is required - the x-ray CT scan. Second, the 3D alignment of the transmission and emission data from the two modalities is not straightforward and is still a subject of much research [104,105]. Transmission computed tomography provides, generally, lower resolution information than X-ray CT but has the distinct advantage that it can be performed simultaneously with the typical nuclear medicine imaging SPECT acquisition procedure [106,107]. Much research effort is focused on creating simultaneous transmission and emission imaging systems, where both the transmission data (i.e. the linear attenuation coefficient distribution) and the emission data (i.e. the projection of the radioactive source distribution) are collected simultaneously using a multi-headed gamma camera [106,107].

The experimentally determined spatial dependence of the linear attenuation coefficient distribution within the medium is not used directly in this implementation. Instead, the available information is used to identify various components of the medium and the distribution of the components within the medium. Once the distribution has been determined, either using X-ray CT or TCT, the various components, such as tissue, bone, and lung can be identified based on their known linear attenuation coefficient values. The original values in the linear attenuation coefficient distribution can be replaced by integer value indices which identify different components of the medium. A range of the coefficient values will generally be mapped to a single component of the medium, i.e. to one index value. The complete description of the linear attenuation coefficient distribution is given by a 3D matrix whose integer index values identify the component of the medium

present in each voxel. The 3D matrix is accompanied by a set of 1D arrays (as many as the number of different components present) whose values are the actual linear attenuation coefficient for a discrete set of energies for each component of the medium. With such an approach, it is really immaterial what energy or technique is used to obtain the attenuation information as long as the separate components of the medium are distinguishable and identifiable. The energy dependence of the linear attenuation coefficient for each component of the medium can be obtained from standard tables, such as Ref. 41, for practically all the separate components of the medium, including water, tissue, bone, and lung.

Electron Density

The spatial dependence of the electron density distribution must also be known, at least in a discrete form. There is no direct physical relationship between the linear attenuation coefficient and the electron density. However, describing the linear attenuation distribution of the medium as explained above, it is rather straightforward to assign an electron density to each component of the medium. This is possible because in this implementation the attenuation matrix identifies the distribution of components of the medium, each of them having a known electron density.

B. Anger Camera Parameters

Collimation

In the present implementation it is assumed that the collimator is accurately modeled by parallel cylindrical holes of radius R_c and length L_c with center-to-center separation D_c. Different hole types and other types of collimation (i.e. converging, diverging) can be obtained using similar considerations as those presented here. The description of the collimator simply determines the active area $S(\mathbf{R}_i,\mathbf{r}_n)$ seen by a source at $\mathbf{r}_n$ for the collimator hole located at $\mathbf{R}_i$. This area can be easily calculated for parallel cylindrical collimator holes, as well as for other collimator hole types [88]. In this section the active area is calculated for an arbitrary $\mathbf{r}_n$.

Let L_c and R_c, respectively, be the length and radius of the collimator hole centered around $\mathbf{R}_i$. Placing the origin of the coordinate system at the point $\mathbf{R}_i$ with the z-axis perpendicular to the collimator face and directed toward the medium, the cylindrical coordinates of the position $\mathbf{r}_n$ are, as seen in Fig. IV-1, d_n (the distance of the point $\mathbf{r}_n$ from the cylindrical coordinate axis), z_n (the distance along the line of sight of the cylinder), and an azimuthal angle ϕ_n which is irrelevant in this analysis. The circular back face of the collimator hole, back-projected onto the plane containing its front face by rays converging at $\mathbf{r}_n$ is a circle of radius

$$R_c' = \frac{z_n R_c}{z_n + L_c} \tag{IV.1}$$

and the distance of its center away from the center of the front face of the collimator hole is

$$d = \frac{d_n L_c}{z_n + L_c}. \tag{IV.2}$$

The projected circle fits entirely within the actual front opening of the detector (i.e. $d + R_c' < R_c$) if $(d_n < R_c)$, so the active area of the detector is just $S(\mathbf{R}, \mathbf{r}_n) = \pi(R_c')^2$ in this case (Fig. IV-1a). If $(|R_c - R_c'| < d < (R_c + R'))$ then both circles overlap partially (Fig. IV-1b) and the active area of the collimator hole is equal to the overlap area,

$$S(\mathbf{R}, \mathbf{r}_n) \equiv S(\mathbf{R}, d_n, z_n) = R_c^2 \cos^{-1}\left(\frac{R_c^2 - R_c'^2 + d^2}{2R_c d}\right) + R_c'^2 \cos^{-1}\left(\frac{R_c'^2 - R_c^2 + d^2}{2R_c' d}\right) - \frac{1}{2}\sqrt{(2R_c R_c')^2 - (R_c^2 + R_c'^2 - d^2)^2} \tag{IV.3}$$

which depends on $\mathbf{r}_n$ through R_c and d. No photon originating from $\mathbf{r}_n$ can be detected by the collimator if $(d > R_c + R_c')$, i.e. when both circles do not overlap, as seen in Fig. IV-1c. This completes the specification of the active area $S(\mathbf{R}, \mathbf{r}_n)$ needed in Eqs. (III.21) - (III.23).

Energy Dependent Detection Probability

To calculate the energy-dependent detection probability requires specifying the intrinsic energy resolution of the detector, the detector energy window, and the crystal thickness. The intrinsic energy resolution is assumed to be modeled by a Gaussian distribution, as discussed in Chapter 2, typically with a FWHM equal to 10-12% of the primary emission energy, i.e. Eq. (II.18). The crystal thickness and its energy-dependent photoelectric interaction coefficient must also be known.

Once the above parameters are given, the intrinsic energy-dependent detection probability for a given incident photon depends only on the photon energy, i.e. E_n, through the functions $F(E_n;W_{\min},W_{\max})$ and $A_E(E_n)$ given by Eqs. (II.20) and (II.21), respectively. These functions can be calculated on the fly but it is more useful and numerically more efficient to pre-calculate the product of $F(E_n;W_{\min},W_{\max})A_E(E_n)$ for a number of discrete sampled energies and store the results as a 1D vector (i.e. lookup array). The product of $F(E_n;W_{\min},W_{\max})A(E_n)$ varies smoothly as a function of E_n, as shown in Fig. II-6, and for a sufficiently large number of sampled energies simple linear interpolation provides accurate values. An extension of this binning technique which allows the calculation of the energy spectra to be performed simultaneously with the kernel calculations is discussed later.

C. Calculation of the Kernel Expressions

Once the imaging situation is defined as outlined above, the multi-dimensional integrals must be calculated. Inspection of the integrands in Eqs. (III.21) - (III.23) shows that they have quadratic singularities. The integrals exist, however, provided the other functions are regular. Numerically, however, special care must be exercised to handle these singularities because otherwise the numerical convergence of the integrals may be very inefficient or even impossible to achieve. There is no difficulty from a numerical perspective in evaluating any of the other functions which appear in the integrands. For the purposes of the numerical integration, Eqs. (III.21) - (III.23) are rewritten as

$$K^{(1)}(\mathbf{R}_i,\mathbf{r}_0)=\int d^3\mathbf{r}_1\ \frac{1}{|\mathbf{r}_1-\mathbf{r}_0|^2}\,\mathrm{K}^{(1)}(\mathbf{R}_i,\mathbf{r}_1,\mathbf{r}_0), \tag{IV.4}$$

and

$$K^{(2)}(\mathbf{R}_i,\mathbf{r}_0)=\int d^3\mathbf{r}_1\ \frac{1}{|\mathbf{r}_1-\mathbf{r}_0|^2}\int d^3\mathbf{r}_2\frac{1}{|\mathbf{r}_2-\mathbf{r}_1|^2}\,\mathrm{K}^{(2)}(\mathbf{R}_i,\mathbf{r}_2,\mathbf{r}_1,\mathbf{r}_0), \tag{IV.5}$$

where

$$\begin{aligned}\mathrm{K}^{(1)}(\mathbf{R}_i,\mathbf{r}_1,\mathbf{r}_0)=&\frac{\rho_e(\mathbf{r}_1)}{4\pi}\frac{S(\mathbf{R}_i,\mathbf{r}_1)}{|\mathbf{R}_i-\mathbf{r}_1|^2}\left(\frac{d\sigma}{d\Omega}(E_0,\theta_1)\right)_C\\ &\times A(\mathbf{r}_1,\mathbf{r}_0;E_0)A(\mathbf{R}_i,\mathbf{r}_1;E_1)F(E_1;W_{\min},W_{\max})A_E(E_n)\end{aligned}, \tag{IV.6}$$

and

$$\begin{aligned}\mathrm{K}^{(2)}(\mathbf{R}_i,\mathbf{r}_2,\mathbf{r}_1,\mathbf{r}_0)=&\frac{\rho_e(\mathbf{r}_1)\rho_e(\mathbf{r}_2)}{4\pi}\frac{S(\mathbf{R}_i,\mathbf{r}_2)}{|\mathbf{R}_i-\mathbf{r}_2|^2}\left(\frac{d\sigma}{d\Omega}(E_0,\theta_1)\right)_C\left(\frac{d\sigma}{d\Omega}(E_1,\theta_2)\right)_C\\ &\times A(\mathbf{r}_1,\mathbf{r}_0;E_0)A(\mathbf{r}_2,\mathbf{r}_1;E_1)A(\mathbf{R}_i,\mathbf{r}_2;E_2)F(E_2;W_{\min},W_{\max})A_E(E_n)\end{aligned}, \tag{IV.7}$$

to make the presence of the singularities explicit in the integral Eqs. (IV.4) and (IV.5). The functions $\mathrm{K}^{(1)}$ and $\mathrm{K}^{(2)}$ in Eqs. (IV.6) and (IV.7) are never singular because the collimator at $\mathbf{R}_i$ is always located outside both the attenuating medium and the radiation source. Numerical evaluation of the zeroth order kernel $K^{(0)}(\mathbf{R}_i,\mathbf{r}_0)$ is straightforward because it amounts to a simple evaluation of an algebraic expression Eq. (III.21) for a given set of source and collimator coordinates. The numerical evaluation of the integrals in Eqs. (IV.4) and (IV.5) is discussed next.

First-Order Calculation

The integration region for the first-order kernel is shown in Fig. IV-2. This cone-like region is easily defined by the collimator hole parameters R_c and L_c. The most obvious choice of the integration variables would be cylindrical variables with the collimator hole face center at the origin of the coordinate system. Although this choice of coordinate system and integration variable allows the integration volume to be easily specified, it is inefficient for handling the inverse square singularity numerically because the Jacobian (i.e. $dz'\,d\phi'\,d\rho'\,\rho'$) does not tend to zero as the singularity is approached, i.e. $\mathbf{r}_1\to\mathbf{r}_0$, in general.

A better choice of integration variables for Eq. (IV.4) and for the integration volume depicted in Fig. IV-2 is obtained by placing the origin of the cylindrical integration coordinate system at the singular point $\mathbf{r}_0$. This leads to a more complicated description of the boundaries of the integration region, but ensures that the Jacobian (i.e. $dz'\,d\phi'\,d\rho'\,\rho'$) goes to zero as the singularity is approached since $\rho' \to 0$ as $\mathbf{r}_1 \to \mathbf{r}_0$, i.e. the order of the singularity is lowered. The integration over $\mathbf{r}_1$ for this choice of integration variables can be written as

$$\int_{\substack{\text{Collimator}\\\text{Cone}}} d^3\mathbf{r}_1 \Rightarrow \int_{\substack{\text{Collimator}\\\text{Cone}}} d^3\mathbf{r}' = \int_0^{\mathbf{R}_{1,z}-\mathbf{r}_{0,z}} dz' \int_{\phi_{\min}}^{\phi_{\max}} d\phi' \int_{\rho_{\min}(\phi',z')}^{\rho_{\max}(\phi',z')} d\rho'\,\rho', \tag{IV.8}$$

where $\mathbf{r}_1$ and $\mathbf{r}'$ are related through

$$\mathbf{r}_1 = \mathbf{r}_0 + \mathbf{r}', \tag{IV.9}$$

and

$$\rho_{\min}(\phi', z') = \begin{cases} 0 & , \ \rho_0 < R_c(z_c) \\ -\rho_0 \cos(\phi' - \phi_0) - \sqrt{R_c^2(z_c) - \rho_0^2 \sin^2(\phi' - \phi_0)} & , \ \rho_0 \geq R_c(z_c) \end{cases}$$

$$\rho_{\max}(\phi', z') = -\rho_0 \cos(\phi' - \phi_0) + \sqrt{R_c^2(z_c) - \rho_0^2 \sin^2(\phi' - \phi_0)}, \tag{IV.10}$$

and the integration limits for $d\phi'$ are given by

$$[\phi_{\min}, \phi_{\max}] = \begin{cases} [0,\ 2\pi] & , \ \rho_0 < R_c(z_c) \\ [\phi_0 + \pi - \Delta\phi,\ \phi_0 + \pi + \Delta\phi] & , \ \rho_0 \geq R_c(z_c) \end{cases}, \tag{IV.11}$$

with

$$\Delta\phi = \arcsin\left(\frac{R_c(z_c)}{\rho_0}\right), \tag{IV.12}$$

$$R_c(z_c) = R_c\left(1 + \frac{2z_c}{L_c}\right), \tag{IV.13}$$

and

$$z_c = \mathbf{R}_z - \mathbf{r}_{0,z}, \tag{IV.14}$$

and are shown graphically in the panels of Fig. IV-3 for a fixed z'. The quantity ρ_0 is the distance between the central axis of the collimator cone and the z'-axis of the integration

coordinates system (i.e. the primed coordinate system). This choice of integration variables allows for the efficient calculation of the first order integral with a high degree of accuracy, especially when integration over the singularity is required. When ρ_0 lies outside the collimator cone, at a given depth, other integration choices will be equally valid since the inverse square singularity is not approached. In fact a simple, non-adaptive integration grid can provide acceptable results if $\rho_0 \geq 2R_c(z_c)$.

Note that, although the above derivation was specifically presented for the first-order kernel calculation, the same approach can be applied to the integration over the last scattering site for all orders above and including the first order. This is because the last scattering position must always lie, simultaneously, within the collimator cone extended from $\mathbf{R}_i$ and within the attenuating medium. Thus, the above method is used in the next section for the integration over the position of second-order scattering in the expression for the second-order contribution to the kernel Eq. (IV.5).

Second-Order Calculation

Calculation of the second-order kernel contribution, Eq. (IV.5), is more complicated than the first-order contribution since there are two singularities and two scattering position vectors to integrate over. A significant problem is that the first-order scattering site may in theory occur anywhere within the attenuating medium and, thus the integration region for $\mathbf{r}_1$ is the complete volume of the attenuating medium. Further, the integration over $\mathbf{r}_1$ encounters a singularity as $\mathbf{r}_1 \to \mathbf{r}_0$. This singularity at $\mathbf{r}_0 = \mathbf{r}_1$ is handled by choosing a spherical coordinate system centered at $\mathbf{r}_0$ for the integration over $\mathbf{r}_1$, i.e.

$$\int d^3\mathbf{r}_1 \frac{1}{|\mathbf{r}_1 - \mathbf{r}_0|^2} \Rightarrow \int d^3\mathbf{r}' \frac{1}{|\mathbf{r}'|^2} = \int_0^{r'_{max}} dr' \int_{\theta_{min}}^{\theta_{max}} d\theta' \int_0^{2\pi} d\phi' \left(r'^2 \sin\theta'\right) \frac{1}{r'^2}, \qquad \text{(IV.15)}$$

where

$\mathbf{r}_1 = \mathbf{r}_0 + \mathbf{r}'$. The singularity is obviously removed by the Jacobian r'^2 which vanishes for $\mathbf{r}_1 \to \mathbf{r}_0$. The integration over $\mathbf{r}_2$ is evaluated using the approach described in the previous section with $\mathbf{r}_2$ taking on the role of $\mathbf{r}_1$ and $\mathbf{r}_1$ taking on the role of $\mathbf{r}_0$. This approach

takes care of the singularity at $\mathbf{r}_1 = \mathbf{r}_2$ as discussed in the previous section. The only difficulty remaining is an adequate sample of the integration region over $\mathbf{r}_1$. This region may be restricted somewhat by employing the fact that a photon can only lose so much energy before it has a negligible probability of being detected by the camera system due to the finite energy window of the camera, c.f. Eqs. (II.22) and (III.17).

Energy Spectra Calculation

The energy dependence of the kernel can also be calculated from the expressions in Eqs. (III.21) - (III.23). Further, the energy dependence or energy spectra can be calculated in parallel (i.e. simultaneously) with the spatial dependence of the kernel with minimal additional computational effort. An arbitrary kernel element describes the probability that a photon emitted from a source voxel will be detected at $\mathbf{R}_i$. Implicit in the kernel definition is its dependence upon the energy window, and it describes the probability for detection for a given window, i.e. for given $W_{\min}$ and $W_{\max}$. To emphasize this fact, an arbitrary kernel order can be rewritten as

$$K^{(n)}(\mathbf{R}_i, \mathbf{r}; W_{\min}, W_{\max}), \tag{IV.16}$$

with the dependence upon the energy window parameters explicitly indicated. The energy response function, $F(E; W_{\min}, W_{\max})$, which describes the probability that a photon of energy E will trigger detection for an energy window from $W_{\min}$ to $W_{\max}$, is the only function in the expression for $K^{(n)}$ which depends upon the energy window parameters. The kernel for an energy window from $W_{\min}$ to $W_{\max}$ can be decomposed into the sum of kernels for a number of discrete, equally spaced, non-overlapping energy windows contained within the range of $W_{\min}$ to $W_{\max}$ as

$$K^{(n)}(\mathbf{R}_i, \mathbf{r}_j; W_{\min}, W_{\max}) = \sum_{l=1}^{N} K^{(n)}(\mathbf{R}_i, \mathbf{r}_j; W_{\min}^l, W_{\max}^l), \tag{IV.17}$$

where $W_{\min} \le W_{\min}^l < W_{\max}^l \le W_{\min}^{l+1} \le W_{\max}$. Substituting Eq. (IV.17) into any of Eqs. (III.21) - (III.23) demonstrates that the integrand for the kernel for each distinct energy window does not change, but the weighting from the energy response function does change. Thus the integration sampling is performed just as for a single energy

window except that the integrand contribution from each sample to each energy window is obtained through proper weighting by the energy response function at the inner-most step. To demonstrate how this is accomplished in practice, assume that $F_{i,j}$ is a 2D matrix representing the probability of detecting a photon of energy E_i within the small energy window $W_{\min}^j$ to $W_{\max}^j$, and that f_i is the probability that a photon of E_i will be detected in any of the N energy windows covering the energy window range $W_{\min}$ to $W_{\max}$, i.e.

$$f_i = \sum_{j=1}^{N} F_{i,j} . \tag{IV. 18}$$

Also, assume the integrand for the n^{th}-order kernel can be written symbolically as

$$\begin{aligned} K^{(n)}(\mathbf{R}_i, \mathbf{r}_j; W_{\min}, W_{\max}) &= \sum_{\mathbf{r}_1, \mathbf{r}_2, \ldots \mathbf{r}_n} w(\mathbf{r}_1, \mathbf{r}_2, \ldots, \mathbf{r}_n) I(\mathbf{r}_1, \mathbf{r}_2, \ldots, \mathbf{r}_n; E_k = E_n) \sum_{l=1}^{N} F_{k,l} \\ &= \sum_{\mathbf{r}_1, \mathbf{r}_2, \ldots \mathbf{r}_n} w(\mathbf{r}_1, \mathbf{r}_2, \ldots, \mathbf{r}_n) I(\mathbf{r}_1, \mathbf{r}_2, \ldots, \mathbf{r}_n; E_k = E_n) f_k \end{aligned} , \tag{IV.19}$$

where the first sum is over all discrete integration sampling points, w's are the numerical integration weights associated with each set of integration sampling coordinates $(\mathbf{r}_1, \mathbf{r}_2, \ldots, \mathbf{r}_n)$ for which the integrand is calculated, and I denotes a symbolic representation of the integrands in Eqs. (IV.4) and (IV.5) without the energy response function $F(E_n; W_{\min}, W_{\max})$. The kernel for a single energy window can be similarly expressed as

$$K^{(n)}(\mathbf{R}_i, \mathbf{r}_j; W_{\min}^l, W_{\max}^l) = \sum_{\mathbf{r}_1, \mathbf{r}_2, \ldots \mathbf{r}_n} w(\mathbf{r}_1, \mathbf{r}_2, \ldots, \mathbf{r}_n) I(\mathbf{r}_1, \mathbf{r}_2, \ldots, \mathbf{r}_n; E_k = E_n) F_{k,l} . \tag{VI.20}$$

The following shows two code fragments which demonstrate how Eqs. (IV.19) and (IV.20) can be used to calculate the energy spectra in parallel with the kernel calculation:

Single energy window $K^{(n)}(\mathbf{R}_i,\mathbf{r}_j;W_{\min},W_{\max})$	Simultaneous multiple energy window $K^{(n)}(\mathbf{R}_i,\mathbf{r}_j;W^l_{\min},W^l_{\min}),\ l=1,...,N$

Kn = 0.0;
for (r1,r2,..., rn) {
  temp = w(r1,r2,...,rn) *I(r1,r2,...,rn);
  Ek = En(r1,r2,....,rn);
  Kn += temp * f(Ek);
}
	for (l=0; l<N; l++) Kn[l] = 0.0;
	for (r1,r2,..., rn) {
	  temp = w(r1,r2,...,rn) * I(r1,r2,...,rn);
	  Ek = En(r1,r2,....,rn);
	  for (l=0; l<N; l++) Kn[l] += temp * F(Ek,l);
	}

The window widths can be chosen arbitrarily small and therefore the energy dependence can be obtained to practically any accuracy. It must be emphasized that the energy spectrum obtained is only accurate within the photopeak range $W_{\min}$ to $W_{\max}$. To obtain energy spectra information outside the lower energy window limit, $W_{\min}$, will generally require calculating the contributions beyond 2^{nd}-order.

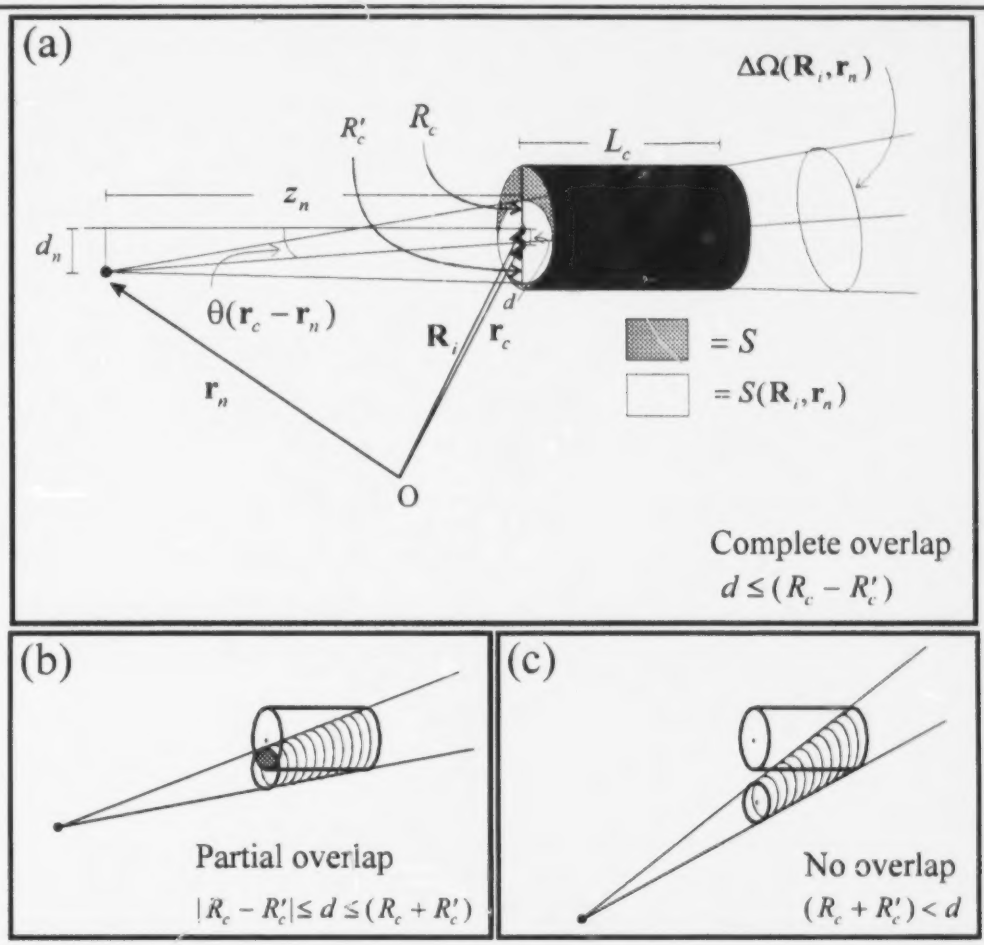

Figure IV-1: Detection geometry for cylindrical hole collimator explaining symbols introduced in the main text, and in particular Eqs. (IV.1) through (IV.3): (a) complete back/front window overlap, (b) partial overlap, and (c) no overlap.

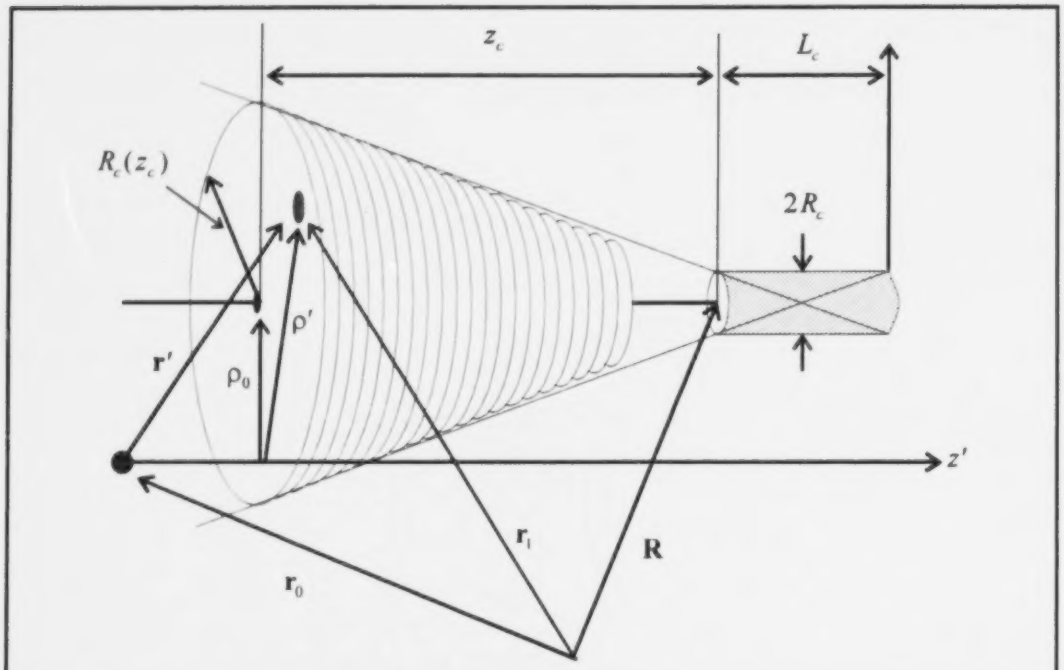

Figure IV-2: Schematic representation of the cone-like integration volume for $d_3\mathbf{r}_n$ for calculating $K^{(1)}(\mathbf{R}_1, \mathbf{r}_0)$.

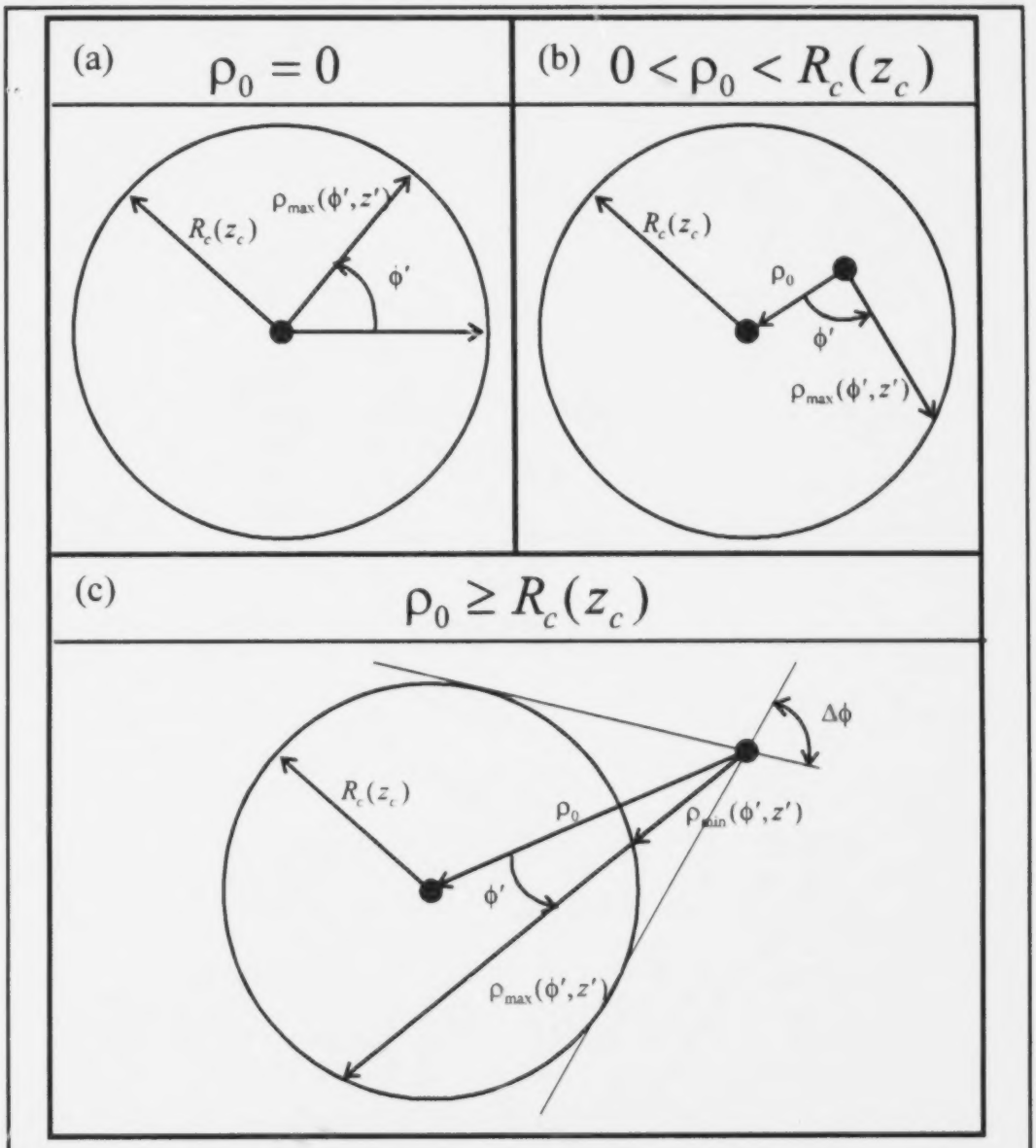

Figure IV-3: Schematic representation of the integration coordinate system used by Eqs. (IV.8) through (IV.14) at a fixed depth from the collimator hole.

V. Experimental Validation

The numerical code developed in the previous chapter to calculate the analytical expressions for the kernel orders, Eqs. (III.21) - (III.23), is experimentally validated in this chapter. Experimental validation is a necessary and fundamental step that must be performed before the numerical code can be used to calculate kernel elements for reconstruction purposes. The numerical code allows the kernel elements, $K_{i,j}$, to be calculated for a given source voxel, j, and a given projection pixel, denoted by i, for a properly defined imaging situation. To calculate the projection data for n^{th}-order photons due to an extended source distribution, described by the matrix s_j, Eq. (II.28) can be used, i.e.

$$P_i^{(n)} = \sum_{s_j \neq 0} K_{i,j}^{(n)} s_j , \tag{V.1}$$

where $P_i^{(n)}$ is the number of n^{th}-order photons detected at pixel i and $K_{i,j}^{(n)}$ is the n^{th}-order kernel matrix element relating $P_i^{(n)}$ to the source distribution s_j. Thus, for the purpose of calculating projection data, only those kernel elements for which $s_j \neq 0$ need to be calculated, and these kernel elements can be calculated as required, i.e. on the fly, for use in Eq. (V.1). Furthermore, for a point source, only one source voxel has a non-zero value and therefore only one kernel element needs to be calculated for each pixel of the projection. Experimentally, it is generally only possible to measure projection data due to all scattering orders, P_i

$$P_i = \sum_{k=0}^{N=\infty} P_i^{(k)} . \tag{V.2}$$

However, for some very simple imaging situations it is possible to obtain both P_i and $P_i^{(0)}$. The value of $P_i^{(0)}$ can be obtained by performing the experiment for the source distribution in the absence of an attenuating medium. The results must subsequently be corrected for the attenuation that would be present if the source was located within an attenuating medium (see below).

Two methods are used to compare the calculated projection data with the experimentally acquired projection data in this investigation: (i) direct visual comparison of projection profile plots, and (ii) comparison of projection scatter fraction values. Projection profile plots are simply a plot of the values recorded by the pixels versus the pixel location. The projection profile is usually plotted for the projection row bisecting the center of the source distribution perpendicular to the axis of rotation (see Figs. I-2 through I-4). The scatter fraction registered at all pixels within a projection due to photons of a given order is a quantity that can also be used to compare the calculated and experimentally acquired data. It is defined as

$$SF^{(n)} = \frac{\sum_i P_i^{(n)}}{\sum_i P_i^{(0)}}, \tag{V.3}$$

and can be easily calculated from the theory. The summation in Eq. (V.3) is over *all* collimator holes or imaging elements of the gamma camera projection. Of course, $SF^{(n)}$ cannot be measured experimentally, at least not directly, but one can estimate experimentally the total scatter fraction using the method of Manglos *et.al.* [108] by measuring the projections for both an air filled and a water filled phantom and calculating

$$SF_{\text{exp}}^{(total)} = \frac{\sum_i [P_i^{(water)} - k P_i^{(air)}]}{k \sum_i P_i^{(air)}}. \tag{V.4}$$

In Eq. (V.4), P_{water} and P_{air} are the experimental counts acquired for the source in water and in air, respectively (corrected for the difference of the acquisition times if necessary), and $k = \exp(-\mu(E_0)x)$ is the average attenuation which the primary photons would suffer before reaching the camera if they were propagating in water for a distance x. Having defined the quantities to be investigated, the experimental and numerical methods used are discussed next.

A. Experimental Methods

In all experiments the basic phantom used to enclose the attenuating medium was a hollow polystyrene cylinder with inner radius 11.2 cm and inner length 22.0 cm. The walls

of the phantom were approximately 0.5 cm thick and the base and lid were approximately 1 cm thick. The central axis of the cylinder coincided with the rotation axis of the camera, whose radius of rotation was 13.2 cm . The interior of the phantom was filled with water to simulate a uniform attenuating medium and is referred to as the *uniform phantom* configuration. A non-uniform attenuating medium was obtained by inserting one or two air-filled cylinders of radius 3.6 cm and lengths equal to the complete interior length of the phantom. The central axes of the air-filled inserts were parallel to the central axis of the phantom and located at a radial distance of 4.8 cm from it. With the air inserts in place the phantom is referred to as the *non-uniform phantom* configuration. For one set of experiments it was necessary to leave the phantom empty (i.e. air filled) and this phantom is referred to as the *air-filled phantom* configuration. Cross sections of the uniform and nonuniform phantoms used are shown in Figs. V-1 through V-4. Figure V-1 also defines the coordinate system for the phantom and the imaging geometry for the experiments. The central axis of the phantom lies along the y-axis and the base of the phantom is centered at the origin of the coordinate system. The imaging plane (i.e. the camera plane) lies in the xy-plane and is located at a distance 13.2 cm from the y-axis (i.e. the axis of rotation).

Three source distributions of ^{99m}Tc were investigated in conjunction with the above described phantoms. All three source distributions were centered at the midpoint of the phantom along the axis of rotation, which coincided with the midpoint of the projection plane. The first and the simplest was a point source whose volume (approx. 0.1 cm^3) was considerably smaller than that of a single source voxel ($\geq 0.22\,cm^3$). At calibration time the point source contained an activity of 68 MBq , and it was imaged separately for a number of locations within the air-filled, the uniform, and the non-uniform phantom configurations. The second source was a short thin cylindrical source of radius 0.45 cm and length 4.8 cm and contained an activity of 100 MBq at calibration time. Finally, the third source considered was an extended cylindrical source with radius 3.6 cm and length equal to the complete interior length of the phantom (19.2 cm). The extended source had

an activity of 250MBq at calibration time. The point, short cylindrical, and extended cylindrical source distributions were imaged at a number of locations within both the uniform and non-uniform phantom configurations. The source locations for each source and phantom configuration are shown in Figs. (V-1) through (V-4), which are cross-sectional views of the phantom bisecting the center of the source distribution. The numerals (1 through 36) used to identify the source and phantom configurations are defined in Figs. (V-1) through (V-4) and listed in Table V-1.

A single headed GE400 SPECT gamma camera was used to acquire the projection data for all experiments. The camera was operated with a 20% symmetric energy window centered at 140 keV, and was assumed to have an intrinsic energy resolution well-described by a Gaussian distribution with a FWHM of $0.12E_0$, i.e. 12%. The gamma camera employed a NaI crystal 0.95cm (3/8 inches) thick. A low energy general purpose (LEGP) collimator with hexagonal holes arranged in a close-packed hexagonal arrangement was used for collimation. The projection data was acquired using a 128×128 pixel collection matrix with 16 bits per pixel. This collection matrix corresponds to a physical pixel area of approximately $0.3\text{cm} \times 0.3\text{cm}$. The acquired images were subsequently compressed to 64×64 pixel images with a pixel area of approximately $0.6\text{cm} \times 0.6\text{cm}$ for numerical and presentation purposes.

For each source and phantom configuration shown in Figs. (V-1) through (V-4) and listed in Table V-1, projection data was acquired using the gamma camera. In order to directly compare the experimental data with the calculated data, the experimental data was corrected for the count loss due to the exponential decay of the source activity. For each experimental situation, the projection data was multiplied by a constant, as discussed in Chapter 2, given by Eq. (II.16), i.e.

$$\left[\frac{(1-e^{-\lambda \Delta T})}{e^{\lambda T}\lambda \Delta T}\right]^{-1},$$

where T is the time interval between the calibration of the source and the start of the acquisition of the projection data for each source and phantom configuration, and ΔT is the data acquisition interval. This correction factor accounts both for the decay of the source from calibration to the start of imaging as well as for the decay during the imaging. Background measurements were also taken to ensure that it was negligible.

Finally, many quantities that appear in the theoretical expression for the PDK were assumed to be ideal in the preceding formulation. In practice it is difficult, if not impossible, to specify all of these quantities. For example, the assumption that the collimator can be modeled by cylindrical holes preserves the geometric response of the collimator, but may reduce or increase the efficiency of the collimator. Likewise, any bias in the well counter could result in a systematic error in the measured total activity, which in turn would lead to an error in absolute quantification in the calculations. Such factors can be incorporated into a single multiplicative calibration factor which is independent of the attenuating medium and source distribution, but is dependent upon the experimental equipment and radionuclide used. This factor can be determined, for example, by measuring experimentally and calculating theoretically the total count recorded for a simple source distribution in air. The totals obtained should only differ by a constant overall multiplication factor. The factor, which calibrates the theoretical expressions with the experiments, can be used for all other imaging situations involving the same radioisotope and experimental equipment. It is stressed that this factor is not arbitrary, but is due to limitations in applying the theoretical expressions to actual situations. Thus, the experimentally measured data and calculated data are related as,

$$\text{Calibration Factor} = \frac{\text{Calculated Value}}{\text{Experimental Value}},$$

where the Calibration Factor is a constant for all the imaging situations considered in this work.

B. Numerical Methods

The numerical calculation of the projection data follows the outline given in Chapter IV. The cross-section for the short and extended source distributions perpendicular to the phantom's central axis (i.e. the *xz*-plane) was specified on a 512×512 matrix which was collapsed to 64×64 before numerical implementation. The description of the source distribution parallel to the phantom's central axis (i.e. along the y-axis) was obtained by calculating the cross-section representations for 64 equally spaced locations along the axis. The total description of the source distribution is given as a matrix with $64 \times 64 \times 64$ elements whose values represent the average activity of the source distribution within each of the voxels. For the point source distribution, however, a single matrix element in the source distribution was non-zero and the rest of the elements were set to zero. The source matrix element was chosen by determining the source voxel closest to the actual point source placement within the phantom, and thus partial volume effects were not taken into account. Therefore, there is a small ($\approx \frac{1}{2}$ pixel or 0.3 cm) inherent misalignment between the experimental and calculated point source locations with respect to the discrete placement of the pixels.

Similarly, the cross-section of the linear attenuation coefficients and the electron density perpendicular to the phantom's central axis were also specified on 512×512 matrices which were subsequently collapsed to 64×64 matrices before implementation. Again, 64 equally spaced samples of these distributions were taken along the direction parallel to the axis. The total description of the linear attenuation coefficient and electron density distributions were given as $64 \times 64 \times 64$ matrices whose values represent the average of these quantities over the small volume of a voxel. The simplicity of the phantom configurations allowed the attenuation and electron density distributions to be obtained analytically, without the need for and complications associated with either the CT or TCT methods discussed in Chapter IV. The collimator's hexagonal holes were modeled by cylindrical holes with radius $R_c = 0.128\text{cm}$, length $L_c = 4.0\text{cm}$, and center to center separation 0.3cm. The collimator parameter R_c provided the same open area as the actual

hexagonal holes of the collimator. Finally, the energy response function was modeled with FWHM = 2.35σ at 140keV, where FWHM=16.8 keV (i.e. 12% of E_0).

With the above data and parameters, Eqs. (III.21) - (III.23) and Eq. (V.1) were used to calculate, for each source-phantom configuration listed in Table V-1 and shown in Figs. V-1 through V-4, the projection data for the projection row lying in the plane perpendicular to the rotation axis (i.e. in the *xz*-plane) of the camera and bisecting the camera plane. This row, schematically represented by a broken line in Fig. V-1, will be referred to as a *central projection row* and the *central pixel* of the camera is at its center. Only the primary, first-order, and second-order scattered photons are accounted for in these calculations under the assumption that, for a 20% symmetric energy window, the contributions from higher order scattered photons are negligible [98,102]. The terms *total calculated signal* or *total projection* thus refer to the sum of the primary, first-order, and second-order contributions. For the purpose of calculating scatter fractions (and investigating the kernel connectivity in the next chapter) the complete 64×64 projection for each scattering order was also calculated for experiments involving the point source. Further, the energy spectrum for the entire 64×64 projection was calculated for the experiments involving the point source using 64 discrete energy windows equally spaced within the energy acceptance range $W_{\min} = 126\,\text{keV}$ and $W_{\max} = 154\,\text{keV}$. No adjustable parameters were used and the theoretical results presented in this paper represent values obtained directly from these calculations.

C. Results

The projection profiles along the central projection row are plotted in Figs. V-5 through V-40 for each configuration shown in Figs. V-1 through V-4 and listed in Table V-1. In Figs. V-5 through V-40, the open circles correspond to experimentally acquired data. The vertical error bars associated with the experimental data denote the 68% confidence range for each experimental data value assuming they are drawn from a Poisson distribution, i.e. the error bars represent a range equal to $\pm$ one standard

deviation. Also shown in Figs. V-5 through V-40 are the corresponding calculated profile data for the three lowest Compton scattering orders as well as their sum total. The thin line, squares, triangles, and the thick line correspond to the zeroth-order, first-order, second-order, and the total calculated counts, respectively. The experimental values plotted in Figs. V-5 through V-40 were obtained by averaging projection profiles from 3 and 10 projection rows adjacent to the central row for the thin source and for the extended source, respectively. This averaging reduces the statistical fluctuations present in the experimental profiles. No averaging was performed for the point source data. Since the theory provides the expectation result and does not contain any statistical noise, there is no need to average the theoretical results over the adjacent projection rows. Other than averaging adjacent projection rows, no corrections were introduced so the values plotted represent the absolute measured counts.

The energy spectra for each point source configuration listed in Table V-1 are plotted in Figs. V-41 through V-46. In Figs. V-41 through V-46, the thin line, squares, triangles, and the thick line correspond to the zeroth-order, first-order, second-order, and total energy spectra respectively. Unfortunately, the experimental energy spectra could not be obtained from the camera in a way which would allow for direct comparison with the calculated total spectra in Figs. V-41 through V-46.

The scatter fractions for each point source configuration listed in Table V-1 are plotted in Figs. V-47 and V-48 for the uniform and nonuniform phantoms respectively. The scatter fractions are plotted as a function of the source's effective water depth in the phantom, which are given for each source location in column five of Table V-1. The experimental scatter fraction values were obtained using the method of Manglos described around Eqs. (V.3) and (V.4) and are shown as open circles in Figs. V-47 and V-48. The vertical error bars associated with the experimental data represent the scatter fraction range assuming a ± 0.3cm error in the value of x used to calculate the attenuation factor k in Eq. (V.4). The calculated scatter fractions were obtained using Eq. (V.3) and are

shown in the figures as squares, triangles, and solid line for the 1st order, 2nd order, and the 1st+2nd order scatter fraction, respectively.

Finally, in Table V-2 the results of the comparison are summarized by listing the relative differences, defined as

$$\Delta P = 1 - \frac{\sum_i P_i^{(\text{total})}}{\sum_i P_i^{(\text{exp})}}, \tag{V.5}$$

where the summation runs over the pixels of either: (i) the entire 2D projection plane (i.e. all 64×64 pixels) for the point source configurations; or (ii) the central projection row (i.e. 64 pixels) for the extended source distribution configurations (since this was the only data calculated for these distributions). In Eq. (V.5), $P_i^{(\text{exp})}$ and $P_i^{(\text{total})}$ are the counts recorded at pixel i for the experimental and calculated projection data, respectively. The relative difference, ΔP, is useful for demonstrating that the calculated results require no arbitrary, overall scaling factor for absolute, quantitative comparison with corresponding experimental results.

D. Discussion of Results

In all cases (Figs. V-5 through V-40), the agreement between the calculated profiles and those obtained from experiment is very good, both in shape and in magnitude. It is worthwhile to note how closely the theoretical profiles follow the experimental ones along sharp turns and edges (c.f. Figs. V-16, V-17, V-19 through V-23, V-25, V-32 through V-34, and V-40) which are due to sharp nonuniformities in the medium. The results for the point source demonstrate that the calculated elements of the detection kernel accurately render the detection probability at the pixels receiving counts due to the emission from a point source. The results for the small and the large cylindrical sources demonstrate that the theoretically predicted kernel also accurately describes the recorded projection data for extended source distributions.

Slight asymmetry of the recorded projections with respect the central pixel, seen in some of Figs. V-5 through V-40, is most likely due to configuration errors made in aligning the camera with respect to the phantom and source. When judging the agreement between the theoretical and experimental results note that (i) no adjustable parameters were used so the theoretical values plotted represent the absolute calculated projection counts, and (ii) a logarithmic scale is used so the discrepancy between the simulated and experimental profiles, seen in the wings, is two to three orders of magnitude below the signal maximum. This small discrepancy may be attributed to a few causes: (i) detection of lower energy photons may not be modeled perfectly by the idealized Gaussian energy response function, (ii) collimator penetration and scattering are ignored, (iii) third- and higher-order scattered photons are not accounted for even though they certainly make up a larger (but still negligible) fraction of the signal in the wings than they do closer to the center of the profile, and (iv) Rayleigh scattered photons which make up a small (up to 2%) contribution to the experimental results are not accounted for in the calculations. The observed discrepancy is largest when the source is closest to the collimator and quite shallow in the medium, suggesting that collimator penetration and scattering might be more important in these situations than the higher order or Rayleigh scattering. Note, however, that the statistics of the experimental data in the wings is rather poor (particularly for a shallow source) due to the low absolute counts there. In fact, Table V-2 demonstrates that for all source configurations investigated the total predicted counts obtained numerically differs by no more than ±5% from the total experimental counts. More importantly, the calculated results correctly model the experiments for non-uniform phantoms (Figs. V-5 through V-40) and fully demonstrate the importance of scattered photons in forming broad shoulders of the profiles and in determining the overall dependence of the projections on the nature of the attenuating medium.

The assumption that Rayleigh, third-order, and higher-order scattered photons contribute little to the total signal (except, possibly, in the wings) for narrow energy windows appears to be well justified by the agreement between the experimental and the theoretical data presented here. In fact, even the second-order photons do not make much

of a contribution to the total signal. For most practical situations, the sum of the primary and the first-order photons accounts accurately for both the magnitude and the shape of total projection signal, and the second-order contributions can probably be ignored, thus easing the computational effort required.

Figures V-47 and V-48 further demonstrate good agreement between the calculated and the experimental scatter fractions, providing a more global measure of the agreement than the projection profiles. The differences between $SF^{(1)} + SF^{(2)}$ and $SF_{\exp}^{(total)}$ are well within the typical experimental error of 15% reported by Manglos for this method. More importantly, the scatter fractions presented demonstrate that for sources located deep within an attenuating medium with respect to the camera plane, it is possible that the counts recorded by all pixels due to scattered photons may exceed those due to primary photons.

E. Calculation times

The amount of CPU time required to produce the profiles for a given imaging situation is always an important consideration. The times required to calculate the entire 64×64 pixel projection for each point source and phantom configuration are given in Table V-3 and are reported for each order separately. We note that the second-order contribution requires much more CPU time than the lower-order ones. This is due to an extra integration (over all possible first-order scattering sites) present in the second-order calculations.

F. Summary

In this chapter, calculated projection data for point and extended source distributions in uniform and nonuniform media were compared against the projection data obtained experimentally. Very good agreement was obtained in all cases investigated. The distribution of counts for calculated projection profiles agrees well with the same obtained from the experimental data, both in shape and in magnitude. The calculated and experimental scatter fractions also show good agreement, and provide a more global

measure of the agreement between the two data sets. The total predicted counts for the entire projection plane obtained numerically differ by at most 5% from the total counts recorded experimentally for both the point and the extended source distributions. Finally, the importance of scattered photons in forming the projections was quantitatively demonstrated by the presented results.

Admittedly, however, there are some elements present in the photon detection problem which we have not accounted for in our approach. In particular, we did not attempt to correct the projections for the effects related to the intrinsic resolution of the scintillation crystal nor for the attenuation within the septa of the collimator. Although the discrepancies between our theoretical and experimental results might in part be attributed to these processes, we have deliberately decided against incorporating them in order to demonstrate what our theory, based solely on first principles, is capable of doing. Any phenomenological corrections to it would inevitably weaken the argument that a proper physical description of the photon propagation, absorption, and especially scattering within the medium is the most important factor which must be accounted for. From this perspective any further corrections, phenomenological or not, are of secondary importance. We do not want to mix a purely first-principles, theoretical approach with ad hoc phenomenological corrections often designed to partially compensate for many factors already accounted for by this theory. In principle, the attenuation within the septa can be attacked from first principles using methods which we have used in our work, but the benefit of doing this would be negligible considering the price which would have to be paid in terms of the complication of the theory and the additional computational effort. In conclusion, the theory presented and its numerical implementation appear to be validated, at least for the imaging geometries considered here. In the next chapter the validated code is used to calculate the kernel elements for use with the MLEM reconstruction method.

Table V-1. Source and phantom configuration specifics corresponding to Figs. V-5 through V-46. PD is the actual depth of the source in the phantom perpendicular to the camera and EWD is the effective water depth seen by the source. For the uniform phantom configurations PD is always equal to EWD. All values are given in cm.

Point Source and Uniform Phantom Configurations - Figure V.1				
Configuration	x	z	PD	EWD
1	0.0	8.4	2.80	2.80
2	-8.4	0.0	7.41	7.41
3	0.0	-8.4	19.60	19.60
4	0.0	5.6	5.60	5.60
5	-5.6	0.0	9.70	9.70
6	0.0	-5.6	16.80	16.80
7	0.0	2.8	8.40	8.40
8	-2.8	0.0	10.84	10.84
9	0.0	-2.8	14.00	14.00
10	0.0	0.0	11.20	11.20
Point Source and Nonuniform Phantom Configurations - Figure V.2				
Configuration	x	z	PD	EWD
11	0.0	8.4	2.80	2.80
12	-8.4	0.0	7.41	7.41
13	0.0	-8.4	19.60	19.60
14	0.0	5.6	5.60	5.60
15	-5.6	0.0	9.70	9.70
16	0.0	-5.6	16.80	16.80
17	0.0	2.8	8.40	8.40
18	-2.8	0.0	10.84	6.32
19	0.0	-2.8	14.00	14.00
20	0.0	0.0	11.20	11.20
21	0.0	0.0	11.20	4.00

Table V-1. Continued

Short Cylindrical Source and Uniform Phantom Configurations - Figure V.3a				
Configuration	x	z	PD	EWD
22	0.0	5.6	2.80	2.80
23	-5.6	0.0	10.84	7.41
24	0.0	-5.6	19.60	19.60
25	0.0	0.0	11.20	11.20
Short Cylindrical Source and Nonuniform Phantom Configurations- Figure V.3b				
Configuration	x	z	PD	EWD
26	0.0	5.6	2.80	2.80
27	-5.6	0.0	10.84	7.41
28	0.0	-5.6	19.60	19.60
29	0.0	0.0	11.20	11.20
30	0.0	0.0	11.20	4.00
Extended Cylindrical Source and Uniform Phantom Configurations - Figure V.4a				
Configuration	x	z	PD	EWD
31	0.0	4.8	NA	NA
32	-4.8	0.0	NA	NA
33	0.0	16.0	NA	NA
Extended Cylindrical Source and Nonuniform Phantom Configurations - Figure V.4b				
Configuration	x	z	PD	EWD
34	0.0	4.8	NA	NA
35	-4.8	0.0	NA	NA
36	0.0	16.0	NA	NA

Table V-2: Relative differences (in %) between the experimental and calculated total counts as defined in Eq. (V.5) for each source configuration investigated and listed in Table V-1. The summations in Eq. (V.5) run over all 64×64 pixels of the projection for the point source configurations (i.e. 1-21), but only over the 64 pixels of the central projection row for extended source configurations (i.e. 22-36).

Point Source Configurations	ΔP	Extended Source Configurations	ΔP
1	-2.58%	22	-4.13%
2	4.79%	23	0.12%
3	-1.03%	24	3.55%
4	0.36%	25	0.47%
5	4.40%	26	-1.43%
6	-4.94%	27	4.70%
7	-2.60%	28	-0.42%
8	-0.43%	29	2.24%
9	0.55%	30	-5.09%
10	0.64%	31	3.85%
11	-2.66%	32	-0.34%
12	3.70%	33	-3.51%
13	-1.28%	34	2.63%
14	0.49%	35	-1.61%
15	3.63%	36	-1.02%
16	0.61%		
17	-2.85%		
18	1.41%		
19	-1.41%		
20	-2.18%		
21	-5.26%		

Table V-3: CPU usage times (in seconds) for a Sun Sparc 2 workstation to calculate the three lowest order contributions to the kernel for all 64×64 pixels of the camera plane for the uniform phantom configurations (columns 2-4) and for the nonuniform phantom configurations (columns 5-7) as defined in Fig. V-1 and V-2, respectively.

	Uniform Phantom (1-10)			Nonuniform Phantom (11-21)		
Position	0th	1st	2nd	0th	1st	2nd
1, 11	0.88	13.39	451.66	0.88	13.34	455.16
2, 12	0.95	51.31	4493.81	0.93	47.64	2915.42
3, 13	1.21	95.58	12624.15	1.22	85.3	8839.23
4, 14	0.9	24.36	1749.82	0.91	24.27	1750.06
5, 15	0.97	50.5	5223.42	0.93	46.06	3423.65
6, 16	1.09	82.02	10473.15	1.13	72.51	6654.84
7, 17	0.91	37.96	3625.84	0.92	37.74	3622.36
8, 18	0.96	50.15	5360.38	0.95	45.37	3362.47
9, 19	1.02	65.64	7921.07	1.01	54.48	4379.98
10, 20	0.94	49.85	5402.39	0.95	46.43	4205.66
21	NA	NA	NA	0.95	45.47	3366.33

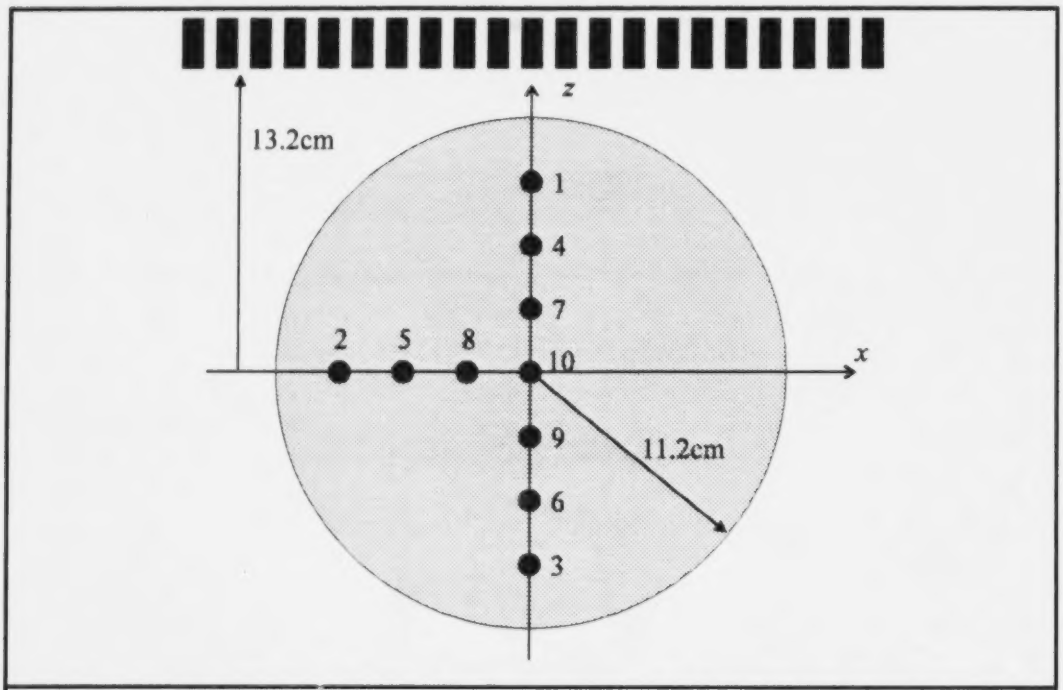

Figure V-1: Cross section of the point source configurations for the uniform phantom. The geometry shown here is used throughout the remainder of the figures presented. The indices (1-10) are used for reference to source configurations shown. Only one source is present at any given time.

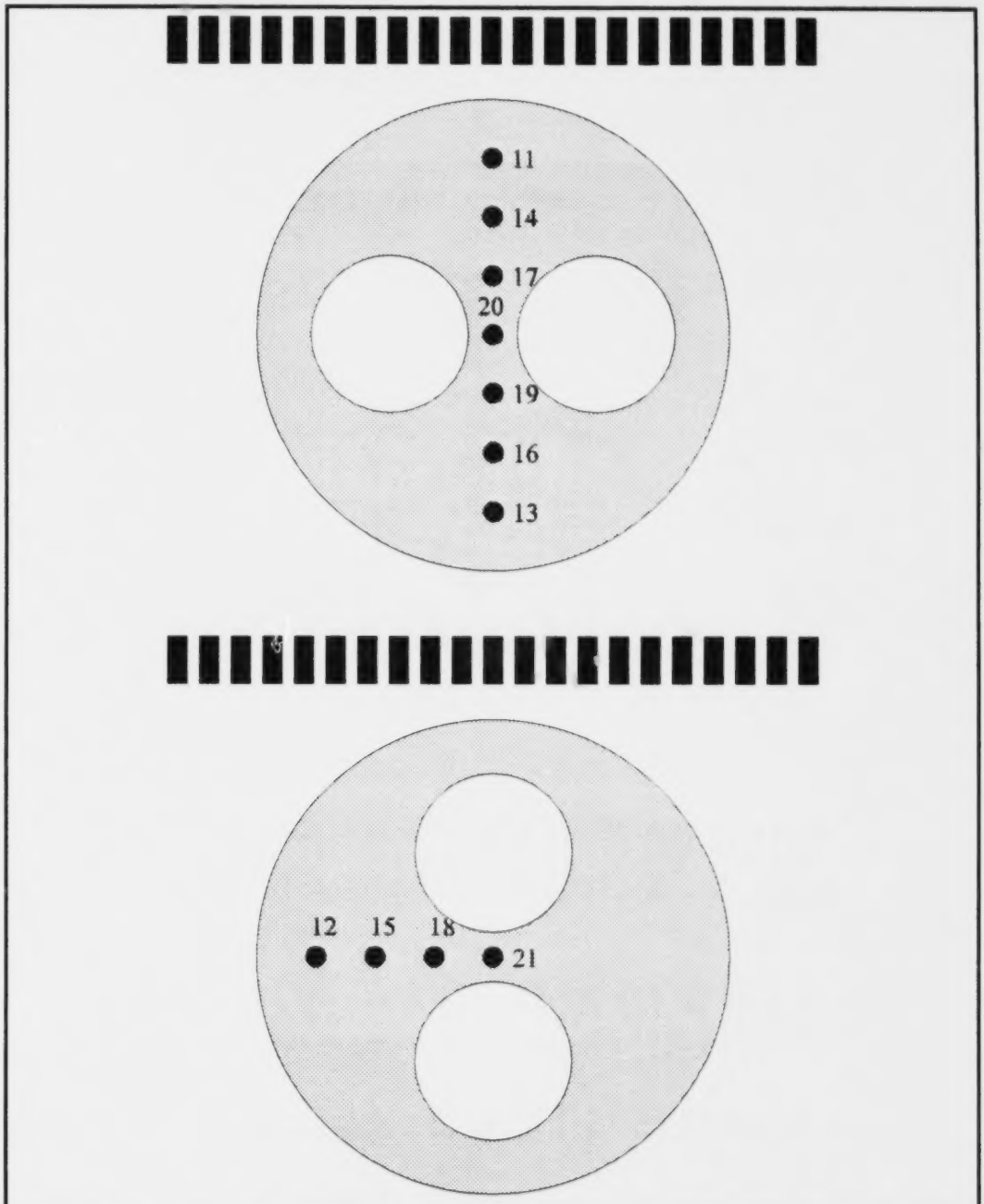

Figure V-2: Cross section of the point source configurations for the non-uniform phantom and their corresponding configuration indices (11-21).

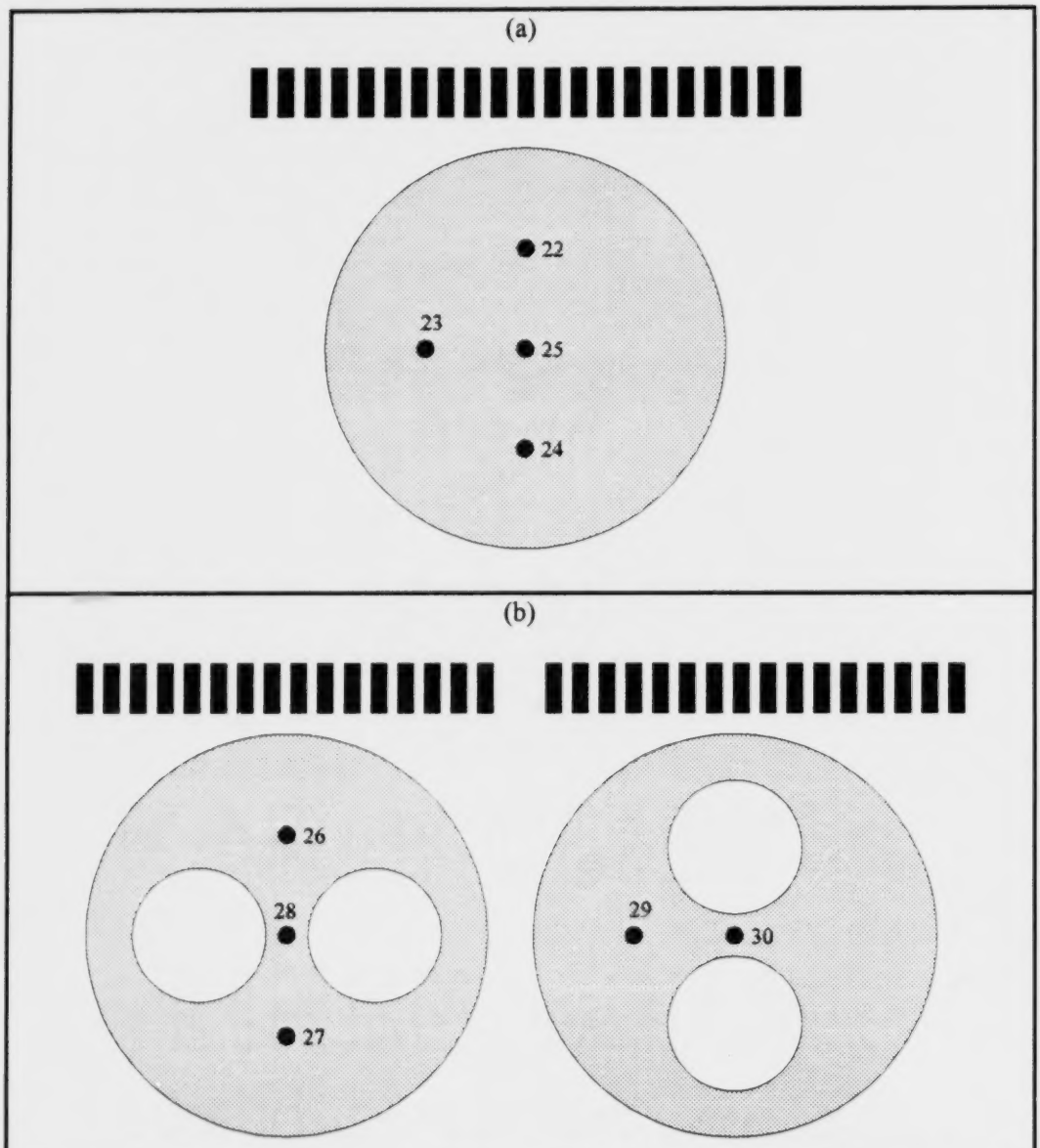

Figure V-3: Cross section of short thin cylindrical source configurations for (a) uniform phantom and (b) nonuniform phantom and their corresponding configuration indices.

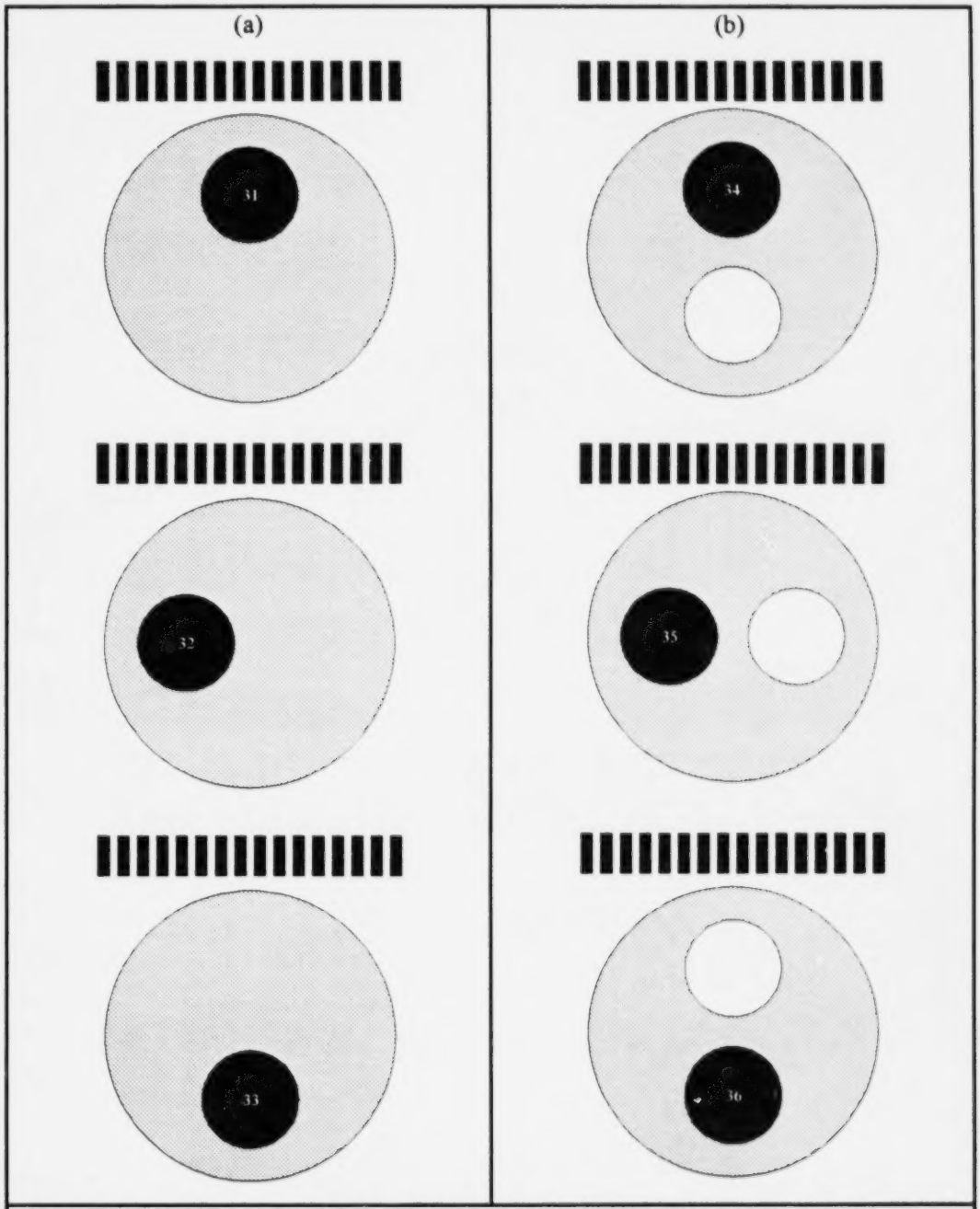

Figure V-4: Cross section of extended cylindrical source configurations for (a) uniform phantom and (b) nonuniform phantom configurations, and their corresponding configuration indices.

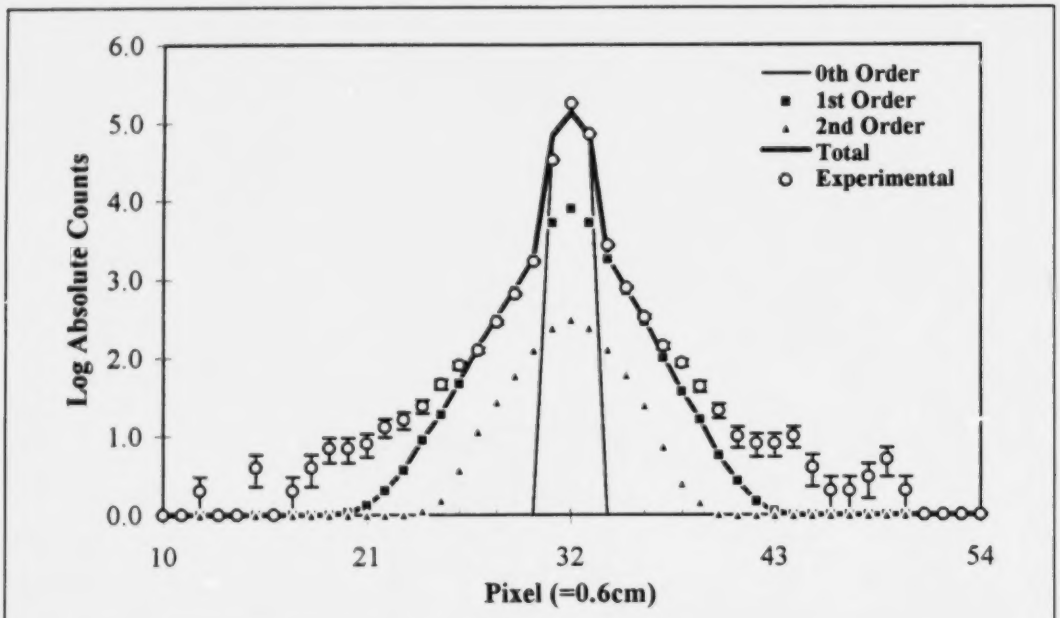

Figure V-5: Projection profiles for the central row for the point source located at position 1 within the uniform phantom. Experimental results: open circles with vertical error bars. Calculated results: thin line - 0^{th}-order, open squares - 1^{st}-order, open triangles - 2^{nd}-order, and thick thin - total (the sum of the 0^{th} through 2^{nd}-orders).

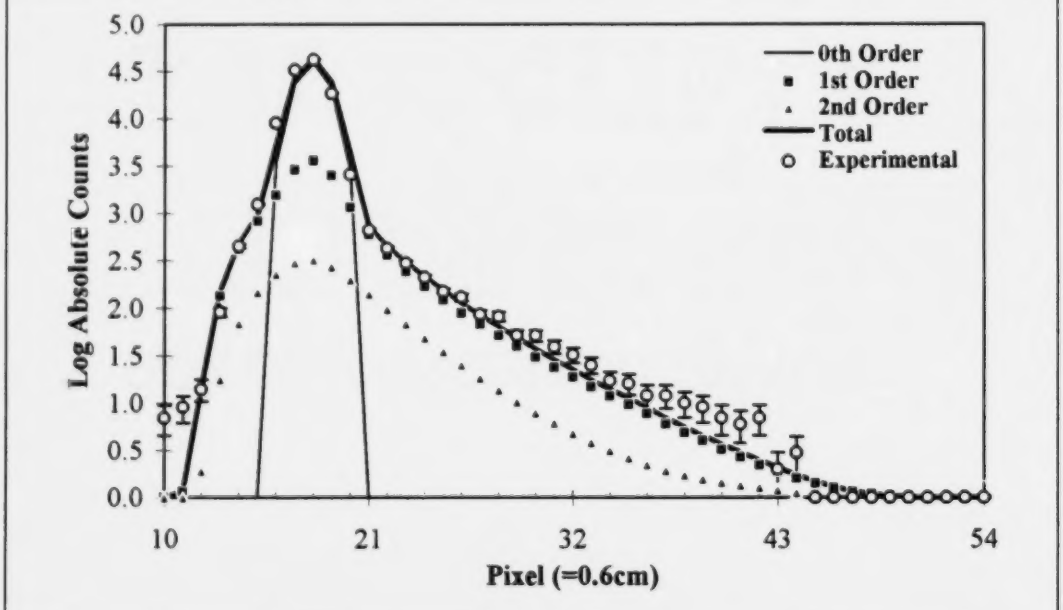

Figure V-6: Same as Figure V-5 except for the point source located at position 2 within the uniform phantom.

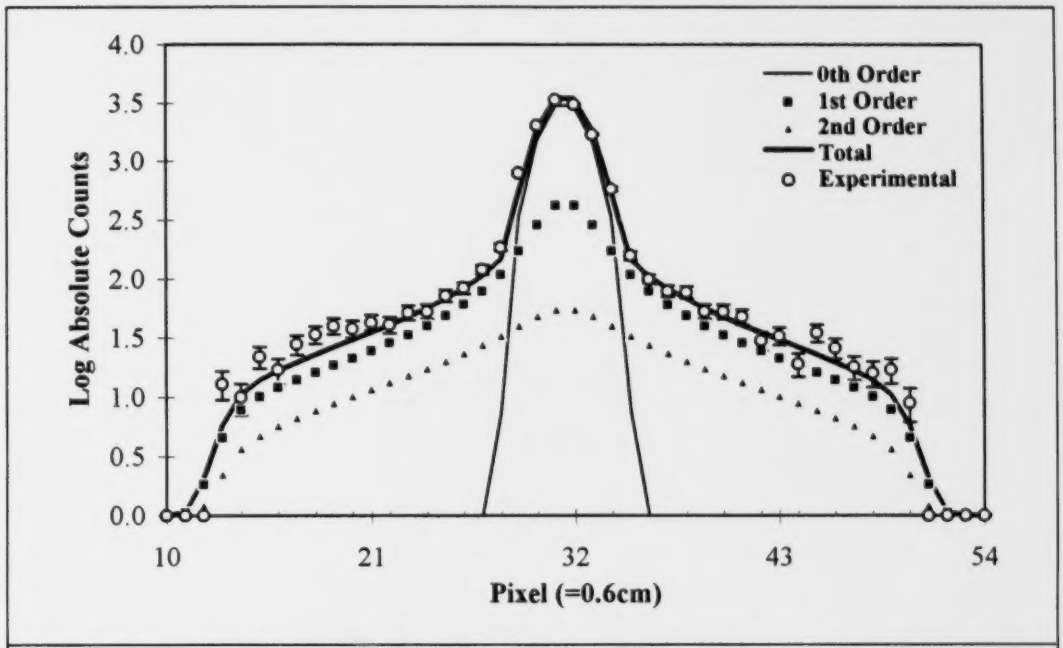

Figure V-7: Same as Figure V-5 except for the point source located at position 3 within the uniform phantom.

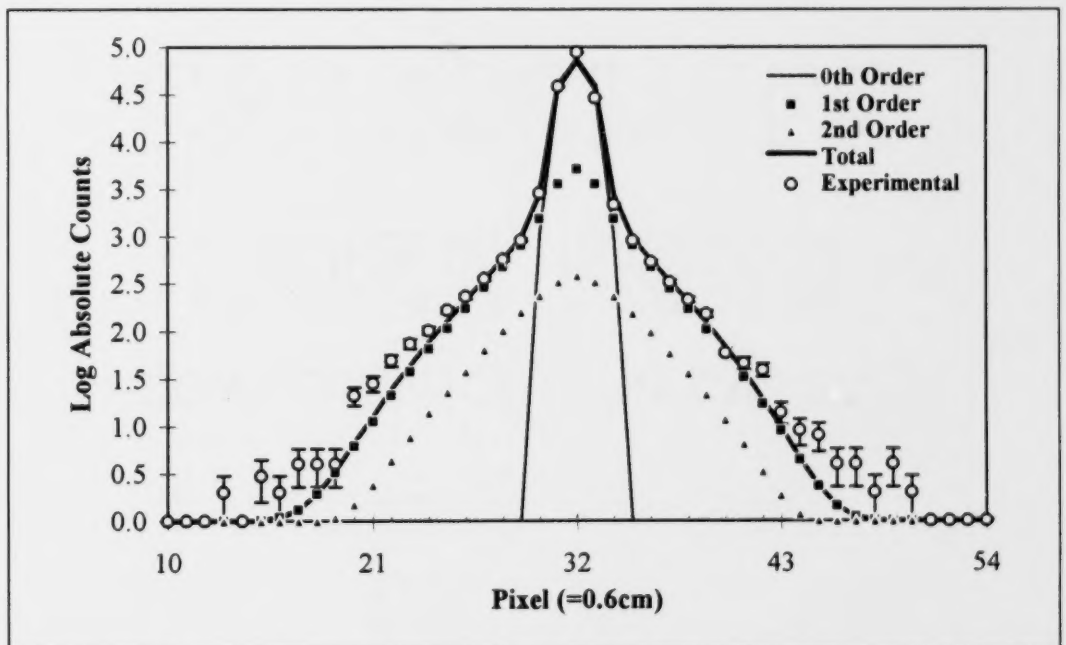

Figure V-8: Same as Figure V-5 except for the point source located at position 4 within the uniform phantom.

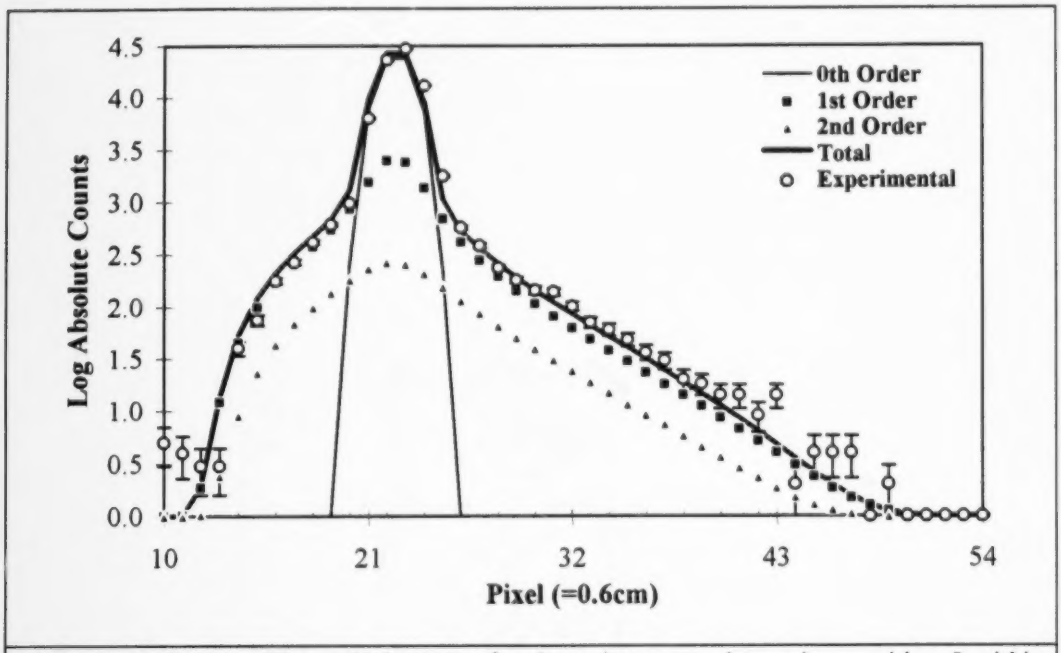

Figure V-9: Same as Figure V-5 except for the point source located at position 5 within the uniform phantom.

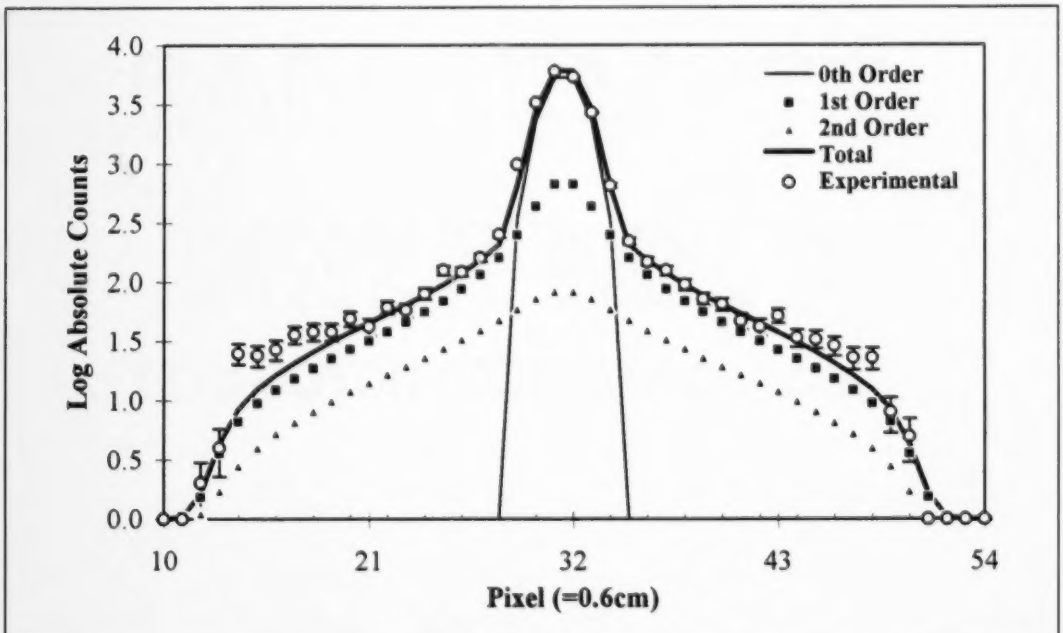

Figure V-10: Same as Figure V-5 except for the point source located at position 6 within the uniform phantom.

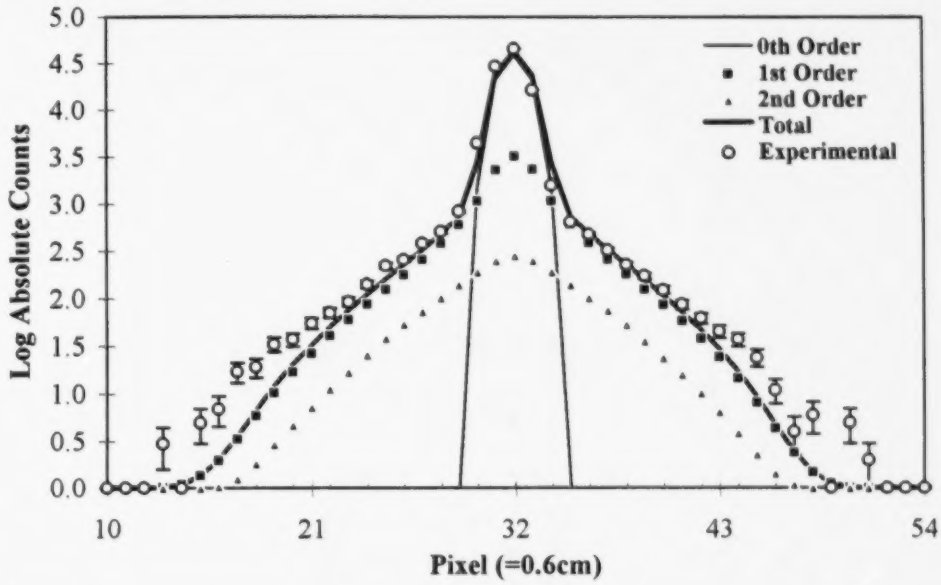

Figure V-11: Same as Figure V-5 except for the point source located at position 7 within the uniform phantom.

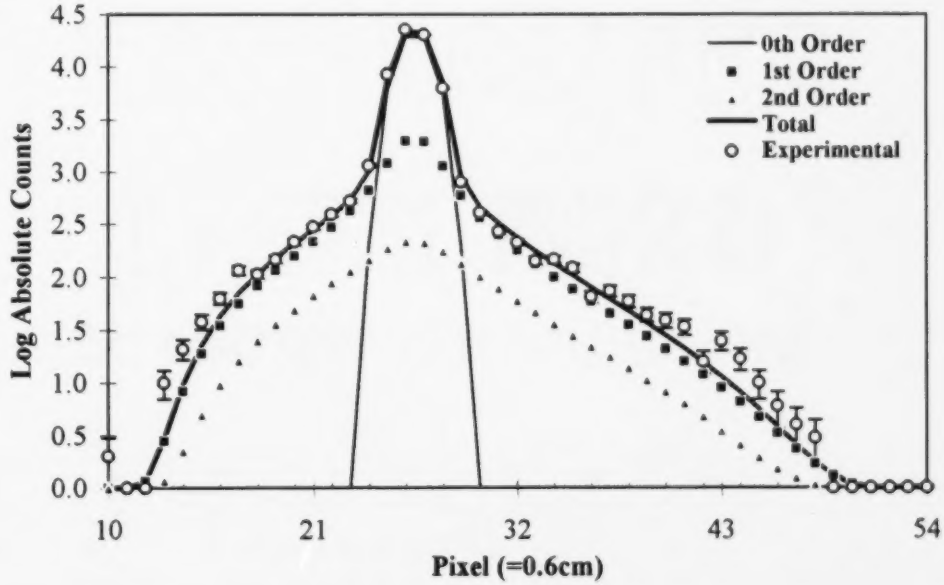

Figure V-12: Same as Figure V-5 except for the point source located at position 8 within the uniform phantom.

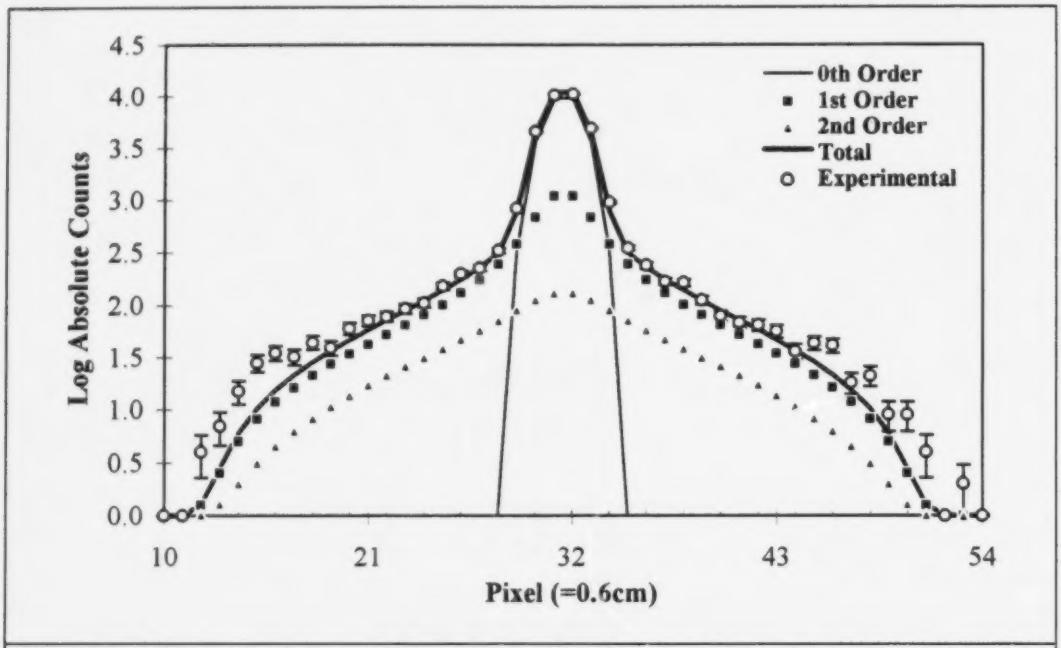

Figure V-13: Same as Figure V-5 except for the point source located at position 9 within the uniform phantom.

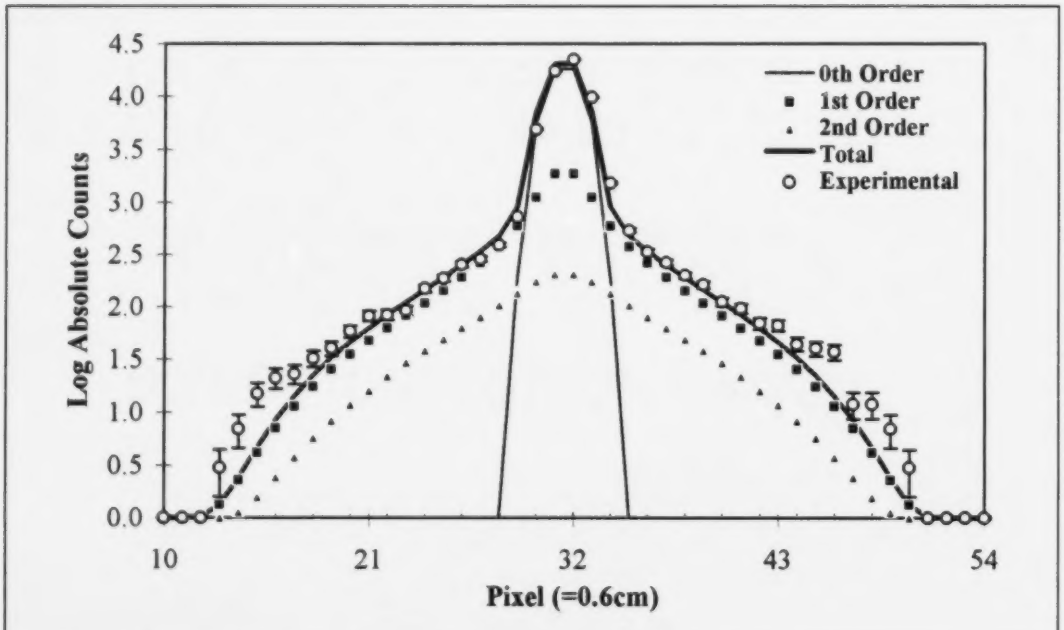

Figure V-14: Same as Figure V-5 except for the point source located at position 10 within the uniform phantom.

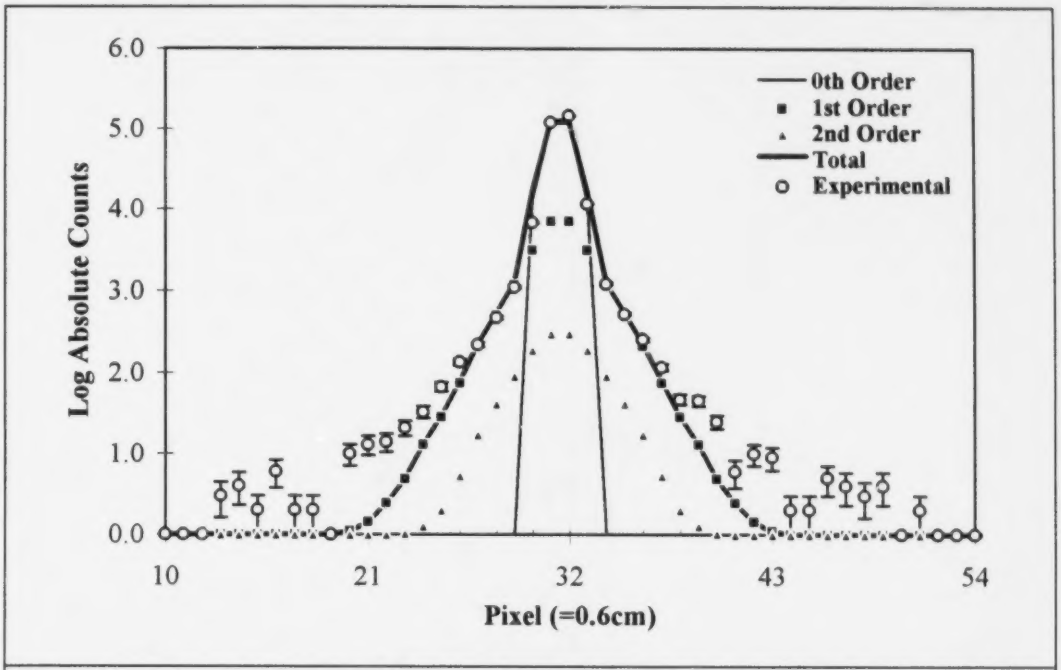

Figure V-15: Same as Figure V-5 except for the point source located at position 11 within the nonuniform phantom.

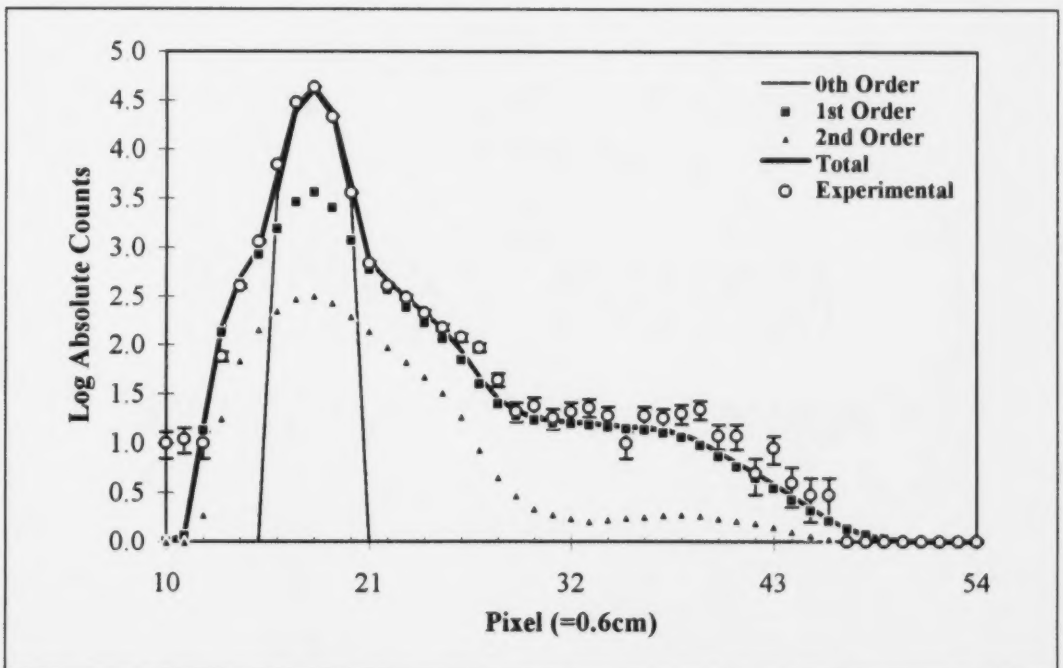

Figure V-16: Same as Figure V-5 except for the point source located at position 12 within the nonuniform phantom.

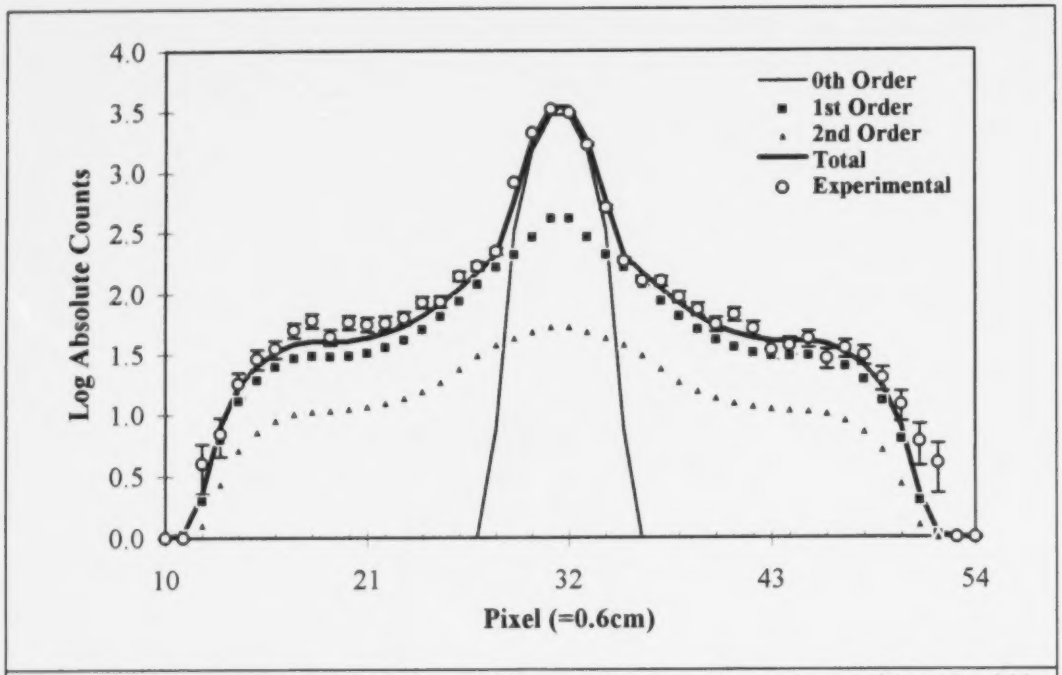

Figure V-17: Same as Figure V-5 except for the point source located at position 13 within the nonuniform phantom.

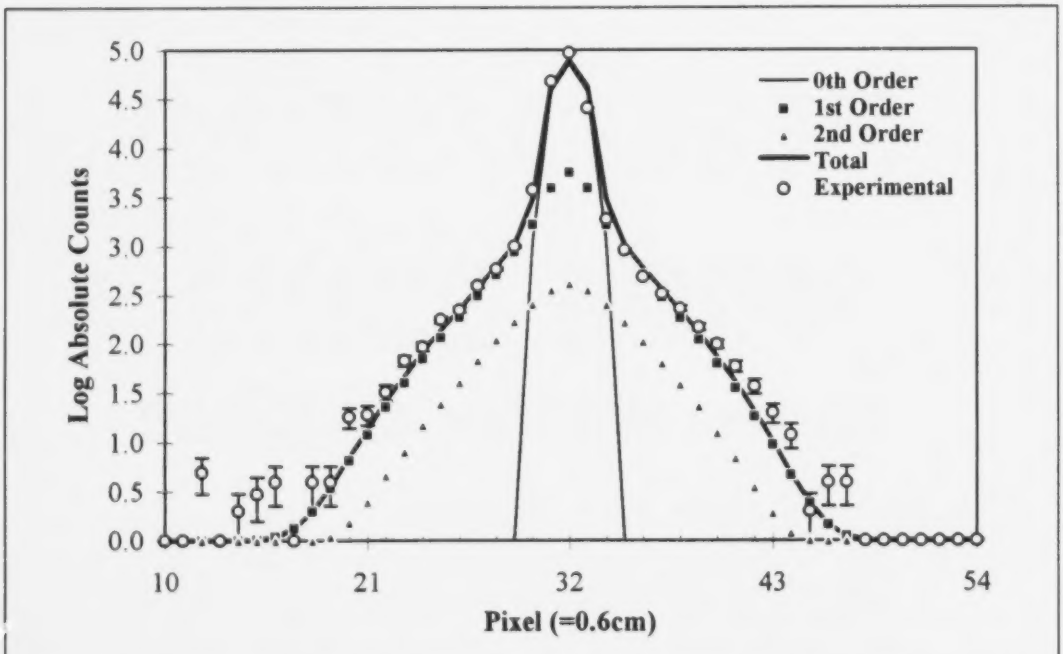

Figure V-18: Same as Figure V-5 except for the point source located at position 14 within the nonuniform phantom.

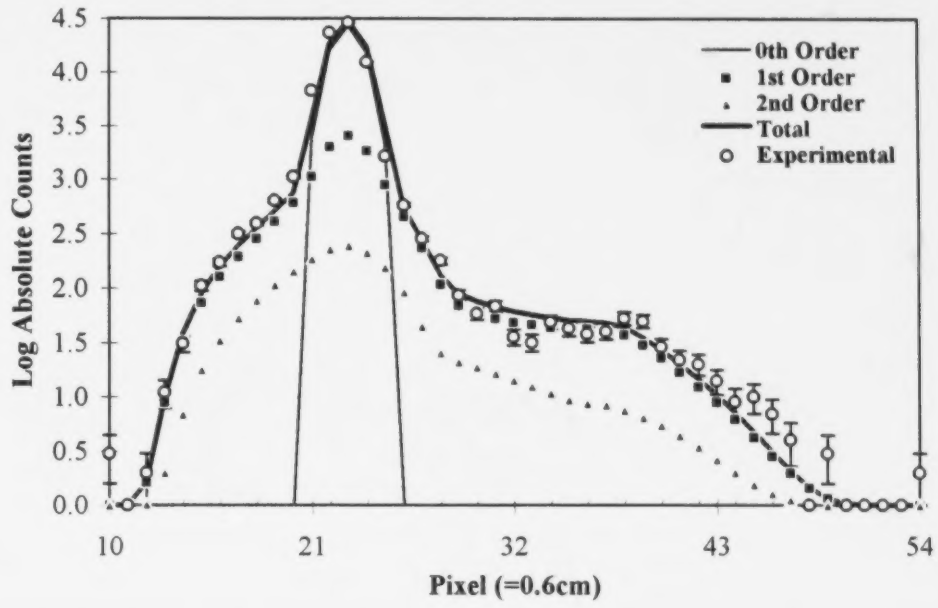

Figure V-19: Same as Figure V-5 except for the point source located at position 15 within the nonuniform phantom.

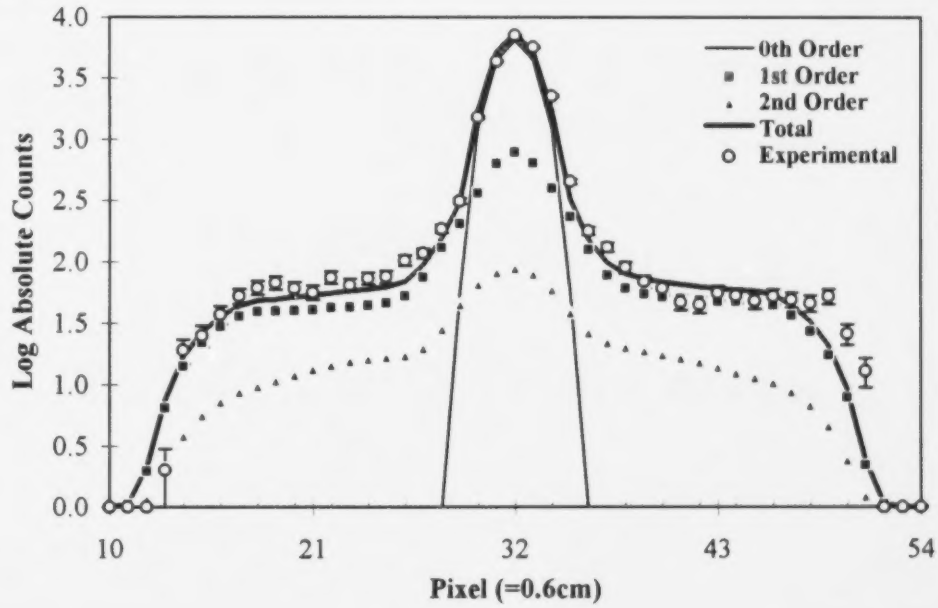

Figure V-20: Same as Figure V-5 except for the point source located at position 16 within the nonuniform phantom.

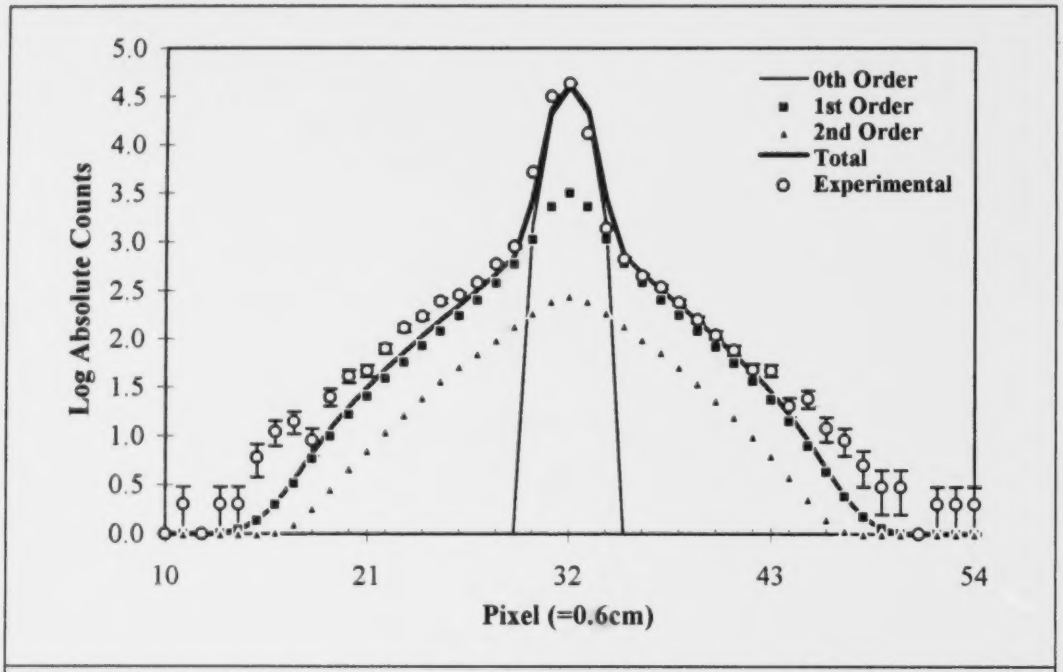

Figure V-21: Same as Figure V-5 except for the point source located at position 17 within the nonuniform phantom.

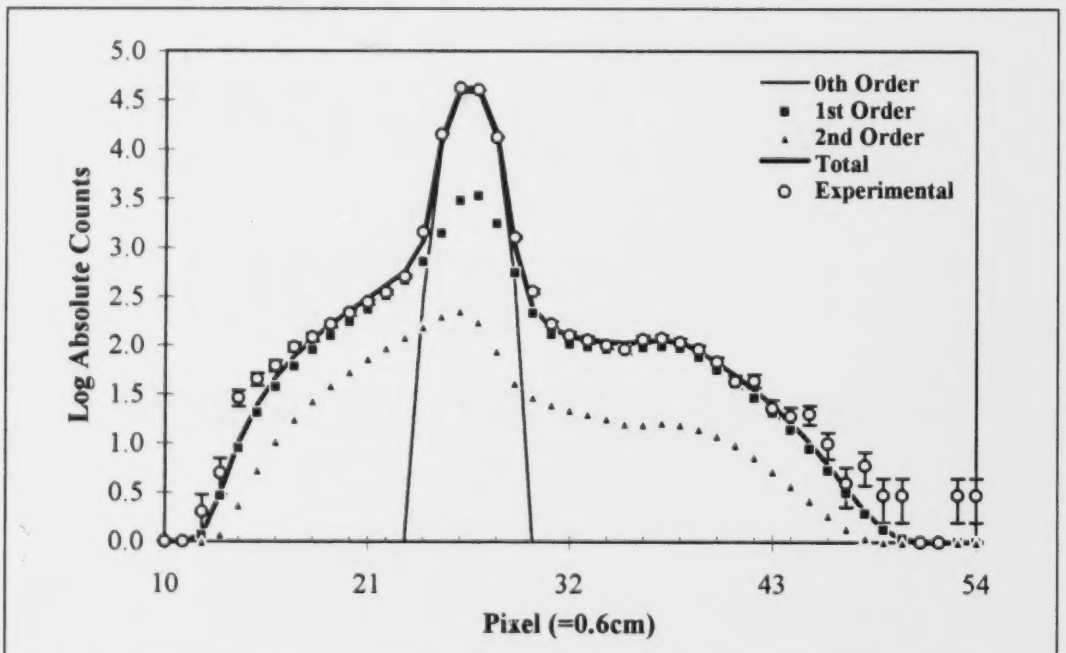

Figure V-22: Same as Figure V-5 except for the point source located at position 18 within the nonuniform phantom.

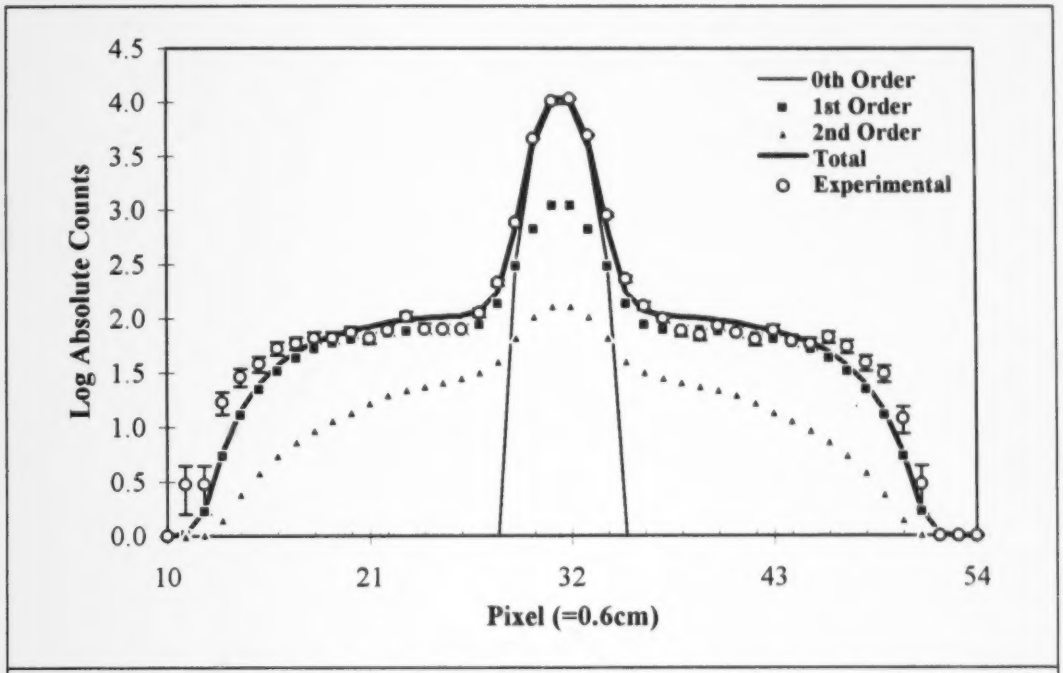

Figure V-23: Same as Figure V-5 except for the point source located at position 19 within the nonuniform phantom.

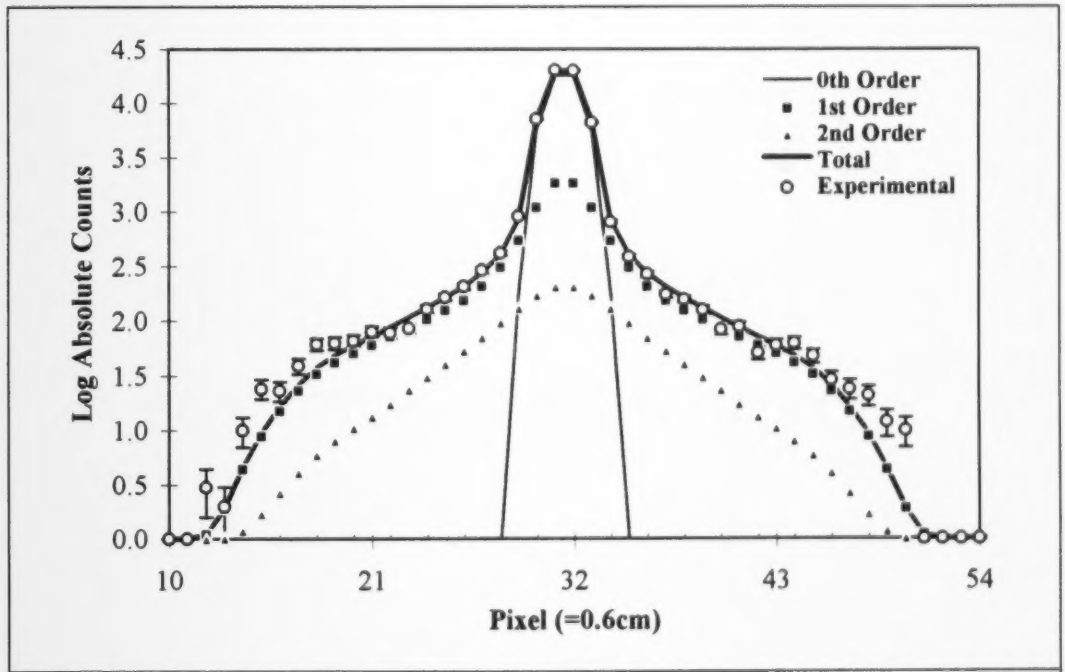

Figure V-24: Same as Figure V-5 except for the point source located at position 20 within the nonuniform phantom.

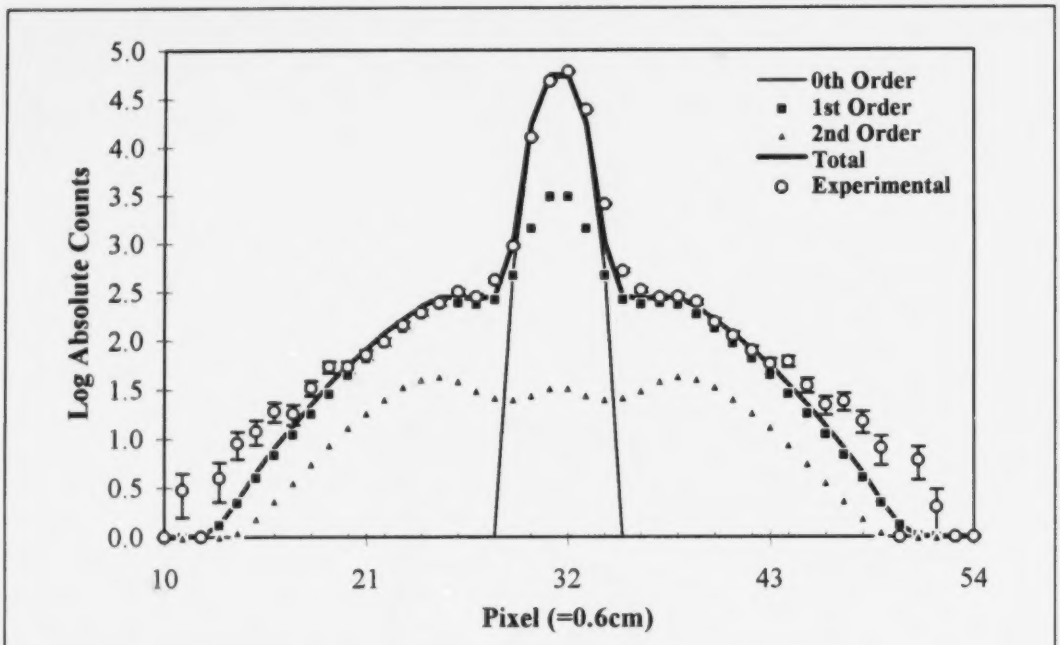

Figure V-25: Same as Figure V-5 except for the point source located at position 21 within the nonuniform phantom.

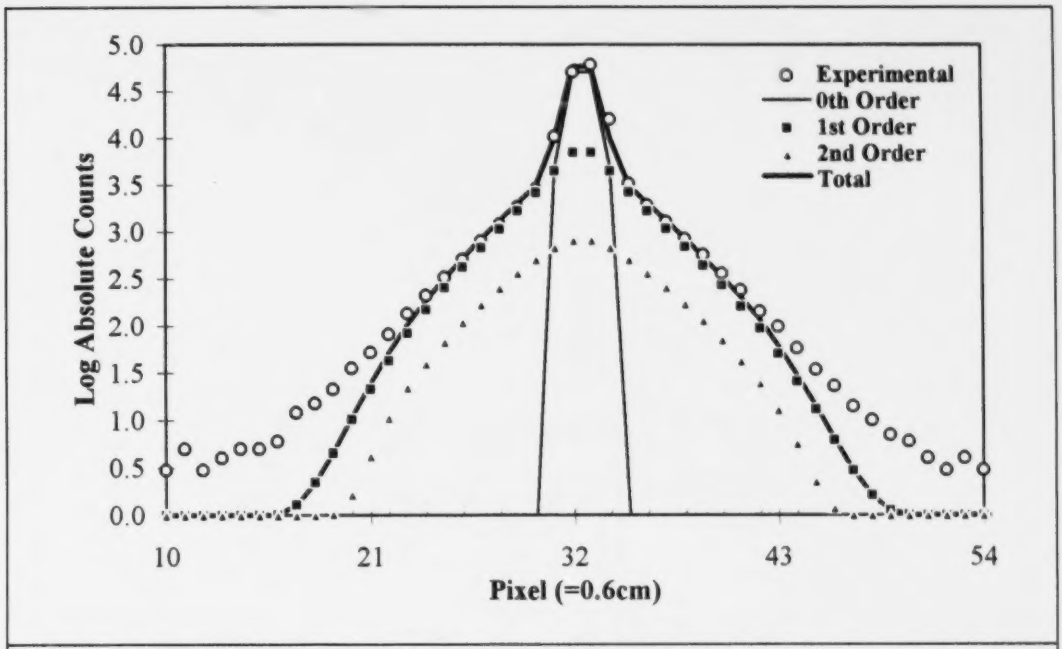

Figure V-26: Same as Figure V-5 except for the short cylindrical source located at position 22 within the uniform phantom.

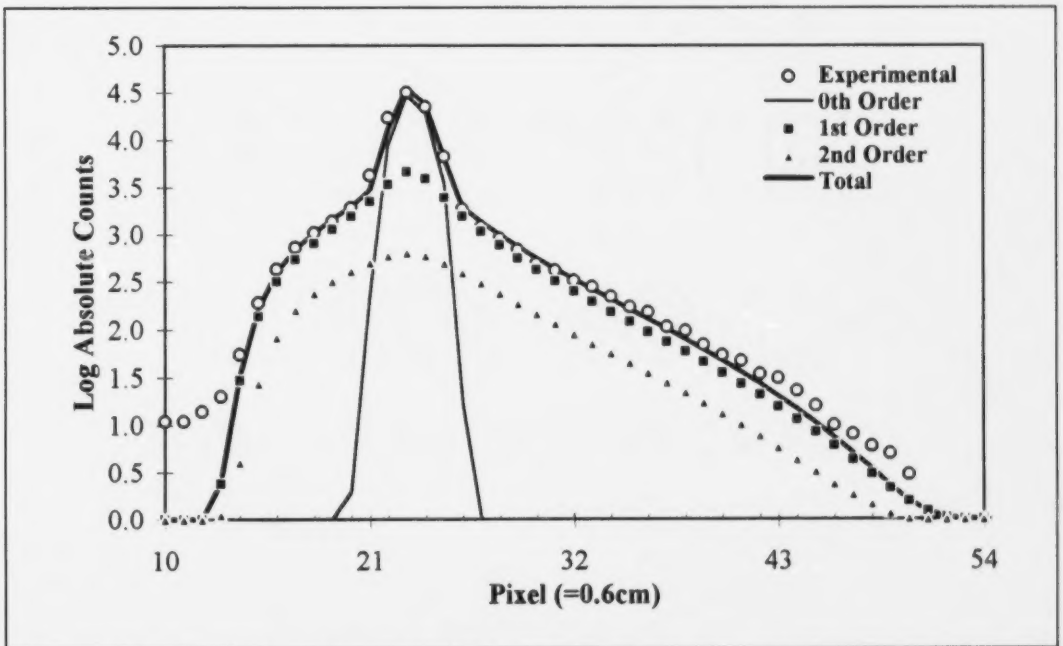

Figure V-27: Same as Figure V-5 except for the short cylindrical source located at position 23 within the uniform phantom.

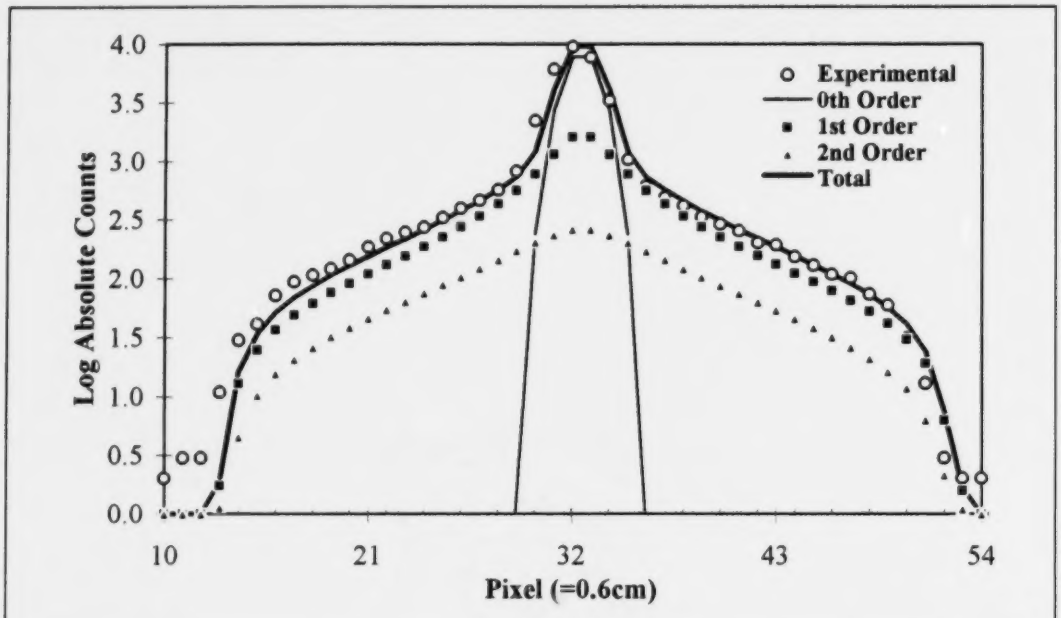

Figure V-28: Same as Figure V-5 except for the short cylindrical source located at position 24 within the uniform phantom.

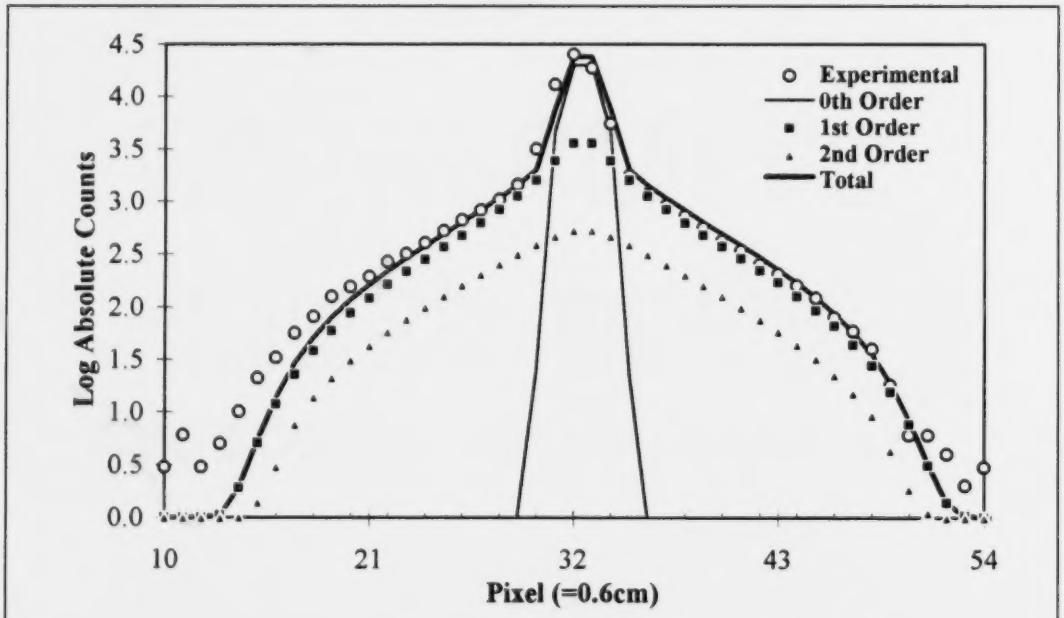

Figure V-29: Same as Figure V-5 except for the short cylindrical source located at position 25 within the uniform phantom.

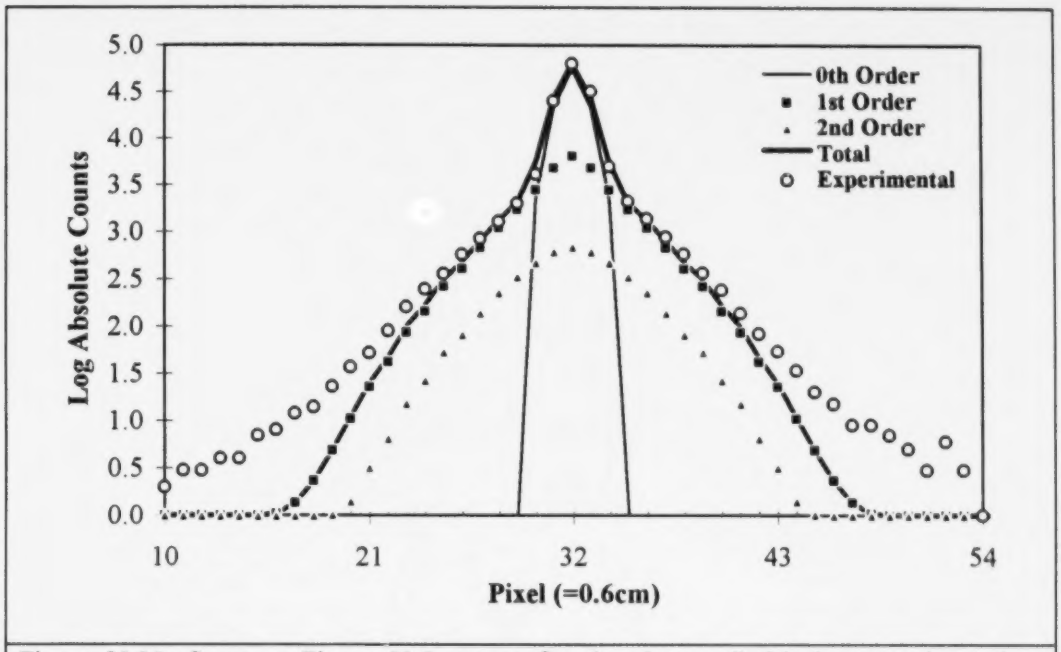

Figure V-30: Same as Figure V-5 except for the short cylindrical source located at position 26 within the nonuniform phantom.

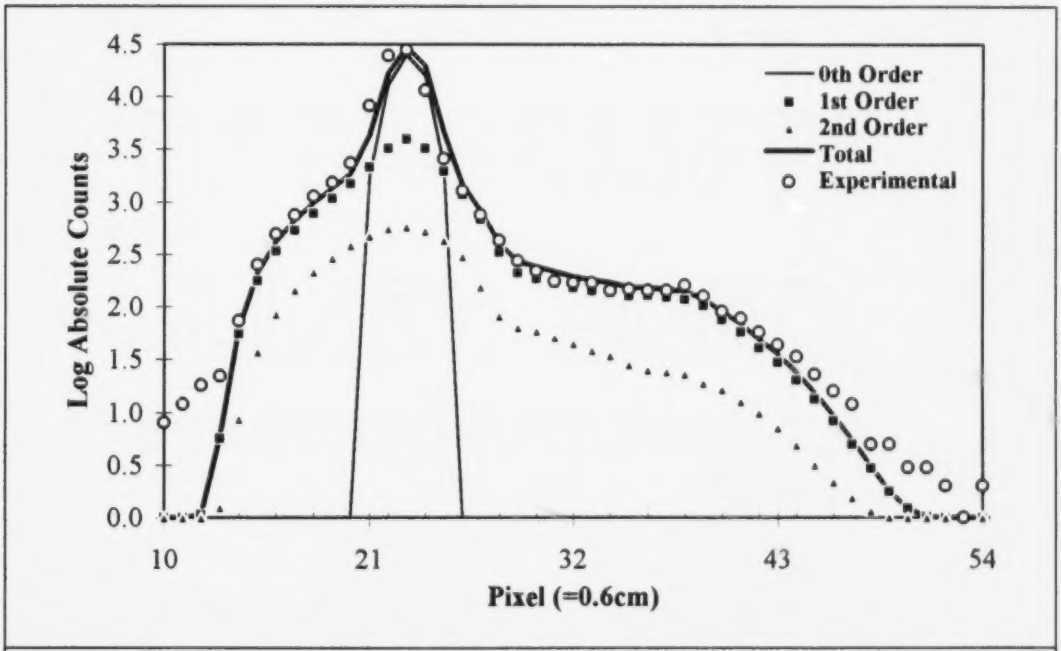

Figure V-31: Same as Figure V-5 except for the short cylindrical source located at position 27 within the nonuniform phantom.

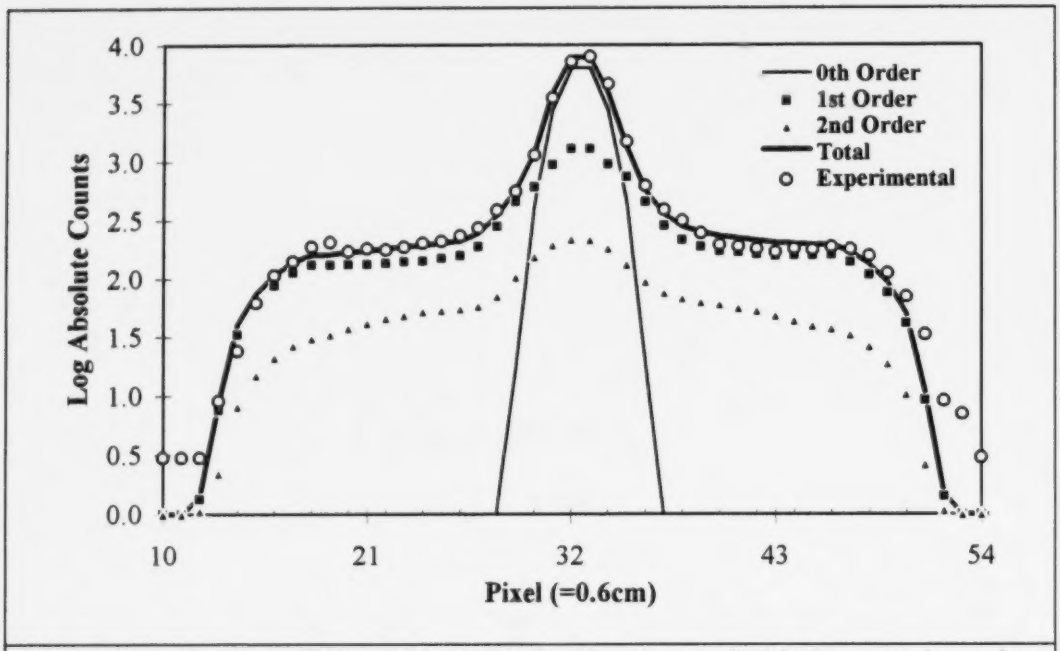

Figure V-32: Same as Figure V-5 except for the short cylindrical source located at position 28 within the nonuniform phantom.

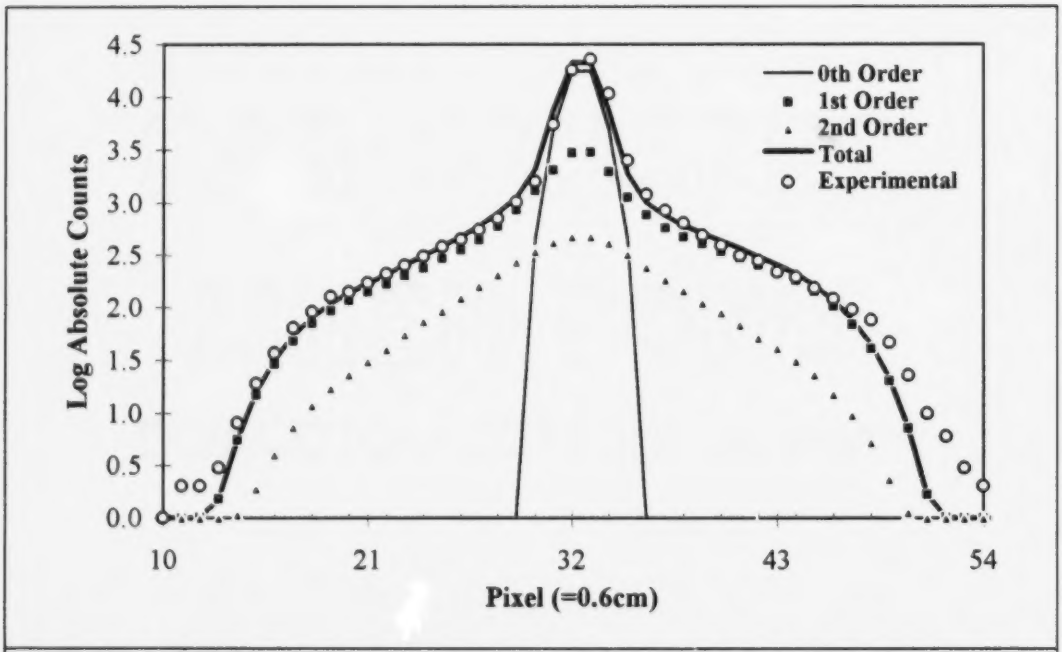

Figure V-33: Same as Figure V-5 except for the short cylindrical source located at position 29 within the nonuniform phantom.

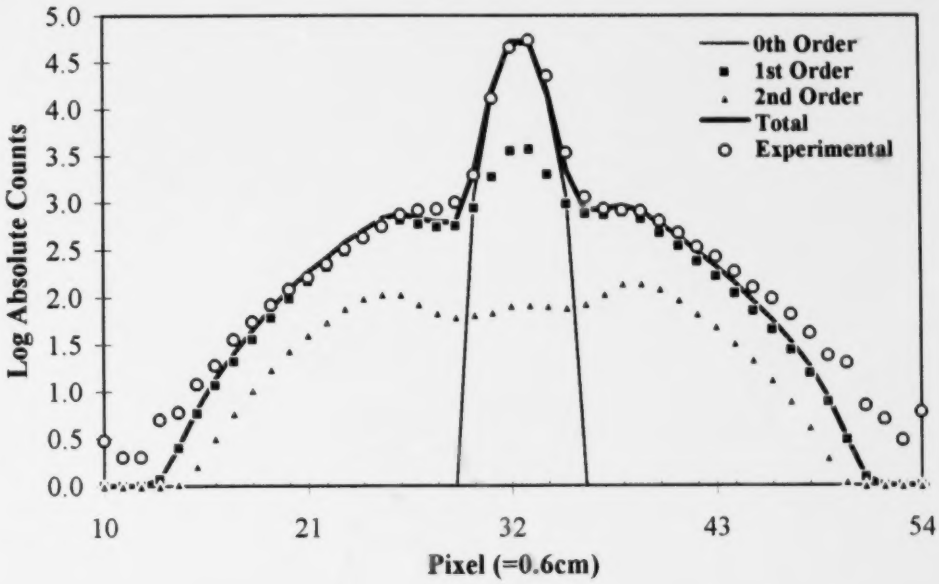

Figure V-34: Same as Figure V-5 except for the short cylindrical source located at position 30 within the nonuniform phantom.

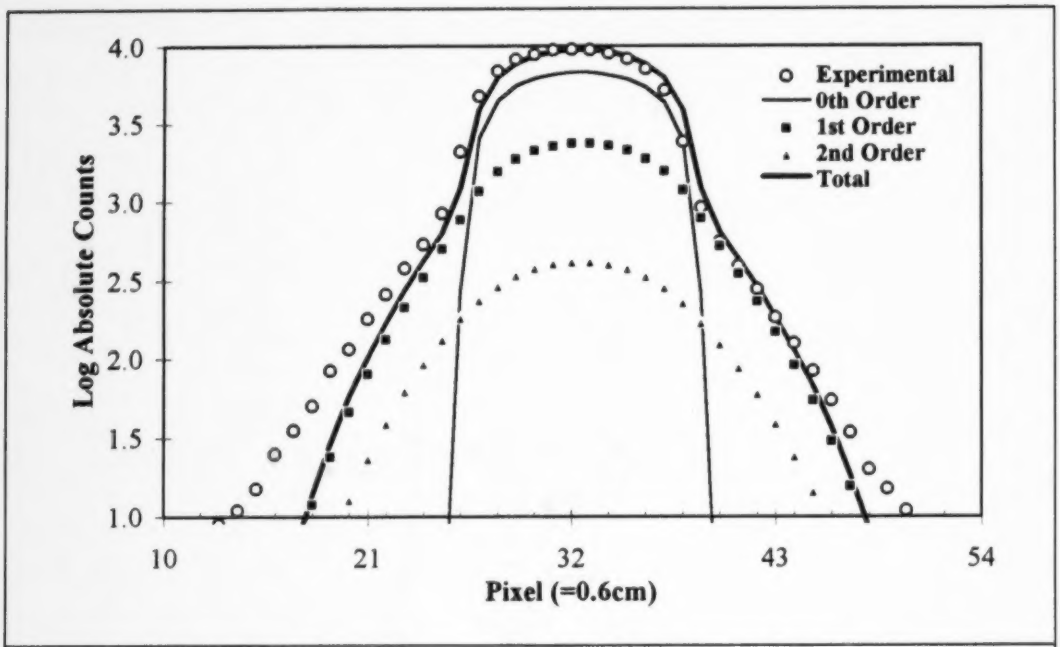

Figure V-35: Same as Figure V-5 except for the large cylindrical source located at position 31 within the uniform phantom.

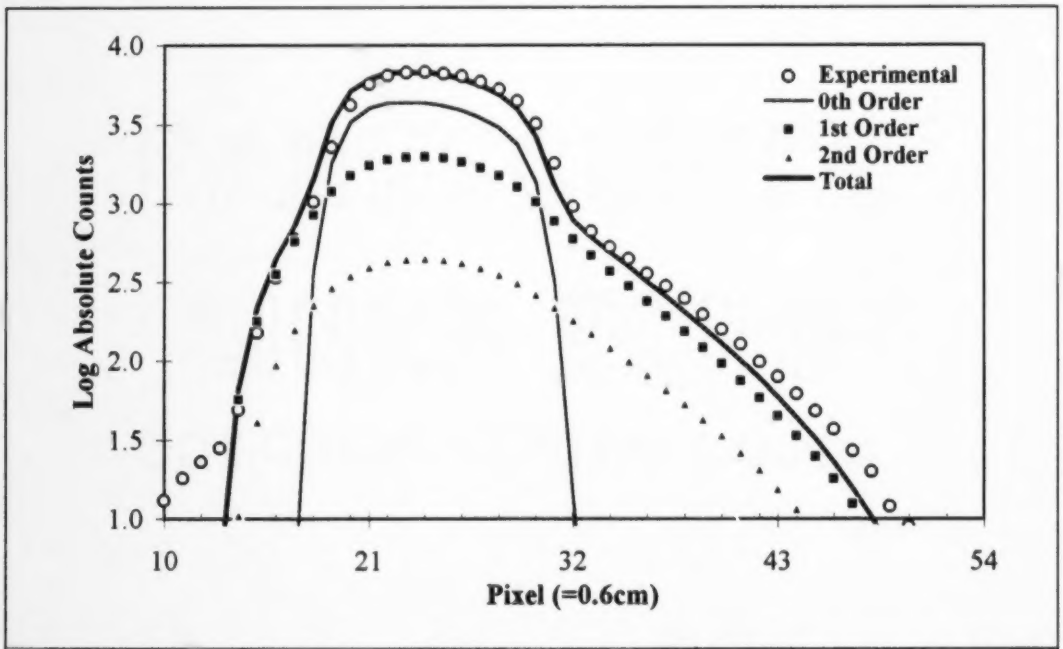

Figure V-36: Same as Figure V-5 except for the large cylindrical source located at position 32 within the uniform phantom.

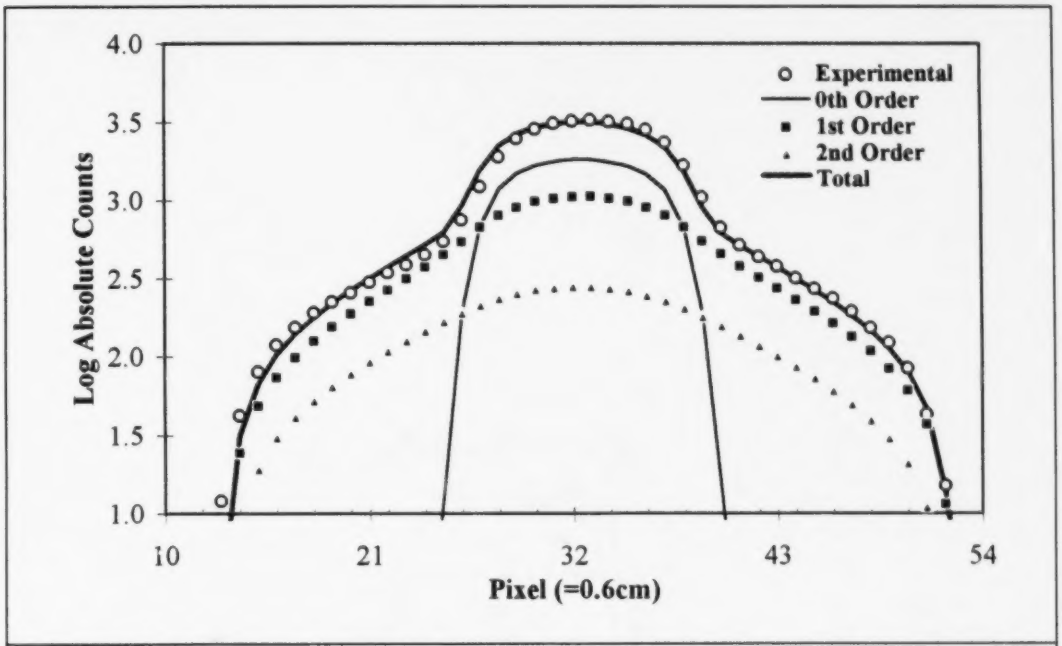

Figure V-37: Same as Figure V-5 except for the large cylindrical source located at position 33 within the uniform phantom.

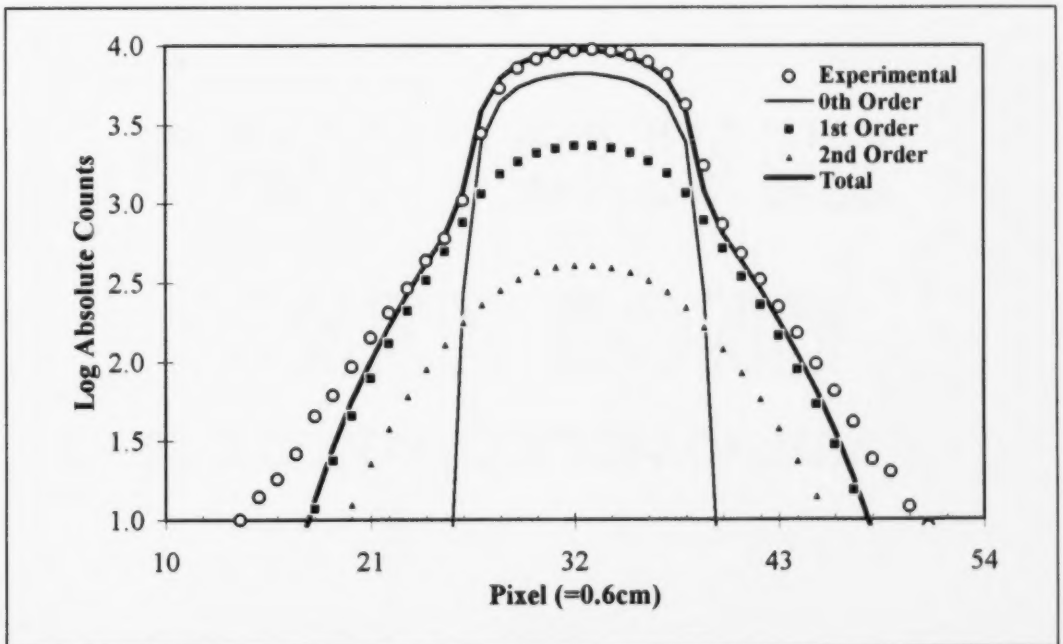

Figure V-38: Same as Figure V-5 except for the large cylindrical source located at position 34 within the nonuniform phantom.

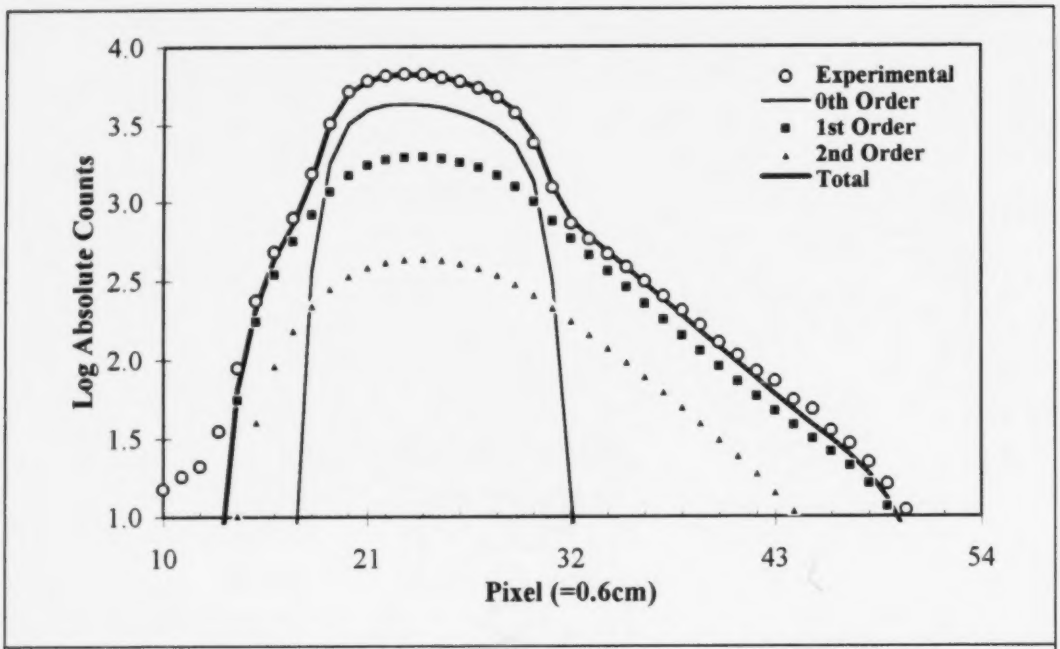

Figure V-39: Same as Figure V-5 except for the large cylindrical source located at position 35 within the nonuniform phantom.

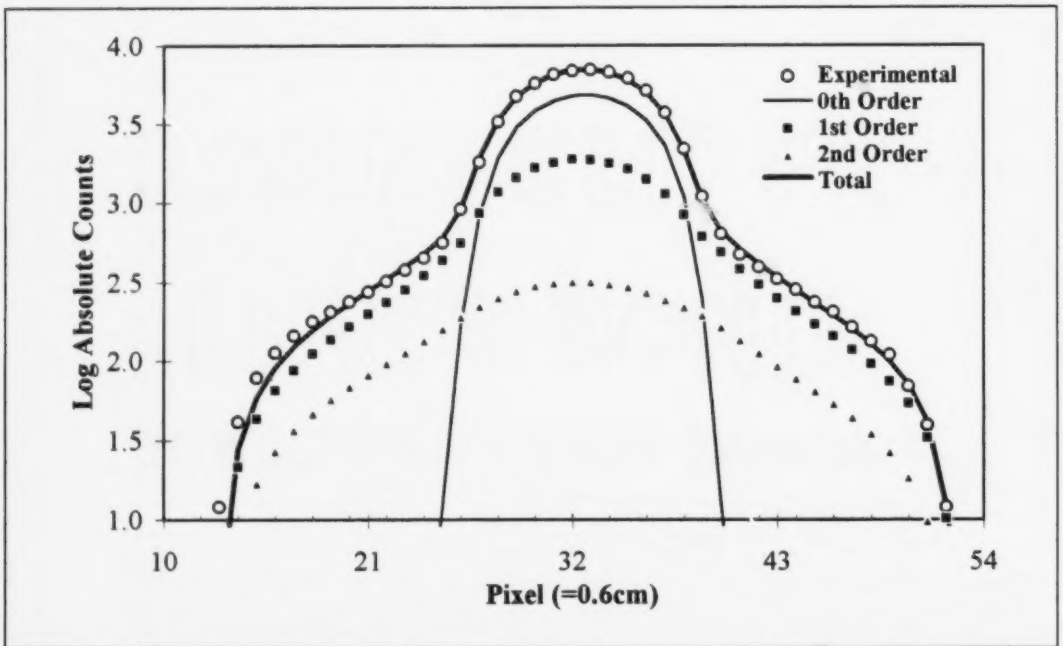

Figure V-40: Same as Figure V-5 except for the large cylindrical source located at position 36 within the nonuniform phantom.

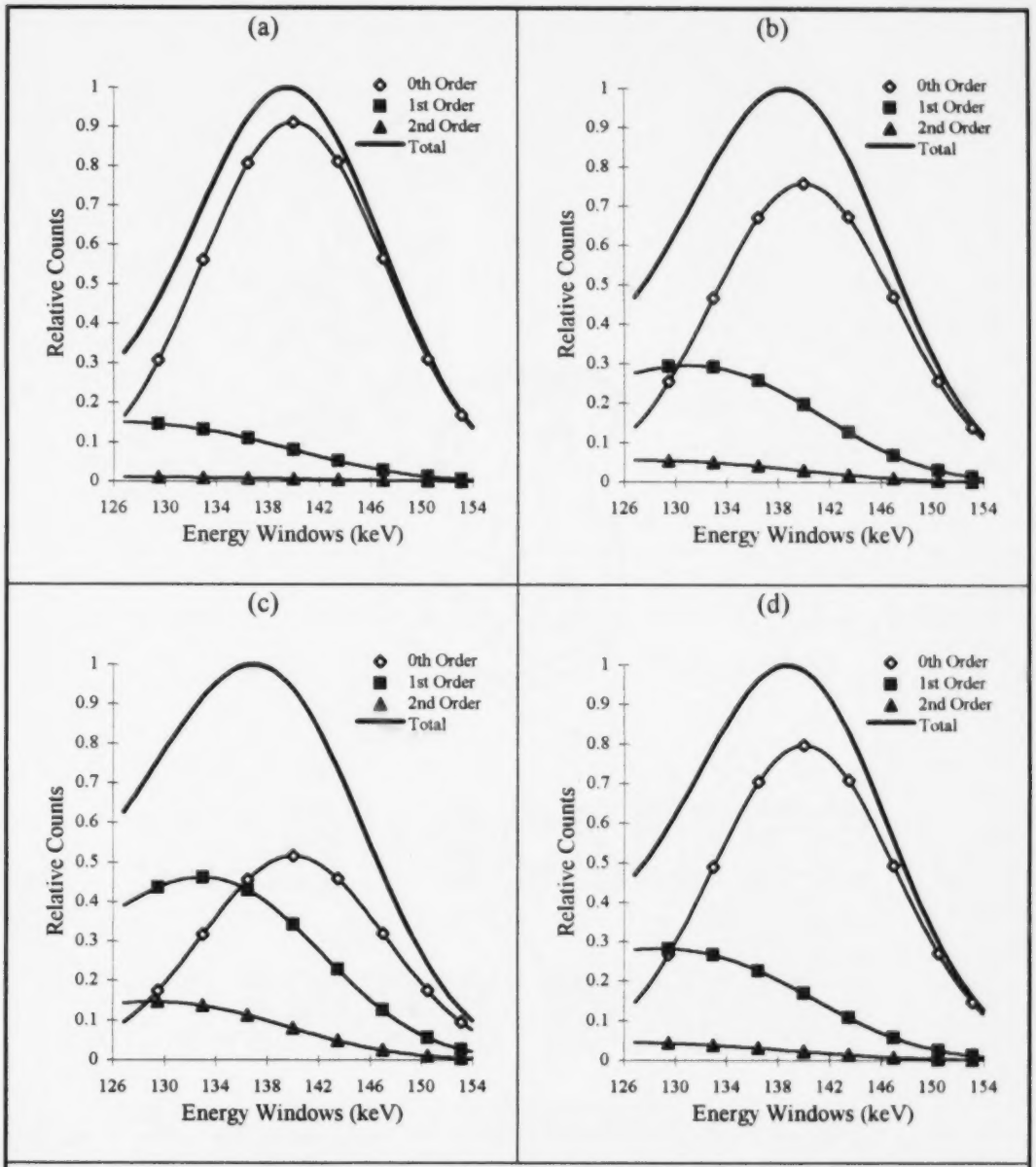

Figure V-41: Energy spectra for the point source located within the uniform phantom for (a) position 1, (b) position 2, (c) position 3, and (d) position 4.

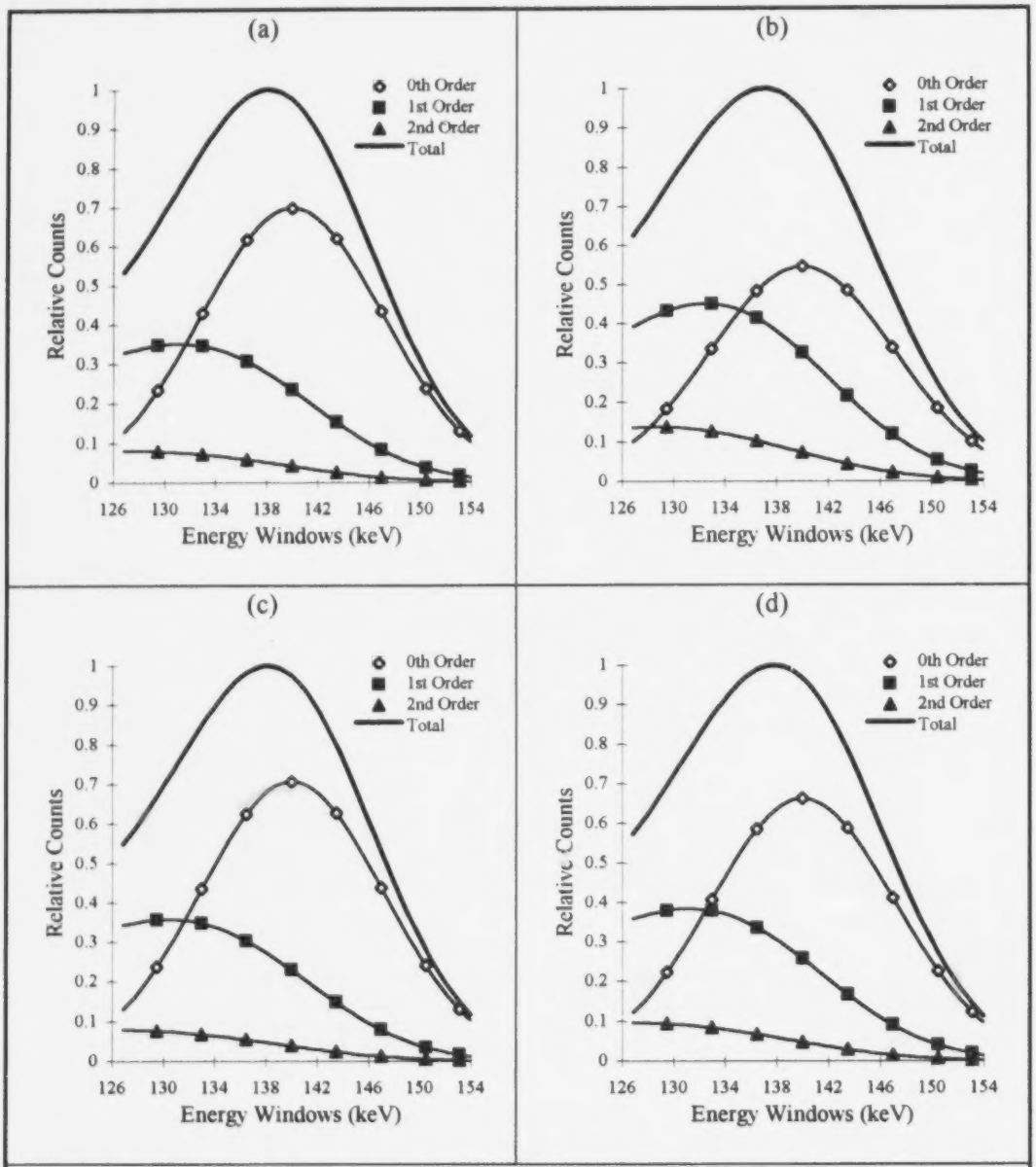

Figure V-42: Same as Figure V-41 except for (a) position 5, (b) position 6, (c) position 7, and (d) position 8.

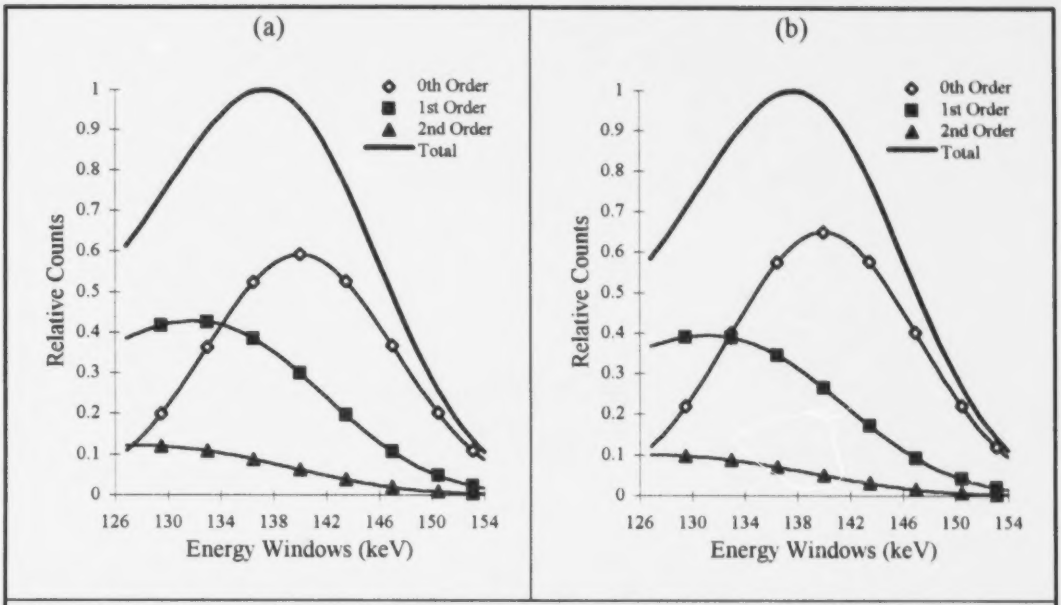

Figure V-43: Same as Figure V-41 except for (a) position 9 and (b) position 10.

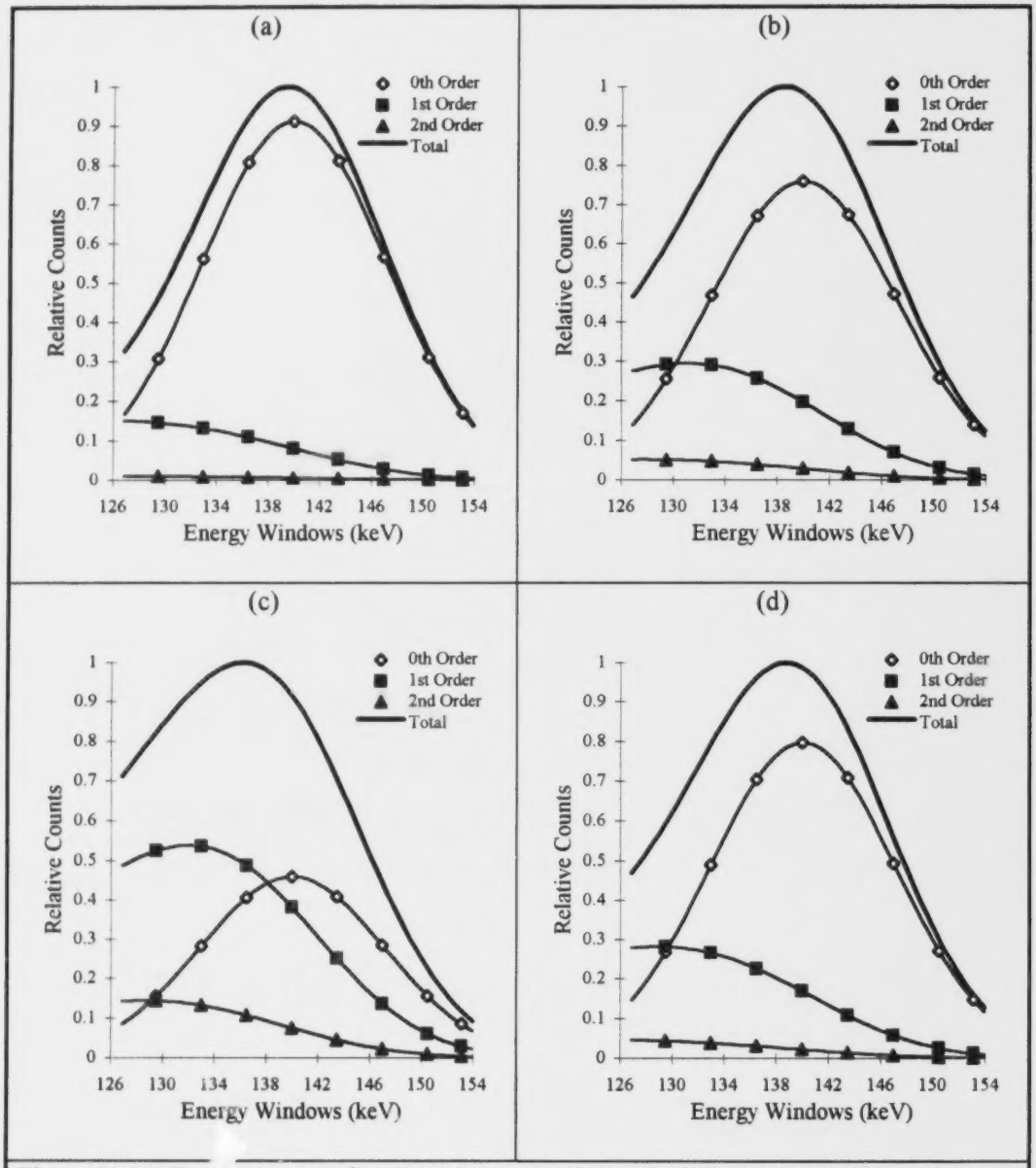

Figure V-44: Energy spectra for the point source located within the nonuniform phantom for (a) position 11, (b) position 12, (c) position 13, and (d) position 14.

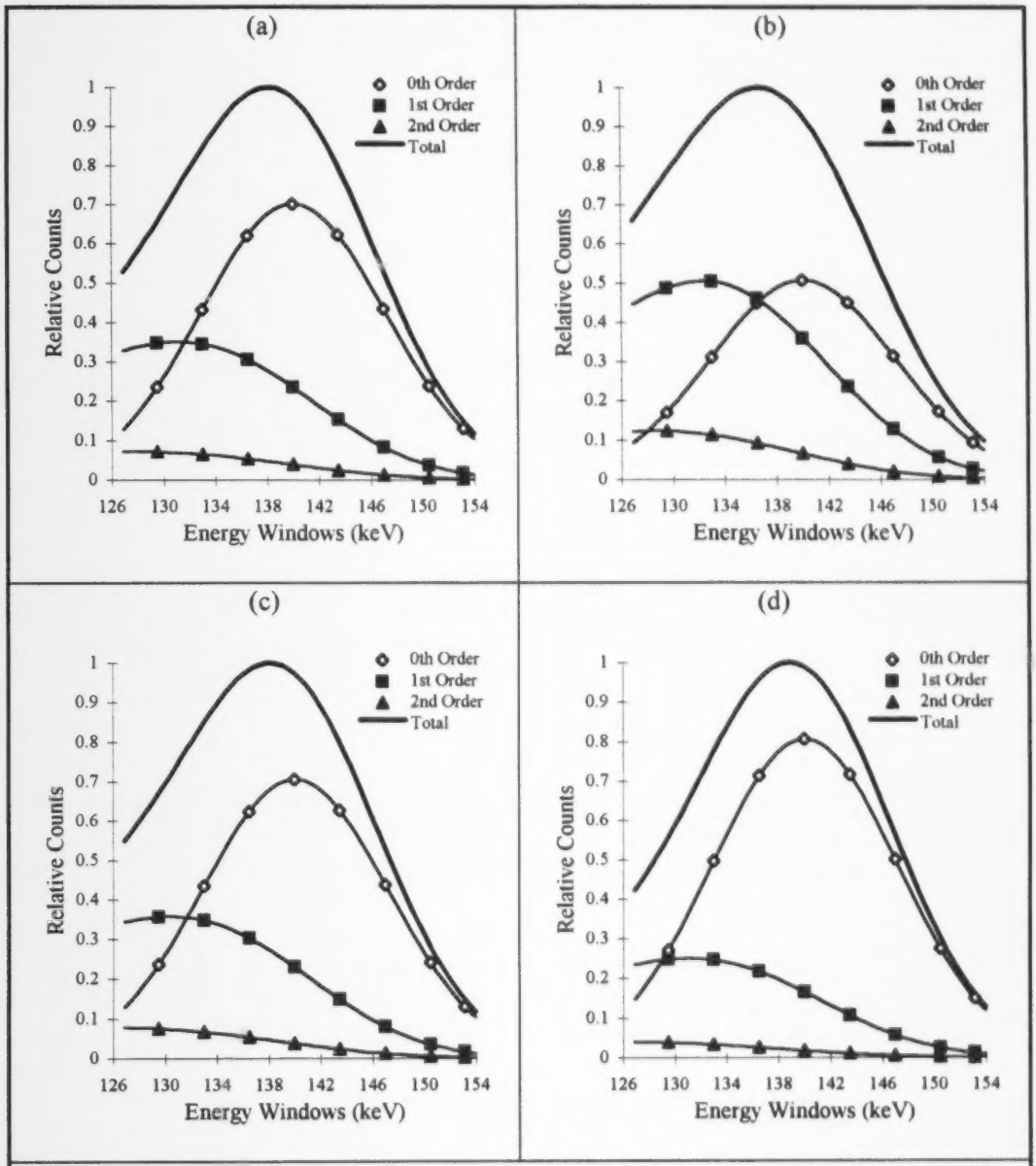

Figure V-45: Same as Figure V-44 except for (a) position 15, (b) position 16, (c) position 17, and (d) position 18.

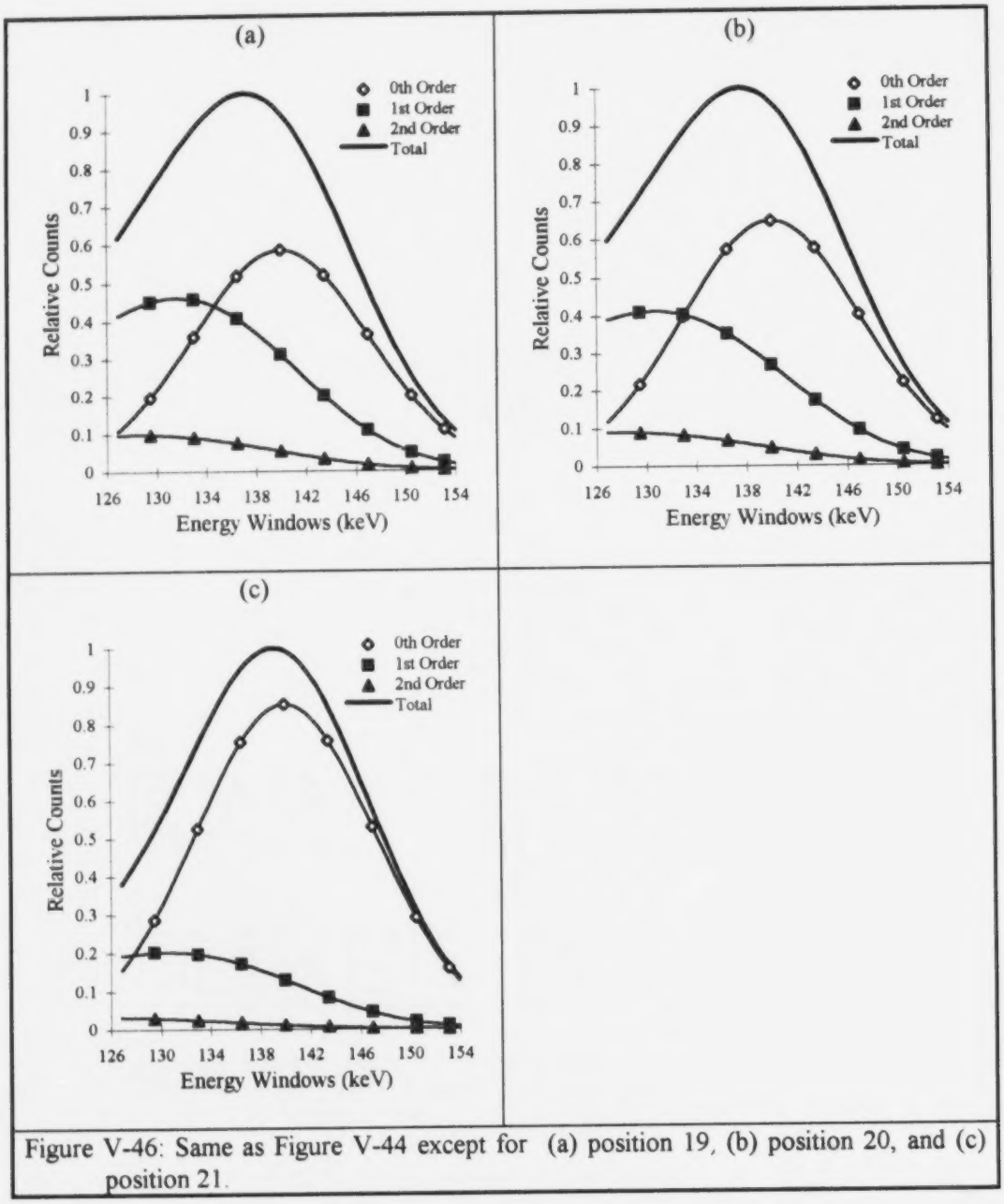

Figure V-46: Same as Figure V-44 except for (a) position 19, (b) position 20, and (c) position 21.

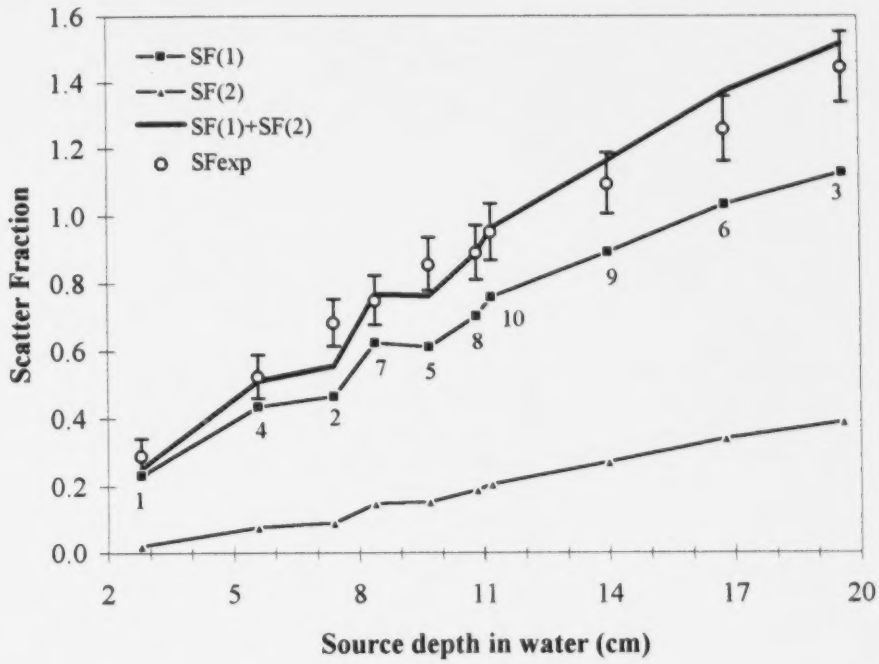

Figure V-47: Scatter fractions for the 10 point source positions within the uniform phantom as a function of the depth of the source in water (see Table V.1). Experimental results: open circles with vertical error bars corresponding to a +/- 3mm error in source placement. Calculated results: squares - 1st-order, triangles - 2nd-order, and solid line total scatter fraction.

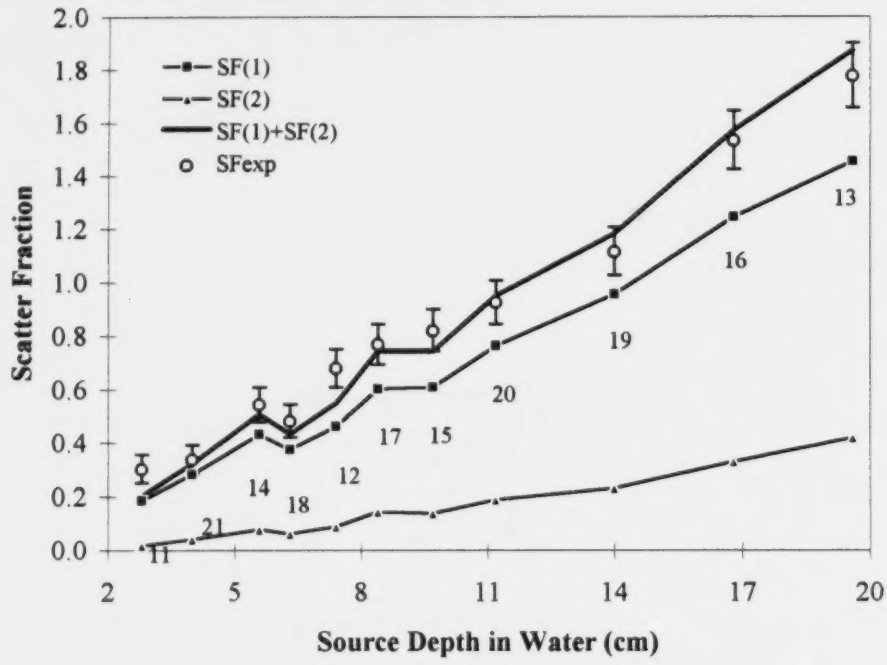

Figure V-48: Scatter fractions for the 11 point source positions within the nonuniform phantom as a function of the depth of the source in water (see Table V.1). Experimental results: open circles with vertical error bars corresponding to a +/- 3mm error in source placement. Calculated results: squares - 1st-order, triangles - 2nd-order, and solid line total scatter fraction.

VI. Investigation of Reconstruction Kernels

Having validated the numerical implementation of the theoretical expressions for the kernel, they are now used in this chapter to investigate the application of the theoretical reconstruction kernel within an MLEM-type reconstruction algorithm. First, the question of the size of the reconstruction kernel required is addressed by investigating the connectivity between a given source voxel and the projection pixels receiving counts from it. In the second part of this chapter, a complete reconstruction kernel is calculated and applied to a simple, but realistic, imaging situation.

A. Kernel Connectivity

In traditional filtered backprojection reconstruction algorithms the full 3D reconstruction problem is reduced to the reconstruction of a set of 2D source slices from projections recorded by the projection row in the same transaxial plane. Basically, only the information recorded by projection pixels *geometrically connected* (c.f. Figs. I-2 through I-4 and II-13) to source voxels is used. The assumption justifying such simplification is that photons emitted from a given source voxel contribute significantly only to the signal recorded by the pixels geometrically connected to it, assuming ideal collimation. A slice-by-slice reconstruction is used because it is the most convenient approach for the camera rotated around the medium. The main advantage of such an approach is its simplicity, as was discussed in Chapter 2. The geometrically connected kernel would be a good approximation only if scattered photons could be ignored (or rejected by whatever means) and if the 3D collimator depth-dependent resolution could also be ignored.

Geometrical connectivity is, of course, the simplest approximation possible and currently, some iterative reconstruction algorithms attempt to do better by truncating the connectivity between the source voxels and the projection pixels on the basis of a 3D collimator depth-dependent resolution. Therefore, in the kernel matrix $K_{i,j}$, a given source voxel j is linked not only to its geometrically connected pixel i (as in the geometrically connected kernel) but also to the pixels in the neighborhood of the latter, as

required by the collimator depth-dependent resolution (c.f. Fig. II-4). This would be a good approximation only if scattered photons were not detected. In the language of our theory, the kernel resulting from this procedure is just the lowest (0^{th}) order kernel given in Eq. (III.21), which accounts for contributions due to the primary photons only. In fact, this term in our theory also accounts for a non-uniform attenuation of the primary photons. A kernel which accounts for scattered photons requires greater connectivity, and theoretical expressions obtained in Chapter III allow us to investigate this connectivity quantitatively.

Methods

The connectivity of the kernel may be established by considering a point-like (i.e. single voxel) source at various positions of interest within the phantom and identifying those pixels for which the recorded signal is larger than some predetermined value. In this work we investigate the connectivity of point sources placed within the central transaxial plane of the phantom, for which we have presented the experimental data in the preceding chapter. The connectivity of the kernel's matrix elements linked to the source voxel is investigated by calculating the *neighborhood cumulative fraction*. The quantity is defined as the ratio of the signal due to a given scattering order recorded within the N-pixel $\times$ N-pixel neighborhood around the pixel geometrically connected to the source voxel to the cumulative signal due to the same order recorded by the entire camera plane

$$NCF^{(n)}(N) = \frac{\sum_{i=i'}^{N\times N} P_i^{(n)}}{\sum_{i} P_i^{(n)}}. \qquad \text{(VI.1)}$$

In Eq. (VI.1) i' denotes the pixel geometrically connected to the point source, the sum in the numerator is over the $N \times N$ neighborhood centered on the pixel i' where N must be odd, and the sum in the denominator is over all pixels of the projection plane. Experimentally, it is generally only possible to measure the total neighborhood cumulative fraction from acquired projection data. It is given by

$$NCF^{(\exp)}(N) = \frac{\sum_{i=1}^{N\times N} P_i^{(\exp)}}{\sum_i P_i^{(\exp)}} \qquad \text{(VI.2)}$$

The corresponding total theoretical fraction is defined similarly using

$$P_i = \sum_k P_i^{(k)}, \qquad \text{(VI.3)}$$

where the sum is over all scattering orders accounted for in the theory. Note that $NCF(N) \neq \sum_k NCF^{(k)}(N)$. For these calculations a pixel size of $(0.6\,\text{cm})^2$ was used (i.e. 64×64 pixel projections).

Results and Discussion

In Figs. VI-1 through VI-6 the neighborhood cumulative fractions are plotted as a function of the $N \times N$ pixel neighborhood of a pixel geometrically connected to the point (i.e. single voxel) source placed in the central slice of the medium at positions (1 through 21 in Table V-1) for which experimental data were collected and discussed in the preceding chapter. For each N, the signal due to a given scattering order recorded in $N \times N$ pixels centered about the geometrically connected pixel is summed, and divided by the total signal due to the same order recorded by all 64×64 pixels in the camera plane, as required by Eqs. (VI.1) and (VI.2).

One can introduce a measure of the *connectivity extent* of the kernel to be the minimum neighborhood size N for which the neighborhood cumulative fraction approaches 1 within a predetermined tolerance. The results in Figs. VI-1 through VI-6 demonstrate that $N \cong 3$ (or, at most 5) would be a sufficient connectivity in the majority of cases if only the primary photons were to be taken into account. This is the connectivity extent for the kernel based solely on 3D depth-dependent collimator hole resolution. However, long scatter tails are present in a kernel due to Compton scattering. Naturally, for practical applications the connectivity extent of the kernel must be truncated, but such a truncation cannot be solely based on the depth-dependent resolution. Rather, the scatter tails seen in Figs. VI-1 through VI-6 must be the main factor determining it. Our results

demonstrate that, in most cases, at least an $N = 21\text{-}27$ connectivity extent might be required to account for about 90% of the kernel. Actually, the connectivity extent depends strongly upon the source depth and the detailed description of the medium. Considerations similar to the ones presented here should be a starting point in constructing a kernel which accounts for Compton scattering and which could be used in reliable iterative source reconstruction techniques.

Note that in Figs. VI-1 through VI-6, as the *NCF* goes from 50% to 100% of the total collected count, the agreement between the theory and experiment (i.e. between "Total" and "Experiment" data) deteriorates. The main reason for this is that it is impossible for photons to be detected by pixels outside the "geometrical shadow" the phantom casts onto the image plane of the camera. In experiments, however, some counts are recorded by pixels within this region of the camera plane due to background noise and collimator scattering and/or penetration. Considering that neither of these processes is accounted for in the calculations, the agreement between the "total" and "Exp" data is good, and therefore these results provide further validation of the numerical code used for the calculations.

We close this section with a remark which has motivated us throughout the course of this work. Compton scattering is often treated as an unavoidable yet annoying process that *degrades* an image, and attempts are generally made to remove it using, for example, subtraction or filtering techniques. The scatter information can be useful, however, if its contribution to the image formation can be quantitatively understood and accurately modeled within the reconstruction kernel. Since projection images are often count-poor and noisy, the scatter information should not be rejected or ignored, but rather used to augment the information provided by the unscattered photons.

B. Application of Theoretical Kernel to Reconstructions

Before concluding, some very recent reconstruction results are presented which were obtained from the MLEM reconstruction algorithm using a kernel calculated from the

integral expressions Eqs. (III.21) through (III.23). The reconstruction algorithm was developed and implemented by Dr. David Gilland of Duke University Medical Center. A complete reconstruction kernel was calculated using the numerical code developed and discussed in this work.

The experimental imaging situation involved a uniform water filled cylindrical phantom with two spheres of volume 95 ml and 21.4 ml, respectively, with each sphere containing a uniform distribution of ^{99m}Tc. Both spheres were centered in the phantom with the central transaxial slice through the phantom also bisecting the spherical sources. Further, the larger sphere was centered on the axis of rotation, whereas the smaller sphere was located at about a distance of 3 cm from it. Sixty projections were taken using a Trionix Anger camera at regular angular intervals about the phantom. The camera operated with a high resolution collimator and a 15% symmetric energy window. The intrinsic energy resolution of the camera was assumed to be Gaussian with a FWHM equal to 14 keV (i.e. $10\%E_0$). The camera operated in the 64×64 collection matrix mode which corresponds to an approximate pixel area of $(0.7\text{cm})^2$. The camera's radius of rotation was 13.2 cm.

Using the above parameters, a kernel for the imaging situation was calculated. The complete kernel was not calculated because that is beyond the present computer resources available. Instead, a more computationally feasible truncated kernel retaining the full 3D connectivity between the source voxels and projection pixels was calculated. Firstly, only the zeroth-order and first-order scattering contributions were calculated for this kernel because, as shown in the preceding chapter, the small role played by the second-order contributions does not justify the extensive computing effort needed to calculate them. The elements of the kernel for each calculated order were stored separately. Secondly, only the kernel elements for which the source voxel lies within the central transaxial plane were calculated. The kernel elements for source planes adjacent to the central plane were assumed to have the same kernel elements but translated along the axis of rotation. This assumption is justified since the edge effects of the phantom only become important for

planes close to the edges. Finally, due to the rotational symmetry about the central axis of the phantom, the kernel elements need only be calculated for one projection angle. The kernel elements for other projection angles can be obtained mathematically, by "rotating" the known values due to the symmetry of the problem.

For each source voxel lying in the central plane, kernel elements were calculated for a 44×44 pixel area centered on the projection plane. The geometrical shadow cast by the phantom onto the projection plane was totally enclosed by this 44×44 pixel area. Further, kernel elements were only calculated for the smallest square which completely enclosed the central slice of the phantom, which was 44×44 voxels. The total size of the kernel matrix was:

$$44 \times 44 \times 44 \times 44 = 3{,}748{,}096 \text{ kernel elements.}$$

In Figs. VI-7 and VI-8, the kernel elements for 4 sample source voxel positions within the central slice are displayed. The four sample source positions shown in Figs. VI-7 and VI-8 correspond to configurations 4, 5, 6, and 10 in Table V-1, respectively. The images displayed in Figs. VI-7 and VI-8 are equivalent to the projection contributions that would be observed for a unit point source at the specified locations for a projection area of 44×44 pixels centered on the central projection pixel. In fact, the projection data acquired experimentally for configurations 4, 5, 6 and 10 have excellent agreement with those shown in Figs. VI-7 and VI-8.

The experimentally acquired projection data were used to reconstruct the source distribution for 14 source slices centered on the spheres. First, the projection data was reconstructed using the MLEM algorithm of Gilland employing the above-described kernel. The projection data was reconstructed a second time using the traditional filtered backprojection (FBP) method of reconstruction employing only simple ramp filter for the same source slices. It must be stressed that no effort was used to optimize the reconstruction methods, and that the results obtained are raw reconstructed images. The reconstructed slices are shown for both reconstruction methods in Figs. VI-9 and VI-10, and a profile along the line shown in Figs. VI-9 and VI-10 is plotted in Fig. VI-11. The

MLEM images were obtained after 25 iterations of the algorithm and no stopping criteria was used. It is fairly obvious that the two methods provide similar results, except the MLEM images appear quite noisy. However, analysis of Fig. VI-11 shows that the MLEM method has provided better spatial resolution within the reconstructed plane than the FBP method, providing a little better separation between the two sources and better contrast. A detailed comparison between the two methods of reconstruction is not available at this time due to the computational effort required and more investigation is obviously required before any statements about the quantitative performance can be made.

When viewing Figs. VI-9 and VI-10, one must keep in mind that this is an extremely simple imaging situation and it should be expected that FBP should perform reasonably well. A more interesting comparison would be provided by investigating a non-uniform imaging situation in which it is known that the FBP method performs poorly. However such an imaging situation does not possess any symmetries or translational invariances like those in the present case, and therefore such an investigation would require computing resources beyond what is presently available.

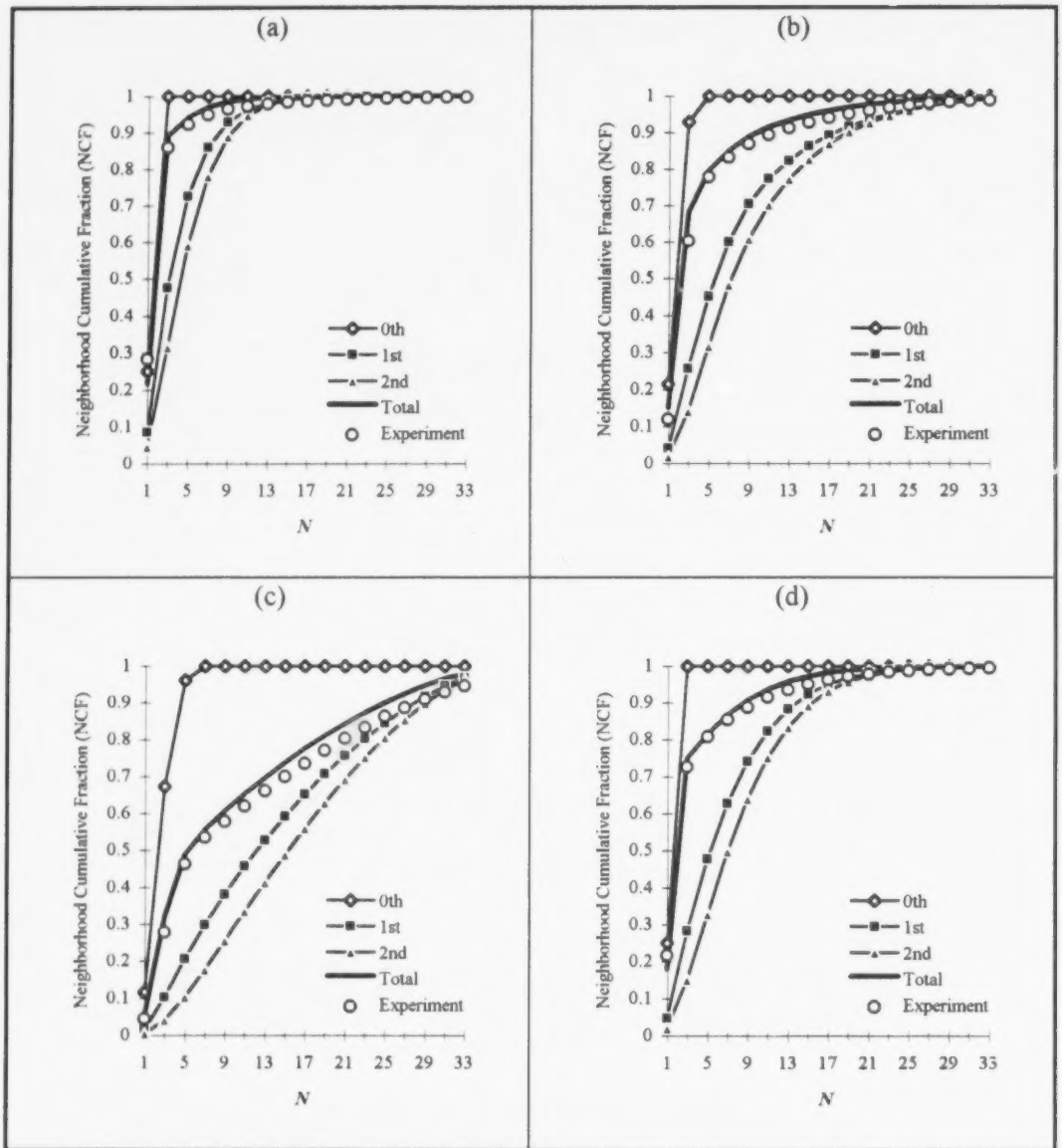

Figure VI-1: The neighborhood cumulative fraction for an N by N neighborhood centered at the pixel geometrically connected to the point source for each position within the uniform phantom for: (a) position 1, (b) position 2, (c) position 3, and (d) position 4 as given in Table V.1.

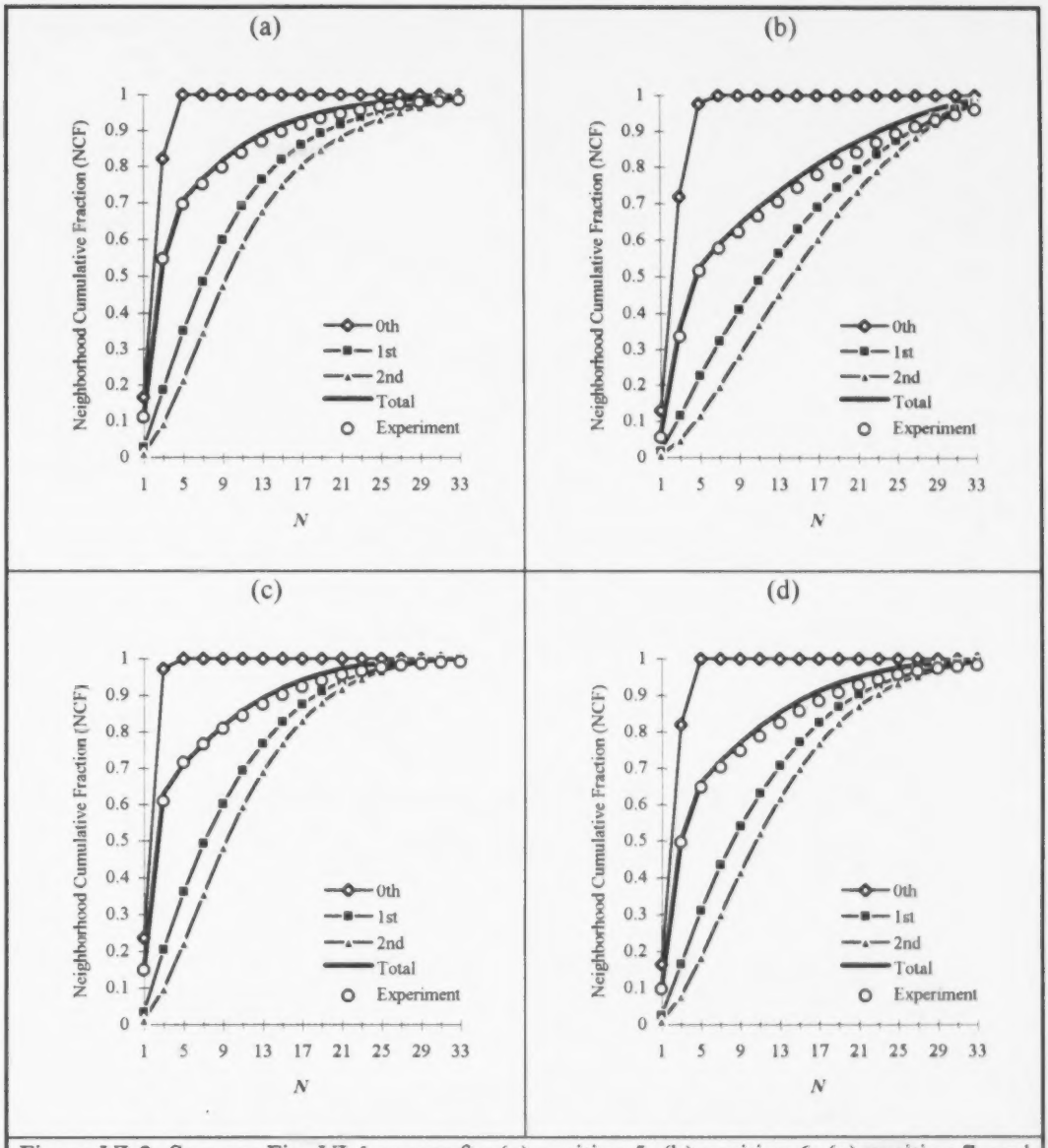

Figure VI-2: Same as Fig. VI-1 except for (a) position 5, (b) position 6, (c) position 7, and (d) position 8.

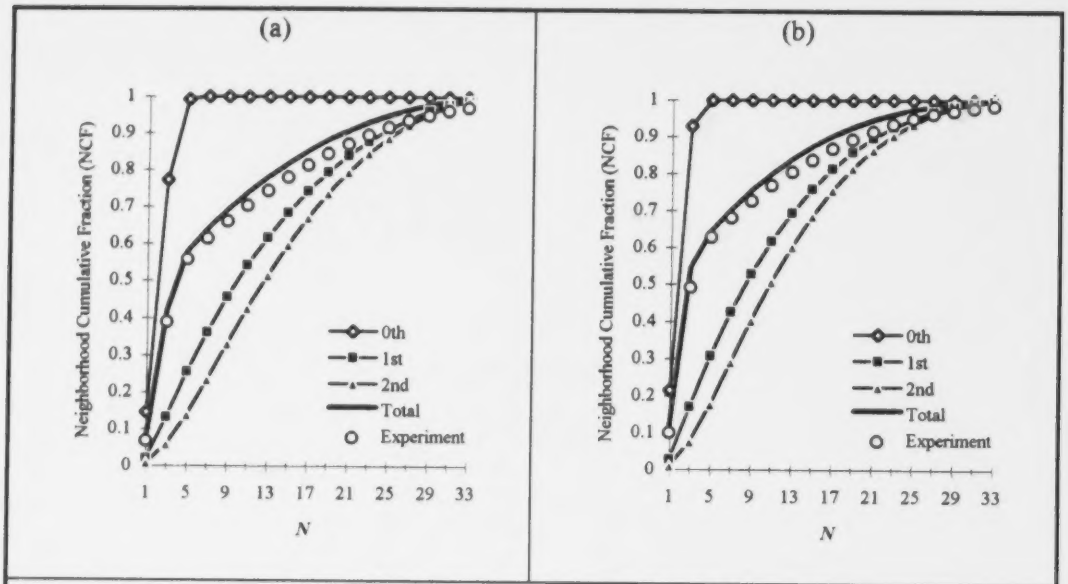

Figure VI-3: Same as Fig. VI-1 except for (a) position 9 and (b) position 10.

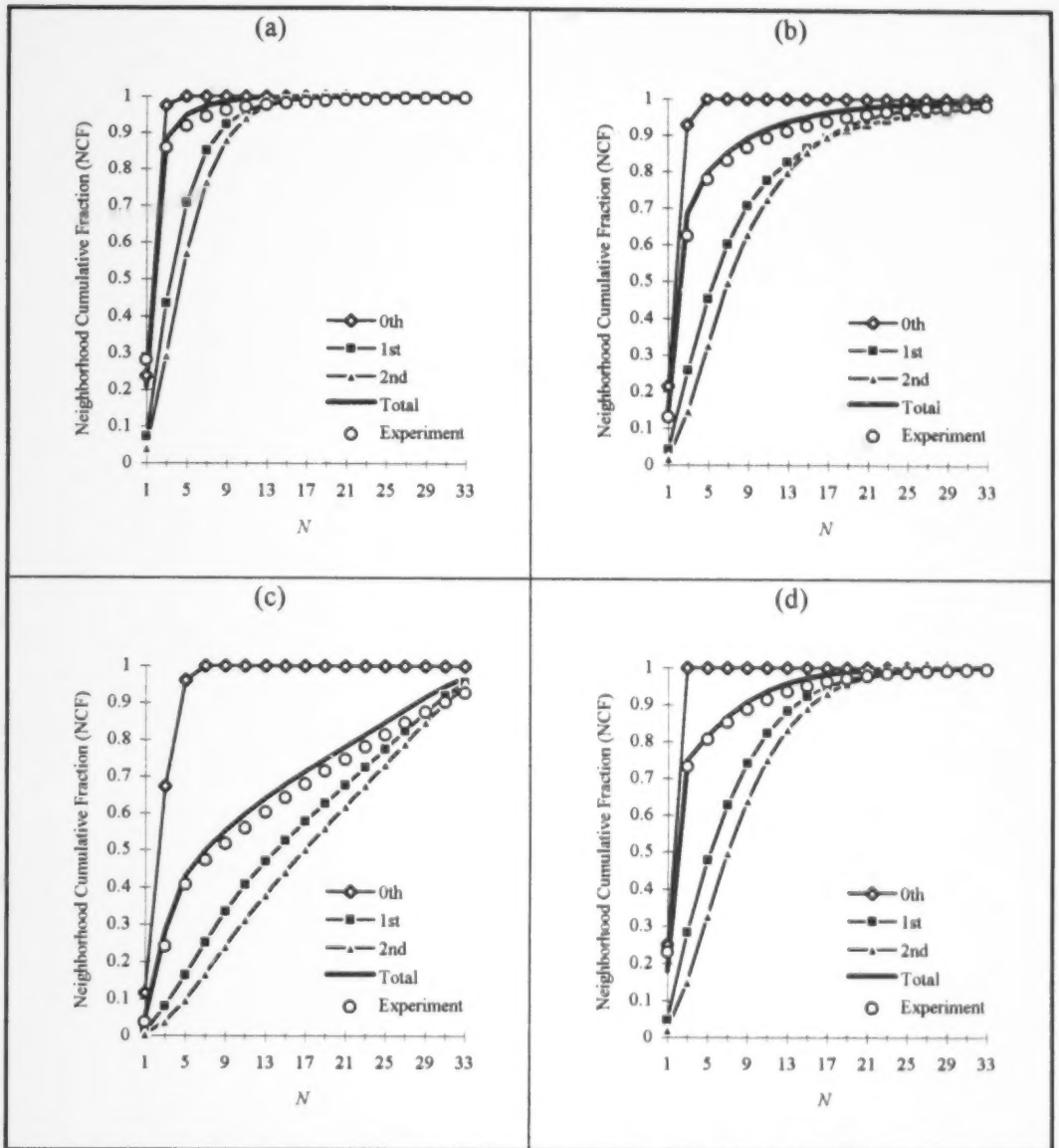

Figure VI-4: The neighborhood cumulative fraction for an N by N neighborhood centered at the pixel geometrically connected to the point source for each position within the nonuniform phantom for: (a) position 11, (b) position 12, (c) position 13, and (d) position 14 as given in Table V-1.

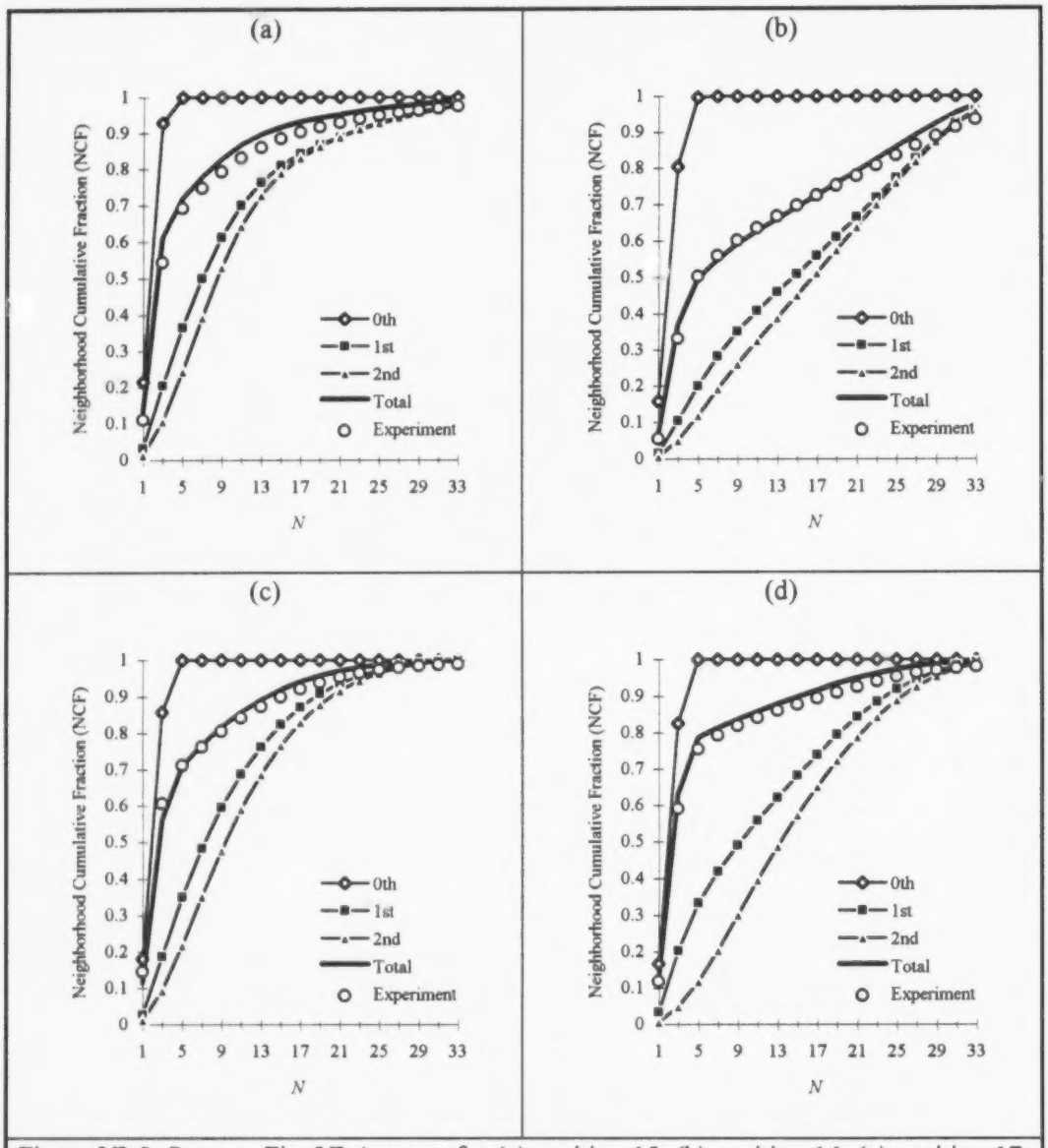

Figure VI-5: Same as Fig. VI-4 except for (a) position 15, (b) position 16, (c) position 17, and (d) position 18.

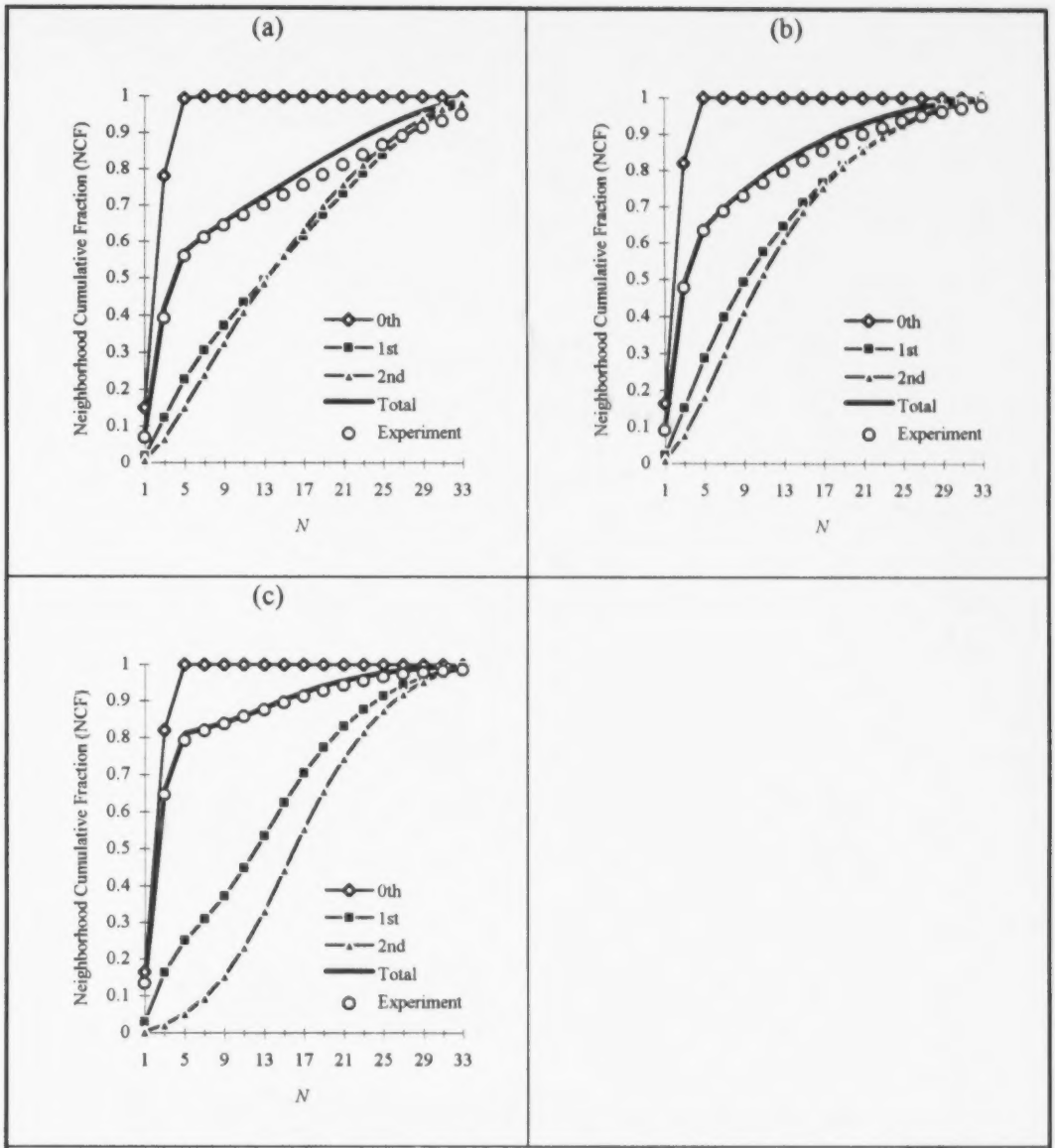

Figure VI-6: Same as Fig. VI-4 except for (a) position 19, (b) position 20, and (c) position 21.

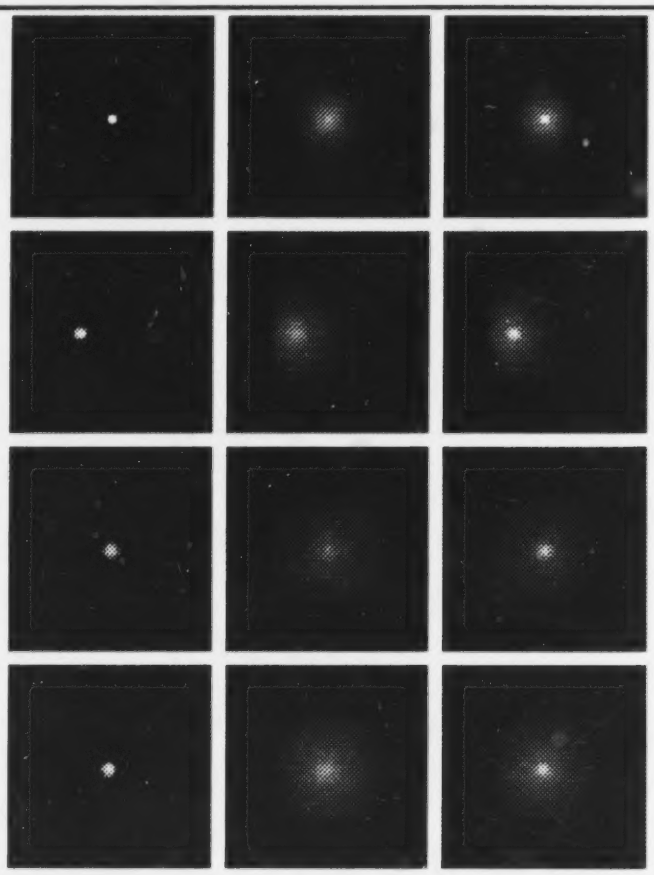

Figure VI-7: Plot of the kernel matrix elements for one projection angle for a point source located as given in Table V-1 for (1st row) position 4, (2nd row) position 5, (3rd row) position 6, and (4th row) position 10. The images in each column correspond to the 0th-, 1st-, and 0th+1st-order kernel elements from left to right for each source position.

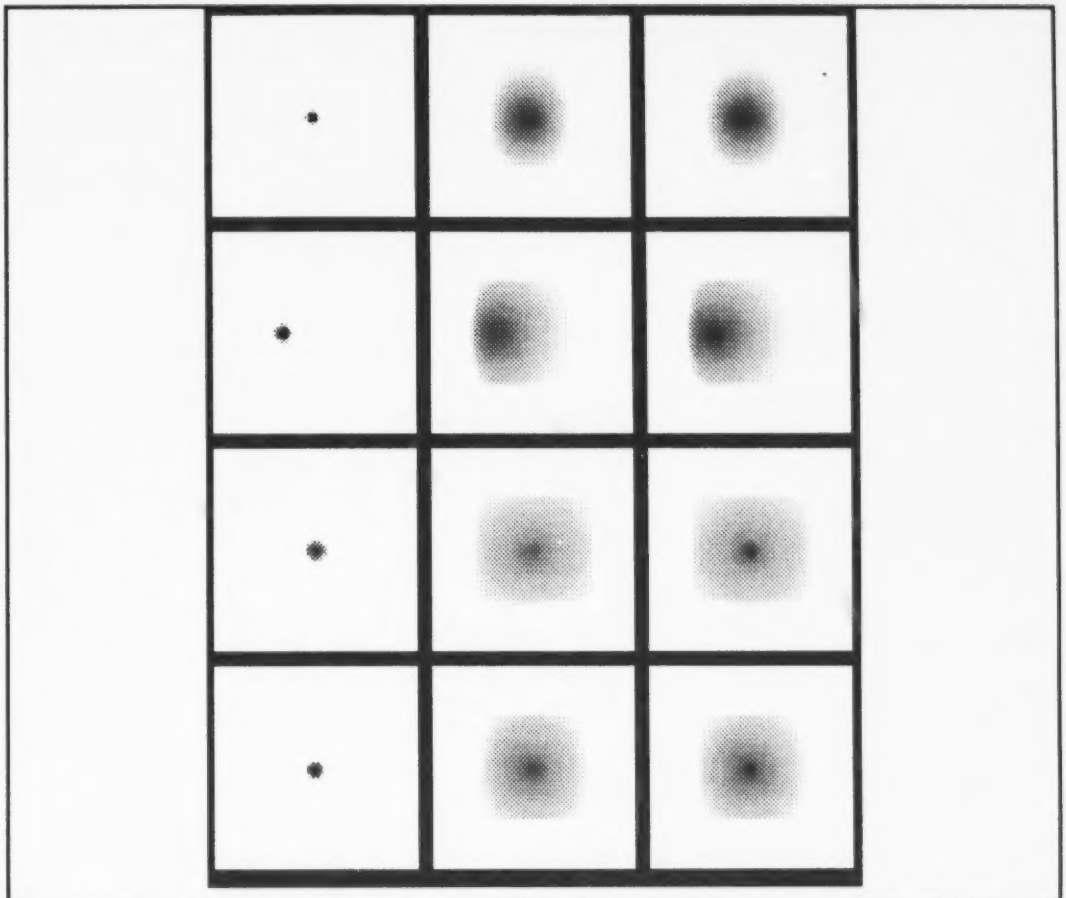

Figure VI-8: Same as Fig. VI-7 except inverted gray scale.

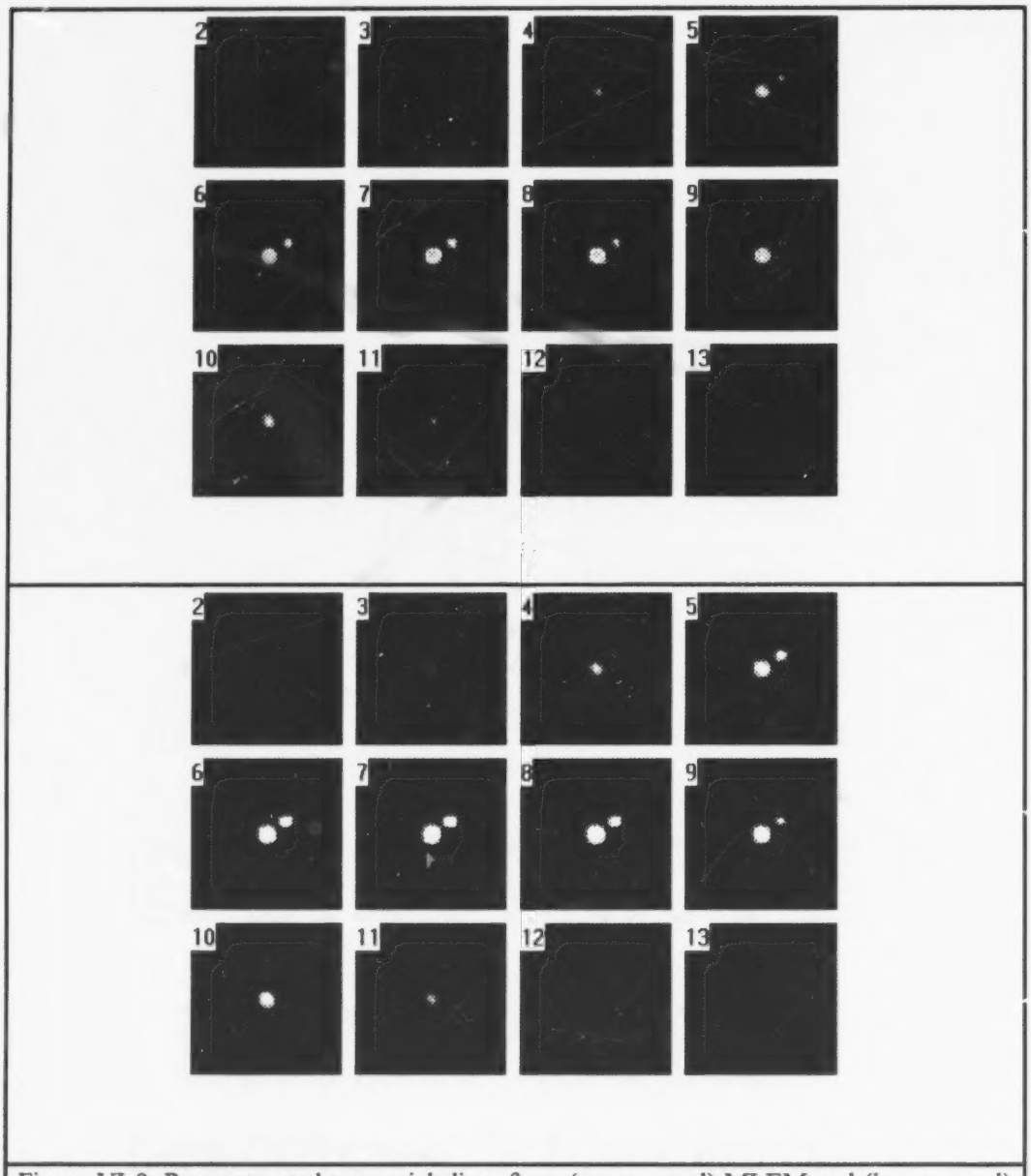

Figure VI-9: Reconstructed transaxial slices from (upper panel) MLEM and (lower panel) filtered backprojection. A profile line has been superimposed on image 7, which is plotted in Fig. VI-11.

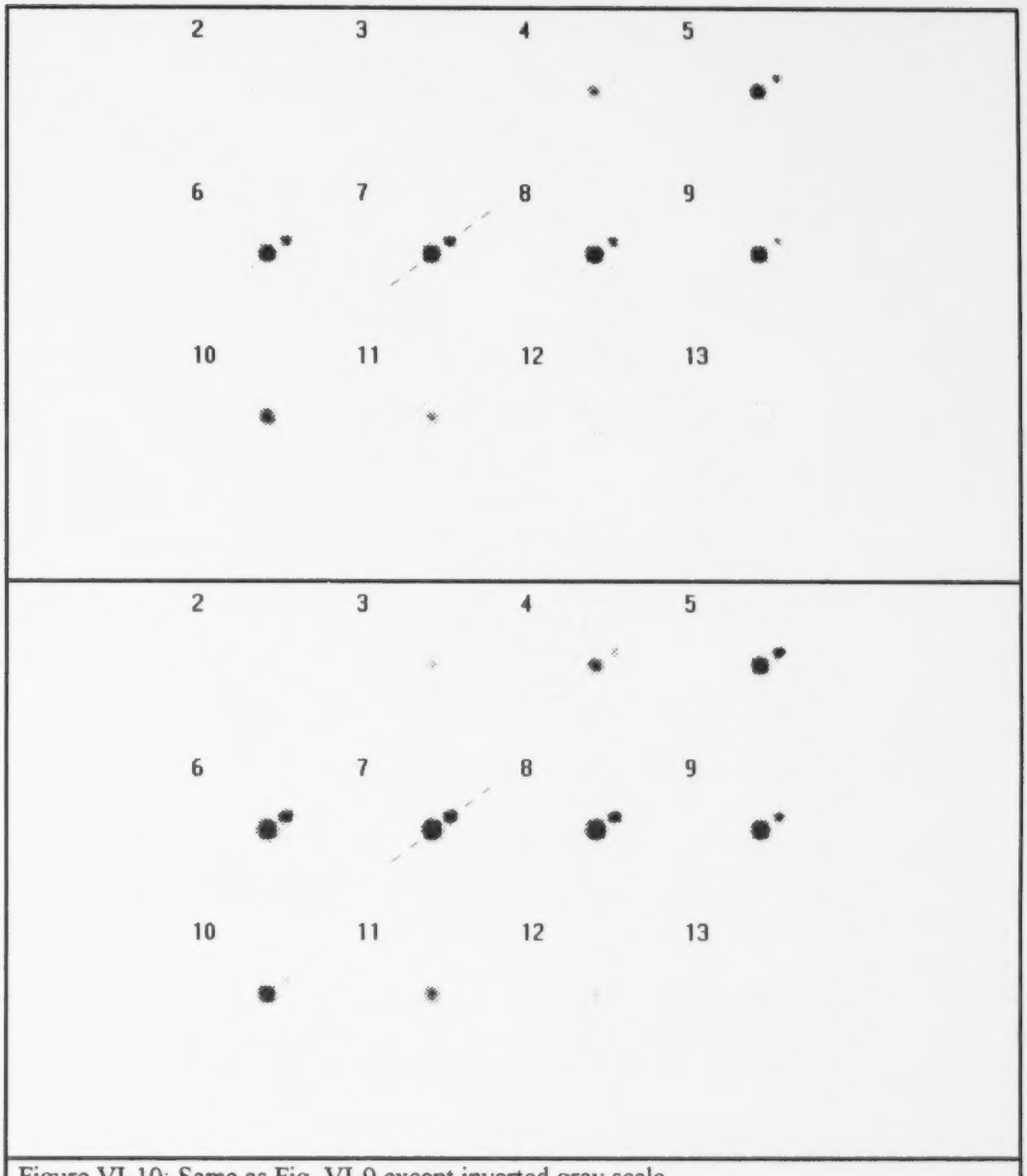

Figure VI-10: Same as Fig. VI-9 except inverted gray scale.

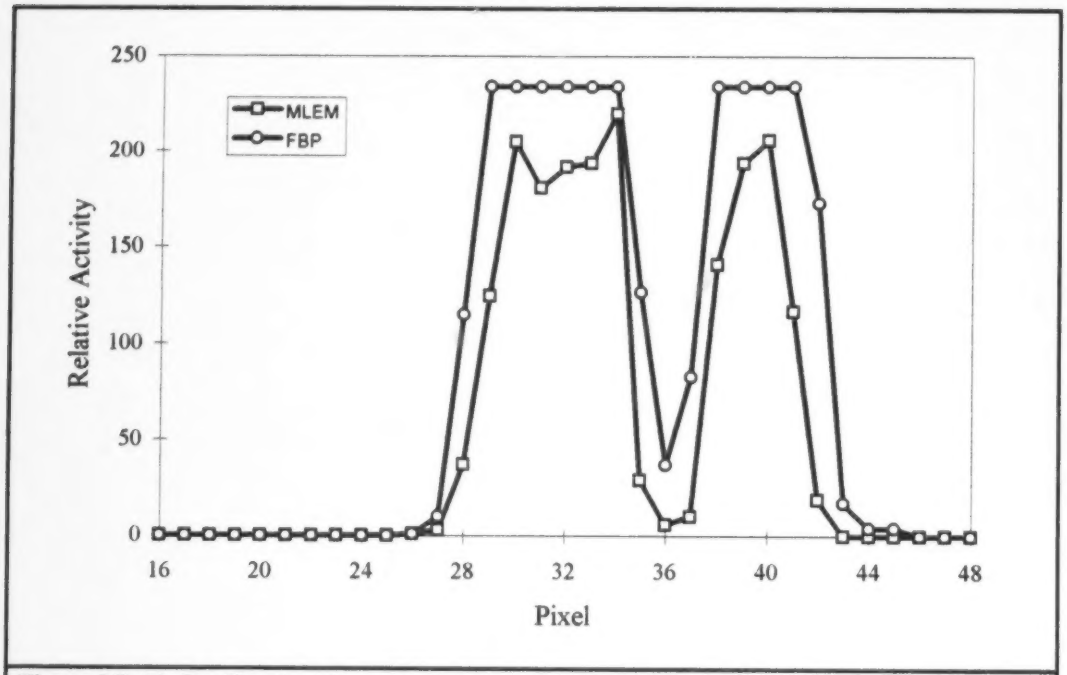

Figure VI-11: Profile plot along the line shown in Figs. VI-9 and VI-10.

VII. Conclusions

In this thesis an analytical theory describing photon propagation and detection for SPECT has been presented. The theory accurately and analytically accounts for most of the physical processes involved with photon propagation and detection for SPECT, and in particular, nonuniform attenuation (including photoelectric absorption and all orders of Compton and Rayleigh scattering combinations and possibilities), the three dimensional depth-dependent collimator resolution, and the intrinsic energy-dependent detection probability function of the Anger camera (i.e. intrinsic energy-dependent detection efficiency and the intrinsic energy resolution of a NaI(Tl) scintillation crystal). The theory presented is applicable to all photon emission problems involving energies below the pair production threshold, and further, is applicable to all collimator types used in clinical nuclear medicine. As such it provides a fundamental framework for solving photon emission imaging problems. Finally, the theory developed provides a better, more intuitive understanding of the complex image formation process in SPECT.

The theory allows well-defined closed-form integral expressions for each scattering order of the photon detection kernel to be formulated separately. From a physics perspective, the photon detection kernel provides a complete physical description of the imaging problem and can be used to exploit the full potential of iterative reconstruction techniques such as the MLEM algorithm.

Numerical integration code was developed to calculate the lowest three orders of the kernel for general nonuniform imaging situations. The code developed is most suitable for calculating kernels for narrow energy window imaging situations in which the energy window parameters lie in the energy range 100 keV - 200 keV. This is because the numerical integration code developed implements a simplified version of the theory presented in Chapter 3. Firstly, collimator scatter and penetration have been ignored in the code, and therefore it will not accurately model the imaging situations for which these effects become more predominant, i.e. for photon energies above 300 keV. Secondly, the

code does not account for contributions due to Rayleigh scattering, and therefore does not accurately model the scatter contribution for energies below approximately 100 keV. Finally, the code only accounts for contributions up to second-order, and therefore will not account for the contributions due to the higher orders required for wide energy windows (>30%).

Accounting for collimator scattering and penetration effectively requires incorporating the collimator as part of the attenuation medium, and propagating the photons through the collimator to the scintillation crystal. However, the collimator provides a particularly difficult attenuating medium from a numerical perspective due to rapid and abrupt variations in the medium between the holes and the septa. This problem will require additional effort before a satisfactory solution can be obtained.

Extending the code to include Rayleigh scattering is straightforward and poses only a limited numerical challenge. It was not modeled within the current code because it is not a significant factor for the energy range considered (100 keV-200 keV). No extra integrations are required to calculate the Rayleigh contribution for each kernel order, but the integrand becomes significantly more complicated for higher order scattering contributions.

The code will only accurately model the experimental imaging situation for narrow energy windows (i.e. <25%) centered on the primary emission energy. To accurately model situations in which a wide energy window or lower energy window (i.e. Compton energy window) is used requires accounting for scattering events beyond the second-order. This is because the higher orders contribute a significant fraction of counts to the total for such windows. The direct numerical integration method used in development of the code can be used to calculate these higher orders, but such a method would be time consuming considering the increase in computing time required in going from zeroth-order to first-order and first-order to second-order. A better choice of integration method for

the higher order kernel calculation would be the Monte Carlo integration methods, and work in this area has begun.

Results calculated from the numerical code were compared with experiment, and the code was shown to accurately model the nonuniform experimental situation for both point and extended source distributions, provided a narrow energy window is used. Firstly, the calculated projections for point and extended sources in uniform and non-uniform attenuating media were compared with the projections obtained experimentally for the same imaging situation. Excellent agreement was obtained without any fitting parameters. The importance of scattered photons in forming the projections was quantitatively demonstrated. Secondly, the scatter fractions recorded for the entire 2D projection for both the calculated and experimental data were shown to be in good agreement, and well within the experimental error associated with the calculation of experimental scatter fractions. In all cases investigated, the difference between results calculated from the numerical code and those obtained from experiment was less than $\pm 5\%$.

The connectivity problem of the kernel was quantitatively investigated, within the context of source voxel – projection pixel connectivity. Such investigations should eventually allow for the calculation of kernels required for reliable application of iterative source reconstruction methods. It was demonstrated that the main factor determining the extent of such connectivity is photon scattering, with 3D depth-dependent collimator hole resolution being of secondary but still significant importance.

On a practical level, the analytical theory may be a starting point for developing the approximation schemes allowing much more efficient calculation of the photon detection kernel than in this work. The analytical theory may be used to calculate the parameters required for empirical scatter models of the kernel, in much the same way that Monte Carlo simulations have been exploited for these purposes. The advantage of such an approach is that a parameterized model of the scatter may eventually allow for the complete calculation of a reconstruction kernel for use with iterative reconstruction

methods such as the MLEM algorithm. The results calculated, being theoretical predictions of experiments or simulated results, are free of statistical error and, more importantly, can be obtained with readily available computer hardware. Another perhaps less obvious advantage of the analytical theory is the fact that it allows one to concentrate on a given region of the detector plane (i.e. a select subset of collimator holes such as a profile), and to calculate the contribution to this part due to each order separately. This opens the possibility of concentrating the numerical efforts on "difficult" regions of the projection or source volume, such as quantifying the uptake in a restricted volume (i.e. uptake in a localized tumor).

Having developed an accurate and efficient method of modeling the kernel, we hope that the statistical reconstruction techniques such as maximum likelihood and expectation maximization will perform better, allowing for accurate quantitative reconstruction of radioactive regions from Anger camera projections. In this work results of such a reconstruction were presented and qualitatively compared with reconstructions obtained using the popular Radon transform approach. It was observed that the MLEM reconstructions appeared to demonstrate better spatial resolution in the reconstructed transaxial planes as well as between the planes. More detailed analysis of results from such investigations is required before the true advantages of such a reconstruction procedure can be evaluated fully.

In conclusion, the theory presented provides a transparent tool for visualizing physical processes involved in photon propagation, attenuation and detection. It is also a robust and practical tool for calculating photon detection kernels for arbitrary source – attenuating medium configurations, provided the latter are known from some other complementary measurements. We believe that the theory may and should become a central tool for studying, in a unified fashion, the major image degradation effects associated with SPECT, including photon absorption, Compton scattering, depth-dependent collimator resolution, and intrinsic energy-dependent response of the detector. This theory provides a well-defined framework for numerical evaluation of accurate

kernels. However, before such kernels can be implemented in iterative reconstruction methods, more work is required to reduce them to a manageable size. For practical applications, further progress in computer algorithm coding and storage will also be necessary.

References

1. M. Brucer, "Nuclear medicine begins with a Boa Constrictor," in The Heritage of Nuclear Medicine, M. Brucer, C.C. Harris, W.J. MacInttyre, and G.V. Taplin (Eds.), the Society of Nuclear Medicine, (v-xxvi) 1979.

2. W.G. Myers and H.N. Wagner, "How it began," in Nuclear Medicine, H.N. Wagner (Ed.), H.P Publishing, New York, (3-16) 1974.

3. W. K. Roentgen, Ueber Eine Neue Art. 132, 1895.

4. H. Becquerel, "Sur les radiations invisibles émises par les corps phosphorescents," Comptes rendus de l'Academie des Sciences, Paris, 122: 501-503 (1896).

5. E. Rutherford, "A radio-active substance emitted from Thorium compounds", Phil. Mag. S. 5, (1900).

6. Curie M, Radioactive Substance 37, 1904.

7. E. Rutherford and F. Soddy, "The cause and nature of radioactivity," Phil. Mag. 6 (iv), 370-396, (1902).

8. G. Hevesy, "The absorption and translocation of lead by plants. A contribution to the application of the method of radioactive indicators in the investigation of the change of substance in plants.", Bioch. XVII, 29 (1923).

9. H. L. Blumgart and O.C. Yens, "Studies of the velocity of blood flow," J. Clinical Investigations, Vol. IV, No. 1, 1926.

10. E. Rutherford, "The scattering of a and b particles by matter and the structure of the atom," Phil. Mag. S. (xxi), 669-688 (1911).

11. F. Joliot and I. Curie, "Artificial production of a New kind of radio-element," Nature Feb. 1934.

12. E. Lawrence and M. S. Livingston, "Production of high speed light ions without the use of high voltages," Phys. Rev. 40, 19- (1932)

13. J. Chadwick, "Possible existence of a neutron," Letter to the Editor, Nature No. 3252, Vol. 129, Feb.1932.

14. E. Fermi, "Radioactivity induced by neutron Bombardment," Letter to the Editor, Nature May 1934.

15. J. J. Livingood and G. T. Seaborg, "Radioactive Iodine Isotopes," Letter to the Editor, Phys. Review 53, 1015 (1938).

16. E. Segrè and G. T. Seaborg, "Nuclear isomerism in element 43," Phys. Rev. 54, 772 (1938).

17. Manhattan Projection, "Availability of radioactive isotopes. Announcement from Headquarters, Manhattan Project, Washington, DC," Science 103, 697-705 (1946).

18. H. Geiger and W. Muller, "The electron counting tube," Z. Phys. 29, 839-841 (1928).

19. H. Kallman, Natur and Technik (July 1974)

20. R. Hofstadter, "Alkali Halide Scintillation Counters," Phys. Review 74, 100 (1948).

21. B. Cassen, L. Curtis, C. Reed, and R. Libby, "Instrumentation for I131 use in medical studies," Nucleonics 9, 46-50 (1951)

22. H. O. Anger, "Scintillation camera," The review of scientific instruments 29, 27-33 (1958).

23. D. E. Kuhl and R. Q. Edwards, "Image separation radioisotope scanning," Radiology 80, 653-662, 1963.

24. D. E. Kuhl and R. Q. Edwards, "Cylindrical and section radioisotope scanning of the liver and brain," Radiology 83, 926-935 (1964).

25. A. M. Cormack, "Representation of a function by its line integrals with some radiological applications," J. Appl. Phys. 34, 2722-2727 (1963).

26. A. M. Cormack, "Representation of a function by its line integrals with some radiological applications (II)," J. Appl. Phys. 35, 2908-2913 (1964).

27. A. M. Cormack, "Reconstruction of densities from their projections with applications in radiological physics," Phys. Med. Biol. 18, 195 (1973).

28. J. Radon, "Uber due bestimmung von funktionen durch ihre intregralwerte langs gewisser mannigfaltigkeiten", Berichte Saechsische Akademie der Wissenschaften 29, 262-277 (1917).

29. R. T. Anger, "The Anger scintillation camera - A review," in Physics in Nuclear Medicine - Recent Advances. D.V. Rao, R. Chandra, M.C. Graham (eds.), American Institute of Physics, New York, 32-35 (1984).

30. R. Chandra, Introductory Physics of Nuclear Medicine, (Lea & Gebiger, Philadelphia, 1982), Chapters 11 and 12.

31. R. L. Richardson, "Anger scintillation camera," in Nuclear Medicine Physics, Instrumentation, and Agents. F.D. Rollo (ed.), C.V. Mosby Company, St. Louis, 231-270 (1977).

32. J. A. Sorenson and M. E. Phelps, Physics in Nuclear Medicine, 2ed, (Grune & Stratton, Orlando, Fl, 1987).

33. R. E. Zimmerman, "Recent developments in Anger cameras," in Physics in Nuclear Medicine - Recent Advance. D.V. Rao, R. Chandra, M.C. Graham (eds.), American Institute of Physics, New York, 59-67 (1984).

34. T. F. Budinger, G. T. Gullberg, R. H. Huesman, "Emission computed tomography," in Image Reconstruction from Projections - Implementation and Applications. G.T. Herman (ed.), Springer-Verlag, New York, Chapter 5 (1979).

35. G. T. Herman, Image Reconstruction from Projections - The fundamentals of Computerized Tomography, (New York, Academic Press, Inc., 1980).

36. A. C. Kak and M. Slaney, Principles of Computerized Tomographic Imaging, (New York, IEEE Press, 1988).

37. R. J. Jaszczak, "SPECT," in Physics in Nuclear Medicine - Recent Advances. D.V. Rao, R. Chandra, M.C. Graham (eds.), American Institute of Physics, New York, 457-482 (1984).

38. A. H. Compton, "A quantum theory of the scattering of x-rays by light elements," Phys. Rev. 21, 483-502 (1923).

39. O. Klein and Y. Nishina, "Uber die streuung von strahlung durch frei elektronen nach der neven relativistischen quantendynamik von Dirac," Z. Physik 52, 853-868 (1929).

40. W. R. Leo, Techniques for Nuclear and Particle Physics Experiments, (Springer-Verlag, Berlin Heidelberg, 1987), pp. 53.

41. H. Attix, Introduction to Radiological Physics and Radiation Dosimetry, (John Wiley and Sons, Inc., 1986).

42. H. E. Johns and J. R. Cunningham, The Physics of Radiology, 3ed., (Charles C. Thomas, Illinois, 1977), Chapter 5.

43. L. Rayleigh, Phil. Mag. XLI, 107, 274 (1899).

44. F. D. Rollo and C. Craig, "Factors affecting image formation," in Nuclear Medicine Physics, Instrumentation, and Agents. F.D. Rollo (ed.), C.V. Mosby Company, St. Louis, 231-270 (1977).

45. G. T. Gullberg, G. L. Zeng, F. L. Datz, P. E. Christian, C-H Tung, and M. T. Morgan, "Review of convergent beam tomography in single photon emission computed tomography," Phys. Med. Biol. 37, 507-534 (1992).

46. E. C. Frey and B. M. W. Tsui, "Parameterization of the scatter response function in SPECT imaging using Monte Carlo simulations," IEEE Trans. Nuc. Sci. 37, 1308-1315 (1990).

47. X. Wang and K. F. Koral, "A regularized deconvolution-fitting method for Compton-scatter correction in SPECT," IEEE Trans. Med. Im. 11, 351-360 (1992).

48. G. F. Knoll, Radiation Detection and Measurement, (New York, Wiley and Sons, 1979), pp. 335-336.

49. Natl. Bur. Stand. Appl. Math. Ser. No. 55, Edited by M. Abramowitz and I. A. Stegun (U.S. GPO, Washington, D.C., 1965).

50. J. W. Beck, R. J. Jaszczak, R. E. Coleman, et al, "Analysis of SPECT including scatter and attenuation using sophisticated Monte Carlo modeling methods," IEEE Trans. Nucl. Sci. NS-29, 506-511 (1982).

51. R. J. Jaszczak, R. E. Coleman, and F. R. Whitehead, "Physical factors affecting quantitative measurements using camera-based single photon emission tomography (SPECT)," IEEE Trans. Nucl. Sci. 28, 69 (1981).

52. F. D. Rollo, "Factors affecting image formation," in Nuclear Medicine Physics, Instrumentation, and Agents. F.D. Rollo (ed.), C.V. Mosby Company, St. Louis, 387-435 (1977).

53. P. M. Martin, "Nuclear medicine statistics," in Nuclear Medicine Physics, Instrumentation, and Agents. F.D. Rollo (ed.), C.V. Mosby Company, St. Louis, 479-512 (1977).

54. M. F. Smith, C. E. Floyd, R. J. Jaszczak, and R. Edward, "Three-dimensional Photon Detection Kernels and their application to SPECT reconstruction," Phys. Med. Biol. 37, 605-622 (1992).

55. M. A. King, P. W. Doherty, R. S. Schwinger, "Digital image filtering of nuclear medicine images," in Physics in Nuclear Medicine - Recent Advances. D.V. Rao, R. Chandra, M.C. Graham (eds.), American Institute of Physics, New York, 310-331 (1984).

56. T. A. Riauka, "Scatter and attenuation correction techniques for single photon emission computed tomography," M.Sc. Thesis, Department of Physics, University of Alberta, Edmonton, 1991.

57. R. J. Jaszczak, C. E. Floyd, Jr., and R. E. Coleman, "Scatter compensation techniques for SPECT," IEEE Trans. Nuc. Sci., NS-32, 786-793, (1985).

58. P. Msaki, B. Axelsson, C. M. Dahl, and S. A. Larsson, "Generalized scatter correction method in SPECT using point scatter distribution functions," J. Nuc. Med. 28, 1861-1869 (1987).

59. J. C. Yanch, M. A. Flower, and S. Webb, "Improved quantification of radionuclide uptake using deconvolution and window subtraction techniques for scatter compensation in single photon emission computed tomography," Med. Phys. 17, 1011-1021 (1990).

60. S. D. Egbert and R. S. May, "An integral-transport method for Compton-scatter correction in emission computed tomography," IEEE Trans. Nuc. Sci. NS-27, 543-547 (1980).

61. T. Herbert, P. Murphy, W. Moore, R. Dhekne, R. Wendt, and M. Blust, "Experimentally determining a parametric model for the point source response of the gamma camera," IEEE Trans. Nuc. Sci. 40, 967-971 (1993).

62. P. Msaki, B. Axelsson, and S. A. Larsson, "Some physical factors influencing the accuracy of convolution scatter correction in SPECT," Phys. Med. Biol. 34, 283-298 (1989).

63. P. Msaki, K. Erlandsson, L. Svensson, and L. Nolstedt, "The convolution scatter subtraction hypothesis and its validity domain in radioisotope imaging," Phys. Med. Biol. 38, 1359-1370 (1993).

64. M. Ljungberg, P. Msaki, and S-E Strand, "Comparison of dual-window and convolution scatter correction techniques using the Monte Carlo method," Phys. Med. Biol. 8, 1099-1110 (1990).

65. J. C. Yanch, M. A. Flower, and S. Webb, "A comparison of deconvolution and window subtraction techniques for scatter compensation in SPECT," IEEE Trans. Med. Im. 7, 13-20 (1988).

66. R. J. Jaszczak, K.L. Greer, C. E. Floyd, Jr., C.C. Harris, and R. E. Coleman, "Improved SPECT quantitation using compensation for scattered photons," J. Nuc. Med. 25, 893-900 (1984).

67. B. E. Oppenheim, "Scatter correction for SPECT," J. Nuc. Med. 25, 928-929 (1984).

68. K. F. Koral, F. M. Swailem, S. Buchbinder, N. H. Clinthorne, W. L. Rogers, and B. M. W. Tsui, "SPECT dual-energy-window Compton correction: Scatter multiplier required for quantification," J. Nuc. Med. 31, 90-98 (1990).

69. J. J. Hamill and R. P. DeVito, "Scatter reduction with energy-weighted acquisition," IEEE Trans. Nuc. Sci. 36, 1334-1339 (1989).

70. S. Bellini, M. Piacentini, C. Cafforio, and F. Rocca, "Compensation of tissue absorption in emission tomography," IEEE Trans. Acoustics, Speech, and Sig. Proc. ASSP-27, 213-218 (1979).

71. L. T. Chang, "A method for attenuation correction in radionuclide computed tomography," IEEE Trans. Nucl. Sci. 25, 638-643 (1978).

72. K. Lange, M. Bahn, and R. Lettle, "A theoretical study of some maximum likelihood algorithms for emission and transmission tomography," IEEE Trans. Med. Im. MI-6, 106-114 (1987).

73. K. Lange and R. Carson, "EM reconstruction algorithms for emission and transmission tomography," J. Comp. Assist. Tomogr. 8, 306-316 (1984).

74. A. J. Rockmore and A. Macovski, "A maximum likelihood approach to emission image reconstruction from projections," IEEE Trans. Nuc. Sci. NS-23, 1428-1432 (1976).

75. L. A. Shepp and Y. Vardi, "Maximum likelihood reconstruction for emission tomography," IEEE Trans. Med. Im. MI-1, 113-122 (1982).

76. T. Herbert, R. Leahy, M. Singh, "Fast MLE for SPECT using an intermediate polar representation and a stopping criterion," IEEE Trans. Nuc. Sci. 35, 615-619 (1988).

77. J-S. Liow and S. C. Strother, "Practical tradeoffs between noise, quantitation, and number of iterations for maximum likelihood-based reconstructions," IEEE Trans. Med. Imaging 10, 563-571 (1991).

78. D. R. Gilland, B. M. W. Tsui, C. E. Metz, R. J. Jaszczak, and R. Perry, "An evaluation of maximum likelihood-expectation maximization reconstruction for SPECT by ROC analysis," J. Nucl. Med. 33, 451-457 (1992).

79. S. C. Liew, B. H. Hasegawa, J. K. Brown, and T. F. Lang, "Noise propagation in SPECT images reconstructed using an iterative maximum-likelihood algorithm," Phys. Med. Biol. 38, 1713-1726 (1993).

80. G. L. Zeng, G. T. Gullberg, B. M. W. Tsui, and J. A. Terry, "Three-dimensional iterative reconstruction algorithms with attenuation and geometric point response correction," IEEE Trans. Nuc. Sci. 38, 693-702 (1991).

81. T. J. Herbert and S. S. Gopal, "The GEM MAP algorithm with 3-D SPECT system response," IEEE Trans. Med. Im. 11, 81-90 (1992).

82. T. J. Herbert and R. Leahy, "Fast methods for including attenuation in the EM algorithm," IEEE Trans. Nuc. Sci. 37, 754-758 (1990).

83. B.M.W. Tsui, H-B. Hu, D.R. Gilland, and G.T. Gullberg, "Implementation of simultaneous attenuation and detector response correction in SPECT," IEEE Trans. Nuc. Sci. 35, 778-783 (1988).

84. Z. Liang, T. G. Turkington, D. R. Gilland, R. J. Jaszczak, and R. E. Coleman, "Simultaneous compensation for attenuation, scatter and detector response for SPECT reconstruction in three dimensions," Phys. Med. Biol. 37, 587-603 (1992).

85. J. E. Bowsher and C. E. Floyd, Jr., "Treatment of Compton scattering in maximum-likelihood, Expectation-Maximization reconstruction of SPECT images," J. Nucl. Med., 32, 1285-1291, (1991).

86. E. C. Frey, Z.-W. Ju, and B.M.W. Tsui, "A fast projector-backprojector pair modeling the asymmetric, spatially varying scatter response function for scatter compensation in SPECT imaging," IEEE Trans. Nuc. Sci. 40, 1192-1197 (1993).

87. E. C. Frey, Z.-W. Ju, and B.M.W. Tsui, "A practical method for incorporating scatter in a projector-backprojector for accurate scatter compensation in SPECT," IEEE Trans. Nuc. Sci. 40, 1107-1116 (1993).

88. C. E. Metz, F. B. Atkins, and R. N. Beck, "The geometric transfer function component for scintillation camera collimators with straight parallel holes," Phys. Med. Biol. 25, 1059-1070 (1980).

89. E. C. Frey and B. M. Tsui, "Parameterization of the scatter response function in SPECT imaging using Monte Carlo simulation," IEEE Trans. Nuc. Sci. 37, 1308-1315 (1990).

90. E. C. Frey and B. M. Tsui, "Spatial properties of the scatter response function in SPECT," IEEE Trans. Nuc. Sci. 38, 789-794 (1991).

91. E. C. Frey and B. M. Tsui, "Modeling the scatter response function in inhomogeneous scattering media for SPECT," IEEE Trans. Nuc. Sci. 41, 1585-1593 (1994).

92. Z-J. Cao, E. C. Frey and B. M. Tsui, "A scatter model for parallel and converging beam SPECT based on the Klein-Nishina formula," IEEE Trans. Nuc. Sci. 41, 1594-1600 (1994).

93. K. Ogawa, Y. Harata, T. Ichihara, A. Kubo, and S. Hashimoto, "A practical method for position-dependent Compton -scatter correction in single photon emission CT," IEEE Trans. Med. Im. 10, 408-412 (1991).

94. M. Lungberg and S-E. Strand, "Attenuation and scatter correction in SPECT for sources in a nonhomogeneous object: A Monte Carlo study," J. Nucl. Med. 32, 1278-1284 (1991).

95. F. J. Beekman, E. G. J. Eijkman, M. A. Viergever, G. F. Borm, and E. T. P.Slijpen, "Object shape dependent PSF model for SPECT imaging," IEEE Trans. Nuc. Sci., 40, 31-39 (1993).

96. T. Mukai, J. M. Links, K. H. Douglass, and H. N. Wagner Jr., "Scatter correction in SPECT using non-uniform attenuation data," Phys. Med. Biol. 33 (10), 1129-1140 (1988).

97. D. E. Rayside, "Monte Carlo principles and applications," Phys. Med. Biol. 21, 181-197 (1976).

98. C. E. Floyd, R. J. Jaszczak, C. C. Harris, and R. E. Coleman, "Energy and spatial distribution of Multiple order Compton scatter in SPECT: a Monte Carlo investigation," Phys. Med. Biol. 29, 1217-1230 (1984).

99. C. E. Floyd, R. J. Jaszczak, C. C. Harris, and R. E. Coleman, "Revised scatter fraction results for SPECT," Phys. Med. Biol. 32, 1663-1666 (1987).

100. C. E. Floyd, R. J. Jaszczak, and R. E. Coleman, "Inverse Monte Carlo: a unified reconstruction algorithm for SPECT," IEEE Trans. Nuc. Sci. NS-32, 779-785 (1985).

101. C. E. Floyd, R. J. Jaszczak, and R. E. Coleman, "Maximum likelihood reconstruction for SPECT with Monte Carlo modeling: Asymptotic behavior," IEEE Trans. Nuc. Sci. NS-34, 285-287 (1987).

102. T. A. Riauka and Z. W. Gortel, "Photon propagation and detection in single photon emission computed tomography - an analytical approach," Med. Phys. 21, 1311-1321 (1994).

103. W. Press, B.P. Flannery, S.A. Teukolsky, and W.T. Vetterling, Numerical Recipes, (Cambridge University Press, New York, 1986), Chapter 4, pp. 102-130.

104. J. S. Fleming, "A technique for using CT images in attenuation correction and quantification in SPECT," Nucl. Med. Comm. 10, 83-97 (1988).

105. K. F. Koral, R. K. Ten Haken, D. L. McShan, M. L. Kessler, S. Buchbinder, F. M. Swailem, I. R. Francis, M. S. Kaminski, and R. L. Wahl, "Superposition of SPECT and CT images and transfer of ROI for quantification", J. Nucl. Med. 31, 872 (1990).

106. R. J. Jaszczak, D. R. Gilland, S. Jang, K. L. Greer, and R. E. Coleman, "Fast transmission CT for determining attenuation maps using a collimated, shuttered line source and fan beam," J. Nucl. Med. 34, 1577-1586 (1993).

107.K. Murase, S. Tanada, T. Inoue, Y. Sugawara, and K. Hamamoto, "Improvement of brain single photon emission tomography (SPET) using transmission data acquisition in a four-head SPET scanner," European J. of Nucl. Med. 20, 32-38 (1993)

108.S. H. Manglos, C. E. Floyd, R. J. Jaszczak, K. L. Greer, C. C. Harris, and R. E. Coleman, "Experimentally measured scatter fractions as a test of Monte Carlo Simulations," Phys. Med. Biol. 32, 335-343 (1987).